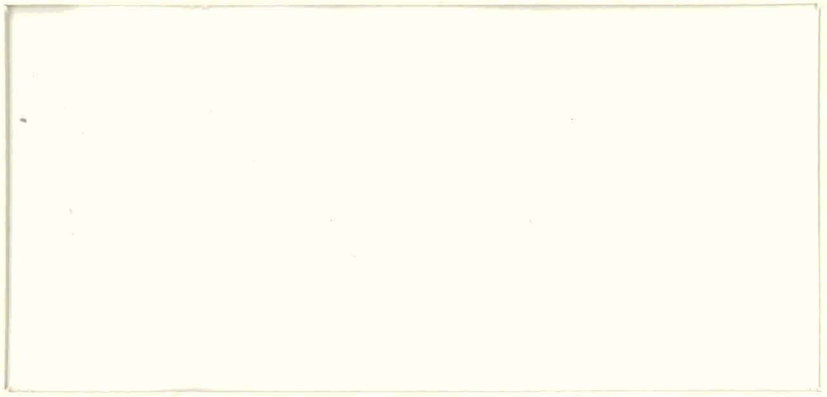

Materials Science Center

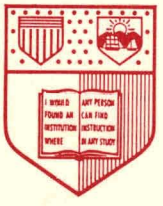

Cornell University
ITHACA, NEW YORK
14853

DISCLAIMER

This report has been prepared by
the Central Report Facility of the
Materials Science Center.

DOE/ER/03158-92

DIRECT OBSERVATION OF THE PRIMARY STATE OF DAMAGE IN ION-IRRADIATED PLATINUM AND TUNGSTEN

by

Dipankar Pramanik

September 1980

Report #4300

Issued by

The Materials Science Center

Prepared for

THE U.S. DEPARTMENT OF ENERGY UNDER CONTRACT

No. DE-AC02-76ER03158

MSC Report #4300
DOE/ER/03[illegible]8-92

DIRECT OBSERVATION OF THE PRIMARY STATE OF DAMAGE IN ION-IRRADIATED PLATINUM AND TUNGSTEN

by

Dipankar Pramanik

. D. Thesis
August 1980

Research Group:
Prof. D. N. Seidman
MS&E

ACKNOWLEDGEMENTS

The author wishes to thank Professor David N. Seidman for serving as his major advisor and for his enthusiastic assistance and continuous encouragement throughout the course of this work. The author also wishes to thank Professor A.J. Sievers for serving as the chairman of his committee and Professor G.V. Chester for serving as his minor advisor.

Special thanks are accorded to Mr. R.F. Whitmarsh for his enthusiastic technical assistance and to Mrs. J. Givot for assistance in many stages of this work.

Special thanks are also extended to Dr. M.I. Current, Dr. M. Yamamoto and Mr. Roman Herschitz for many useful discussions.

This work was supported by the United States Department of Energy. Additional support was received from the National Science Foundation through the use of the technical facilities of the Materials Science Center at Cornell University.

TABLE OF CONTENTS

LIST OF TABLES

LIST OF FIGURES

DIRECT OBSERVATION OF THE

PRIMARY STATE OF DAMAGE IN

ION-IRRADIATED PLATINUM AND TUNGSTEN

Dipankar Pramanik, Ph.D.

Cornell University 1980

The primary state of damage in platinum and tungsten caused by ions of varying mass and energy, was investigated using the field ion microscope (FIM). The damage could be classified into three morphological types: (a) depleted zones (DZs); (b) voids; (c) dislocation loops. Platinum specimens of 99.999% purity were irradiated in situ at 60 K with 20 keV Kr^{+} ions to a dose of (3 to 5) x 10^{12} ion cm^{-2} and examined by the pulse field-evaporation technique at 60 K. The experimental conditions were created such that each depleted zone was created by a single incident ion. All three morphological types were observed. The average damage level, given by the number of vacancies per cascade (ν), was satisfactorily described by the modified Kinchin-Pease expression. The dimensions of the DZs is satisfactorily explained by the linear cascade theory. The cumulative damage profile obtained by summing over the damage due to individual DZs very rapidly approaches the theoretical damage profile as the number of DZs considered increased. The average structure of the DZs were similar to those produced in tungsten by ions of the same mass and energy. The dislocation loops were Frank loops and both vacancy and interstitial loops were observed. Evidence was obtained that the vacancy type dislocation loops were produced by the collapse of dense DZs. A detailed study was also made of the damage produced in four-pass zone-refined tungsten irradiated in situ at 10 K with

20, 45 and 60 keV W^+ ions to a dose of (2 to 10) x 10^{12} ions cm^{-2} and examined by pulse field-evaporation technique at 10 K. The quantity ν increased linearly with increasing projectile energy (E_1) according to the modified Kinchin-Pease formula. However, the dimensions of the DZs did not increase with E as expected from linear cascade theory and indicated a possible breakdown of this theory for dense DZs, produced by heavy ions incident on heavy targets. Evidence of the break up of DZs into subclusters at 60 keV was obtained. The fraction of DZs that collapsed to dislocation loops increased with increasing E_1. The effect of nonlinear cascades on the damage in tungsten was determined by comparing the damage produced by 20 keV W^+ and Ag^+ with that produced by 40 keV W_2^+ and Ag_2^+. The value of ν for the individual components of the dimer was 1.55 times the ν for the single atom ions, having the same energy. This clearly indicated the nonlinear effects associated with dense cascades. The fraction of DZs that collapsed to dislocation loops was also greater in the case of dimer irradiations of tungsten than for single atom ion irradiations.

I. INTRODUCTION

The topic of interaction of energetic ions with solids has led to an enormous volume of literature dealing with various physical aspects of the problem. Of immense importance is the damage which is produced when an energetic particle passes through a solid. The damage that is produced by a single ion occurs on an atomic scale, and its detailed observation therefore requires instruments that are capable of atomic resolution. The field-ion microscope (FIM) is the only instrument that is routinely capable of looking at single atoms and it is therefore extremely valuable in analyzing the damage caused by a single ion. The first application of FIM to the study of radiation damage was reported by Professor Erwin Müller[1-3] in 1960; this report was based on the research work of Sinha and Müller,[4] which was not published until 1964. Since then there have been numerous other reports on efforts to solve major problems in the field of radiation damage with the aid of the FIM technique.[5-8] Review articles on the FIM studies of radiation damage through 1968 have been written by both Müller[9] and Galligan.[10] An extensive review has also been written by Seidman in four recent articles.[11-14] Wei[15] described a method of accurately mapping out and displaying in three dimensions the damage created by a single incoming ion and used it to show the effect of increasing ion mass, on the damage in tungsten (W).

The point defect structure of the damage is dependent on the mass and energy of the incoming ion, the mass of the target atoms, the material properties of the target and the irradiation temperature. We are in the main interested in the primary state of damage, that is, the damage

created by the incoming ion when the point defects that are produced are immobile. The effect of temperature on the nature of damage is itself a big subject, and we will not discuss this aspect in any detail. All our experimental work was done at low temperatures where all defects are immobile or at a temperature where a single defect type was mobile. In this thesis we used the FIM to study how the damage is affected by:

(i) the nature of the target material by comparing the results in platinum and tungsten;

(ii) the effect of increasing the energy E_1 of the incoming ion for self-ion irradiations of tungsten; and,

(iii) the nature of the bombarding ion by comparing the results of atomic (monomers) and molecular (dimer) ion irradiations of tungsten.

In order to give a perspective of the nature of the problems that have been addressed in this thesis, a brief outline of the fundamental problems in radiation damage is given below. We have underlined terms and concepts that are important and are used over and over again in the thesis, when they are first introduced.

I.1 Energy loss

All the damage that is produced inside a target by ion-irradiation is the result of the loss of all or part of the energy of the projectile ion inside the target. The projectile loses energy through a series of collisions with the target atoms. In these collisions, energy is given to the target electrons (inelastic process) and momentum is transferred (elastic process) to the target nuclei during collisions. The different energy loss mechanisms, i.e., electronic and nuclear, are generally treated separately.[16-18]

The inelastic energy loss to the target electronic system can cause structural damage in both insulators and semiconductors,[19] whereas in metals this is not possible because of the very weak coupling between the conduction electrons and the lattice. In this case, the electronic energy loss is largely dissipated as heat. In metals, the exclusive process leading to damage, which is in the form of point defects, is a result of nuclear collisions in which elastic energy is transferred to the atoms of the target material.

The spatial distribution of the damage energy is important. The quantities that determine this are the energy (E_1), atomic number (Z_1), mass (M_1) of the projectile ion and the atomic number (Z_2), mass (M_2) of the target atom as well as the density (n) of the target material. In the theory of ion-stopping in solids,[18] it is useful to define two dimensionless parameters, the reduced length (ρ) and the reduced energy (ε):

$$\rho = \frac{\pi N a^2 M_1 M_2}{(M_1 + M_2)^2} x \qquad (1\text{-}1)$$

$$\varepsilon = E_1 \frac{a M_2}{Z_1 Z_2 e^2 (M_1 + M_2)} \qquad (1\text{-}2)$$

where x is a length, N is the scattering centers per unit volume, which is related to n, e is the charge on an electron. The quantity a is the screening radius given by:

$$a = 0.8853 a_0 (Z_1^{2/3} + Z_2^{2/3})^{-1/2} \qquad (1\text{-}3)$$

where a_0 is the Bohr radius of the hydrogen atom (0.529 Å).

The quantities ρ and ε are convenient quantities to use as it can be shown by the Linhard-Scharff-Schrott (LSS)[18] theory that electronic

and nuclear losses can be expressed in terms of ε alone, thus allowing various scaling laws to be utilized.

The electronic stopping power, (S_e) in dimensionless units is:

$$S_e = \left(\frac{d\varepsilon}{d\rho}\right)_e = k\varepsilon^{1/2} \qquad (1\text{-}4)$$

where

$$k = \frac{0.0793\ Z_1^{2/3} Z_2^{2/3} (M_1+M_2)^{3/2}}{(Z_1^{2/3}+Z_2^{2/3})^{3/4} M_1^{2/3} M_2^{1/2}} \qquad (1\text{-}5)$$

The variations of electronic and nuclear losses with ε is shown in figure 1 and shows that for small values of ε, nuclear stopping predominates. Consequently, the range of the projectile, that is, the distance the ion penetrates the target, is governed by the nuclear stopping power (S_n).

Winterbon, Sigmund and Sanders (WSS) used the LSS formulation to obtain the projectile's total path length as a function of energy for ε smaller than 0.2. By integrating the nuclear stopping power,

$$S_n = d\varepsilon/(d\rho_{pl})_n = 0.98\varepsilon^{1/3} \qquad (1\text{-}6)$$

they obtained:

$$\rho_{pl}(\varepsilon) = 1.53\varepsilon^{2/3} \qquad (1\text{-}7)$$

where ρ_{pl} is the LSS dimensionless total path length.

I.1.1 Range profiles and damage profiles

In fig. 2 we show the path of three 20 keV. Ag^+ ions incident on tungsten. As pointed out before, the ions come to rest inside the target after dissipating their energy in a series of collisions with the target atoms. Due to statistical fluctuations in the dynamics of

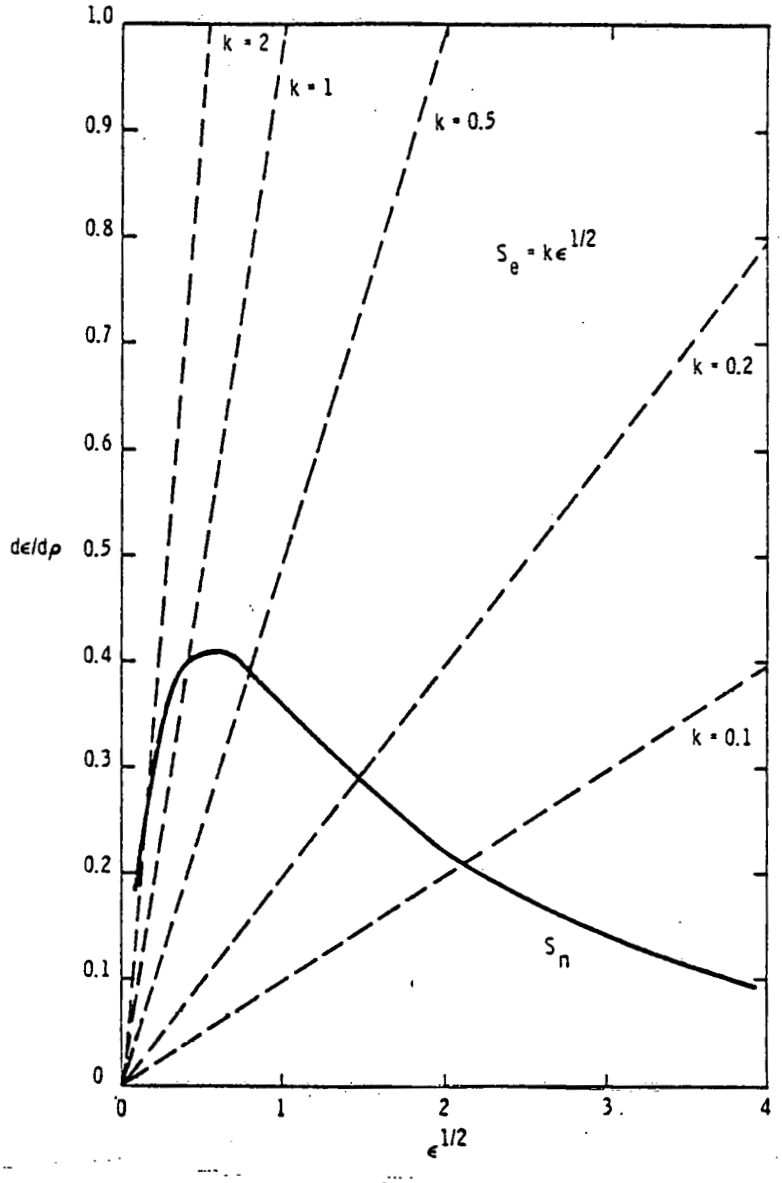

Fig. 1: Nuclear stopping (solid curve) and electronic stopping (dashed curves) as calculated by the LSS theory for various values of k.

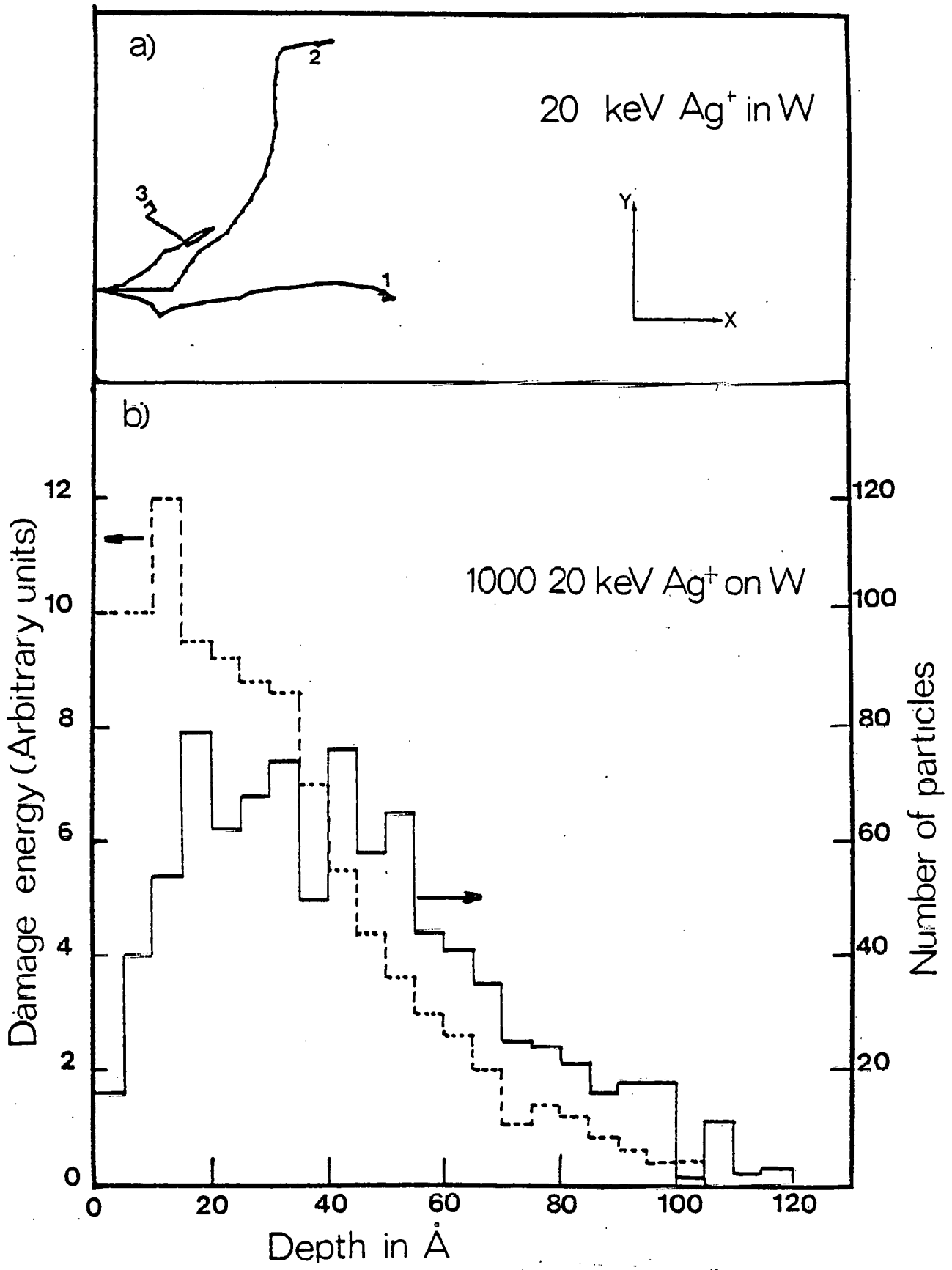

Fig. 2: Illustration of the concepts of range and damage profile produced by ions incident on a solid.

ion-ion collisions, each of the ions loses its energy in different ways and comes to rest at different points within the target. If we consider a beam consisting of many such ions, we can define two distributions. The first, called the range profile, gives the distribution of ions as a function of depth x measured parallel to the direction of the incident ion beam. The second, the damage profile, gives the distribution of the net deposited energy as a function of x. These are displayed in 2(b). Both 2(a) and 2(b) were drawn using the TRIM program of Biersack and Haggmark.

Note that the range profile is governed by the series of binary collisions which the projectile experiences along its path. The damage profile should also be determined by this. Thus, the shape of both profiles is determined by the nature of the interatomic potentials which will determine the cross-sections for energy transfer between the projectile and target atoms in an elastic collision. The recoil energy transferred to the target atoms along the projectile path will cause these to collide with other target atoms, which in turn will collide with others and so on. While this process will not affect the range profile, it may affect the shape of the damage profile.

The theoretical method for determining the range and damage profile are similar and are based on linear transport theories.[21] The damage profiles are obtained by extending Linhard's Thomas-Fermi description to include the recoil atoms as well as the primary ion. Again, the nuclear loss $\hat{E}$ (damage energy) and the electronic loss $\hat{Q}$ can be separated with $E_1 = \hat{E} + \hat{Q}$. Note that $\hat{E}$ is usually 20-30% smaller than the total nuclear stopping power of the projectile because the energetic recoils created along the track of the primary ion lose some of their kinetic energy

by electron excitation.

I.1.2 Collision cascade

As pointed out, the projectile ion loses its energy through a series of collisions with the target atoms, until its energy falls below a certain minimum value and it comes to rest. If, in these collisions, it transfers elastic energy greater than a certain minimum threshold displacement energy (E_d) to a target atom, this atom is displaced. If this recoil atom receives a large enough energy, it can itself cause displacements of other atoms and so on. In this process, a large number of atoms will be displaced and we have what is termed a collision cascade. In fig. 3, we illustrate this process. The thick solid line represents the path of the projectile ion, in this case a 20 keV W^+. The tracks branching out from it represent the path of recoil atoms in the target which is W. The target has been assumed to be amorphous, E_d = 43eV, and the track of all recoil atoms has been followed until their energy falls below 10 eV. The cascade was simulated using the program TRIM of Biersack and Haggmark.[20] Notice that a large fraction of the recoil atoms are the results of third or higher order generation collisions. The collision cascade effectively ends when the energy of all the recoil atoms falls below E_d, because no further displaced atoms can be produced.

The collision cascade gives the manner in which the energy of a single projectile is distributed spatially. Because of statistical fluctuations, the cascades due to different projectiles of the same mass and energy can be very dissimilar. However, the damage profile referred to in the previous section can be obtained by averaging the results of several hundred such cascades. This is the basis for obtaining the

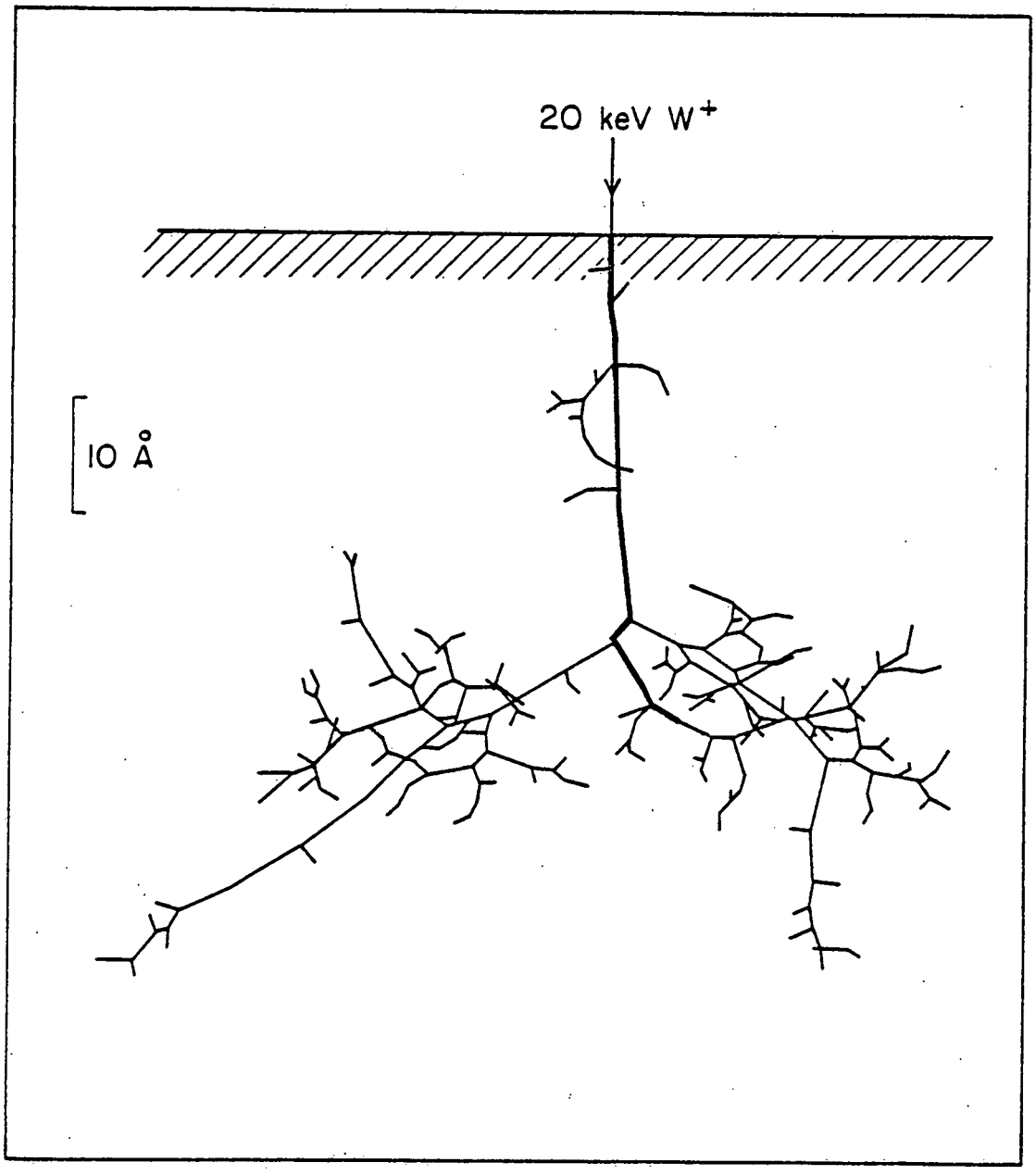

Fig. 3: A collision cascade in tungsten produced by a 20 keV W^+ ion. The solid line indicates the path of the projectile inside the target, and the lighter line the path of the recoil atoms.

damage profile from Monte-Carlo computer techniques. Excellent agreement is obtained between this approach and the analytical techniques based on transport theories.[20,23] The reverse process, i.e., obtaining the deposited energy distribution for individual cascades from the damage profile, is more difficult. Attempts have been made to do this analytically by using contraction factors.[22] In this respect, the Monte-Carlo computer calculations are more useful, as they allow the simulation of individual cascades.

The important problem is how this deposited energy manifests itself physically. In metals, the collision cascade leads to the creation of vacancies. In the simplest picture of damage, it is assumed that a vacancy is produced every time that a target atom is given an energy greater than E_d and the recoiling incident ion has an energy also larger than E_d. In fig. 4, we show a collision cascade for 20 keV Pt^+ on Pt showing only the positions of the vacancies and the ion path. We have not shown the positions of the interstitials. This collection of vacancies formed from the collision cascade we call a depleted zone (DZ).

A measure of the degree of damage is given by the number of vacancies per cascade (ν). ν is directly proportional to E because the vast majority of cascade atoms are generated from low-energy collisions. The Kinchin-Pease formula[24] gives:

$$\nu_{K-P} = \frac{E_1}{2E_d} \qquad (1\text{-}8)$$

which can be derived from simple kinematic considerations, with the assumption of a single E_d and binary collisions. Note that ν_{K-P} is independent of the mass of the ion. The spatial distribution of vacancies is,

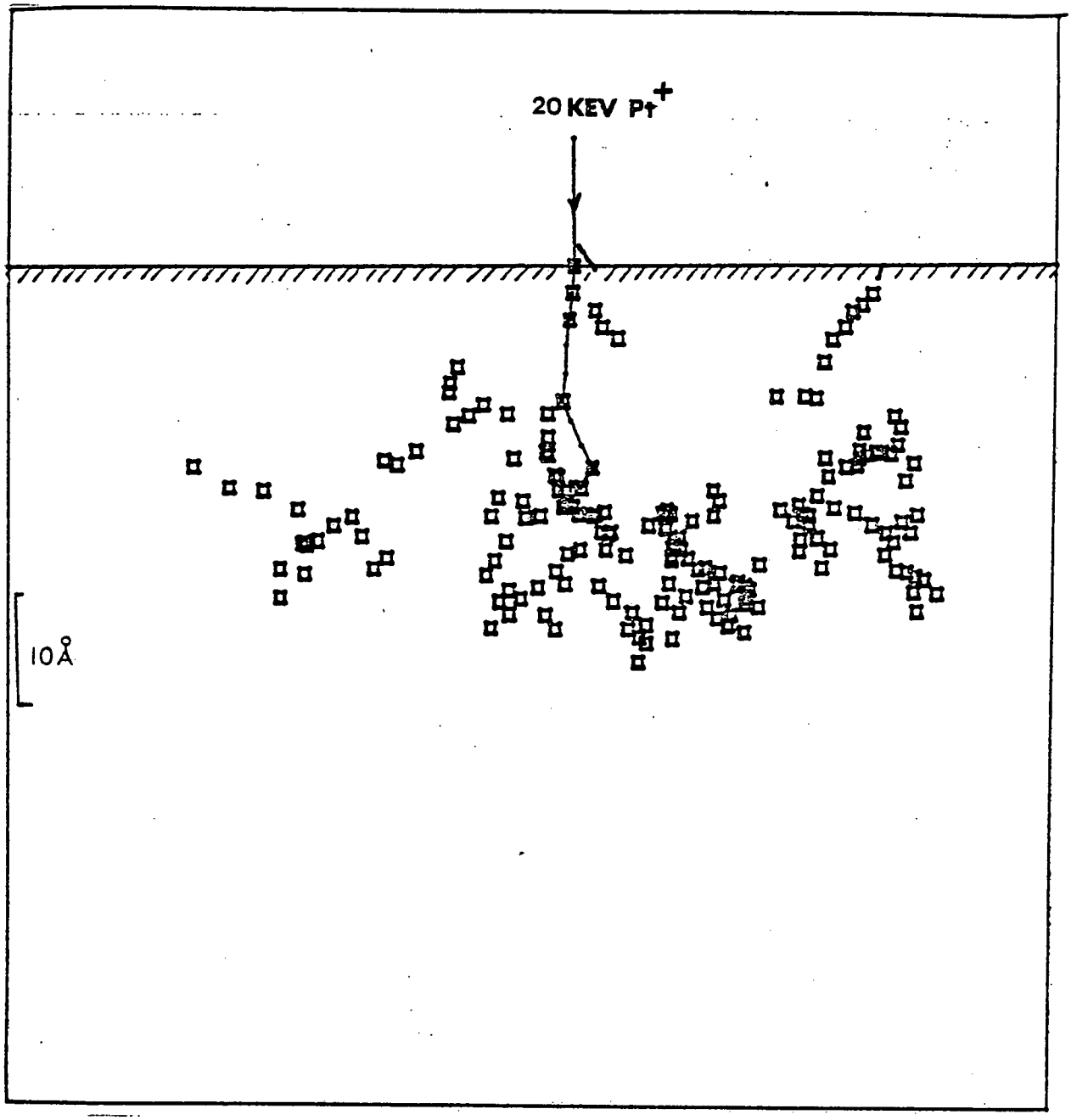

Fig. 4: Depleted zone produced in platinum by a 20 keV Pt^+ ion. The open squares represent vacancies, the solid line the path of the projectile.

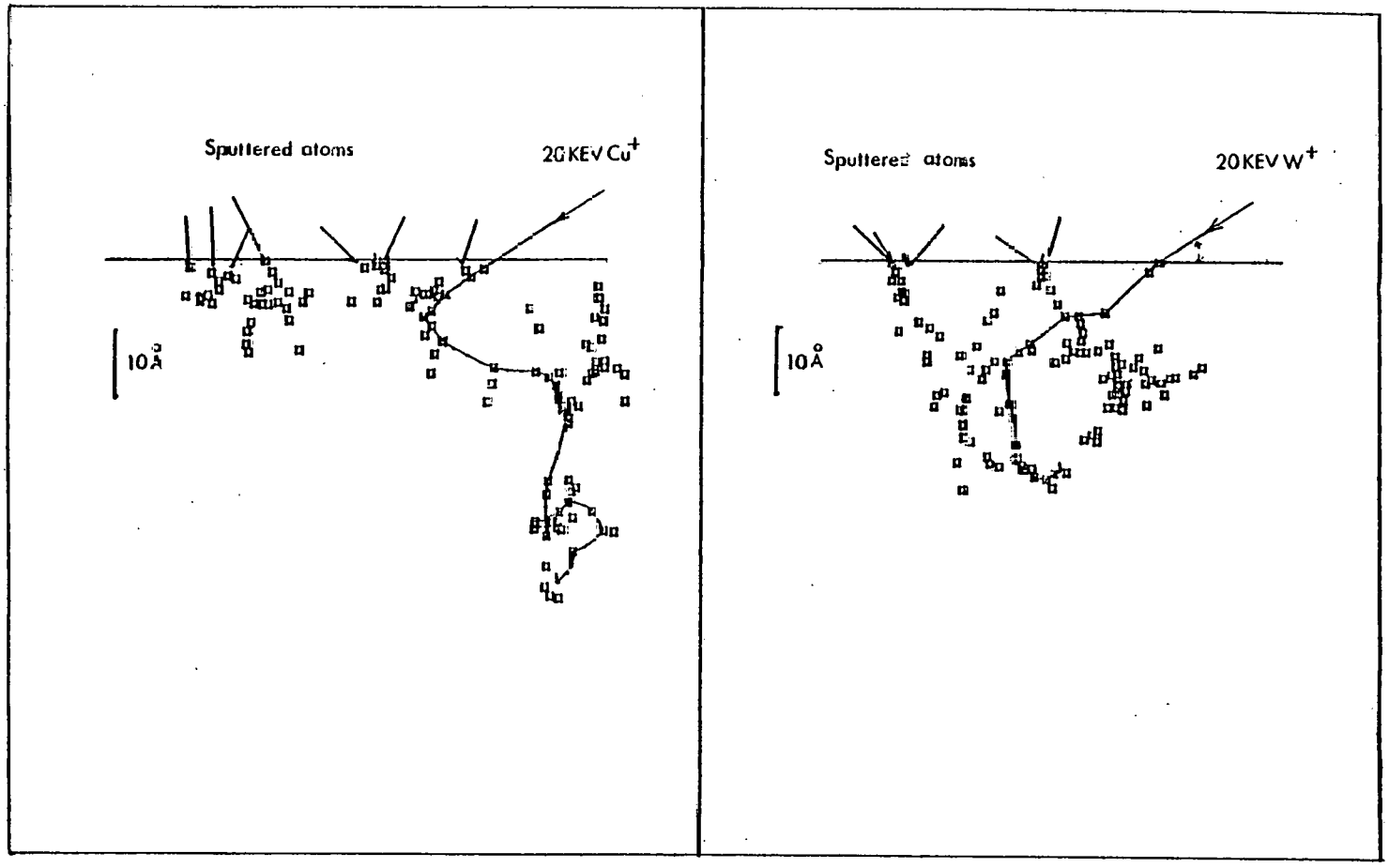

Fig. 5: (a) Depleted zone produced in tungsten by 20 keV Cu^+ ion.
(b) Depleted zone produced in tungsten by 20 keV W^+ ion.
Sputtered atoms produced in the collision cascade are also shown.

however, affected by M_1/M_2. Figure 5, (a) and (b), shows cascades due to 20 keV Cu^+ ions on W and 20 keV W^+ on W respectively. The total path length of the Cu ion is greater than that of the W ion. The Cu cascade is more spread out than the W cascade even though both have approximately the same ν. In general, the cascades become smaller in size as M_1/M_2 increases because the collision cross-section for a large energy transfer decreases with decreasing M_1, Z_1. As a consequence, the energy of a light ion is dissipated in a series of collisions involving the transfer of small amounts of energy to the target atoms, while that of a heavy ion is dissipated in a few collisions involving large transfers, which are spatially close together. The average distance between high recoil energy collisions is called the mean free path (λ^*). The value of λ^* determines the volume in which the energy is distributed and, hence, the energy density (θ) and the related defect concentration (c_v). The quantity, θ, is a crucial factor that can affect the total damage. Figure 6 shows two different ways of how energy may be dissipated by an energetic particle in a solid via elastic collisions. Figure 6(a) shows a linear collision cascade and fig. 6(b) a non-linear cascade. In both cases, the energy is ultimately shared by a great number of atoms. The difference between the two situations lies in the fact that while only a small fraction of all atoms within a certain cascade volume are in motion in fig. 6(a), essentially all atoms within a certain cascade volume move in fig. 6(b). The picture of a linear cascade applies when λ^* is large whereas, in a non-linear cascade, λ^* is very small, so that the energy is shared with all the atoms in a spike volume.

In a linear collision cascade, the approximations of binary

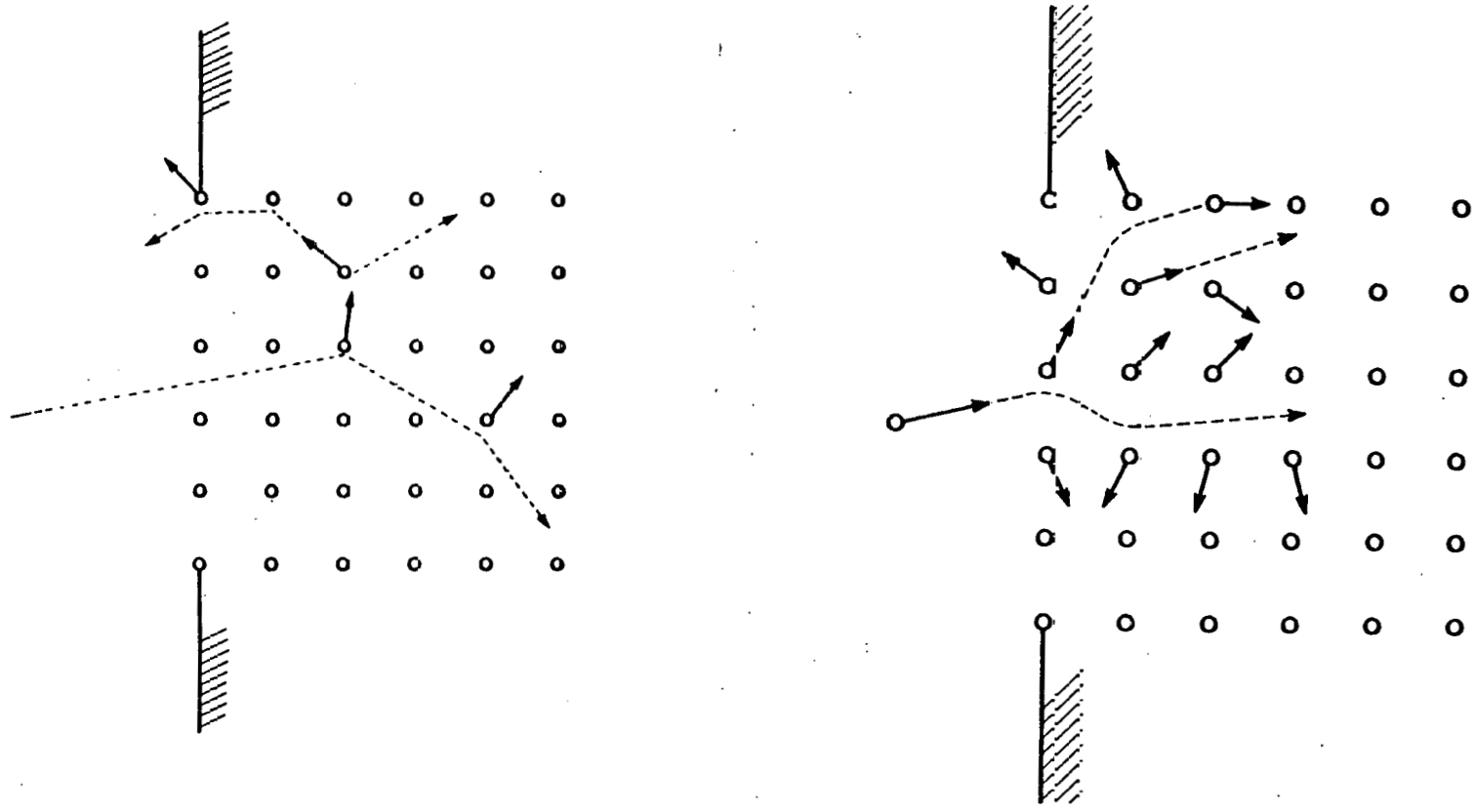

Fig. 6: (a) A linear cascade.
(b) A non-linear cascade.

collisions involved in the analytical theories based on linear transport theory are valid. The recoil energy spectrum, therefore, has an E^{-2} functional dependence[25] and ν, which is dependent on the nature of the recoil spectrum, has the form of eqn (1-8). In a non-linear cascade, these approximations break down; the recoil energy spectrum probably differs from the E^{-2} dependence and the value of ν is greater than ν_{K-P}.

The practical difference between the two situations is characterized most illustratively when two linear cascades (or non-linear cascades) are generated at the same time on top of each other. This can be realized in practice by bombardment with a dimer. When two linear cascades are superimposed, the statistical nature of the collision events will prevent a strict overlap in the two cascades. Because of the small fraction of atoms moving in either case, the two cascades superimpose so that the total number of moving atoms is twice as large as in either cascade, and the energy distribution among the atoms remains essentially unchanged. The system is <u>linear</u>. When two non-linear cascades are superimposed, on the other hand, energy will be dissipated essentially within the same cascade volume, i.e., the total number of atoms in motion will increase only insignificantly. Consequently, the available energy per atom must double approximately. Obviously, such a system is <u>non-linear</u>; hence the name. The non-linearity should appear in the damage levels. In a linear system, the net damage should be proportional to the number of impinging particles. In a non-linear system, such a simple relationship is not expected; for a dimer is expected to differ from the sum of the ν of the constituents of the dimer.

It is clear from the above pictures that the distinction between a

linear and a non-linear cascade is a matter of minimum energy an atom must have in order to be called "in motion." If this minimum energy is sufficiently high, the number of "moving" atoms will always be small enough that the linear cascade concept applies. Conversely, any cascade becomes like a non-linear cascade if the minimum energy is sufficiently small. In the case of radiation damage, this minimum energy will be characterized by E_d--the smaller the E_d, the more likely a non-linear cascade will occur.

On the basis of existing knowledge of ion ranges, it appears that the available spectrum of ion/target combinations as well as ion energies covers the whole range between pronounced linear and non-linear behavior. Roughly, non-linear cascades are generated by heavy ions in heavy targets at not too high ion energies (<100 keV) and vice versa for linear cascades.

The above distinction between linear and non-linear cascades on the basis of the spatial density of atoms set into motion raises the question of time scales, as it is clear that, in the initial stages of the collision cascade, only a few atoms will be in motion and the cascade may still be linear. In the later stages, the number of atoms in motion will be very large and the cascade is non-linear. The concept of linear and non-linear effects separated in time originates in earlier work of Thompson and Nelson.[29]

It is possible to define four basic time zones that exist when a heavy ion is implanted into a solid. These zones and their properties are outlined below.[26]

(1) Prompt collisional regime: (10^{-15} - 10^{-14} seconds). This consists of the first few violent collisions between the incident ion and

the substrate atoms. Note that the time involved is at least an order smaller than the time period of vibration of an atom in the target lattice (10^{-13} sec.) so that the approximation that the target atoms are at rest is quite valid. Linear collision cascade theory can adequately treat this regime and is the reason why it has been successful in predicting the range profiles of ions in solids.

(2) Slow collisional regime: (10^{-14} - 10^{-12} seconds). This is the time period during which the collision cascade develops and energetic knock-on effects, such as defect production and sputtering, occur. As mentioned previously, the earlier stages of development of the cascade should be well described by linear cascade theory, but the later stages may display properties of a non-linear cascade.

(3) Prompt thermal regime: (10^{-12} - 10^{-10} seconds). This is the time zone just after the end of the collision cascade when the energy of all the atoms has fallen below E_d, so that no more defects are produced. Leaving aside the interstitials, which in a crystalline material are transported by Replacement Collision Sequences (RCS's) away from the core of the DZ, many atoms in the collision cascade (which are therefore in the vicinity of the DZ) still possess a large amount of kinetic energy but probably still oscillate about a lattice site. Thus, we have a local region within the lattice which is in a highly excited state. The energy of this region eventually dissipates to the surrounding lattice. This transitional regime is by far the most complex and so far a satisfactory theoretical treatment has not been found. The time scale is too short for Maxwell-Boltzmann statistics to be applied or for the coupling between atomic motion and electronic excitation to reach equilibrium.

Hence, a true "temperature" cannot be assigned. On the other hand, the time scale is long enough for significant atomic motion to become distributed to all atoms in the cascade.

(4) Slow thermal regime: ($<10^{-10}$ seconds). Here, the time scale is long enough for energy sharing between atomic motion (phonons) and electronic excitation, and normal thermal conductivity considerations can be expected to apply. Unfortunately, in most metal or semiconductor implantations, the quenching rate is rapid enough to have already brought the cascade volume almost back to the substrate temperature before this stage.

During zone 3, there is the possibility of movement of atoms within the cascade volume as long as the kinetic energy of the atoms remain high. Significant changes in the local structural properties--such as mixing of components, as well as phase changes in case of alloys--can occur. The changes should be significant if the deposited energy density is very high. If the mean energy per atom θ is converted to temperatures by the thermodynamic relation, $\theta = \frac{3}{2} kT$, then temperatures as high as 10^4K can be obtained in cascades produced by heavy ions of moderate energy incident on heavy targets. This region, having a very high local energy density, is generally termed an "energy spike." During the period when this energy spike persists, which is zone 3, there is the possibility of rearrangement of vacancies in the DZ and the vacancy cluster may change its morphology. Both TEM and FIM results have shown the presence of dislocation loops, which are two-dimensional defect structures, even at very low temperatures, where the defects are immobile. The loops are caused by the collapse of DZ's. The mechanism of collapse is not known but it is

connected with c_v and ν as well as the material properties of the target. Experimental observations are always carried out after time scales that are far in excess of times during which rearrangement takes place and so the observed defect distribution may not necessarily be the distribution stemming from the original collision cascade.

The collapse of the DZ's into loops makes them visible in the TEM, owing to the large strain fields of the loops. However, as not all the DZ's collapse, much of the damage is not visible in the TEM. A quantity called the yield factor (Y) is defined by:

$$Y = \frac{\text{Loops (number cm}^{-2})}{\text{ion dose (number of ions cm}^{-2})}$$

For most materials, Y is less than 1. The FIM is superior to the TEM in this respect that it is capable of resolving all the defects, including individual point defects, defect clusters as well as loops.

Other techniques such as resistivity measurements on ion-irradiated thin films[27] and wire specimens, and Rutherford back-scattering (RBS)[28] have been employed to study defects. Both measure the average damage level for many DZ's and are not capable of telling anything about the spatial distribution of damage within individual DZ's.

The FIM results on DZ's were the experimental analog of the Monte Carlo computer calculations which simulate the effects of each individual projectile. The "cumulative" effects, i.e., the effects of a beam of ions, was obtained by averaging over the results of many ions. The analytical results based on transport theories deal with this cumulative distribution. With the FIM, we were able to see the fluctuations in individual DZ's as well as obtain results for the cumulative distribution

by averaging over the DZ's.

The cumulative distribution washed out the structural features of the individual DZ's. In many applications of ion beams, the properties of the cumulative damage distribution are only desired. However, it must be emphasized that individual events are very important. As pointed out, above the nature of the cascade may affect the damage level and also the morphology of the defect cluster (collapse into loops). The distinction between individual and cumulative effects are important as it underlines the importance of many atomic processes that occur during the collision cascade process. These processes may not be evident, when various gross properties of the material, representing the average over many events, are measured.

We end this section with a few comments on the subject of sputtering, which is closely connected with the phenomenon of radiation damage. In fig. 4 we saw that certain recoil atoms, near the surface--that are involved in the collision cascade--are ejected, provided that they possess sufficient kinetic energy to overcome the surface potential barrier. On the basis of this picture it is clear that the sputtering yield (S) defined by:

$$S = \frac{\text{no. of sputtered ions/cm}^2}{\text{incident ions cm}^{-2}}$$

is determined by the distance of the collision cascade from the surface, the spatial energy distribution as well as the recoil spectrum of the displaced atoms within the cascade. Clearly, the bulk of the sputtered ions will come from cascades close to the surface and the FIM with its high depth resolution is capable of analyzing the DZ's resulting from

these cascades. Note that because S is dependent on the recoil spectrum it should reflect any non-linearities in the cascade. The only problem is that S is an average over many cascades and over many quantities such as the energy and direction of the sputtered ions. The non-linearities have to be very pronounced to be noticeable in S. Here, once again, the ability of the FIM to detect individual DZ's allows fluctuations to be detected more easily than with any other method.

I.1.3 Prospectus of thesis

Chapter III examines the nature of the primary state of damage in Pt and compares it with that in W, so as to determine the effect of the material properties of the target on the final state of damage.

Chapter IV deals with the change in the nature of the damage in W as the energy of self-ions is increased. It examines both the properties of the DZ's as a function of E_1, as well as the change in the defect morphology.

Chapter V deals with the issue of non-linear cascades and non-linearities by comparing the damage state produced in W due to irradiation with heavy monomers (Ag^+ and W^+) with that caused by irradiation with dimers (Ag_2^+ and W_2^+).

REFERENCES FOR CHAPTER I

1. E.W. Müller, in: Proc 4th Intern Symp on the Reactivity of Solids, Ed. J.H. de Boer (Elsevier, Amsterdam, 1960), p. 682.

2. E.W. Müller, in: Direct Observations of Imperfections in Crystals, Eds. J.B. Newkirk and J.H. Wernick (Wiley-Interscience, New York, 1961), p. 77.

3. E.W. Müller, Ann. N.Y. Acad Sci 101 (1963) 585.

4. M.K. Sinha and E.W. Müller, J. Appl. Phys 35 (1964) 1256.

5. J.A. Hudson and B. Ralph, Phil Mag. 25 (1972) 265

6. M.J. Attardo and J.M. Galligan, Phys Rev Letters. 17 (1966) 191, M.J. Attardo and J.M. Galligam, Phys Rev. 161 (1967) 558.

7. P. Petroff and J. Washburn, Phys Status Solidi, 32 (1969) 527.

8. J.T. Buswell, Phil Mag. 23 (1971) 293.

9. E.W. Müller, in: Vacancies and Interstitials in Metals; Eds. A. Seeger, D. Schumacher, W. Schilling, and J. Diehl (North-Holland, Amsterdam, 1970) p. 557.

10. J.M. Galligan, Ibid., p. 575.

11. D.N. Seidman, J. Phys. F. (Metal Phys) 3, 393 (1973).

12. D.N. Seidman, K.L. Wilson and C.H. Nielsen, in: Fundamental Aspects of Radiation Damage in Metals, Eds. M.T. Robinson and F.W. Young, Jr. (National Technical Information Service, US Dept of Commerce, Springfield, VA, 1975), p. 373.

13. D.N. Seidman, in: Radiation Damage in Metals, Eds. N.L. Peterson and S.D. Harkness (American Society for Metals, Metals Park, OH 1976), p. 28.

14. D.N. Seidman, Surf Sci, 70, 532 (1978).

15. C.Y. Wei, PhD Thesis, Cornell University (1978).

16. W.D. Wilson, L.G. Haggmark and J.P. Biersack, Phys. Rev. B15, 254 (1977)

17. D.K. Brice in: Ion Implantation in Semiconductor and Other Materials, ed., B.L. Crowder (Plenum, N.Y., 1973), p. 171.

18. J. Linhard, J.M. Scharff and H.E. Schiott, kgl Danske Videnskab Selskab. Mat.-Fys. Medd. 33, No 14 (1963).

19. J.W. Meyer, L. Erikson and J.A. Davis, Ion Implantations in Semiconductors (Academic Press, NY 1970)

20. J. Biersack and L. Haggmark, unpublished report, to appear in J. Nucl Materials (1980).

21. K.B. Winterbon, P Sigmund and J.B. Sanders, Kgl. Danske Videnskab. Selskab, Mat-Fys. Medd 37, No 14 (1970).

22. P. Sigmund, G.P. Scheidler and G. Roth, in Proc Int Conf: Solid-State Physics Research with Accelerators, Brookhaven National Laboratory Report. No. 50083 (1968), p. 374 (unpublished).

23. O.S. Oen, D.K. Holmes and M-T Robinson, J. App. Phys 34, 302 (1963).

24. G.H. Kinchin and R.S. Pease, Rep Prog. Phys. 18, 1, (1955).

25. M.W. Thompson: Phil Mag. 18, 377 (1968).

26. R. Kelly, Proceedings of the International Conference on Ion Beam Modification of Materials, (Budapest 78).

27. R.S. Averback, R. Benedek, and K.L. Merkle, Phys Rev B 18 (1978) 4156.

28. D.A. Thompson and R.S. Walker, Rad Eff. 36, 91 (78).

29. M.W. Thompson, R.S. Nelson, Phil Mag. 7, 2015 ('62).

II. EXPERIMENTAL DETAILS

II. 1 Experimental set up

The experimental set up consists basically of two main sections, as shown in fig. 7--the ion accelerator and the field-ion microscope (FIM). The pressure in the accelerator, when in operation, was usually 10^{-5} torr while that in the FIM was maintained at $<2 \times 10^{-9}$ torr in the absence of the imaging gas. The pressure differential between the two sections was maintained by operating them by a three-stage differential pumping system. The FIM specimens were irradiated at the temperature at which they were imaged, with the imaging field off, and in the absence of the imaging gas. The time required for the irradiation to the desired dose was usually less than the time required for one monolayer of CO to be adsorbed on the surface of the tip.

The accelerator was equipped with a Hill-Nelson sputtered metal ion source,[1,2] which could produce ions of gases introduced into the plasma chamber, or metallic ions produced by the sputtering of the corresponding metal target in the plasma. The positive ions were extracted through a small aperture and after acceleration to the desired voltage were mass-spectrometrically analyzed by an electromagnet in the horizontal direction. The ion current was measured with a flag in the flight tube placed before the entrance aperture to an FIM. By raising the flag the ion beam was made to impinge on the specimen. The beam current incident on the tip was measured, while simultaneously monitoring the profile of the beam, with a specially-designed Faraday cup. The beam was deflected horizontally and vertically by means of deflection plates placed before the

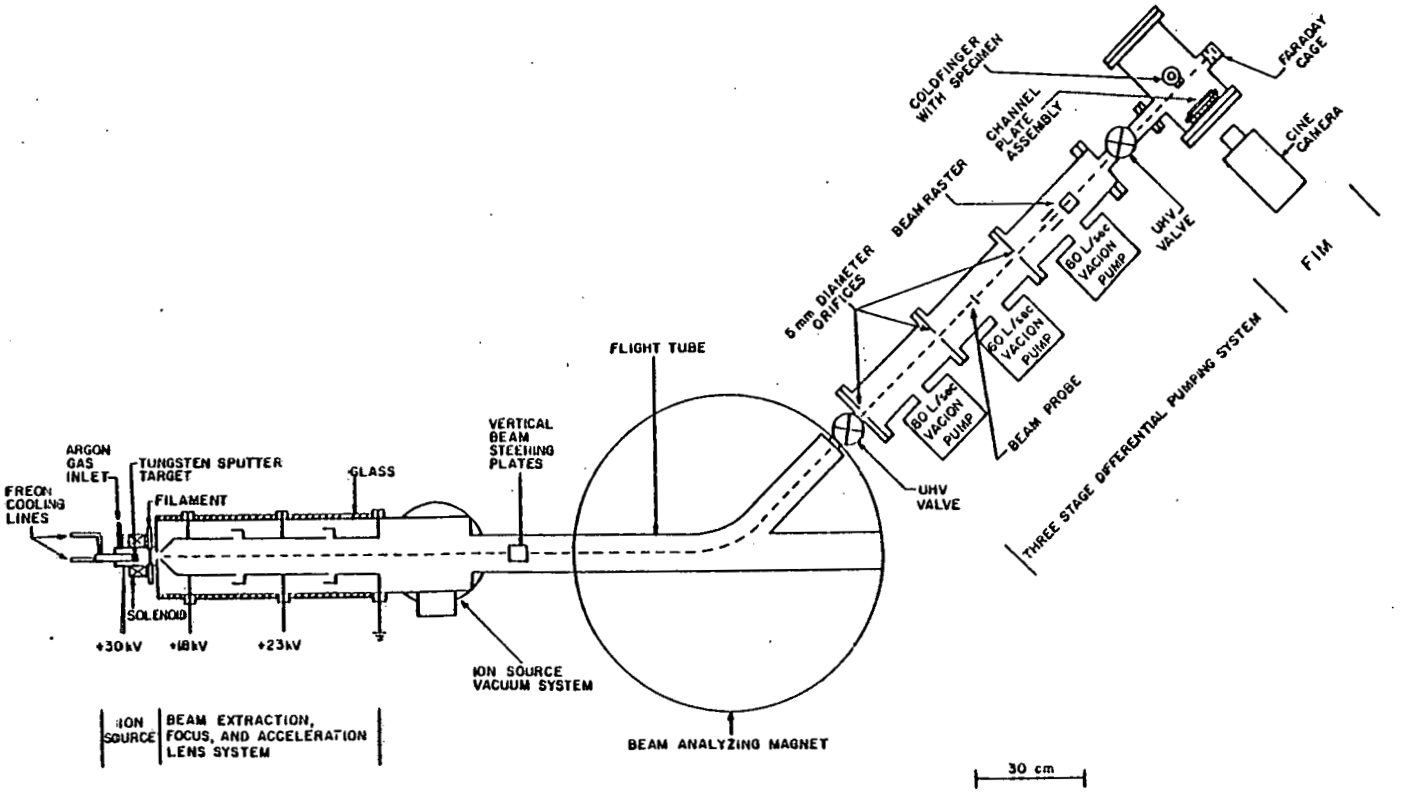

Fig. 7: An overall view of the experimental apparatus.

aperture to the FIM.

The accelerator could be operated to give ions, with as low an energy as 8 keV, although the current was very small compared to that at higher energies. The highest accelerating voltage which could be applied--determined by electrical breakdown in the connections--was 55 kV. However, by using doubly-charged ions the effective energy range of the accelerator could be doubled to 110 keV. The use of doubly-charged ions was also advantageous, as it allowed the use of much lower magnetic fields than was required to bend singly-charged ions of the same energy. This was important because the magnet power supply was not able to provide sufficient current to bend heavy ions like W^+ having energies greater than 50 keV. We used doubly-charged ions for 60 keV and 90 keV self-ion irradiations of tungsten. The main disadvantage of using doubly-charged ions was that their intensities were an order of magnitude less than that of singly-charged ions and as a consequence the irradiation time for a particular dose increased by the same factor. It was possible to obtain ion-beams of doubly-charged species, of sufficient intensity (10^{-8} amps cm^{-2}) for the various gases (such as Xe, Kr and Ar) as well as for targets that have a high sputtering yield like Au, Ag and Cu. However reasonable intensities (10^{-9} amps cm^{-2}) were also obtained for tungsten which has a lower sputtering yield.

In fig. 8 we show a characteristic mass spectrum obtained from the accelerator for a Xenon plasma and with a Ag target. The intensity of the beam was decreased to obtain the best resolution. The peaks of the two isotopes of Ag are clearly resolved as well as those of Xe, showing that the experimental set up is capable of a mass resolution ($\Delta m/m$) better

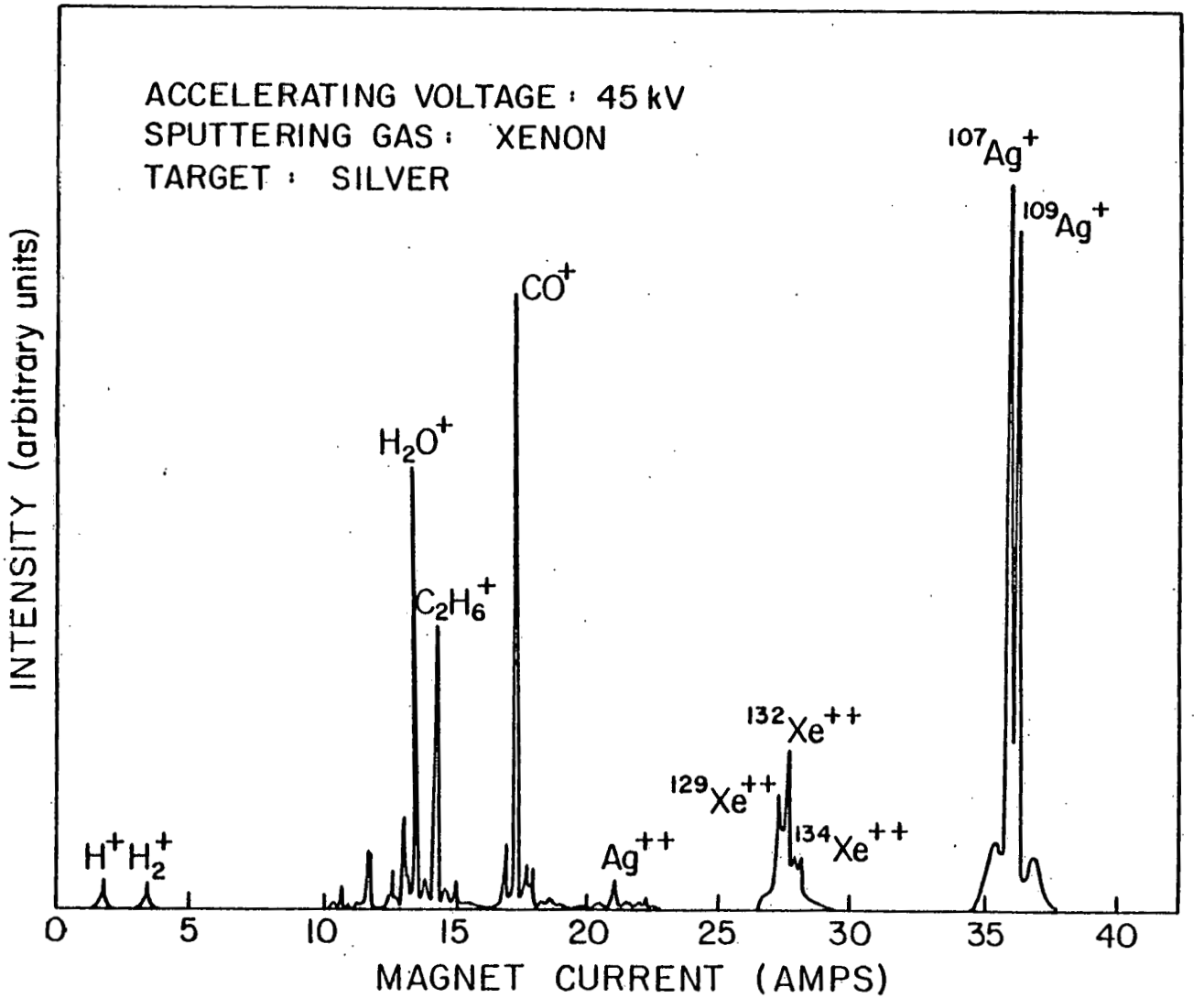

Fig. 8: A typical mass spectrum obtainable from the accelerator.

than 1/100. The Ag^{++} peak is also clearly visible and its intensity is 10^{-2} less than the Ag^{+} peak. The Xe^{++} peak is also clearly visible, but we have omitted the Xe^{+} peak since it is ten times larger than the Ag^{+} peak. It was possible to maximize the Ag^{++} peak by adjusting various parameters such as are voltage, the extraction voltage, the axial magnetic field in the plasma, etc. The doubly-charged ion peak was, in particular, sensitive to the arc voltage, which controls the energy of the exciting electrons. This was anticipated as more energy is required to create a doubly-charged ion than a singly-charged one. The yield was also significantly increased by increasing the axial magnetic field which constricted the plasma further. In the duoplasmatron ion source, where a very intense plasma is created by tightly constricting it through the use of an intermediate electrode, very high yields of multiply-charged ions can be obtained, and thus the effective energy range of an accelerator can be further increased.

In order to carry out irradiations with dimers we used the fact that a fraction of the sputtered atoms form multiatom clusters. While it has been shown that the secondary ions (charged sputtered atoms) form multiatom clusters,[3,4,5] various authors have pointed out the presence of sputtered multiatom clusters among the neutral particles. A thermoionically, sustained, magnetically confined arc discharge in Ar used by Cooper and coworkers to study neutral sputtering products from Cu and GaAs for the bombardment with Ar^{+} ions below 100 eV.[6,7] Cu_2 molecules were detected with a fraction up to 6% while for GaAs, aside from the atomic constituents, only a fraction of 0.6% of GaAs molecules were found. More recently, mass spectrometric investigations of sputtered neutrals using post-ionization in a plasma were performed by Coburn and

Kay,[8,9] using a capacitive high frequency discharge at pressures of 6×10^{-2} torr for Ar and 1.3×10^{-1} torr for Ne and by Oeschner[10,11] using a low pressure radio frequency induced plasma. Oeschner[12] showed that there were multiatom clusters among the sputtered neutrals and that the fraction of dimers was proportional to S^2, where S was the sputtering yield of the element. His results gave strong evidence for a statistical model of the generation of sputtered molecules. In this model, two or more single atoms ejected as a consequence of one individual collision cascade may agglomerate during emission when their relative kinetic energy is smaller than the dissociation energy of the generated molecule. The existence of such a mechanism is confirmed in particular by the energy distribution measurements of sputtered diatomic molecules,[12] since the formation of dimers should be enhanced in the low energy region.

Previous irradiations of materials with dimers were done with Se, Te or Be which have a high fraction of diatomic molecules in the vapor. This is the first reported use of the dimers obtained from the sputtering of targets, for the purpose of irradiation.

On the basis of the S^2 dependence of the dimer current it was obvious that the best candidates for dimer irradiations were Ag_2 or Au_2.

In fig. 9 we show the mass spectrum obtained using Ag as the target, employing an accelerating voltage of 20 kV, that clearly shows the Ag_2^+ peak. We confirmed that this was indeed a dimer peak and not an artifact caused by the charge exchange of Ag^{++} in the region between the accelerating electrodes and the analyzing magnet (which would have led to a peak at the same position as the Ag_2^+) by noting that the intensity of the Ag_2^+ peak was in fact much higher than that of the Ag^{++} peak. The charge

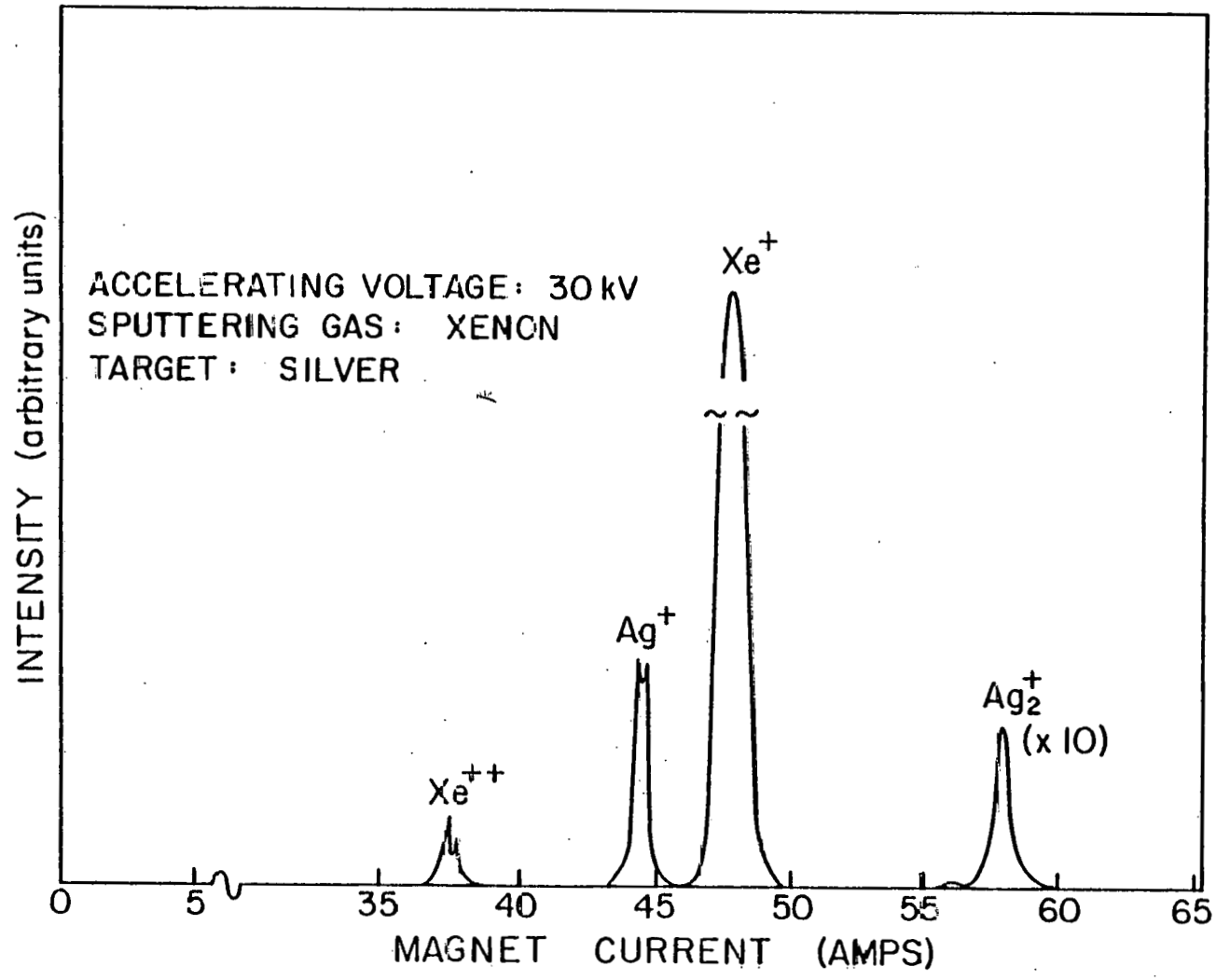

Fig. 9: Mass spectrum showing the Ag^+ and the Ag_2^+ peak.

exchange cross-section would have to be very large, given the pressure (ρ) inside the accelerator and the distance (1) between the accelerating electrodes and the magnet to account for a high conversion of Ag^{++} to Ag^{+}. For example, with a typical cross-section of say, 2×10^{-16} cm^2, and for a pressure of 10^{-5} torr and 1 = 100 cm the fraction conversion is:

$$f = 3.3 \times 10^{16} \, pl\sigma \qquad (2\text{-}1)$$

$$\simeq 10^{-2}$$

Moreover, the Ag^{++} peak increased by increasing the arc voltage, whereas the Ag_2^{+} peak did not increase correspondingly. We also observed the Ag_2^{+} peak increased by varying the gas pressure in the arc without changing the Ag^{+} peak. These two observations showed clearly that the Ag_2^{+} peak was not coupled to the Ag^{++} current which it would have been if it were an artifact that depended on it. Figure 9 shows the mass spectra obtained for W which clearly indicates the W_2^{+} peak.

We measured the dimer currents for several targets, in order to investigate the effect of sputtering yield.

Let I_1 = ion current for monomers; and

I_2 = ion current for dimers.

We can set:

$$I_1 = \alpha\gamma S \qquad (2\text{-}2)$$

where α is the ionization efficiency of the plasma and γ is a transmission factor that would relate to flag current to the ion density inside the plasma. Similarly,

$$I_2 = \alpha\beta\gamma S \qquad (2\text{-}3)$$

where β would be a factor that represents the formation of the dimer from two monomers. Hence,

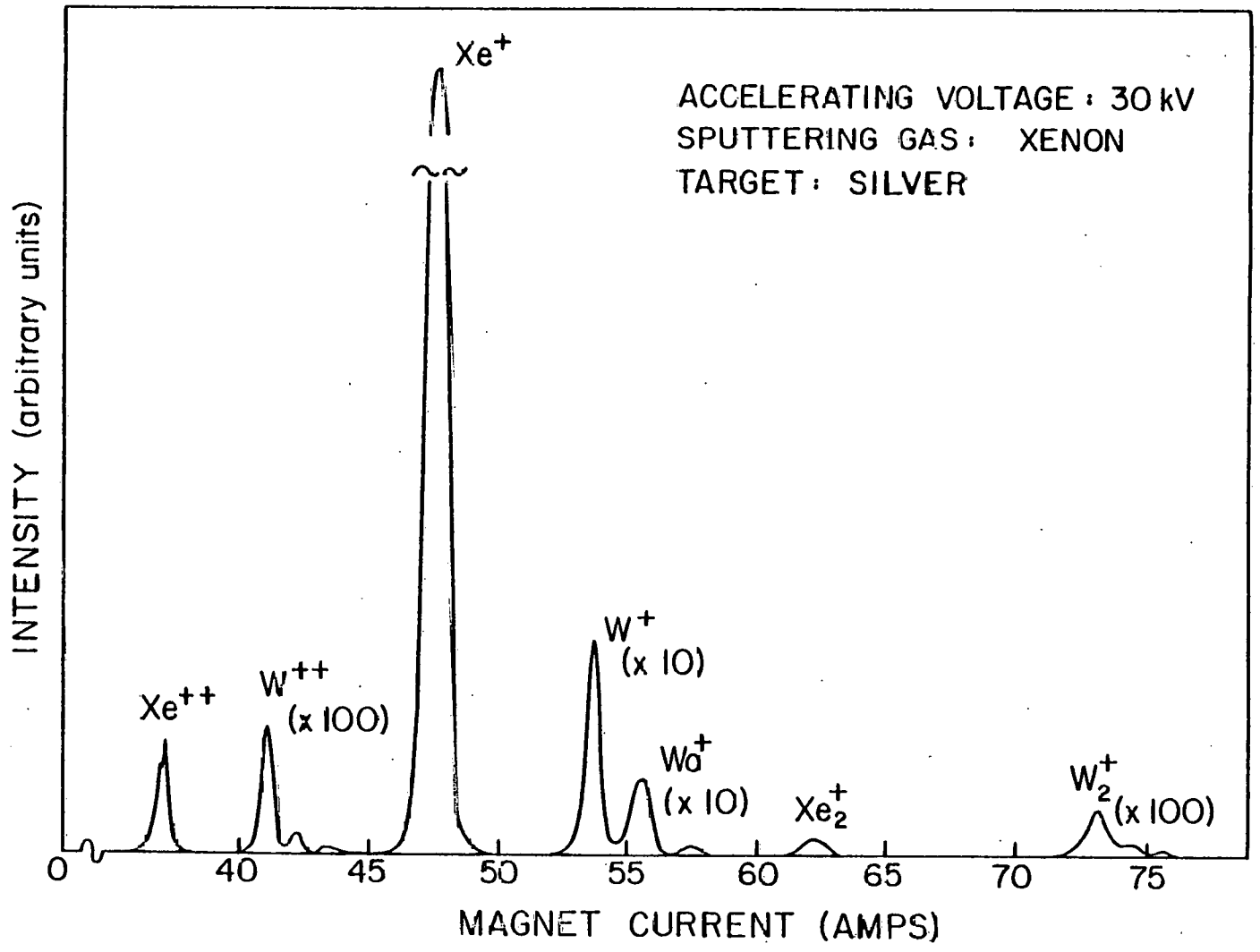

Fig. 10: Mass spectrum showing the W^+ and W_2^+ peak.

$$M_{21} = \frac{I_2}{I_1} = \beta S \qquad (2\text{-}4)$$

i.e., the ratio of the dimer to monomer currents should be proportional to S if the statistical model proposed by Oeschner is valid.

Figure 11 shows the ratio $\frac{I_2}{I_1}$ plotted versus S. It is approximately a straight line, which is consistent with the results of Oeschner.

The FIM images were observed with the help of an internal image-intensification system based on a Galileo 76 mm diameter channel electron multiplier array and the FIM images produced in this manner were recorded on a 35 mm ciné film with the aid of an Automan ciné camera equipped with a 1000 ft film chamber. Each FIM image was recorded after a field evaporation pulse had been initiated. The recorded and developed ciné-film was analyzed with a Vanguard motion analyzer which was equipped with x-y cross-hairs, a position read-out and a zeroing device. The procedure for reconstructing a depleted zone in three-dimensions from the two-dimensional micrographs is described in reference 14.

II. 2 Platinum

II.2.1 Specimen preparation

The FIM specimens were prepared from platinum wire 0.015 cm in diameter and 99.999 wt % pure, obtained from Engelhardt Industries. The wire was given a 9 hr recover anneal at 450°C by the company, which was sufficient to cause primary recrystallization of the cold-drawn wire. Specimens prepared from the as-received wire presented no problems during the imaging and field evaporation processes--prior to irradiation--but all of them fractured after irradiation, when the first few layers were

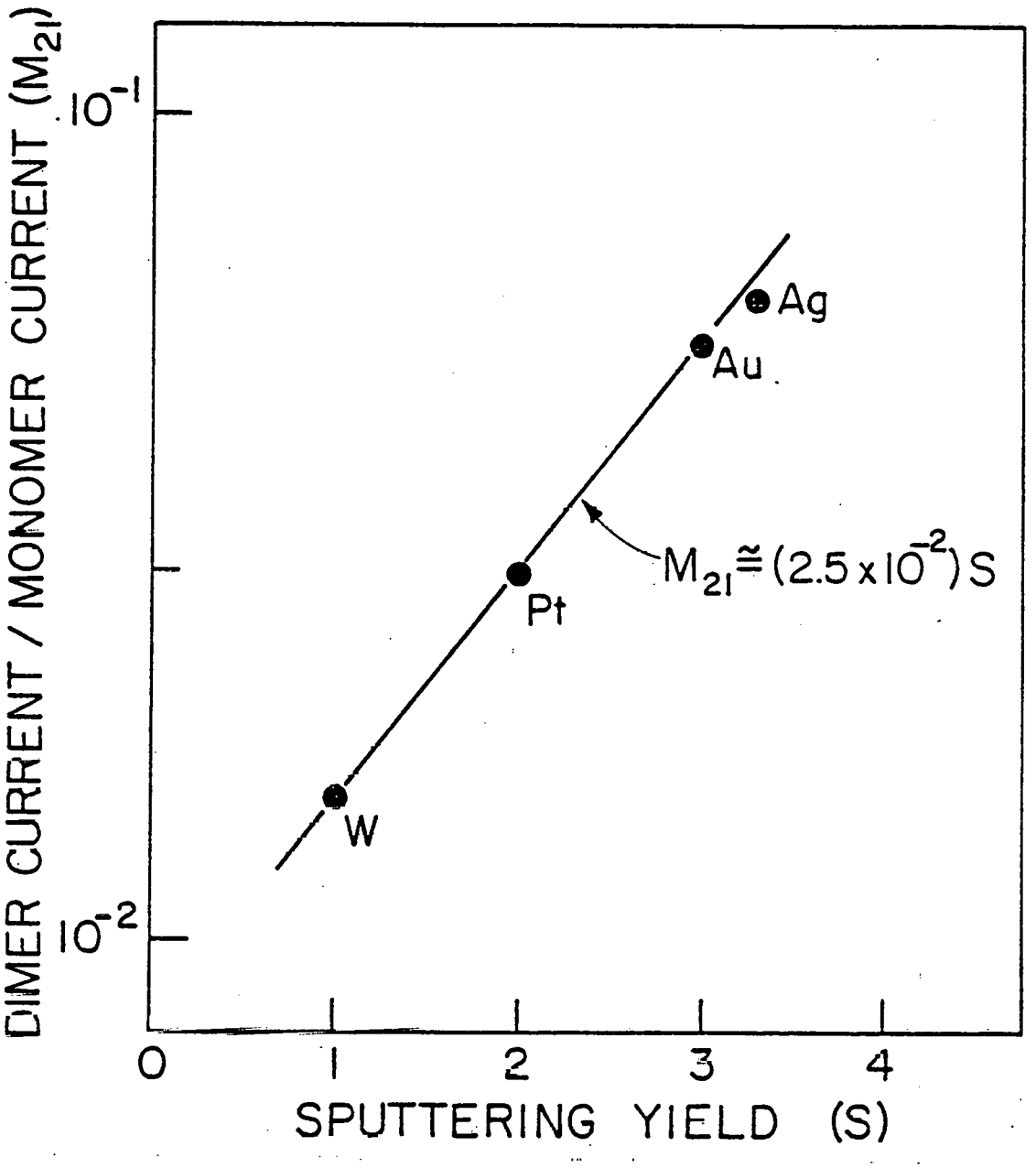

Fig. 11: Dimer / Monomer current as a function of the sputtering yield of the material. The sputtering gas was Xe and the sputtering voltage 750 V.

pulse-field evaporated. Best results were obtained with wire that had been annealed at 1100°C for 24 hrs in air. At this temperature secondary recrystallization grain growth takes place and a large fraction of the FIM specimens were found to have a [111] fiber axis. Specimens with a [111] fiber axis were preferred for the irradiation experiments as a larger number of high index planes were obtained that could be utilized for analyzing, in atomic detail, the displacement cascade--hereinafter referred to as depleted zones (DZ's).

Great care had to be taken to maintain the wires in a stress-free state, after the annealing, since this was found to greatly affect the fracture rate of the FIM specimens after irradiation and during pulse-field evaporation. The importance of this became clear when an annealed piece of wire was work-hardened by merely straightening a small length. FIM specimens prepared from this length fractured at once after bombardment for ion energies as low as 10 keV, before even one or two layers could be field-evaporated.

Sharply pointed FIM specimens were prepared by the standard electropolishing technique at 3 to 4V dc, in a molten solution of $NaNO_3$ and 20% by wt NaCl at 623K. The procedure consisted of dipping a wire specimen, at regular intervals, into the salt bath to a depth of ~5 mm and rapidly removing it after 0.2 sec. Next the FIM specimen was field evaporated continuously at 77K and then pulse field-evaporated at $\lesssim$70K to a final end-form at a background pressure of 1×10^{-4} torr Ne.

II.2.2 Irradiation

All the irradiations were carried out at 60K and the FIM specimens were maintained at this temperature throughout the pulse-field evaporation

process. Attempts to field-evaporate platinum at temperatures lower than 60K were made but the rate of fracture was very high. so that little information on the vacancy structure of the DZ's could be obtained. At 60K, almost all contrast is lost around the (111) and (001) planes, if He is used as the imaging gas. Thus, it was necessary to use Ne as the imaging gas. The resolution with Ne is lower than for He, but the contrast is far superior and allows the analysis of the vicinal planes around 111 and 100 poles. Figure 12 shows a typical FIM image obtained for Pt at 60K, using Ne as the imaging gas.

The energy of the irradiating ions was limited to 20 keV as the fracture rate rose sharply as the energy of the bombarding ions was increased. Almost 100% of the FIM specimens fractured at bombardment energies greater than or equal to 30 keV. The fracture rate is intimately linked up with the nature of defects produced inside the specimen, as discussed later in this thesis.

II.3 Tungsten

II.3.1 Specimen preparation

The specimens were prepared from two-pass zone-refined tungsten rods which were grown from a seed so that the axes of the crystals were along the [222] direction. They were first reduced to 0.55 mm diameter rod by electropolishing at 30 V dc in a solution of 20 g NaOH in one liter of a 60-40 by volume mixture of glycerol and water, with air bubbled through the electrolyte. The thinned rods were then polished and sectioned into 2 cms lengths, 0.1 mm diameter in a 1N NaOH electrolyte at 9 V. A section of the rod was mounted in a specimen holder and polished with a sharply pointed FIM tip by dipping the specimen to a depth of 3-4 mm in

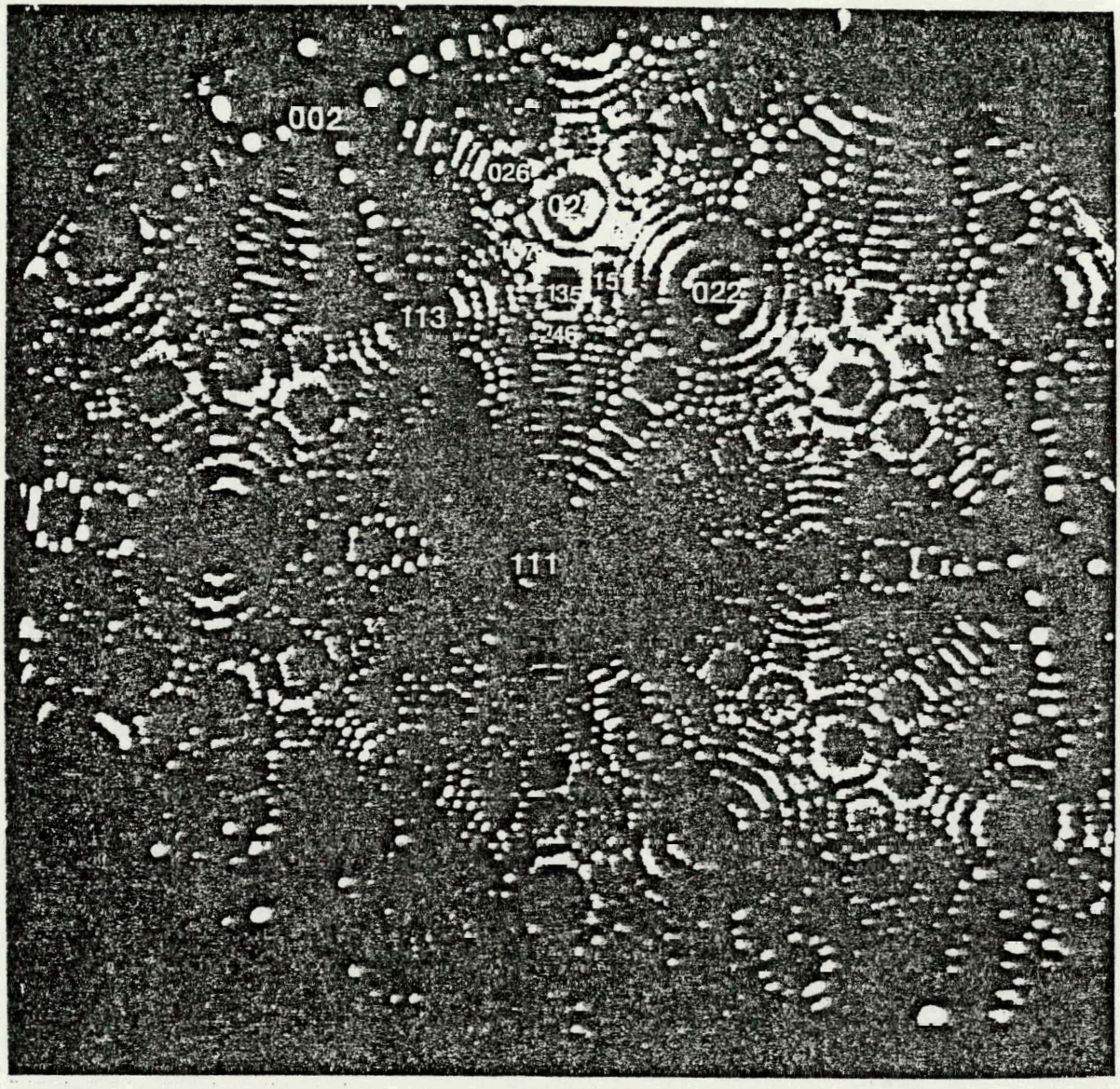

Fig. 12: FIM micrograph of platinum tip imaged with Ne at 60K.

a 1N solution of NaOH and applying a voltage of 4 V A.C. between the specimen and a stainless steel cathode. Normally a tip having the desired radius was obtained when 1 mm of the specimen was removed by electropolishing. Occasionally, certain specimens could not be polished to the desired radius by this technique. To overcome this problem, we applied a very low voltage of <1 V A.C., for some time, to thin the specimen down to a very small diameter (~.005 cm) and then applied sudden pulses of 4 V A.C. Very sharp tips, suitable for FIM imaging could be obtained. In some cases, etching took place faster at a point above the end of the specimen and as a result the lower portion dropped off. The point formed by this drop-off method was found to be excellent for imaging purposes, provided that the end was back-polished slightly after the drop-off. There was no evidence for any strains produced in the material, caused by the drop off as reported by Müller. The initial end form of the electropolished tip was extremely rough on an atomic scale. An atomically smooth end form was obtained by combining dc and pulsed field-evaporation at 78K.

II.3.2 Irradiation

All the irradiations were carried out at 10K and the temperature of the FIM specimens was maintained at this value throughout the pulse field-evaporation process. This temperature is below that for the long range migration of the SIA in tungsten, so that during the entire experiments there was no movement of any defects and the damage distribution represented the primary state of damage. Helium was used as the imaging gas.

The tungsten specimens were bombarded with 20, 45 keV W^{+}, 60 keV W^{++} ion or 20 keV Ag^{+} ions. The typical doses ranged from (5 - 10) x 10^{12} ions cm^{-2}. Irradiations were also performed with 40 keV W_2^{+} and Ag_2^{+}

dimers and similar doses were used. The dimers as well as the 60 keV W^+ currents were low and as a result the irradiation period was much greater than the time required to form one monolayer. However, we were able to check that this introduced no artifact vacancies in the image by keeping the specimen, with the field off, and under the same conditions as during irradiation, but with no ion beam incident on it, and then bringing the voltage back up to the imaging voltage. The exact same image of the tungsten surface was obtained as before with no evidence of any corrosion.

REFERENCES FOR CHAPTER II

1. K.J. Hill, R.S. Nelson and R.J. Francis, AERE (Harwell) Report No. R6343 (1970).

2. Hill, K.J. and R.S. Nelson, Nucl Inst and Methods. 38, 15 (1965).

3. G. Staudenmaier, Radiat Eff. 13, 87 (1972).

4. G. Staudenmaier, Radiat Eff. 18, 181 (1973).

5. R.F.K. Herzog, W.P. Poschenreider, and F.G. Satkiewicz Radiat Eff. 18, 199 (1973).

6. J.R. Woodyard, C.B. Cooper, J. Appl Phys. 35, 1107 (1964).

7. J. Comas, C.B. Cooper, J Appl Phys. 38, 2956 (1967).

8. J.W. Coburn, E Kay, Appl Phys Letters. 19, 350 (1971).

9. J.W. Coburn, E Taglauer, E. Kay, J. Appl. Phys. 45, 1779 (1973).

10. H. Oeschner, W. Gerhard, Phys Letter. 40A, 211 (1972).

11. H. Oeschner, W. Gerhard, Surf Sci. 44, 480 (1974).

12. F. Bernhardt, H. Oeschner, E. Stumpe, Nucl. Instr. Meth. 132, 329 (1976).

13. W. Gerhard, H. Oeschner, Z. Physik. B22, 41 (1975).

14. C.Y. Wei, PhD Thesis. Cornell University (1978).

III. DAMAGE STATE OF ION-IRRADIATED PURE PLATINUM

III.1 Introduction

The present chapter represents an extension of the earlier radiation damage research on body-centered cubic (bcc) tungsten to face-centered cubic (fcc) platinum. Platinum is particularly well-suited for FIM work as clear images can be routinely obtained and the image quality has been well characterized. An added advantage is that it is very close to tungsten (W) in atomic number and weight, so that it is possible to compare directly the damage produced in the two materials by ions of the same mass and energy without having to correct for differences in the target atomic numbers. There is earlier quantitative work on DZ's in fast neutron-irradiated Pt by Attardo and Galligan[1,2] and Inal and Galligan[3]; the main emphasis in this work was in determining size distributions. The first work in determining the spatial distribution of vacancies within and around DZ's was done by Wei and Seidman,[4] who examined a (220) vacancy platelet produced in a specimen of a Pt-4% Au alloy by a single 30 keV W^+ ion at 40K.

In the research on W the point-defect structure of Dz's created at both 18K[5,6] (Stage I) and 473K[7] (near the top of Stage II) were studied. See Ref. 8 for a discussion of Stage II (25°K to 400°K) in pure Pt. The work presented here describes the nature of defects produced in Pt during Stage II by 20 keV Kr^+ irradiations, and compares the experimental results with those predicted by various theories of radiation damage. Finally the results are compared with those from irradiations of W in order to determine the contribution of the nature

of the target material on the damage state. The results are also compared with those from 20 keV Pt^+ irradiations at the same temperature to illustrate the effect of increasing the atomic number (Z_1) of the projectile on the type of defects created.

III.2 20 keV Kr^+ irradiation of Pt

III.2.1 Results

The experimental details regarding specimen preparation and irradiation were described in Chap. II. The results for 20 keV Kr^+ irradiations of pure Pt showed that the primary state of damage due to 20 keV bombardment at 60K could be classified into 3 morphological types: (a) depleted zones; (b) compact vacancy clusters or voids; and, (c) dislocation loops. The voids can be considered as DZ's with very high vacancy concentrations and we have classified them as such, pointing ou the void-like nature, where it was pertinent. We were able to detect seven DZ's (this included void-like DZ's) in planes that had a low point-defect artifact density and we analyzed them completely. In addition, we have observed other defects that were classified as loops by virtue of contrast effects obtained in the FIM images.

In all, eight DZ's and three dislocation loops were detected in three FIM specimens which had been irradiated with 20 keV Kr^+ ions. The tips had a radius of approximately 300 Å which was determined by the method of Dreschler and Wolf.[11] Their expression for the tip radius is:

$$\gamma = \frac{n d_{nkl}}{(1 - \cos\beta)} \qquad (3\text{-}1)$$

where n is the number of rings between the two poles, d_{nkl} is the step height, and β is the crystallographic angle between the two poles. The

local tip radii were measured between the 200 pole and 420, 620, 311 poles and the 111 pole and 202, 313, 642, 311 poles and the average of these was taken as the radius of the tip. All of the tips had an (001) orientation. Figures 13 a, b, and c exhibit the partial standard stereographic projections that show the top view of each specimen. The plane (or planes) on which a DZ was detected is indicated. The cross-sectional side views of the specimen are shown in figs. 13 d, e, and f. The figures show the positions of other damaged regions detected in the specimens but which could not be analyzed in atomic detail. The defects were labelled as DPKr1a and LPKr1a, the first letter "D" or "L" indicating whether the defect is a DZ or a dislocation loop respectively; "P" denotes the material of the specimen (in this case platinum), "Kr" indicates the type of irradiating ion (in this case Kr) and the last two characters indicate the serial number of the tip and the serial number of the defect in the tip, respectively.

Figure 14 shows FIM micrographs of a platinum specimen before and after irradiation with 20 keV Kr^+ ions. The regions in which damage is visible is indicated in fig. 14 b by vees.

We analyzed the DZ's and the dislocation loops that were created by the irradiation.

III.2.2 Analysis of Depleted Zones

Using the method developed by Wei[5] we analyzed in atomic detail the vacancies constituting each DZ. The method required the vacancies to be situated in planes that possess sufficient atomic resolution for each atom in the plane to be seen and which have low artifact vacancy concentrations. Only the regions around the 420-type planes--excluding the

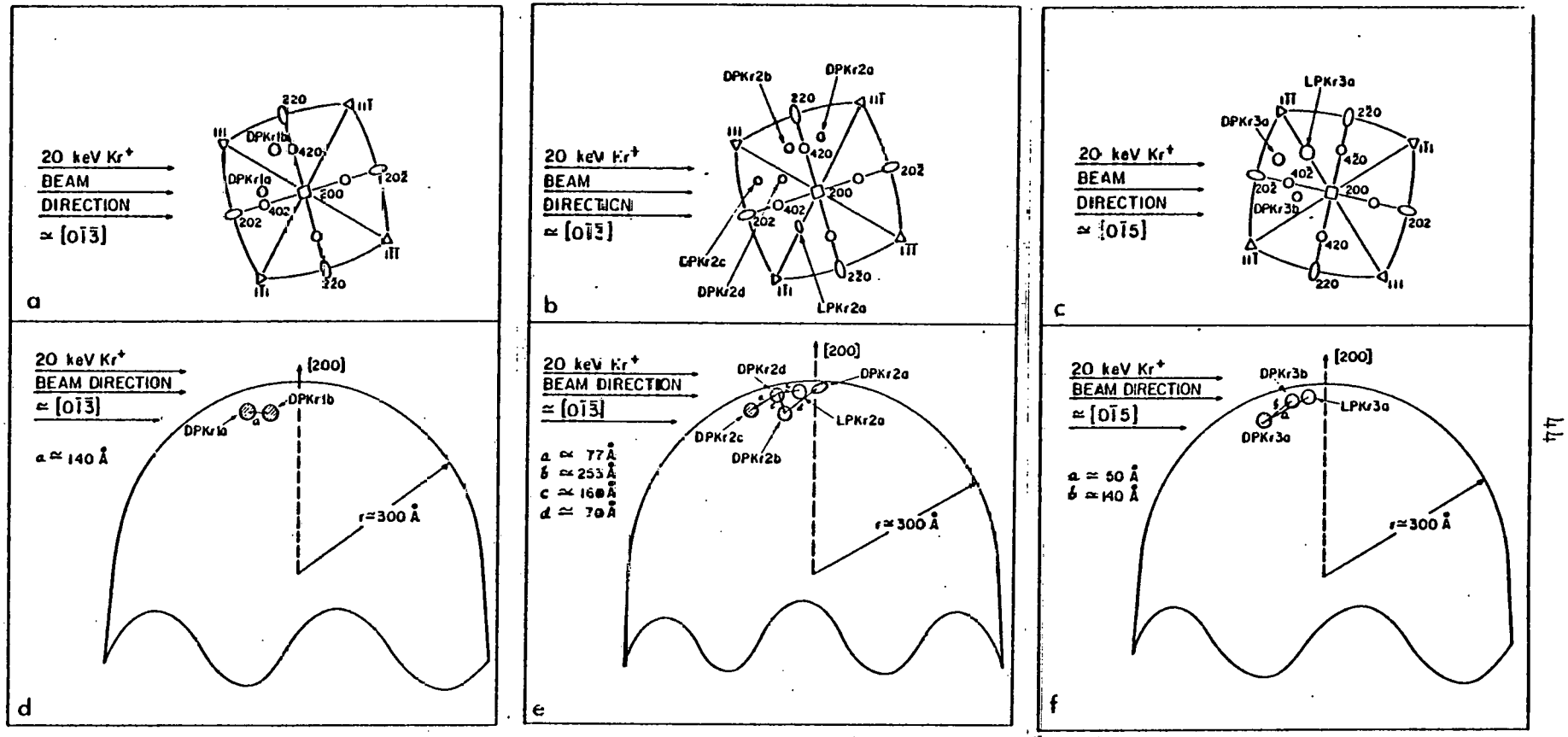

Fig. 13: 200 stereographic projections and sideviews of irradiated platinum FIM specimens, showing the position of depleted zones produced by 20 keV Kr^+ ions.

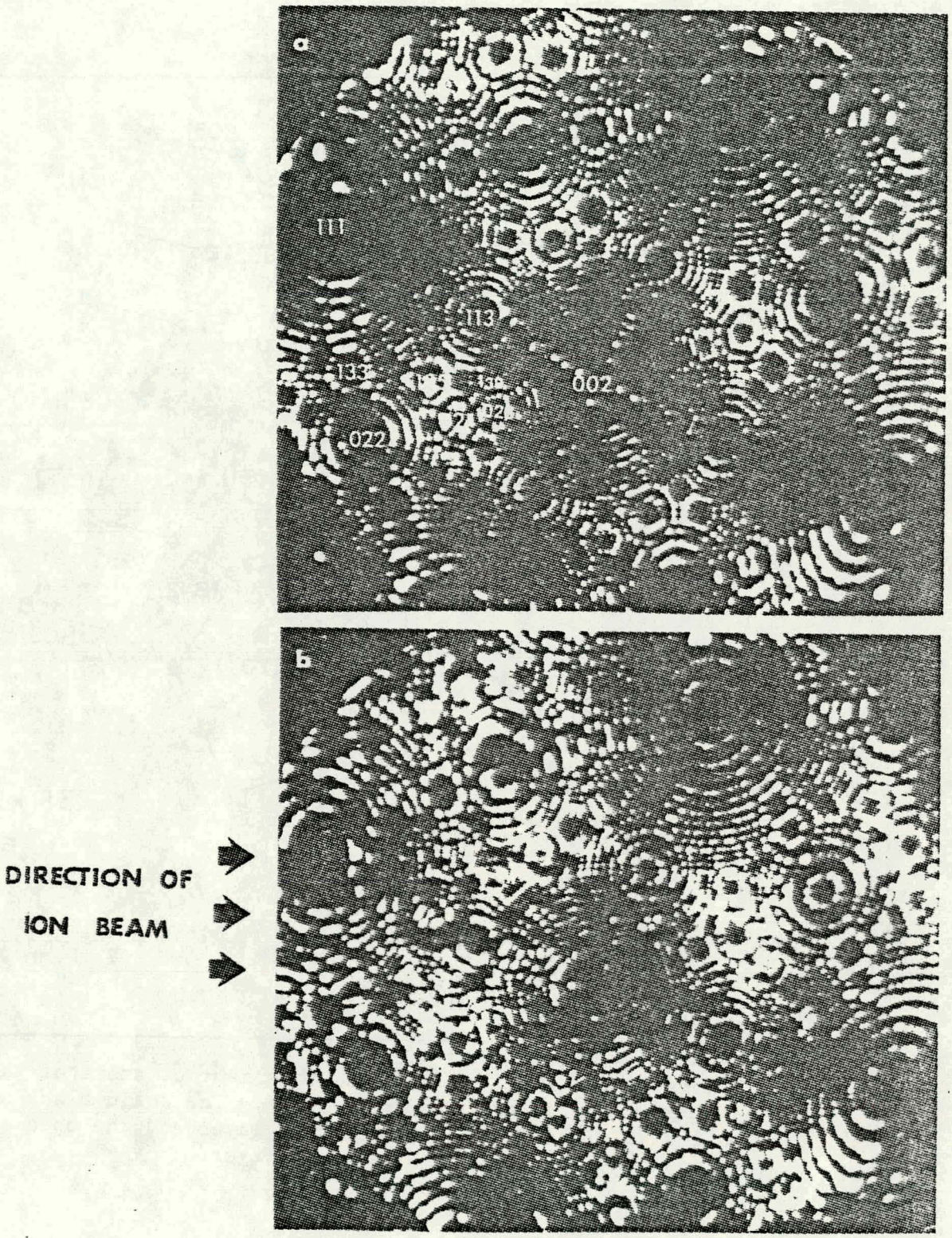

Fig. 14: (a) Platinum FIM specimen before irradiation.
(b) Surface of specimen after irradiation. Regions of damage are indicated with vees.

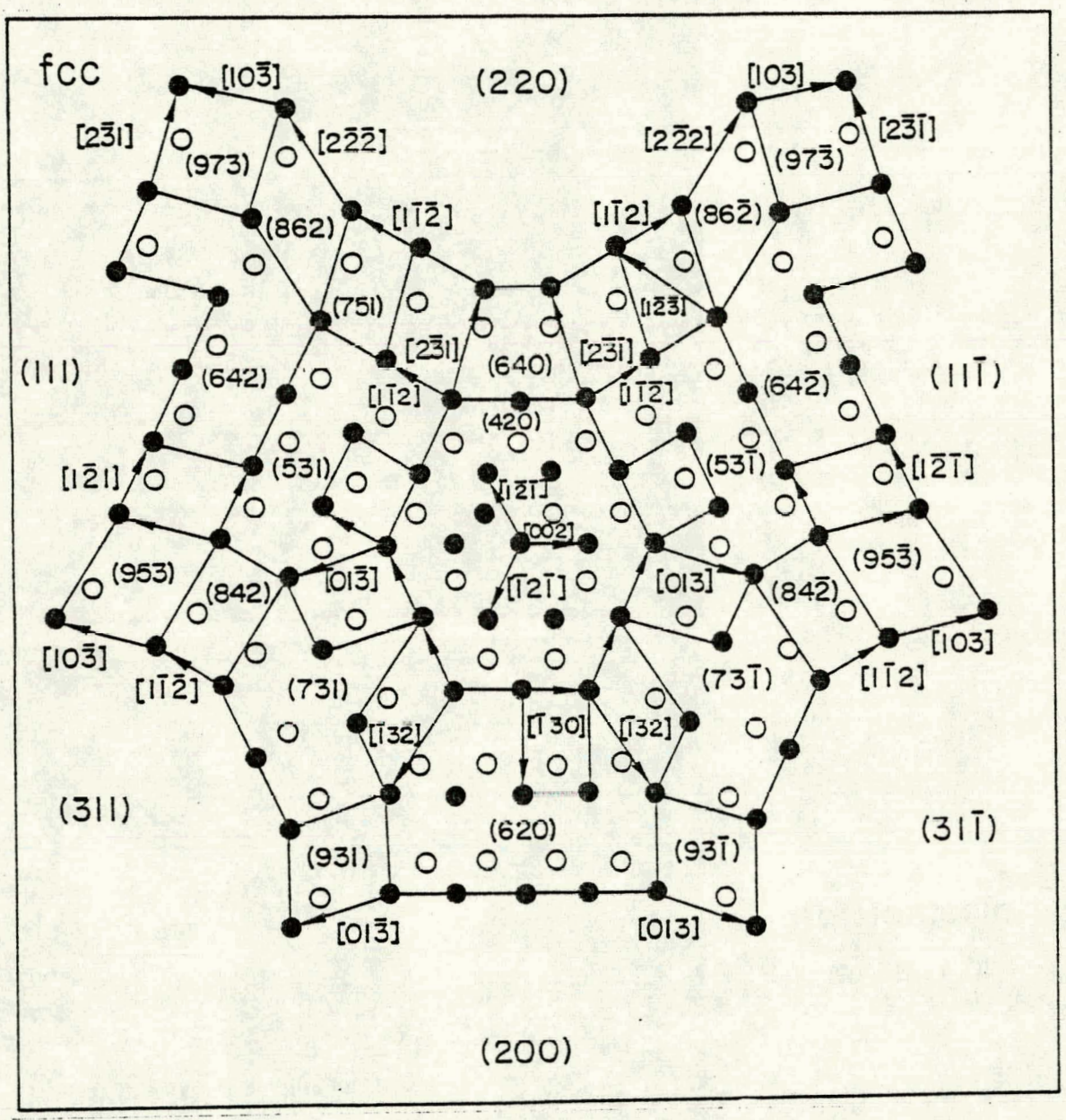

Fig. 15: A schematic diagram showing the arrangement of atoms of various planes in and around the 420 pole. The solid black circles indicate the atoms in the zeroth layer and the open circles indicate the atoms in the first layer.

{420} and {731} planes--satisfy this requirement. In an FIM specimen with a 111 pole, there are six such regions while in a specimen with a 002 pole there are four such regions observed in the FIM pattern. Figure 15 shows a schematic diagram of two successive layers for the 420 pole. The atoms in the zeroth and first layers are indicated by solid black circles and open circles respectively. The Miller indices for each plane are shown in the figure. The vectors which are along the intersection of two neighboring planes are also indicated. The vectors are in units of $a_0/2$ where a_0 is the lattice constant. The diagram was plotted using the procedure and information given in Nicholas' Atlas.[9] Figure 16 is an FIM micrograph showing the location of each plane in the region of the 420 pole. Figure 17 illustrates a field evaporation sequence showing the vacancies on successive planes. Once the atomic positions of the vacancies were obtained it was possible to obtain a three-dimensional visualization of the DZ using the OR TEP program.[10] Also the following quantities of interest were determined for each DZ.

(a) Number of vacancies (ν);

(b) Mean depth of DZ (L);

(c) Spatial arrangement of vacancies;

(d) Mean vacancy concentration (c_v); and,

(e) Radial distribution functions.

We briefly describe the manner in which each of these quantities were determined before presenting the results.

(a) The parameter, ν, is the easiest quantity to determine and was obtained by directly counting the vacancies in the planes. In the cases where the DZ overlaps several planes and vacancies appeared on

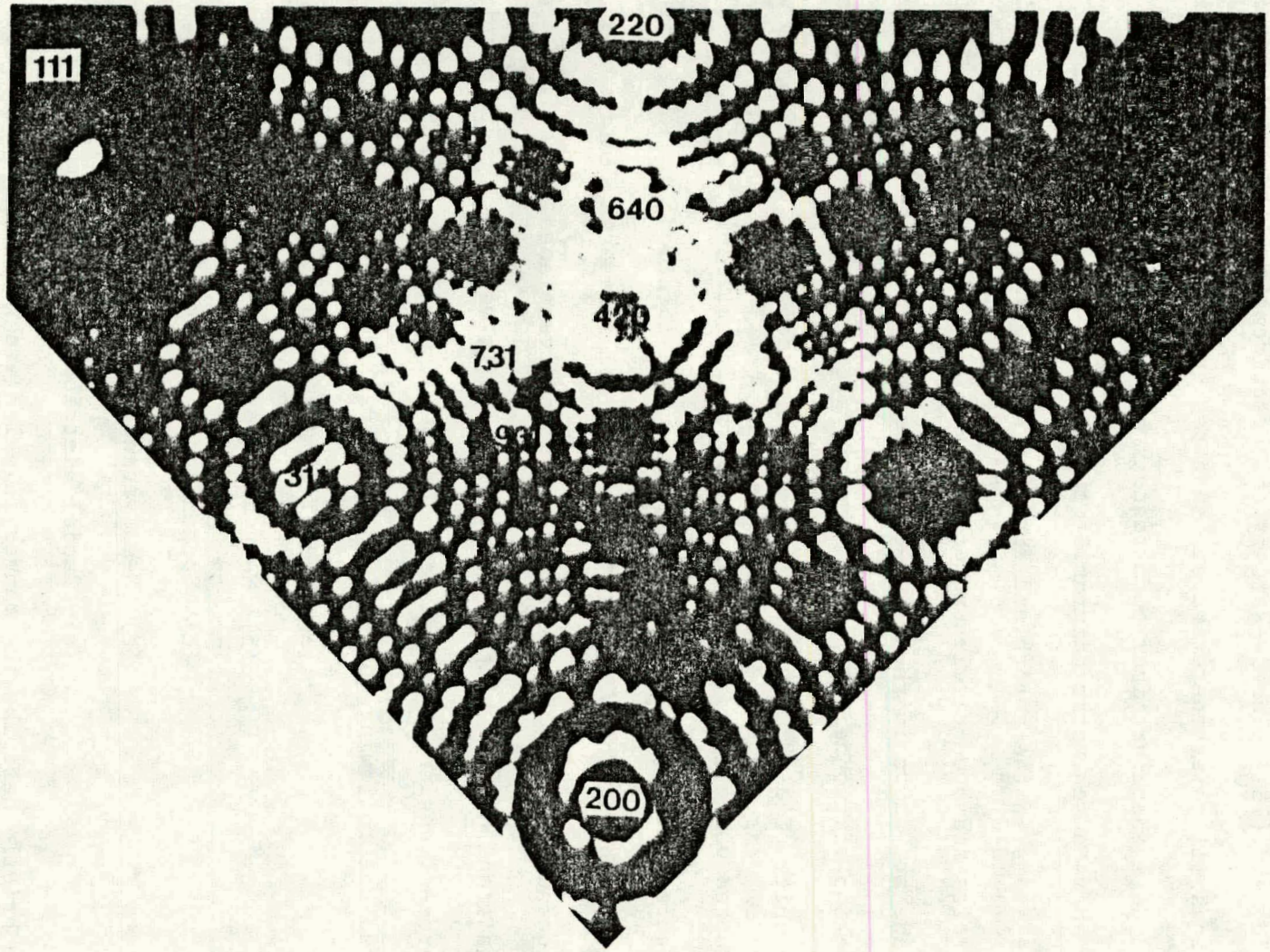

Fig. 16: An FIM micrograph showing the arrangement of planes in the region of the 420 pole.

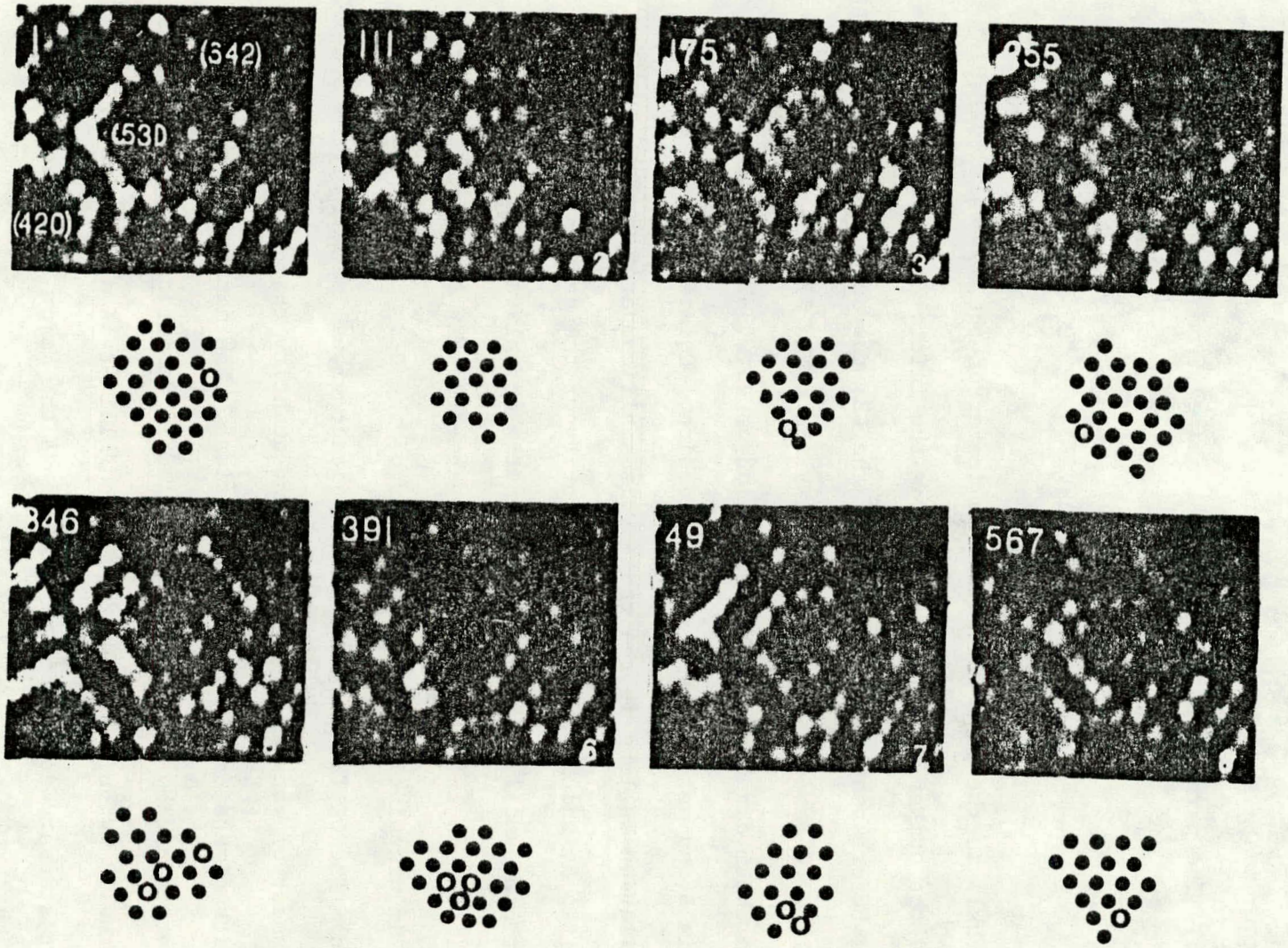

Fig. 17: A series of eight FIM micrographs out of 567 recorded during the atom-by-atom dissection of a depleted zone. The solid black circles indicate normal lattice atoms and the open circles indicate vacant lattice sites.

the edge separating two planes, the computer program checks to see whether a vacancy had been counted twice by comparing coordinates in the cubic coordinate system of the lattice.

(b) The parameter, L, can be calculated from the following expression:

$$L \simeq \frac{n_{hkl} d_{hkl}}{\sin\Phi \cos\theta} \qquad (3\text{-}2)$$

where (hkl) is the plane on which the center of the DZ was situated, n_{hkl} is the number of (hkl) planes from the initial surface, field evaporated before reaching the center of the DZ; the angle Φ is the azimuthal angle with respect to the pole and θ the angle with respect to the incident beam direction. The derivation of eq. (3-2) can be found in appendix B, as well as the exact expression. Equation (3-2) is a good approximation as long as the range L is small compared with the radius of the tip R, which it was in the majority of the cases we considered. In fact, the small differences between the actual value of L and the approximate one calculated from (3-2) are probably less than the uncertainty in pinpointing the exact center of the DZ.

(c) The OR TEP drawings give a direct visualization of the spatial arrangement of vacancies. An important quantity that characterizes the DZ is its dimensions in various directions. The dimensions of each DZ were determined by calculating teh standard deviations for projections along the 13 principal <100>, <110> and <111>-type directions. The largest standard deviation was defined as the major axis--dimension, σ_1. The average value of the standard deviations for the distributions perpendicular to the direction of σ_1 was defined as the minor axis dimension,

σ_2. An average dimension $\langle\lambda\rangle$ was defined as the 2σ average full width by the expression:

$$\langle\lambda\rangle = 2(\sigma_1\sigma_2^2)^{1/3} \qquad (3\text{-}3)$$

The volume of an ellipsoid with major and minor axes of σ_1 and σ_2 is then:

$$V_{DZ} = \frac{4\pi}{3}\left(\frac{\langle\lambda\rangle}{2}\right)^3 \qquad (3\text{-}4)$$

and would include 30% of the total number of vacancies within the DZ.

(d) The determination of the vacancy concentration within an individual DZ depends on the definition of the volume of the lattice occupied by the DZ. We have chosen to calculate the number of atomic sites included in a volume which was made up of a series of rectangular slabs which were fitted to the contours of the DZ and which included all the vacancies in the DZ. The first series of slab-elements are four atomic layers deep, normal to the [100] direction of the W lattice with a lateral extent determined by the largest vacancy concentration along the [010] and [001] directions. The vacancy concentration is then:

$$c_v = \nu/\Sigma_j \Delta V_j \qquad (3\text{-}5)$$

where ΔV_j is the number of atomic sites within the jth slab element and ν is the total number of vacancies in the DZ. In order to compensate for the irregular shape of the DZ's, this calculation was repeated for slab elements normal to [001] and [010] directions. An average of the three results was taken as the vacancy concentration $\langle c_v \rangle$.

In Table 3.1 and 3.2, we have summarized the various quantities listed above, for the seven DZ's that were analyzed in detail. In figs. 18-24, we exhibit the OR TEP visualizations of the 7 DZ's. Each of the

TABLE 3.1

Range, number of vacancies and vacancy concentration for the DZ's produced by 20 keV Kr on Pt

DEPLETED ZONE (DZ)	RANGE (L) Å	NUMBER OF VACANCIES (ν)	c_v (AT %)
DPKr1a	27.5	154	1.7
DPKr1b	5	155	4.5
DPKr2a	5	116	2.5
DPKr2b	45	269	7
DPKr2c	5	85	11
DPKr3a	39.6	209	3.7
DPKr3b	15	269	10.8

TABLE 3.2

Dimensions of DZ's produced by 20 keV Kr^+ on Pt

DEPLETED ZONE (DZ)	ELONGATION DIRECTION	λ_1 † (Å)	λ_2 † (Å)	$\langle\lambda\rangle$ † (Å)
DPKr1a	[001]	57.8	35	41.35
DPKr1b	[001]	30.74	21.4	24.14
DPKr2a	[011]	50.3	29	34.84
DPKr2b	[001]	29.4	20.45	23.08
DPKr2c	[101]	14.8	10.3	11.62
DPKr3a	[011]	36.8	27.16	30.05
DPKr3b	[001]	16.6	13.57	14.51

†See text and eqn. (3-3) for the definitions of λ_1, λ_2, and $\langle\lambda\rangle$.

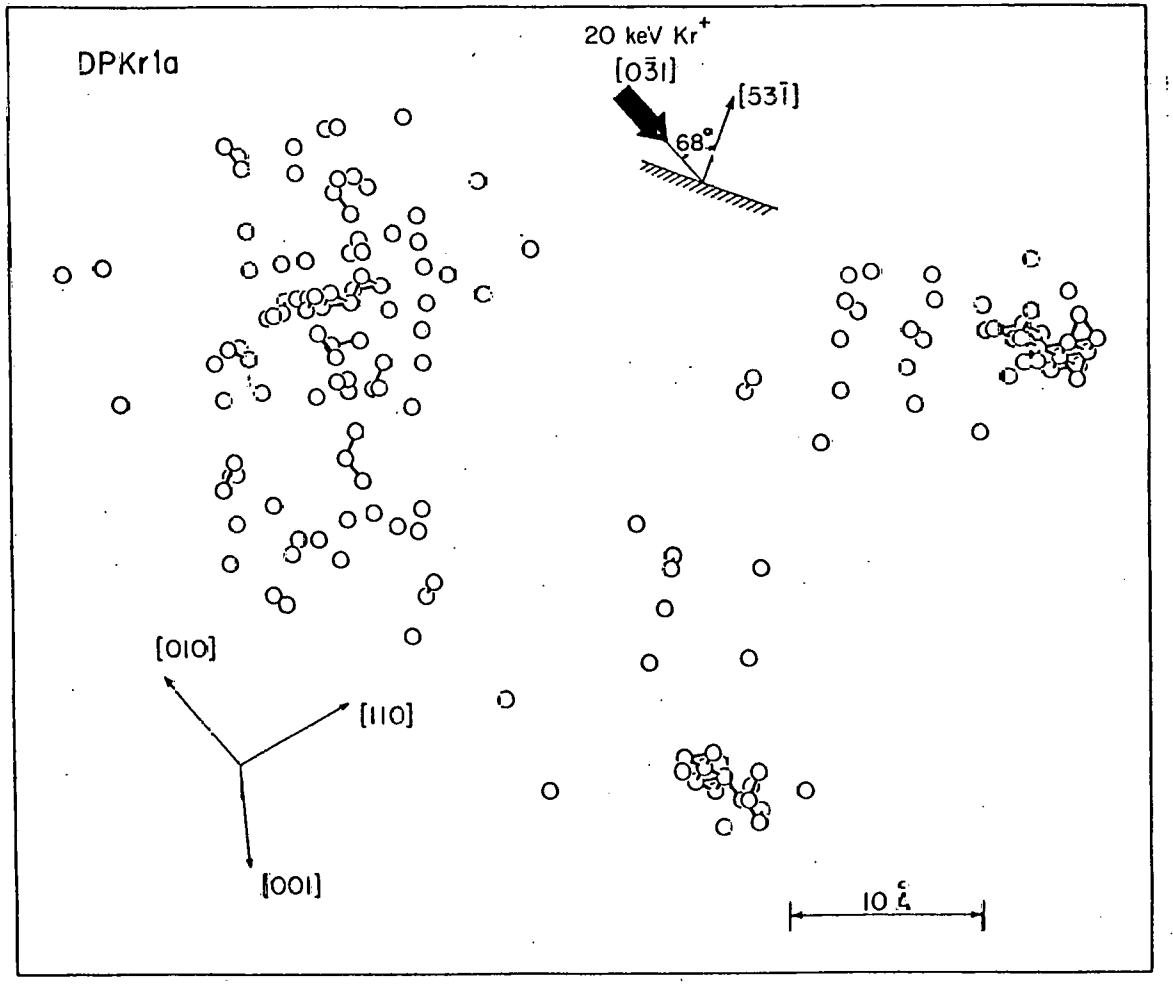

Fig. 18: An OR TEP drawing of depleted zone DPKr1a.

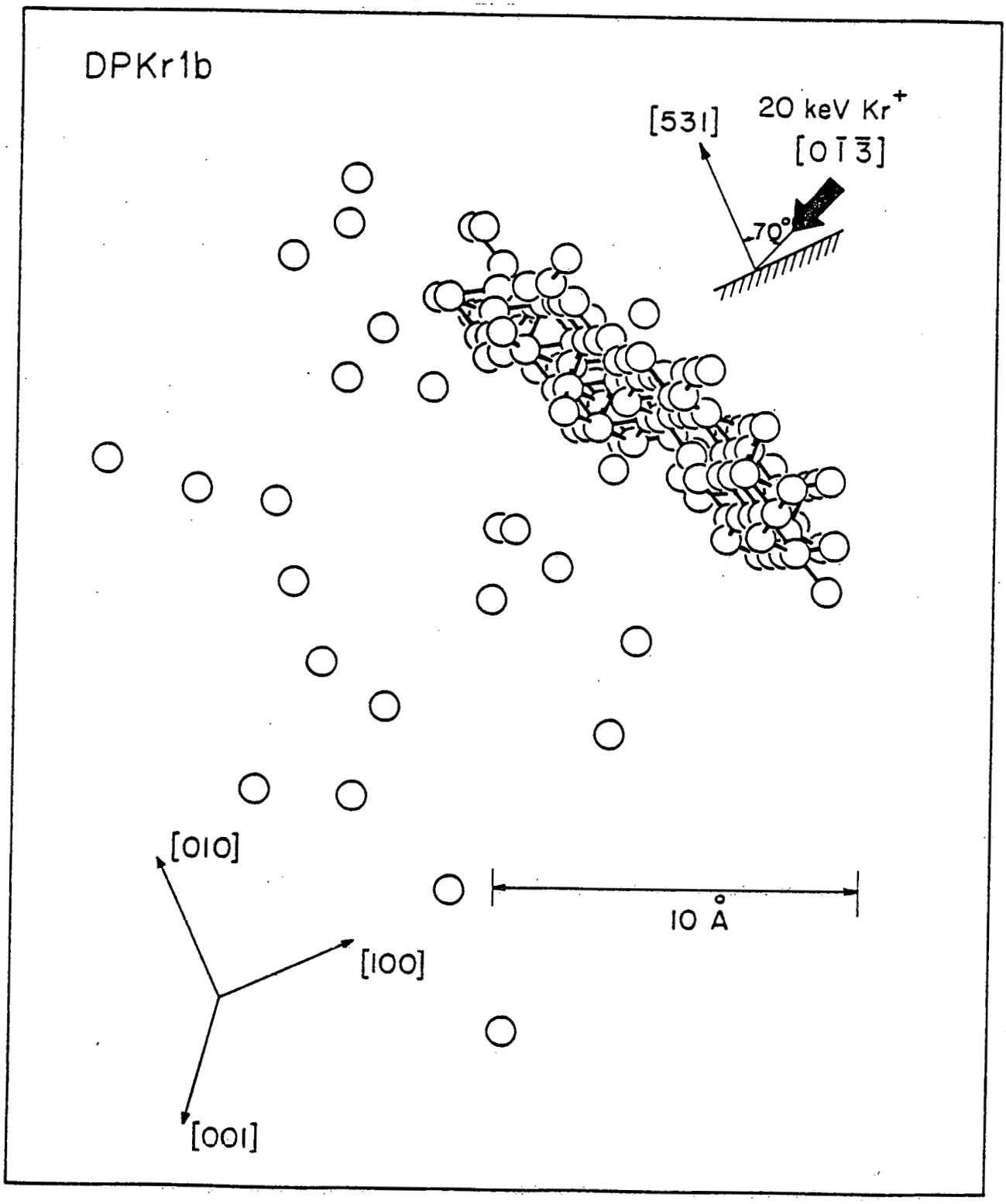

Fig. 19: An OR TEP drawing of depleted zone DPKr1b.

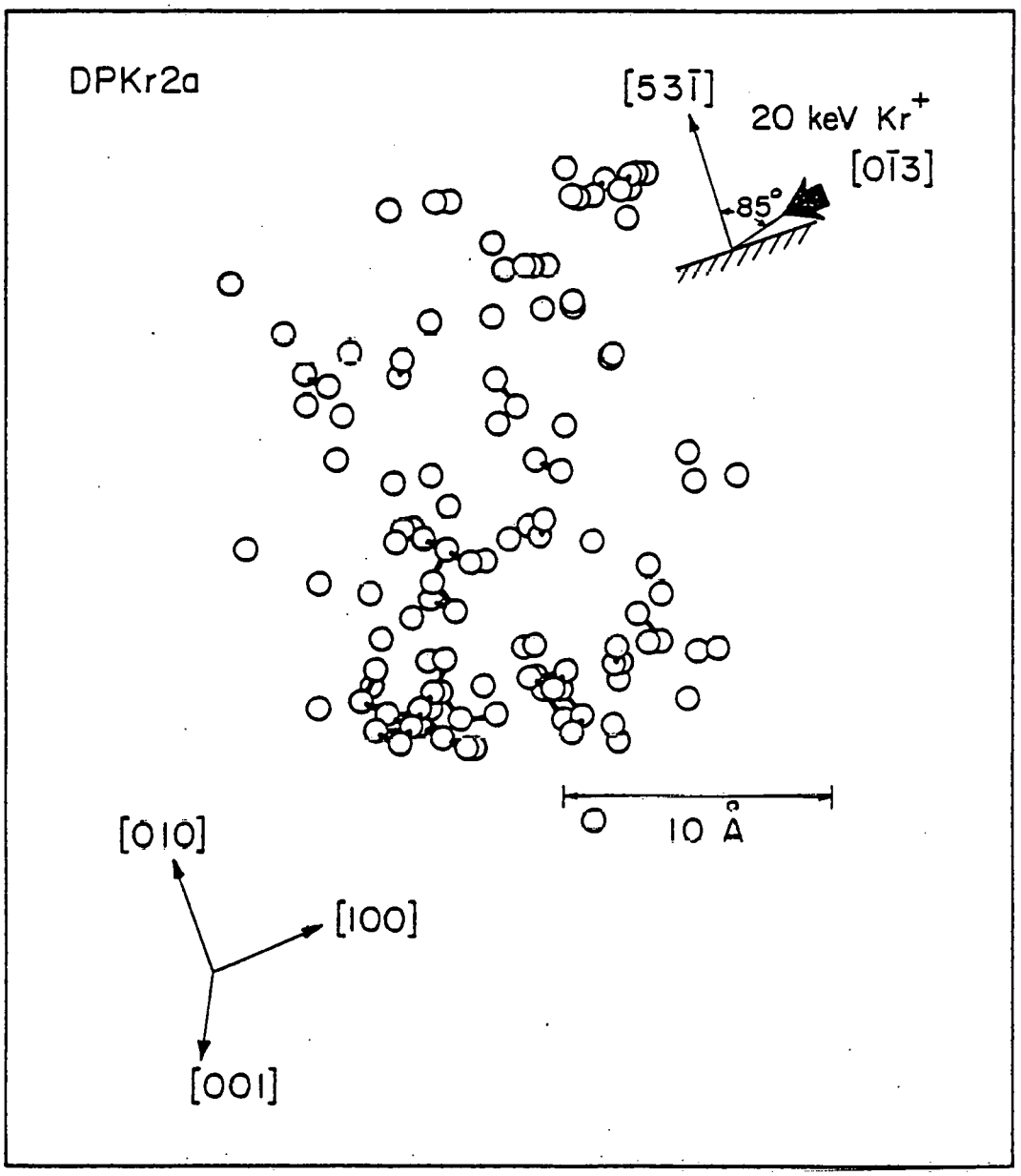

Fig. 20: An OR TEP drawing of depleted zone DPKr2a.

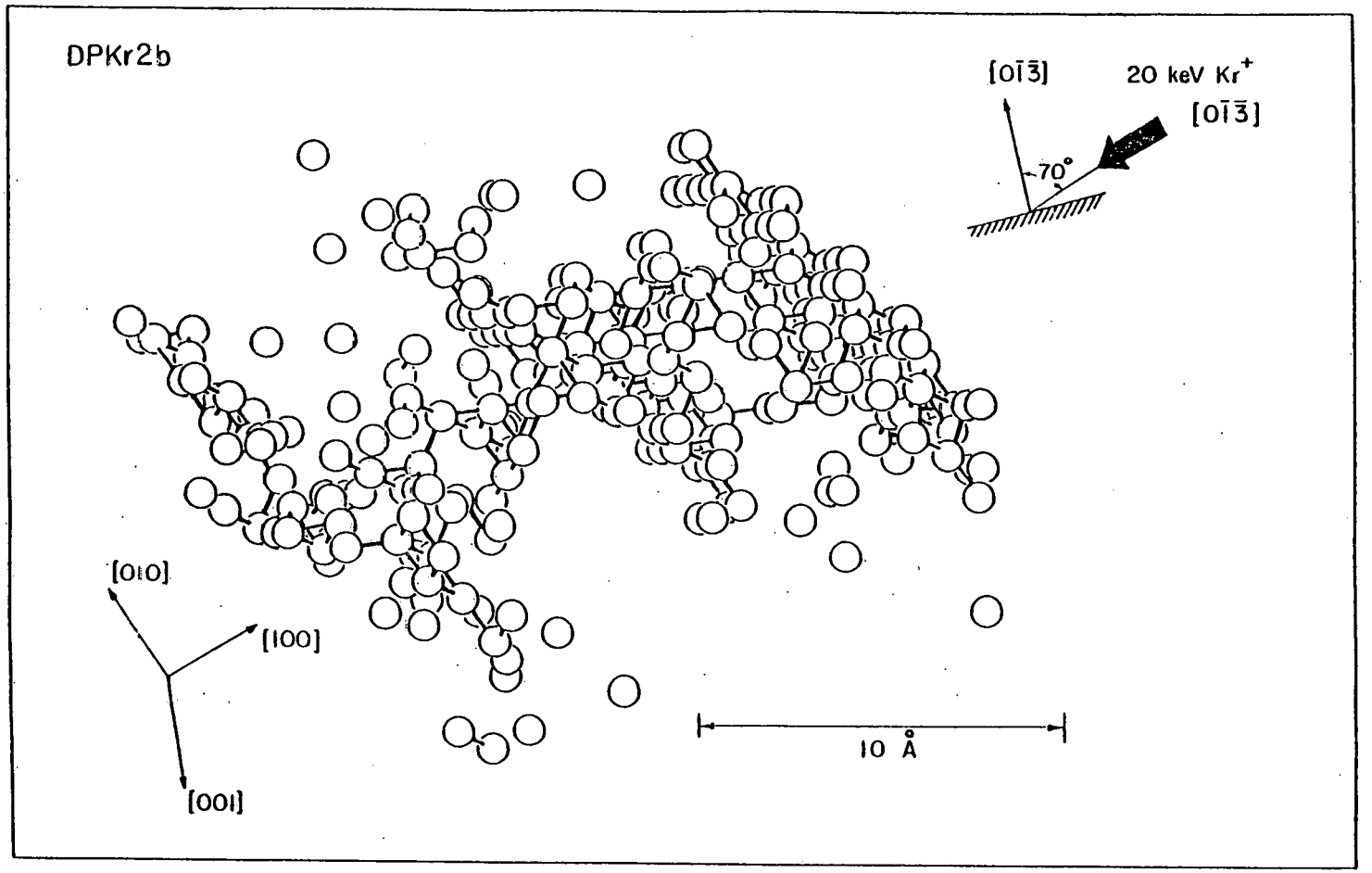

Fig. 21: An OR TEP drawing of depleted zone DPKr2b.

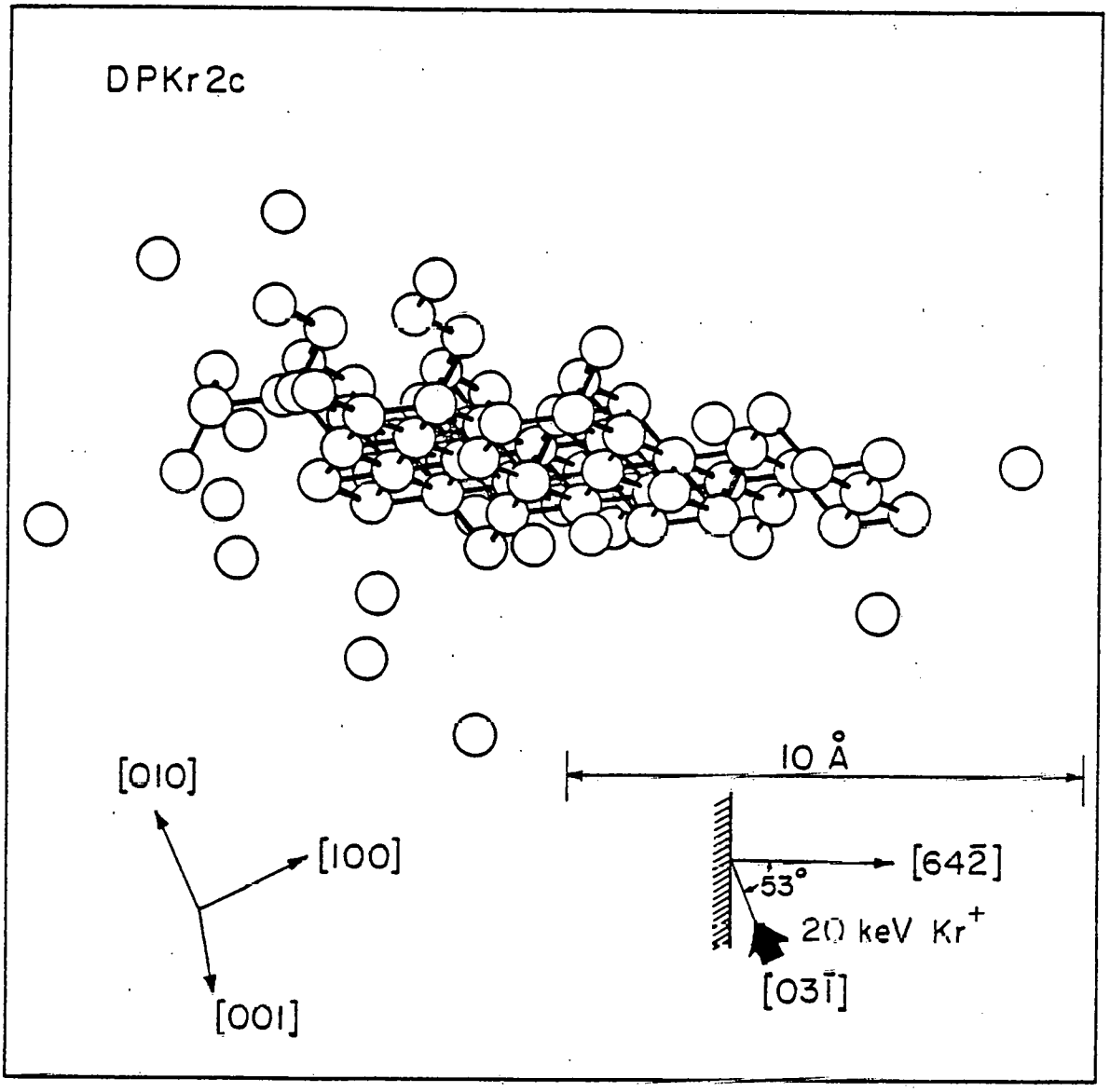

Fig. 22: An OR TEP drawing of depleted zone DPKr2c.

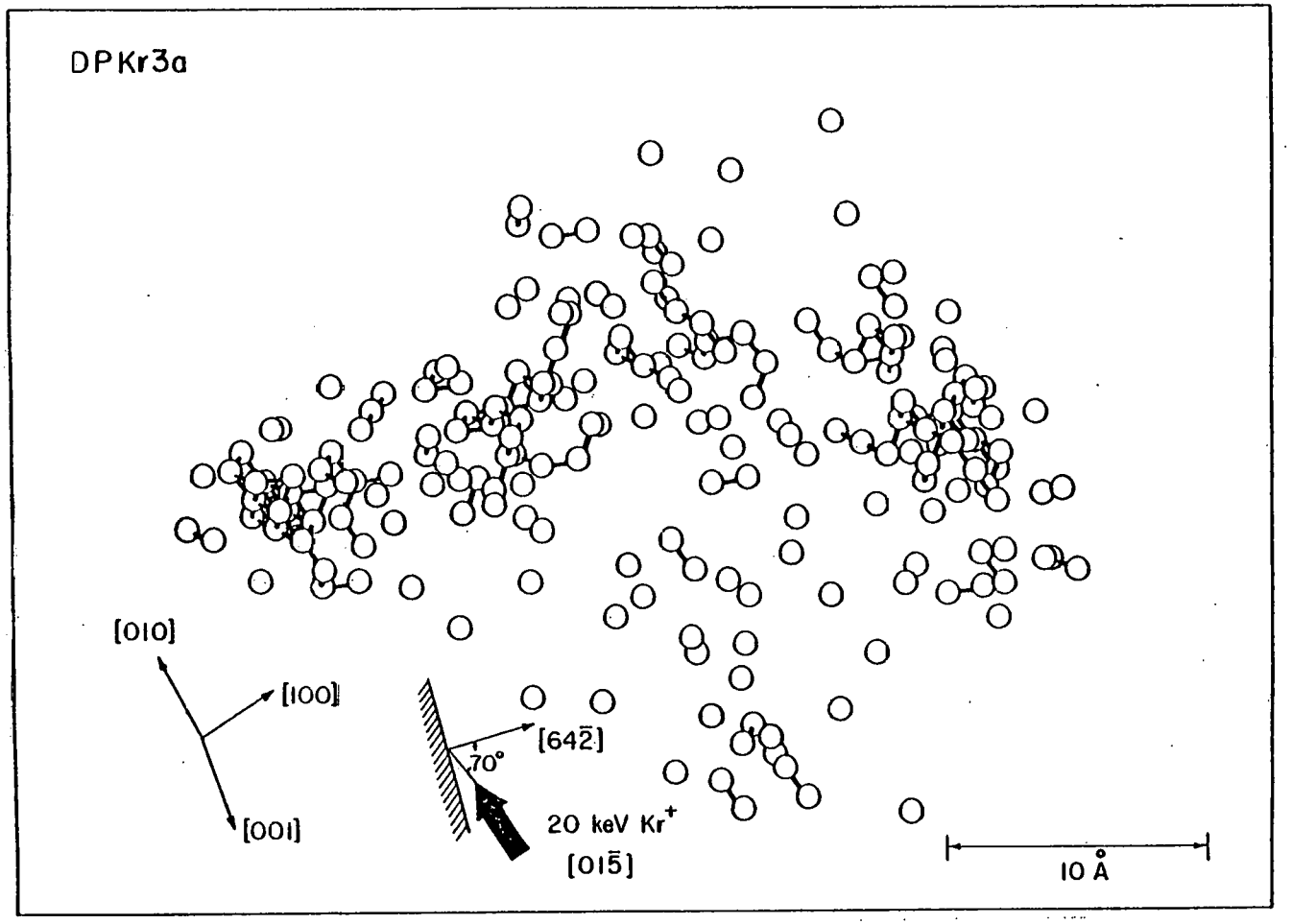

Fig. 23: An OR TEP drawing of depleted zone DPKr3a.

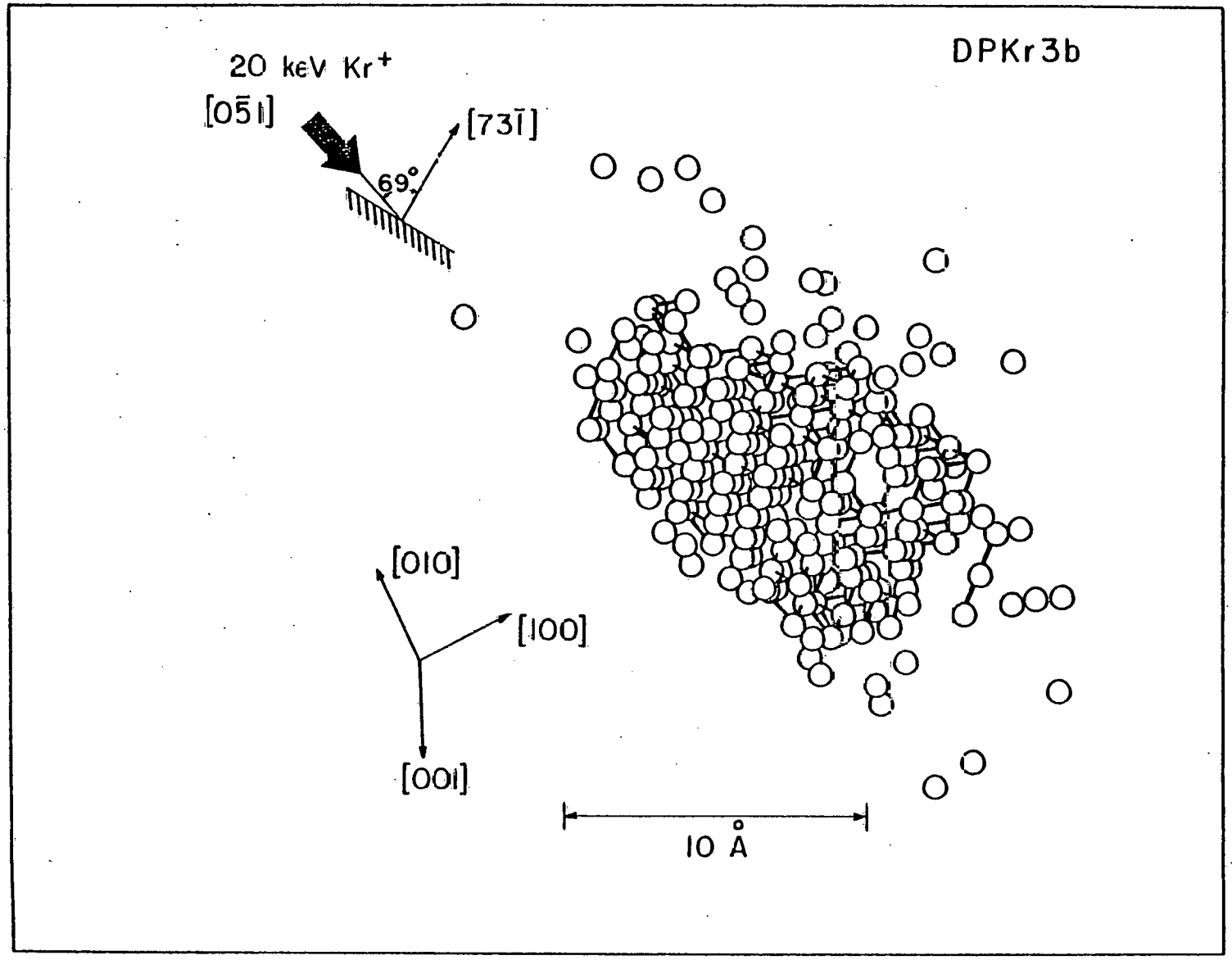

Fig. 24: An OR TEP drawing of depleted zone DPKr3b.

vacancies has been represented by a sphere and the surrounding lattice has been omitted for clarity. Vacancies that lie on first nearest neighbor sites on a lattice have been connected by bonds in order to give an indication of the degree of clustering.

(e) As can be seen from the OR TEP visualizations, the local distribution of vacancies within the DZ's can be highly non-uniform with a strong tendency towards the formation of local clusters of vacancies. In order to characterize these variations within the DZ, we have calculated two types of average radial distribution functions (RDF's). The first is a local RDF, R(i)/Z(i), which measures the average fraction of vacant sites around each vacancy in the DZ out to the 9th nearest neighbor. Here R(i) is the average number of vacancies in the ring of the i-th nearest neighbor lattice sites and Z(i) is the coordination number of the ith shell. The first distribution is a measure of the average local environment around the vacancies.

A second distribution N(i) extends over the entire DZ and is the average number of vacancies in an annular shell of thickness a_0 and radius r_j centered on a vacancy. This second distribution gives a measure of the separation between major clusters of vacancies within the DZ structure.

In fig. 25, we show R(i)/Z(i) for the seven DZ's as well as the average for all the DZ's. The individual R(i)/Z(i) show large variations from DZ to DZ, which is apparent from the OR TEP visualizations. The average R(i)/Z(i) gives the average local distribution around a vacancy when a Pt target is bombarded with a low dose of 20 keV Kr^+ ions such that the individual cascades do not overlap. This average is therefore

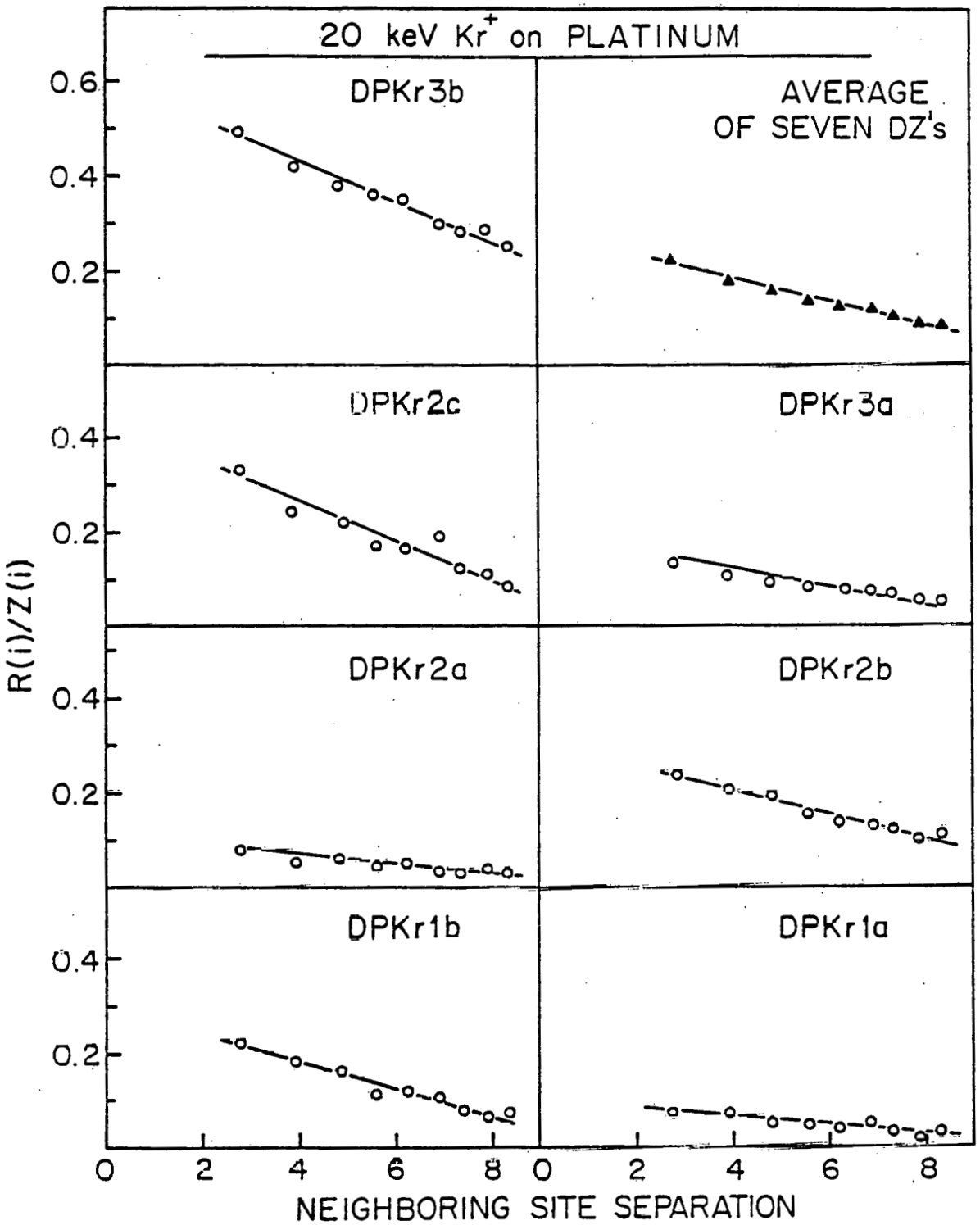

Fig. 25: The normalized radial distribution function [R(i)/Z(i)] for depleted zones produced by 20 keV Kr^+ ions on platinum.

representative of the cumulative damage profile.

In fig. 26, we show <N(i)> for the seven DZ's. The <N(i)>'s reflect the difference in the degree of clustering from DZ to DZ. For example, DPKr1a is a diffuse DZ and its <N(i)> shows no prominent peaks. On the other hand, the compact nature of DPKr3b shows up in a sharp single peak at 3Å.

Since the atomic positions of the vacancies are known, it is possible to determine the degree of association of vacancies into clusters which are linked to each other by nearest neighbor distances. This was carried out with the help of the computer and the following information was obtained for each of the DZ's.

DPKr1b: There were 33 monovacancies, six divacancies, and one each of clusters of four, 47 and 68 vacancies.

DPKr1a: There were 89 monovacancies, 12 clusters of divacancies, two clusters of tri-vacancies and one each of clusters of six, 14 and 16.

DPKr3a: There were 69 monovacancies, 11 clusters of divacancies, four clusters of 3 vacancies, two quadravacancies and one of each cluster of five, six, seven, 24, 26, and 30.

DPKr2a: The number of monovacancies was 61, there were 9 divacancies, two clusters of six and one each of clusters of seven and 17.

DPKr2b: There were 53 monovacancies, 10 divacancies, one each of clusters of three, five and eight vacancies and one jumbo cluster of 182 vacancies.

DPKr2c: There were 19 monovacancies and one big cluster of 65 vacancies.

DPKr3b: There were 41 monovacancies, five divacancies, two clusters

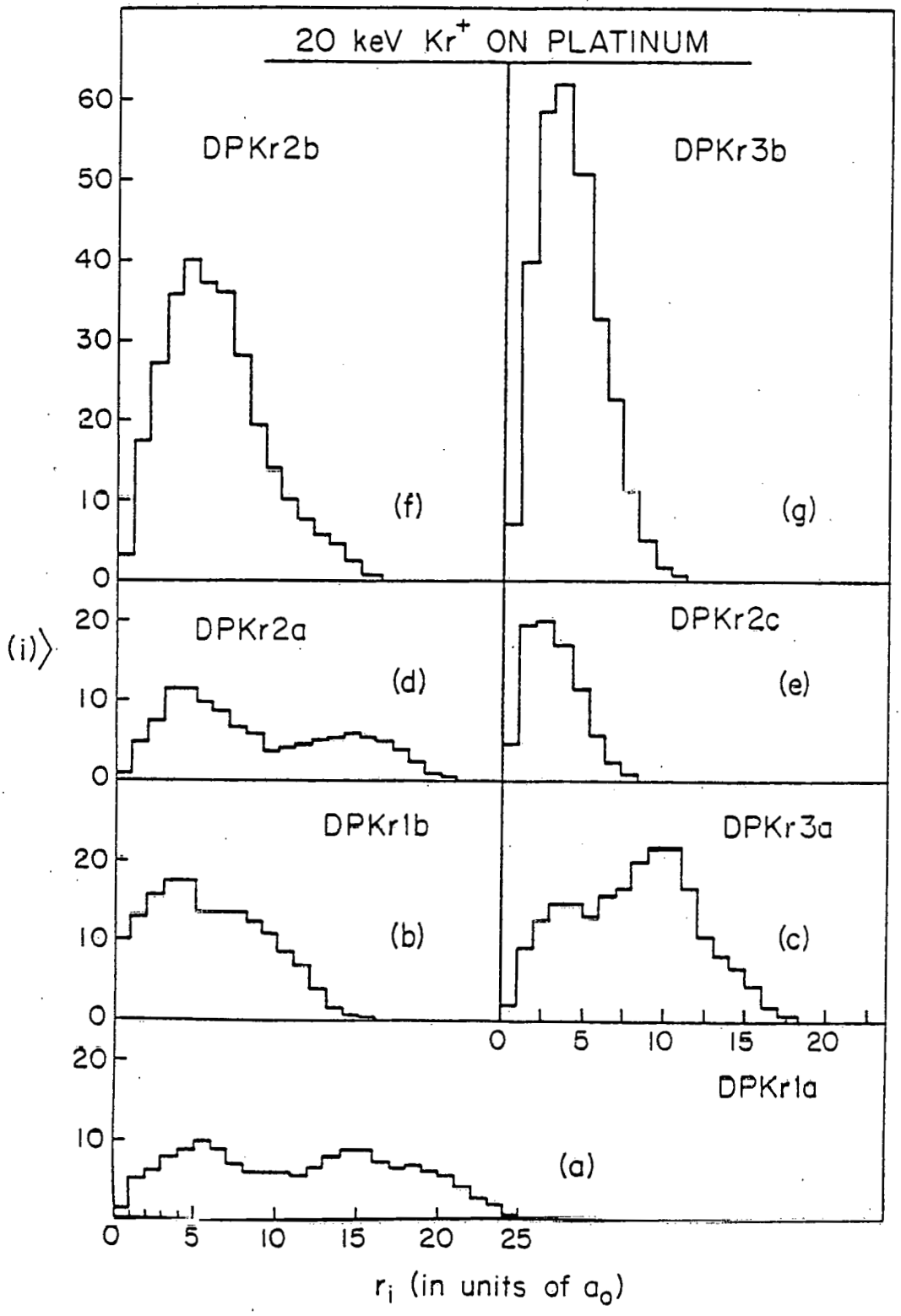

Fig. 26: The spectra of the <N(i)>s for depleted zones produced by 20 keV Kr^+ ion on platinum.

of three and one jumbo cluster of 224 vacancies.

III.2.3 Discussion

In this section, we will compare our experimental results with the predictions of radiation damage theory. In the past, the theory has followed two approaches. The first, the analytical theory, developed to a large extent to by Sigmund[12-14], is based on transport theories, while the second approach, using Monte-Carlo methods, utilizes the computer to simulate the transfer of energy between the irradiating particle and the target atoms[15-18]. It must be emphasized that both approaches depend very heavily on knowledge of the interatomic potentials, which are not very well known--particularly at values of $\varepsilon << 10^{-2}$. Various approximations are in current use and using these, both theories have been successful in dealing with the range of energetic ions in solids. Nevertheless, caution has to be exercised in comparing the theoretical predictions with the experimental results. Agreement between the two does not necessarily indicate the validity of all the assumptions underlying the theory, while disagreement definitely will point out various deficiencies in the theory.

The analytical theories are more difficult to apply to our results than the Monte-Carlo approach because they deal with quantities that are the result of bombardment by a beam, i.e., by a large number of particles, whereas we are dealing with quantities due to a single projectile ion. We shall henceforth refer to quantities related to the beam as "cumulative" quantities and those to single ions as "individual" quantities. For example, the analytical theories give the width of the cumulative damage profile which is obviously going to be larger than the individual width.

Attempts have been made to relate the quantities calculated from analytical theories to individual quantities through contraction factors.[19] In this respect, the Monte-Carlo simulations are closer in spirit to the experiments, as they follow the path of a single ion through the solid and obtain the results for a beam by superposing the results for a large number of ions. The computer codes written for this purpose differ in their sophistication. The Monte-Carlo calculations of Robinson and Torrens[17,18] designation MARLOWE allows the effect of target crystallinity to be studied--but it is time consuming and expensive. The recent TRIM code by Haggmark and Biersack[20] is far more efficient, though it is restricted to amorphous targets. Both TRIM and MARLOWE assume binary collisions between projectile and target atoms, thereby neglecting many-body effects. In the range of energies above 1 keV these effects are assumed to be insignificant.

We have adapted the TRIM program to simulate the creation of cascades within the target by following the trajectories of all the recoil atoms with energies above a threshold energy (E_d), as the incident ion energy is dissipated through a series of recoil events. We then calculated various quantities of interest that could be compared directly with the same quantities for the experimental DZ's. We found the computer simulations to be extremely useful as they allowed for variation of input parameters of the incident ions such as the angle of incidence. The computer simulations were also capable of taking into account the loss of energy due to recoil atoms leaving the surface or the incident projectile being backscattered out through the surface, a feature which the analytical calculations were incapable of accounting for. For large angles of incidence,

and in other cases where the DZ's were formed near the surface this effect can be important in determining the shape and size of the DZ.

The next few subsections will compare the results of theory with various experimental quantities.

III.3.3a Number of defects

The most useful as well as commonly used measure of the damage rate due to an incoming ion is the number of vacancies (ν) created per incident ion. The most elementary theory and the most widely used one for obtaining an estimate of the number of vacancies created in a cascade is that of Kinchin and Pease.[21] They obtained for the number of vacancies:

$$\nu_{K-P}(E) = \frac{E}{2E_d} \qquad (3-6)$$

under the assumption of an amorphous solid, two-body hard sphere atomic collisions, a sharp displacement threshold (E_d), and no inelastic energy losses. If an energy $\hat{Q}$ is lost during the development of the cascade through inelastic processes, the total energy available for elastic collisions, or damage energy is $(E-\hat{Q})$. Also, when a more realistic interatomic potential is used instead of the hard-sphere model, the scattering cross-section favors low-energy transfers, resulting in a smaller number of displaced atoms per cascade. Equation (3-6) may then be written, as pointed out by Robinson and Torrens:[18]

$$\nu_{R-T} = \eta \frac{(E - \hat{Q})}{2E_d} \qquad (3-7)$$

The factor η, known as the displacement efficiency, depends on the scattering law assumed. For a Moliére-type potential η is usually around 0.84. It is independent of the energy E because the vast majority of the

cascade atoms are generated from low-energy collisions, which would make $\nu(E)$ remain directly proportional to E.

For the case of 20 keV Kr^+ on Pt, we obtained the value $\langle E - \hat{Q} \rangle$ from the tables of Winterbon,[22] which were in turn based on a Linhard-Scharff electronic stopping formalism.[24] For Pt, we took E_d = 36 eV[23] and from Sigmund[13] we assume η= 0.84. Equation (3-7) then gives ν_{R-T} = 172. The modified K-P expression gives the mean number of vacancies but gives no indication of the spread in the number of vacancies. There are several sources of fluctuation in ν. They are:

(i) fluctuations due to the differences in the kinematic evolution of the cascade;

(ii) fluctuations in the electronic energy loss $\hat{Q}$; and,

(iii) fluctuations in the threshold energy E_d.

Leibfried[25] has discussed the effects of (i) using hard-sphere scattering and the K-P sharp displacement threshold model. He found the scaled variance, $\langle \Delta\nu^2 \rangle / \langle \nu \rangle$, to be given by:

$$(\langle \nu^2 \rangle - \langle \nu \rangle^2)/\langle \nu \rangle = 0.15 \qquad (3\text{-}8)$$

For $\langle \nu \rangle$ = 180 we obtain the standard deviation for the distribution in the number of vacancies to be $\Delta\nu$ = 5. Lehman[26] showed by an example that increasing the relative importance of forward scattering over the hard-sphere approximation leads to an increase in the scaled variance to ≤ 1. This increases $\frac{\Delta\nu}{\nu}$ to ≈7% for $\langle \nu \rangle$ = 180.

Linhard, Scharff and Schiott[27] provided several estimates of the fluctuation in electronic losses from scattering of the target electrons. Fluctuations in the electronic loss $\Delta\hat{Q}$, results in equal fluctuations in

$(E_1 - \hat{Q})$ and thus the number ν according to the Robinson-Torrens formula. According to one estimate, $\frac{\Delta E}{E_1} \simeq \sqrt{\frac{1}{14}(\frac{\hat{Q}}{E_1})}$ which gives $\frac{\Delta\nu}{<\nu>} \simeq 7\%$ for $\frac{\hat{Q}}{E_1} \simeq 0.25$. Another estimate based on the ratio of electronic to nuclear stopping powers gives $\frac{\Delta\nu}{<\nu>} \simeq 4\%$.

The contribution from (iii) is more difficult to evaluate since it is not immediately evident how the nature of the threshold energy will affect the damage in a cascade. Both computer simulations as well as electron damage experiments indicate that the displacement energy depends on the crystallographic direction.[28-30] It is clear that the assumption of a range of values of E_d will lead to a broader distribution of the number of defects than a single threshold. However, it is likely that when an atom is displaced from its lattice position the displacement will be determined by the minimum threshold energy. In Pt, we have chosen the minimum threshold energy of 36 eV as the threshold energy. Lucasson[31] has proposed an effective threshold energy that is four times the minimum value. Such a threshold energy gives the number of defects as $\nu_L = 43$. which is far below the results obtained from our FIM data.

We have also calculated the number of vacancies produced in a cascade from computer simulations. The same assumptions were made for the production of a vacancy as Kinchin-Pease, namely that a vacancy is created every time the incident and recoil atoms have energies greater than a sharp threshold E_d. If at the end of the collision the recoil atom has an energy greater than E_d--but the incident particle has an energy less than E_d--the number of vacancies is unchanged. The paths of all recoil atoms having an energy greater than E_d were followed until their energy had

dropped below E_d. Using the Lindhard-Scharff expression for the electronic energy loss we obtained $\langle\nu\rangle_{TRIM} = 182$, which is close to $\langle\nu\rangle_{R-T}$. This was not surprising since the same assumptions were contained in both results. The computer simulation has the advantage of giving the value of $\langle\Delta\nu\rangle$ due to kinematic fluctuations. We obtained $\langle\Delta\nu\rangle_{TRIM} = 11$, so that $(\frac{\langle\Delta\nu\rangle}{\langle\nu\rangle})_{TRIM} = 6\%$. Both the analytical as well as the TRIM results indicate a very narrow spread in ν.

The average ν observed experimentally was $\langle\nu\rangle_{exp} = 184$ which agreed very well with $\langle\nu\rangle_{R-T}$ and $\langle\nu\rangle_{TRIM}$ but the experimental fluctuations $\langle\Delta\nu\rangle_{exp} = 79$ were several times greater than the theoretical fluctuations.

In the experimental arrangement the ions were incident on the surface of the specimen at angles greater than 50°. Since a number of the observed DZ's were very close to the surface the effect of loss of energy through the surface, on $\langle\nu\rangle$ was investigated, using the TRIM program. For ions incident at 60° to the surface we obtained $\langle\nu\rangle_{TRIM} = 144$ and $\langle\Delta\nu\rangle = 35$.

As was expected, due to loss of energy through the surface, $\langle\nu\rangle$ was much less for an angle of incidence of 60° than for normal incidence. The value of $\langle\Delta\nu\rangle$ was also three times greater. The cascades produced near the surface, on the average, have a smaller number of vacancies, though a large number still possessed the full complement. A cascade with as few as 12 vacancies and one with 32 were obtained in a sample of 50 cascades. The cascades that were produced deeper inside the target, had on the average, the same number of vacancies as those for normal incidence--

which was to be expected as there was no loss of energy through the surface for these cascades. The larger value of $\langle\Delta\nu\rangle$ for the 60° incidence was a result of cascades with smaller values of ν, that is, the distribution was skewed towards lower values whereas at normal incidence it was approximately a gaussian. The maximum possible value of ν remained the same independent of the angle of incidence. On the basis of this consideration, we regarded an observed ν which was outside $\langle\nu\rangle + 3\langle\Delta\nu\rangle$, calculated for normal incidence to be significant. For 20 keV Kr^+ on Pt, if we obtained an experimental value of ν for a cascade that was greater than $182 + 3(11) = 215$ we regarded this as an indication of a physical process that had not been incorporated in the theory.

The small number of vacancies in DPKr2a and DPKr2c could be interpreted as a result of the loss of energy through the surface. The ν's for DPKr2b and DPKr3b were significantly larger than ν_{R-T}. In each DZ, there were regions with a high local vacancy concentration, which were large in size as was evident from the distribution of a first nearest neighbor cluster sizes.

The high concentration of vacancies indicated that the deposited energy density in this area was very large. The cascade that generated this DZ was therefore very likely a non-linear cascade.[32] In such cascades ν may be very much larger than ν_{R-T} because the assumptions of binary collisions breaks down. Moreover, the large number of atoms that are set into motion would destroy the lattice structure within the cascade during the time that it develops, leading to lower values of E_d for atoms displaced during the later phases of the collision cascade.

A frequently employed measure of cascade energy density is θ_0, the

mean energy density at the core of the cascade. For 20 keV Kr^+ on platinum, we obtained θ_0 = 7 eV/atom. θ_0 represents an average for many cascades, but the statistical fluctuations cause the energy density to vary from one cascade to another produced by ions of the same mass and energy. It is therefore possible for the cascades produced by projectiles with same M_1, E_1 to span the whole range from "linear" to "non-linear". Therefore, the actual fluctuations in ν will be greater than that expected assuming that all the cascades were linear. It is expected on the basis of this reasoning that fluctuations in ν should become greater as we approach the case of heavy ions on heavy targets where the nonlinearity in the cascades should become more prominent.

It has been commented on before that ν will depend on the recoil spectrum of the atoms in the cascade. For the case of a single threshold E_d, eqn. (3-6) arises from the E^{-2} recoil spectrum. A different recoil spectrum will produce a different functional dependence on E_d. Obviously, the largest number of vacancies that can be produced is $\nu_{max} = \frac{\hat{E}}{E_d} = 411$. This value is greater than the largest ν obtained experimentally, assuming E_d = 36 eV.

The FIM data indicated that ν_{R-T} is a good approximation to the average number of vacancies in spite of the large fluctuations. This agrees with other results of FIM on ion-irradiated tungsten for which more statistics are available, but is in sharp disagreement with the conclusions of Averback.[33] He used resistivity measurements, on thin films of Copper and Silver, to determine the point-defect production below 10° K due to irradiation with ion masses between 1 and 209 amu--in the energy

range between 20 and 850 keV. In the experiments, ν was calculated from the expression:

$$\nu_e = \frac{Nt}{\rho_F} \left(\frac{d\Delta\rho}{d\phi}\right)_0 \qquad (3\text{-}8)$$

where N is the atomic density, t is the film thickness, ρ_F is the Frenkel-pair resistivity and $\left(\frac{d\Delta\rho}{d\phi}\right)_0$ is the size-effect corrected initial-damage rate. A cascade efficiency factor was defined by the relationship:

$$\xi = \frac{\nu_e}{\nu_{R-T}} \qquad (3\text{-}9)$$

They found that $\xi = 1$ for light projectiles but that for masses >20 ξ was approximately 0.4 for both Au and Cu. According to our FIM data, even for heavy projectiles $\xi \simeq 1$. The low value of ξ obtained by Averback may be due to the reduced resistivity contribution of vacancies in clusters. A 50% reduction in resistivity per vacancy seems reasonable for clusters containing several hundred vacancies. The effect of clustering on the resistivity is clearly shown by the results for Ag and Au above Stage III,[34] the temperature range in which the vacancies are mobile. TEM data indicates that a large fraction of the vacancies survive as clusters and ξ=0.4. However, the resistivity data showed that $\xi = 0.1$, whereas at low temperatures it was ≃0.4. Since the TEM results indicate that there has been very little decrease in the total number of vacancies in the sample, the decrease in the resistivity can only have been caused by the rearrangement of the vacancies. This confirms the fact that the resistivity contribution per vacancy is dependent on the spatial arrangement of the vacancies and that the residual resistivity measurements considerably underestimated the number of Frenkel pairs in a cascade. While there

appears to be some difficulty in obtaining absolute damage rates from resistivity measurements, the relative comparisons of damage rates should be free from these difficulties. Merkle and Averback[34] studied the isochronal recovery of electrical resistivity in Ag after irradiations with various ions and found that for heavy ions, the total recovery above Stage I, corresponding to long-range interstitial migration was very low. It was ≈10% for self-ion irradiations of Ag and ≈15% for Au. This agreed very well with the FIM results for Pt where we found that ν did not change much from the value expected for no recombination even though the SIA's were mobile. The result can be understood on the basis of the picture of damage indicated by the FIM results on W; of SIA's well separated from the central core of vacancies, possibly as a result of RCS's along close packed directions. Wei, Seidman and Beavan[42] measured the mean separation of SIA's from the vacancy-rich core to be 160 ± 120 Å. In Pt, we also expected that the SIA's should have been separated from the vacancies and as a consequence, during their long-range migration, they were annihilated mainly at the surface, rather than at the DZ's. In the case of three-dimensional diffusion it is well known that the probability for an SIA to return to its origin is ≤0.35.[35]

III.2.3b Radiation damage range and profile

The DZ's were produced at various depths within the sample by incoming ions. The super-position in space of many such DZ's should give the radiation damage profile due to a beam of ions. The mean damage range for such a profile can be calculated from analytical theories and is tabulated for various ion-target combinations and energies by Winterbon. Using these tables we found the mean damage range L = 38 Å. Under certain

simplifying assumptions, it can be shown analytically that the mean depth of the centers of individual cascades is equal to the mean depth of the overall damage distribution. Benedek[36] reports that in the MARLOWE simulations of various ions on Au, the mean of the average damage depth for individual cascades was very close to the mean damage depth for the overall distribution. We used this fact to determine L from the TRIM program for cascades. The TRIM program gave L = 34.45 Å with straggling ΔL = 23.7 Å. All the DZ's, as well as other defects, were found within the expected limits. There is, however, a slight bias to the lower side of the range.

A cumulative damage profile that can be compared with theoretical results can be obtained by adding the total radiation damage due to the seven DZ's. We did this by counting the number of vacancies in 5 Å thick slabs, parallel to the surface of the specimen for each of the DZ's and summing up the total number of vacancies for each slab. Note that in this process the structure of the individual cascades was washed out and was replaced by a smoother distribution. The total vacancy count was 1285. We related the vacancy distribution to the damage profile as follows: Let $\Delta\nu(x)$ equal the number of vacancies in one 5 Å slab at a distance x, measured normal to the surface, i.e., along the direction [hkl] that was perpendicular to (hkl). We assumed that:

$$\Delta\nu(x) = \alpha F_D(x)\Delta x \qquad (3\text{-}10)$$

where $F_D(x)\Delta x$ was the damage energy deposited between x and $x + \Delta x$ (here we have taken $\Delta x = 5$ Å) and where α is a constant. If Δx is large enough we would expect the proportionality to be given by a Robinson-Torrens type formula with:

$$\Delta\nu(x) = \eta \frac{0.8F_D(x)\Delta x}{2E_d} \qquad (3\text{-}11)$$

Since $F_D(x)\Delta x$ is the total energy going into recoils in the volume represented by Δx, we expect that the recoil distribution within this volume would be the same as that within the cascade volume as a whole. This point has been proved rigorously by Sigmund.[37]

If N_v is the total number of vacancies created and $\hat{E}$ is the total damage energy, then:

$$N_v = \eta \frac{0.8\hat{E}}{2E_d} \qquad (3\text{-}12)$$

Thus from eqns. (3-10) and (3-9), we obtained:

$$f_v = \frac{\Delta\nu(x)}{N_v} = \frac{F_D(x)\Delta x}{\hat{E}} \qquad (3\text{-}13)$$

That is, if the fraction of vacancies is plotted as a function of distance, then the curve or histogram would be the same as the damage profile measured in terms of the fraction of the total deposited damage energy as a function of depth. Note that this is not <u>exactly</u> the same as the damage profile referred to in the analytical theories which consider the damage deposited as a fraction of the incoming energy, although the <u>shape of the profiles</u> will be the same. It is necessary to depict the damage profile in this fashion in order to match the calculated profiles to the experimental damage profiles measured from the vacancy counts, without using any scaling factors. We obtained the theoretical damage profile using the TRIM program for 10^3 20 keV Kr^+ ions incident at 60° and 70° to the surface of an amorphous platinum target, with the damage distance measured normal to the surface. Figure 27 exhibits the results of the

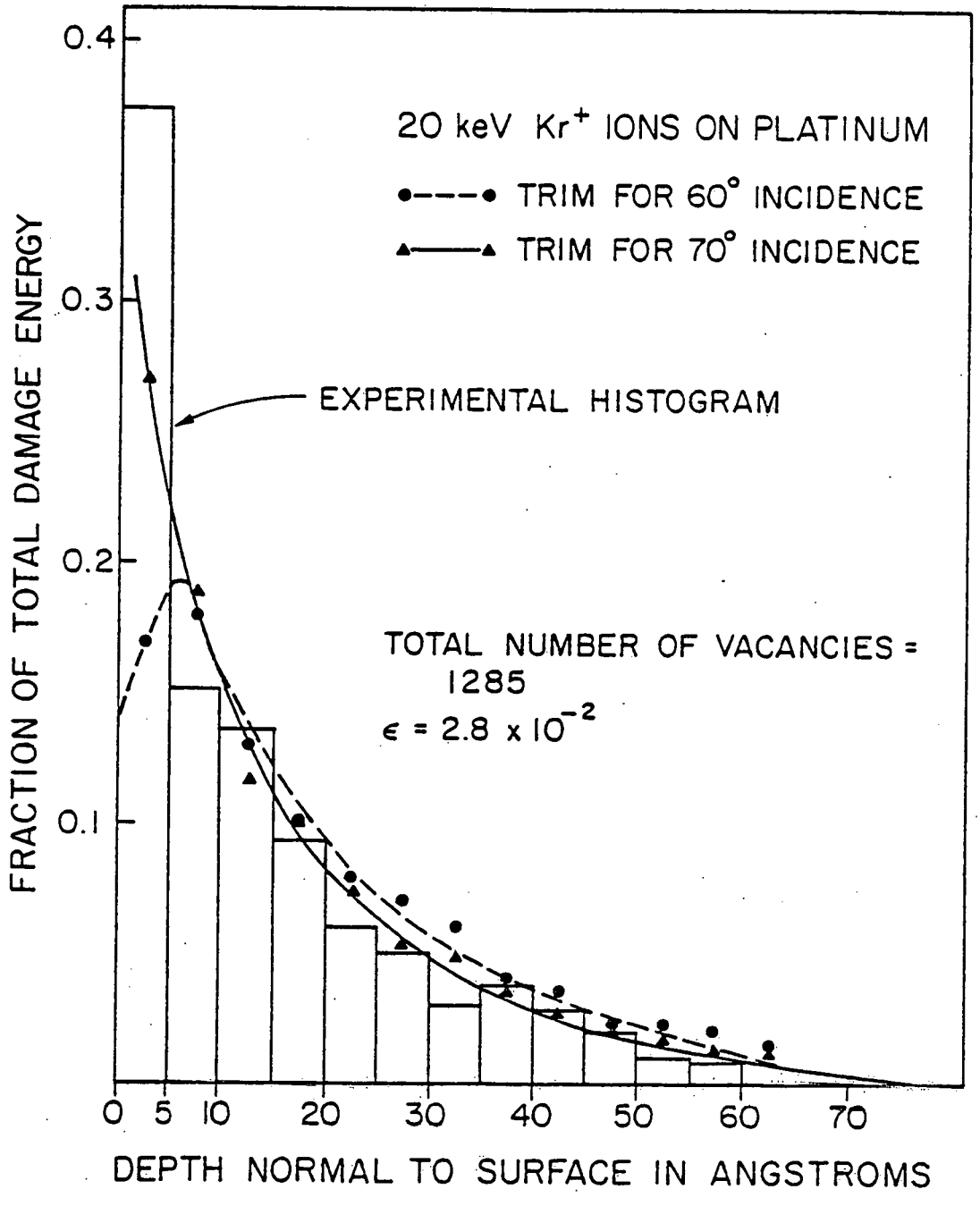

Fig. 27: The measured fraction of the total number of vacancies per 5Å interval summed over the seven DZs produced by 20 keV Kr^+ on platinum (histogram) and the calculated fraction of elastically deposited energy (smooth curve) as a function of depth normal to the irradiated surface [x(A)].

calculations as well as experimental results. The peak in the damage profile moves closer to the surface as the angle of incidence is increased. This is expected from simple geometric considerations, because on the average the larger the angle of incidence of the incident ions, the closer is the path of the average projectile ion to the surface and a larger fraction of the recoil energy is deposited near the surface.

The version of the TRIM program used to calculate the damage profile considers the path of the projectile alone and calculates the damage profile from the energy transfer to the target atoms along its path. The damage distribution representing the energy $\hat{E}$ ultimately left in the motion of the target atoms is calculated from the theory of Linhard.[39] However, note that the spatial extent of the damage profile is determined by the path of the incident projectile--the recoil atoms are not considered at all. In other words, the individual collision cascades will not affect the cumulative damage profile.

The TRIM results for an angle of incidence of 70° agreed well with experimental results. The average angle of incidence for the seven DZ's was ≈70°. In fact, for five out of seven DZ's the angle of incidence was ≈70°. In one case, it was 54° and in the other case it was ≈85°.

The excellent agreement between the experimental profile obtained from summing the damage associated with individual DZ's with the damage profile from TRIM illustrates the comments made above regarding the individual DZ's and the cumulative damage profile. It shows that the approximations introduced in the theory of ion stopping are valid for the particular energy E_1 and the ion-target combination for which $\varepsilon = 2.8 \times 10^{-2}$. It should be noted that, whereas the theory may be adequate to predict

the cumulative damage profile it may not necessarily be able to predict the spatial extent of individual DZ's as the ε for the recoil atoms are very small and in the range where the atomic potentials used are not well known.

This example illustrates the ability of the FIM to carry out measurements of the damage profile with very high resolution and complements the work of Aidelberg[40] on the measurement of damage profiles in order-disorder alloys (Pt_3Co and Ni_4Mo) using the change in the degree of long-range order as a measure of the deposited energy.

We end this section on damage profiles with a brief note on sputtering which is closely related to the deposited energy distribution. According to Sigmund's theory, sputtering is caused by the intersection of a cascade with the surface and the sputtering yield per ion should be closely related to the damage energy deposited near the surface. On the basis of this and the previous comments linking the damage profile to the vacancy distribution, it was found possible to obtain an estimate of the sputtering yield from our results.

Following the treatment of Current and Seidman a near-surface region was defined as the set of lattice sites occupied by hard sphere atoms whose geometric centers were visible, within the two dimensional primitive unit cell of an (hkl) plane, when viewed along a direction normal to this (hkl) plane in a hard sphere model; that is along the [hkl] direction for a cubic crystal. According to this criterion the thickness (d) of the near-surface region was $\simeq$2.5 Å for most of the planes considered. The total number of vacancies within this depth [near surface vacancies (NSV)] was $\Sigma\nu_{ns} = 373$. The yield of vacancies found in the near-surface

region was defined as:

$$S_v = \frac{\Sigma \nu_{ns}}{\text{total number of DZ's detected in FIM specimens}} \qquad (3\text{-}14)$$

Since there were seven DZ's, we obtained $S_v = 53$. If it is assumed that the majority of the sputtered atoms came from the near surface region then S_v should be close to the value of the sputtering yield S. Experimentally the value of S has been determined to be ≈11 for 20 keV Kr on Pt, which is also approximately close to the value obtained from Sigmund's formula. This yield was for normal incidence. Both experimentally and theoretically the sputtering yield should increase with increasing angle of incidence according to the relation

$$\frac{S(\theta)}{S(\theta = 0)} = (\cos \theta)^{-f} \qquad (3\text{-}15)$$

where $f \approx 1.7$[37,38] for $\theta < 70°$. Thus we would expect that

$$S(\theta = 70°) = 11 \times (\cos 70°)^{-1.7}$$

$$= 68$$

which is of the order of the value obtained from the count of NSV's.

If we count the number of vacancies ν_d down to a depth d, equal to the source depth defined by Sigmund and which is ≈5 Å for Pt, we get $\nu_d = 481$ and if all these vacancies were caused by atoms that were sputtered, we would obtain a sputtering yield of 69, which would be the same as the theoretical value.

The FIM data gives an indication of the degree of fluctuation involved in the number of sputtered atoms per DZ. The highest number of NSV's--for d-2.5 Å--was found for DPKr1b and was 118. The lowest number was for DPKr1a and was 9.

III.2.3c The dimensions of the DZ's

The dimensions of the DZ's listed in table 3.2 indicated a large spread in this quantity among the DZ. The average diameter of the DZ was

$$\langle\lambda\rangle = 26.36 \pm 12 \text{ Å}$$

We have estimated the widths of individual DZ's generated by the TRIM program. Since we are dealing with an amorphous solid in this case, there was no particular preference for any one direction and we have calculated the widths in two directions--in the x direction, i.e., along the initial direction of the incident ion and in the y direction perpendicular to this direction. The widths have been calculated in these two directions in the same fashion as for the experimental DZ's in the 13 close-packed directions, so the average dimensions calculated experimentally and theoretically were directly comparable. Note that while in the experimental results we chose special directions to measure the width, the averaging over several directions should remove any directional dependence of the size of the DZ. The mean diameters of the cascades were found to be

$$\sigma_x^* = 14.66 \text{ Å}$$

$$\sigma_y^* = 13.64 \text{ Å}$$

and hence

$$\langle\lambda\rangle_{TRIM} = 2\langle\lambda_x^*\lambda_y^{*2}\rangle^{1/3}$$

$$= 28 \text{ Å}$$

The variation in the diameters of the cascade along the x and y directions was

$$\langle\Delta\lambda_x^*\rangle = 4.81 \text{ Å}$$

$$\langle \Delta\lambda_y^* \rangle = 3.53 \text{ Å}$$

The average size expected from TRIM agrees excellently with the measured sizes. The limits of the diameters of the TRIM cascades include all the seven experimental DZ's including the most diffuse one, DPKr1a. Thus, the seven DZ's mirror the spread in cascade sizes expected from fluctuations in the kinematics of ion-ion collisions.

From Winterbons tables, it was possible to calculate the straggling $\langle \Delta x \rangle_D$ and $\langle y \rangle_D$ for the damage distribution along the initial direction of the ion beam and perpendicular to it, respectively. In order to go from these numbers to those for a single cascade one can multiply these quantities by a contraction factor $\delta^{1/2}$ which is an estimate of the difference between the individual damage diameters and the cumulative damage diameters. For the case of 20 keV Kr^+ on Pt we obtain from these analytical results an estimate of the spatial extent of a DZ to be

$$\langle \lambda \rangle = 2\delta^{1/2} [\langle \Delta x \rangle_D \langle y \rangle_D^2]^{1/3} \qquad (3\text{-}17)$$

From Winterbons table

$$\langle \Delta x \rangle_D = 24.6 \text{ Å}; \text{ and } \langle y \rangle_D = 19.8 \text{ Å}$$

Also $\delta^{1/2} = 0.6$ for this particular case. Hence, $\langle \lambda \rangle = 26.16$ Å which is also close to the experimental value.

III.2.3d Vacancy concentration

The value of the vacancy concentration c_v for the seven depleted zones exhibited a large spread with the largest vacancy concentration being six times the smallest. The fluctuation in c_v mirrors the fluctuations in sizes of the DZ's since ν should be approximately constant. The OR TEP visualizations clearly show the spread of c_v. The average vacancy

concentration $\langle c_v \rangle$ of the seven cascades was 6%.

We calculated the average vacancy concentration c_v^* from the TRIM program by using the diameters measured for the cascades. The value of c_v^* is given by

$$c_v^* = \frac{(0.30)\ \langle \nu \rangle\ \Omega_0}{(4\pi/3)(\sigma_x^* \sigma_y^{*2})} \qquad (3\text{-}16)$$

where Ω_0 is the atomic volume, $4\pi\sigma_x^*\sigma_y^{*2}/3$ measures the volume of the cascade that encompasses 30% of the total number of vacancies. On the basis of this formula we obtained $c_v^* = 7.6\%$ which is slightly greater than the average measured concentration.

It was assumed that the vacancy spatial distribution was given by a Gaussian distribution in accordance with the analytical expression for the deposited energy density. For such a distribution the vacancy concentration is higher at the center and falls off towards the outer periphery of the cascade. The c_v^* calculated from eqn (3-15) represents the average vacancy concentration within a one-σ radius around the center. A lower-bound on $\langle c_v^* \rangle$ was obtained by considering an ellipsoidal volume based on axes $6\sigma_x$, $6\sigma_y$, $6\sigma_y$ that encompassed 88% of all the vacancies. The net volume then increased by 27 times that before but the number of vacancies encompassed was only three times greater. As a consequence $c_v^* = 0.85\%$ for this case.

Comparing $\langle c_v \rangle$ and c_v^* we see that the eqn (3-15) gives a good estimate of the actual average vacancy concentration, calculated using the closest fitting volume to the DZ.

Some care must be exercised in the interpretations of these vacancy concentrations as they represent an average over the entire DZ. As the

OR TEP visualizations indicate the local vacancy concentrations show very large fluctuations within the cascade volume.

III.2.3e Radial distribution functions and clustering

In fig. 26, we have plotted the average R(i)/Z(i) for 20 keV Kr^+ on Pt and compared it with the values obtained for W for different species of projectile ions. It was shown by Current et al.[41] that the average R(i)/Z(i) for different projectile ions on a given target has no pronounced dependence on ion energy but depends only on the projectile mass. As is clear from fig. 28 there is a consistent trend towards decreased local clustering of vacancies as the ion mass is increased.

The atomic weight of Pt and W are very close to each other and the difference in density of the two materials is also very small. As a consequence, the spatial distribution of the deposited damage energy within the two for ions of same mass and energy should be approximately the same. According to the simple K-P type relation the vacancy distribution should be proportional to the deposited damage energy distribution and the number of vacancies will be proportional only to E_d^{-1}. The difference in E_d between Pt and W is 20% and hence there should be 20% more vacancies in Pt than in W for the same deposited energy density. This would reflect itself in a 20% higher R(i)/Z(i) for Pt compared to tungsten. In fig. 28, it is clear than the difference between the two curves for Kr on Pt and W respectively is very small. Thus, it appears that the damage is the same in both materials. As mentioned before, while a single threshold energy model gives approximately $\langle\nu\rangle$ it does not give a good indication of the range of fluctuations in $\langle\nu\rangle$ and the degree of fluctuation within $\langle\nu\rangle$ for either W or Pt is larger than expected difference in

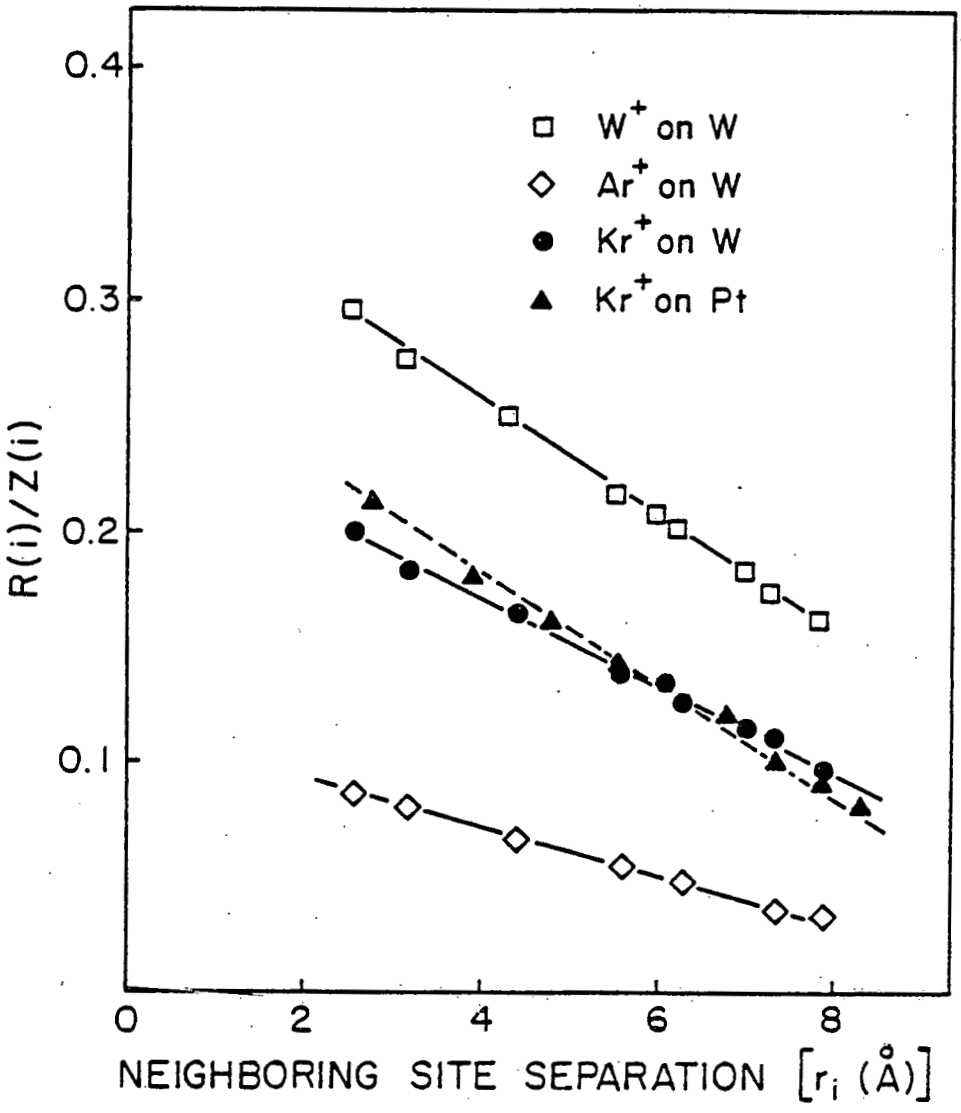

Fig. 28: A comparison of the average normalized radial distribution function <R(i)/Z(i)> in platinum and tungsten for various projectile ions.

<ν> between them based on the K-P model. It is not surprising, therefore, that there is very little difference between the local clustering in Pt and W for the same projectile ions. The results indicated also that the crystal structure did not play a major role in the spatial distribution of the damage when the incident ion was directed along a non-channeling direction. It is now clear why the results for amorphous targets are readily applicable to the case of crystalline targets, as long as channeling effects have not to be considered.

A comparison of the association of vacancies into first-nearest neighbor clusters for Kr irradiation of W and Pt also shows striking similarity in the degree of clustering for the two metals. In W for 30 keV Kr irradiations 28% of the vacancies are monovacancies and 52% are in clusters of size larger than or equal to five vacancies. In the case of Pt, the results of which are shown in table 3.3, the corresponding figures are 29% and 60%. Current et al.[41] showed that there were strong variations in the number of monovacancies and fraction of vacancies contained in large clusters with variations in projectile mass. The fraction of monovacancies rose gradually as the projectile mass decreased and the fraction of large clusters correspondingly decreased. Our results indicated that, on the average, the fraction of monovacancies and clusters is dependent only on the projectile and target masses, and the other properties of the target do not affect the cluster distributions. Current et al.[41] also pointed out that the distribution $\xi = N_n/(\Delta n \Sigma N_j)$ was not significantly effected by variations in ion mass and energy. Here N_n is the number of clusters of size n and the sum is from n = 1 to n = n_{max}, the largest cluster size; Δn is a size interval. The results for DZ's

TABLE 3.3

Fraction of vacancies in first-nearest neighbor clusters of size n for 20 keV Kr^+ on platinum

Size of cluster (n)	1	2	3	4	5
$f = n\frac{N_n}{\nu}$	0.29	.083	.02	.009	0.6

mapped out in W for various ion masses and energy gave

$$\xi = (0.75 \pm 0.05)n^{-(2.5 \pm 0.5)} \qquad (3\text{-}18)$$

In the case of Pt for the 20 keV Kr irradiations, the distribution was given by

$$= 0.8n^{-2.2} \qquad (3\text{-}18)$$

which is virtually similar to the one in W. The variation of ξ with n is shown in fig. 29.

III.2.4 Dislocation loops

The dislocation loops were identified by the contrast patterns they produced in the FIM micrographs. The contrast pattern expected from a dislocation loop can be understood on simple terms, using the fact that the FIM image can be simulated with remarkable success on purely geometric grounds. The details of the geometric theory are outlined in Appendix A. Briefly, the effect of a dislocation emerging near the pole of a low index plane is to change the pattern from a concentric series of circles to a single or multiple spiral. A perfect dislocation loop can be considered as a pair of single dislocations and the spiral started at one dislocation ends at the other one. Plane rings enclosing both dislocations will be unbroken, since the net Burgers vector will be zero. A stacking fault emerging at an angle to a low index plane shifts the rings on one side of the fault relative to the other so that the rings appear stepped at the stacking fault. The contrast expected from a faulted loop such as a Frank loop can be obtained by combining the effect of a perfect dislocation and a fault. Thus the FIM pattern from a faulted loop will be a stepped spiral.

An important quantity for a perfect dislocation is $p = \vec{b} \cdot \vec{g}_{hkl}$

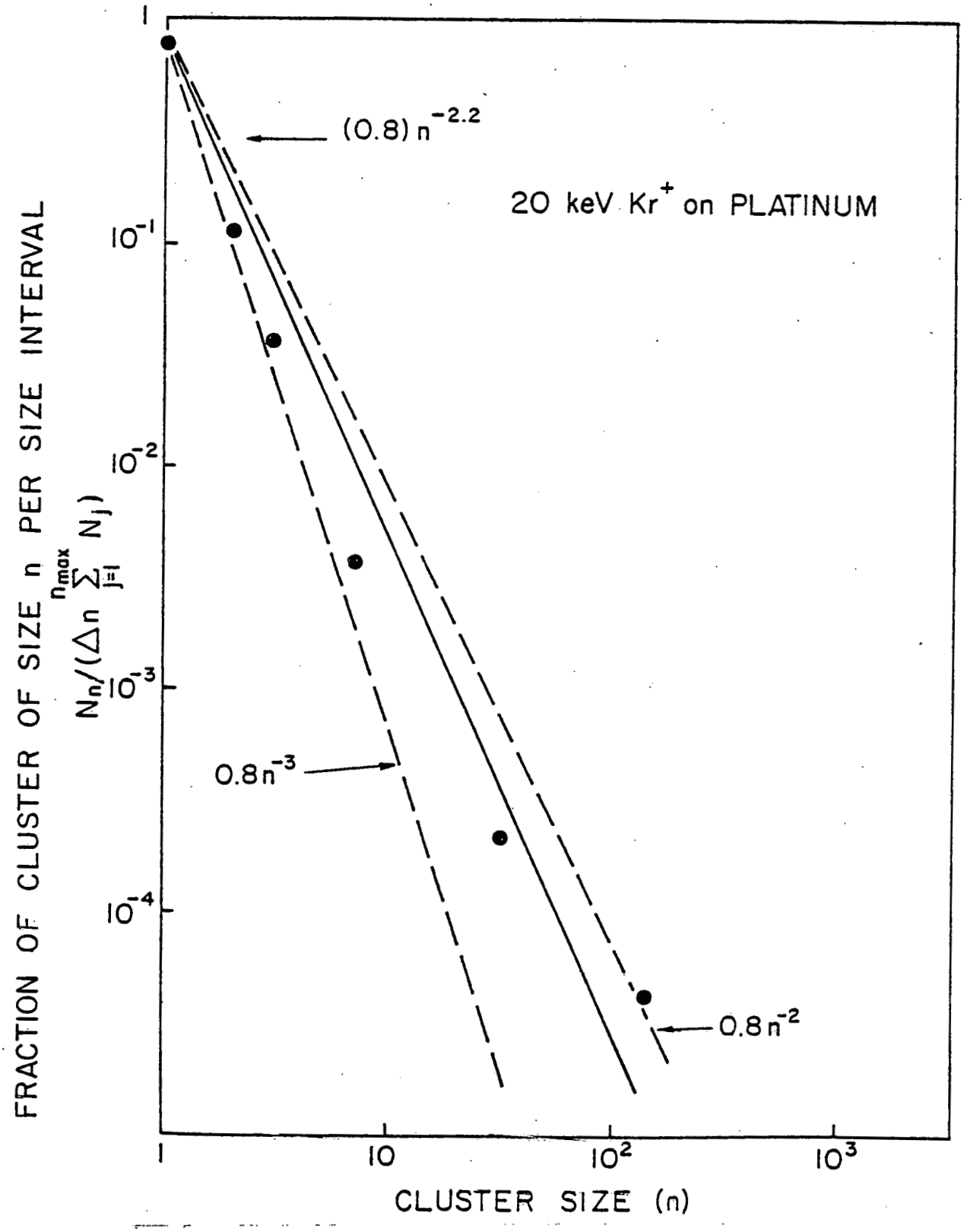

Fig. 29: The distribution of nearest neighbor clusters of size n(f_n) as a function of cluster size (n) for all the DZs produced by 20 keV Kr^+ on platinum.

$\vec{g}_{hkl}$ is the reciprocal lattice vector of the plane (hkl) on which the dislocation emerges. The value of p is an integer that indicates the multiplicity of the image spiral caused by the dislocation. A similar quantity, defined for a faulted dislocation loop is $q = \vec{b}\cdot\vec{g}_{hkl}$ which may or may not be an integer. If it is not an integer then the image spiral shows a step at the fault; if it is an integer, instead of a step at the fault, there will be a kink caused by displacement of atomic rows in the plane.

The habit plane of a faulted loop can be obtained from the trace of the fault plane on the image plane, if it is visible. The habit plane of a perfect loop is more difficult to obtain, unless it appears on a high index plane. Once the habit plane of the loop is known it is possible to determine whether the loop is vacancy or interstitial that is whether it is intrinsic or extrinsic respectively from the sense of the spiral or in the case of a faulted loop, from the size of the rings on either side of the fault line.

In fig. 27, we show two loops A and B inside an FIM specimen. The initial surface with its center at O intersects the top of the loops. Consider the loop A, whose habit plane (hkl) makes an angle with the pole of the specimen. After field evaporation, the surface has moved down to the dotted position with center at O_1 and now intersects the plane of the loop. The trace of the loop on the surface is shown as a solid line on the dotted surface and its diamters is ω_1 at this stage. ω_1 can be measured from the FIM micrograph using the local magnification m which is found as follows. Several high index planes in the immediate vicinity of the loop were chosen and the distance in centimeters between a particular crystallographic row of atoms was measured on one of these planes.

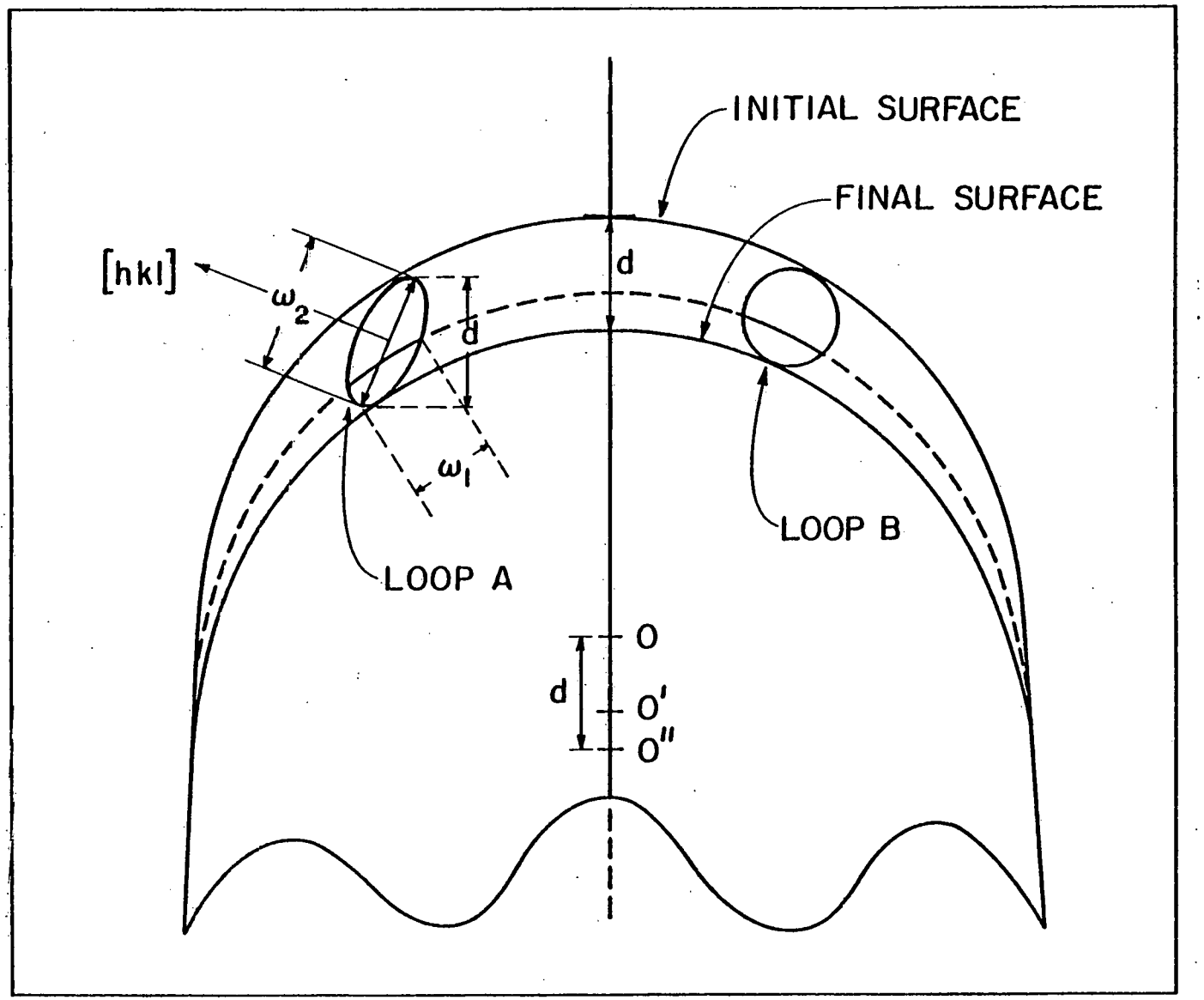

Fig. 30: A schematic diagram of a FIM specimen, showing the diameters ω_1 and ω_2 measured, for a dislocation loop.

From a knowledge of the crystallography of the planes, the actual distance in angstroms was known. The value of m was then determined. By choosing various rows on these planes the value of m in several directions and several areas was determined and the average of these values was taken as m. The distances determined from the local magnification may be slight underestimates of the actual distances because the FIM specimen surface is dilated by the high electric field.

As field evaporation proceeds and the surface of the specimen moves down through the loop, the diameter ω_1 varied according to the shape of the loop. We took ω_1 to be the maximum diameter of the trace of the loop. The diameter ω_2 of the loop in a second direction could also be measured from the field evaporation sequence (see figure 30). If the loop contrast appeared on a $(h_1k_1l_1)$ plane and persisted until n planes were evaporated, then ω_2 is given by

$$\omega_2 = \frac{nd_{h_1k_1l_1}}{\sin \Phi} \qquad (3\text{-}20)$$

Where Φ is the angle between the plane (hkl) and the loop and $(h_1k_1l_1)$, $d_{h_1k_1l_1}$ is the interplanar spacing of $(h_1k_1l_1)$. It has been pointed out by Stoll that the dimensions of the loop determined in this fashion may overestimate the actual dimensions by as much as 20% since the contrast from the loop is visible before the surface intersects the loop. We think that the diameters that we measured by this method are not overestimated by this percentage as the counting of planes is begun only when the contrast is very strong. It is easier to detect small changes in computer simulated FIM patterns than it is in an actual experimental pattern. Hence, we feel that the loop is at the surface or already

intersecting it when we begin counting planes.

Two dislocation loops were detected after the 20 keV Kr^+ irradiations, both of which were located at the surface just after the irradiation. The Burgers vector $\vec{b}$ of the loop, its habit plane and whether it was an interstitial or vacancy loop could be determined in many cases on the basis of the simple geometric theory of contrast outlined above.

Loop LPKr2a appeared on the $(3\bar{1}1)$ plane. Successive frames of a pulse-field-evaporation sequence are shown in fig. 31(a). The last frame indicates the contrast on the plane when the dislocation loop is no longer present. The first frame was taken just after irradiation and a few atoms had been field evaporated (less than one $(31\bar{1})$ plane was field-evaporated). The contrast before irradiation was therefore like that in the last frame and the effect of the loop is immediately evident. The contrast in frame 1 clearly shows the broken ring structure characteristic of a stacking fault and the dislocation loop is therefore a Frank loop. The trace of the loop is immediately evident from the break in the rings in frame 1 and is shown in all the frames where the loop contrast is evident. The $[12\bar{1}]$ direction is shown also in Frame 1 and lies on the zone line joining the 200 and $1\bar{1}1$ pole. From the orientation of the trace with this direction, it was possible to determine which of the four possible $\{111\}$ planes, (111), $(\bar{1}11)$, $(1\bar{1}1)$, $(11\bar{1})$ were the habit planes. The last two are rejected because their trace on the $(3\bar{1}1)$plane make too large an angle with $[1\bar{2}1]$ compared with that observed. The trace of the other two planes make equal but opposite angles with this direction. From the orientation of the trace with $[12\bar{1}]$ we deduced that the habit plane was (111).

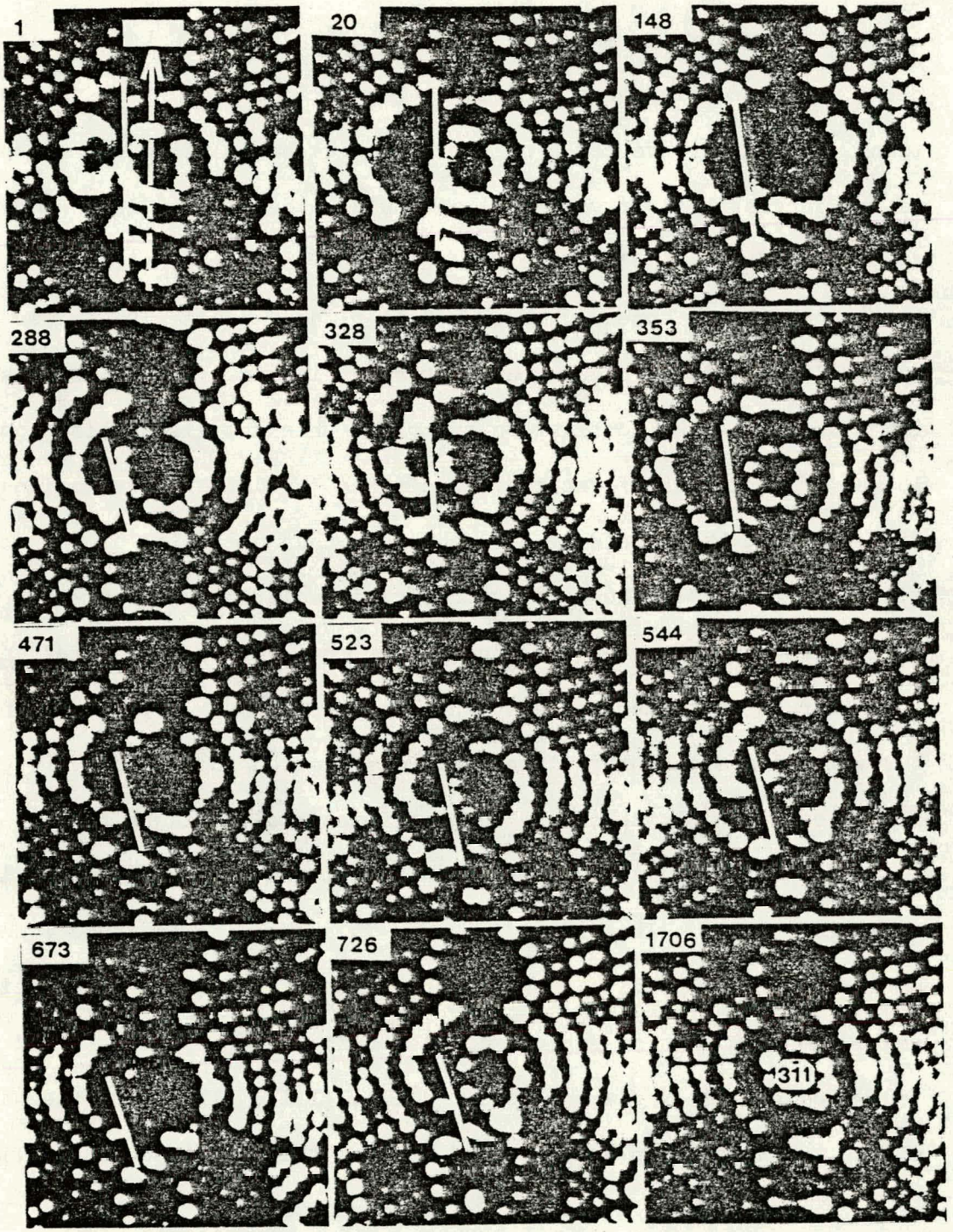

Fig. 31(a): A pulse field evaporation sequence showing contrast from dislocation loop emerging on (3$\bar{1}$1) planes.

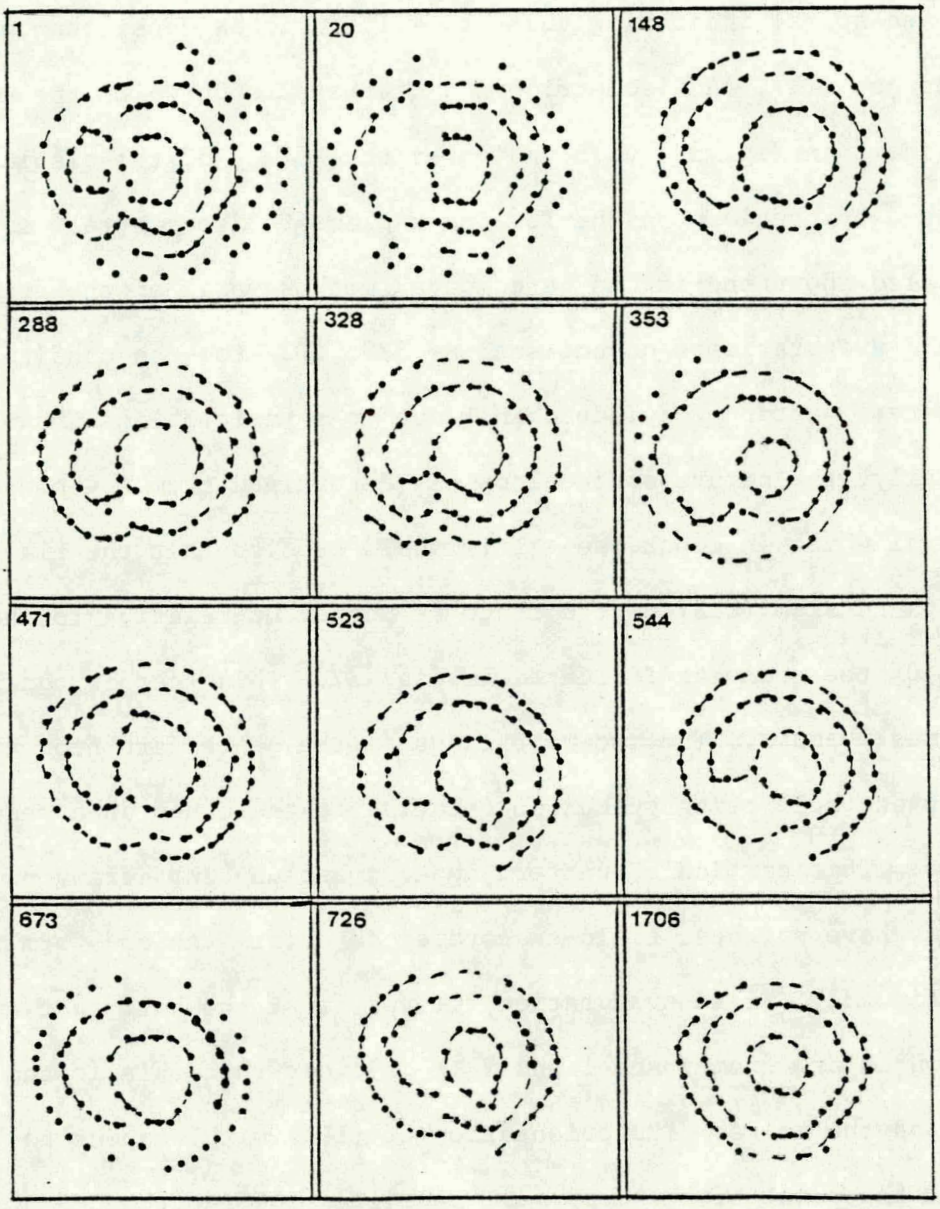

Fig. 31(b): A schematic diagram of atoms near the dislocation loop for the sequence shown in fig. 31(a).

The field evaporation sequences showed the contrast to be a single kinked spiral indicating that $|q| = 1$. This is consistent with a Frank loop on (111). An isometric view of the pole on which the loop emerges is shown in fig. 32 which indicates the effect of the displacements caused by the loop on the low index planes. The contrast to be expected is also shown and it can be compared with several of the frames in the field evaporation sequence such as 328, 523 etc., to confirm that the observed pattern was indeed that due to a faulted loop for which $|q| = 1$. Finally, the nature of the loop was determined from the sense of the spiral which is clockwise. This would require that the planes on the lefthand side (LHS) of the trace be pushed up relative to those on the RHS of the trace as indicated in fig. 32. This fact is confirmed by frames 1 and 2. The two-half rings in the center are from the same plane with one half being pushed up relative to the other as a result of the loop. This particular pattern appears because sufficient number of atoms have not been field-evaporated to obtain the end form that is shown in fig. 32. Field evaporation removes first the half that extends further outwards and from frame 1 and 2 it is clear that this is the half on the LHS of the trace. The orientation of (111) with respect to $(3\bar{1}1)$ is such that the plane of the loop will be tilted towards the LHS of the trace. In order for the LHS to be pushed up this requires that the loop be extrinsic. By the method described above we were further able to determine the diameters of the loop to be $\omega_1 = 26$ Å and $\omega_2 = 7$ Å.

The second dislocation loop LPKr3a was detected on the $(3\bar{1}\bar{1})$ plane. The pulse field evaporation sequence is shown in fig. 33. The last frame indicates the contrast when no loop is present and a comparison with

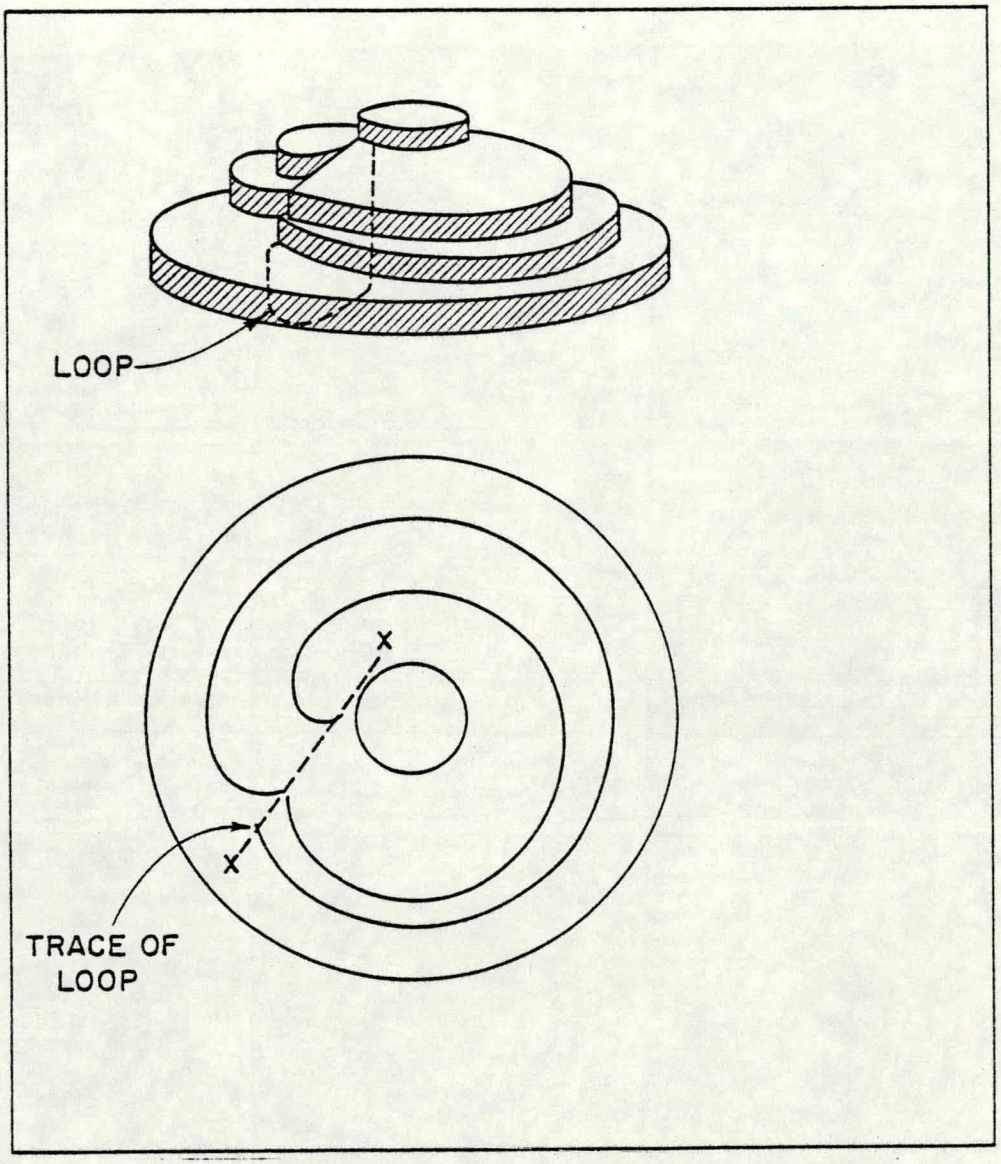

Fig. 32: A three-dimensional isometric drawing illustrating the effect of a dislocation loop emerging on a low index plane and the corresponding contrast expected in the FIM micrograph.

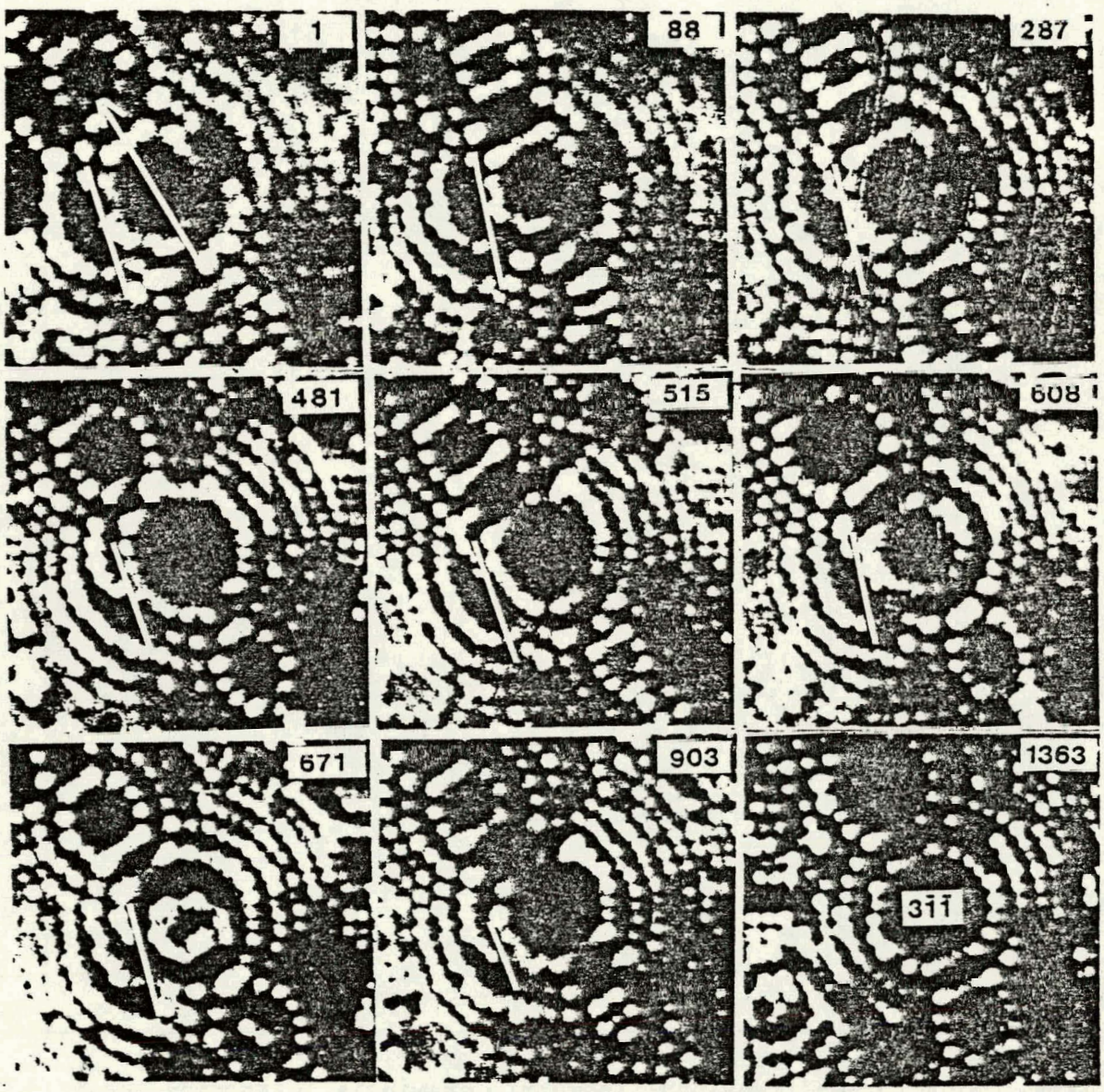

Fig. 33(a): A pulse field evaporation sequence showing the contrast from a dislocation loop emerging on a (3$\bar{1}\bar{1}$) plane.

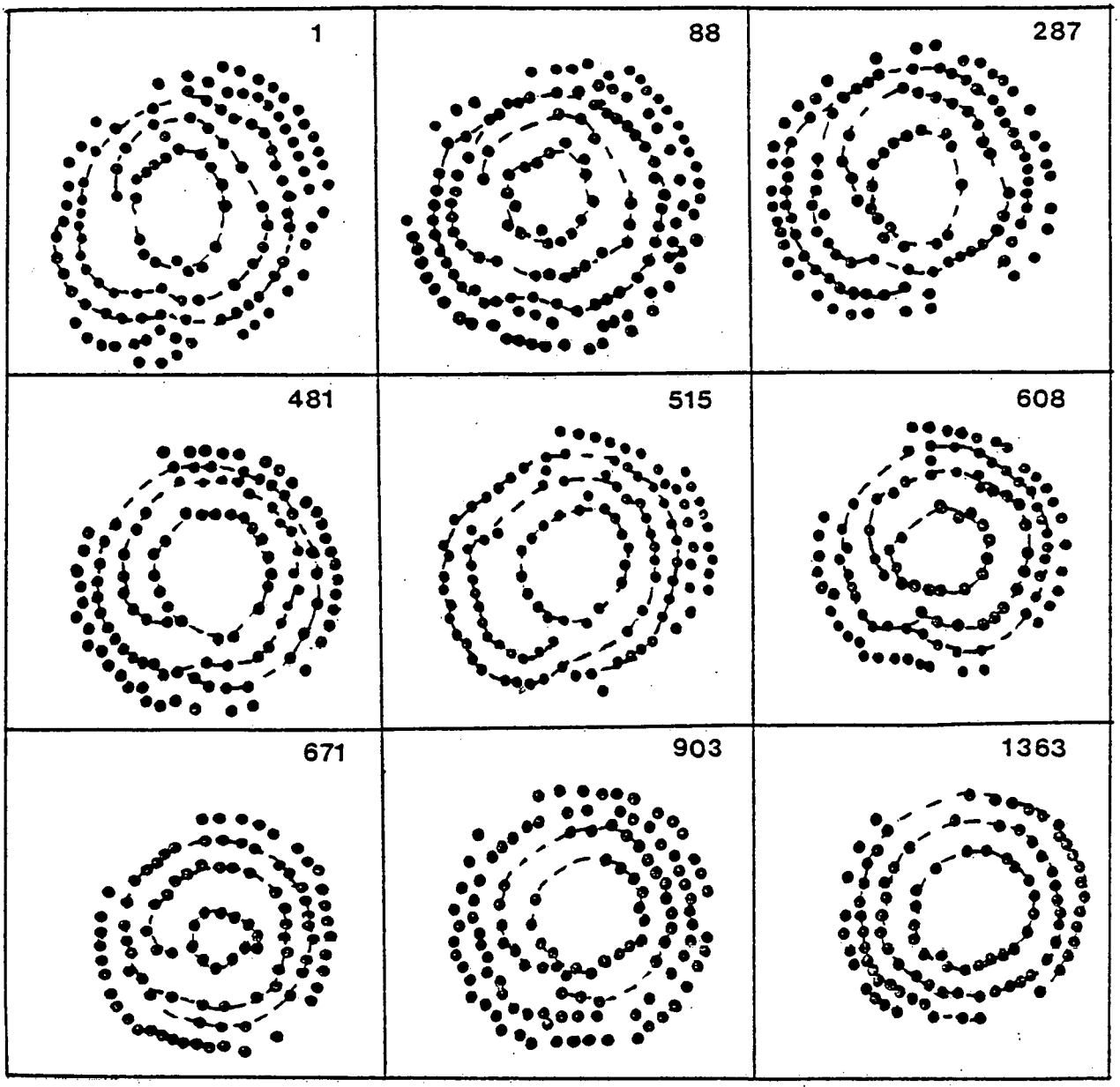

Fig. 33(b): A schematic diagram of atoms near the dislocation loop for the sequence shown in fig. 33(a).

the contrast is the first eight frames indicates very clearly the effect of the dislocation loop. The trace of the loop is deduced from the kinks in the rings, and is shown in the frames where the effect of the loop is visible. The $[1\bar{2}\bar{1}]$ direction is also shown which lies on the zone line joining the 200 and $1\bar{1}\bar{1}$ poles. As described for the previous case the orientation of the trace relative to this direction restricts the habit plane to (111). The loop is a Frank loop because the rings are kinked. The contrast pattern is in fact very similar to the previous loop except that the habit plane is shifted further away from the center of the plane.

The field evaporation sequences clearly showed the contrast to be a single kinked spiral. This is made clear in fig. 33(b) where the spiral has been traced out. Thus $|q| = 1$ and this is consistent with a Frank loop on $(11\bar{1})$. An isometric view of the pole showing the effect of the displacements caused by the loop is shown in fig. 34. The FIM contrast to be expected is also shown and it can be compared with several of the frames in the field evaporation sequences such as 287, 608 etc., to confirm that the observed pattern was indeed that due to a faulted loop for which $|q| = 1$. The nature of the loop was determined from the sense of the spiral and the habit plane. The clockwise sense of the spiral indicated that the planes on the LHS of the trace had been pushed up relative to those on the RHS, and from the orientation of $(11\bar{1})$ relative to $(3\bar{1}\bar{1})$ this required that the loop be intrinsic. The diameters measured for the loop were $\omega_1 = 34$ Å and $\omega_2 = 10$ Å.

Thus both loops are Frank loops; one is intrinsic and the other is extrinsic. TEM data on 60 keV Au^{2+} irradiation of Pt indicated the presence of primarily vacancy-type loops, both Frank loops and perfect

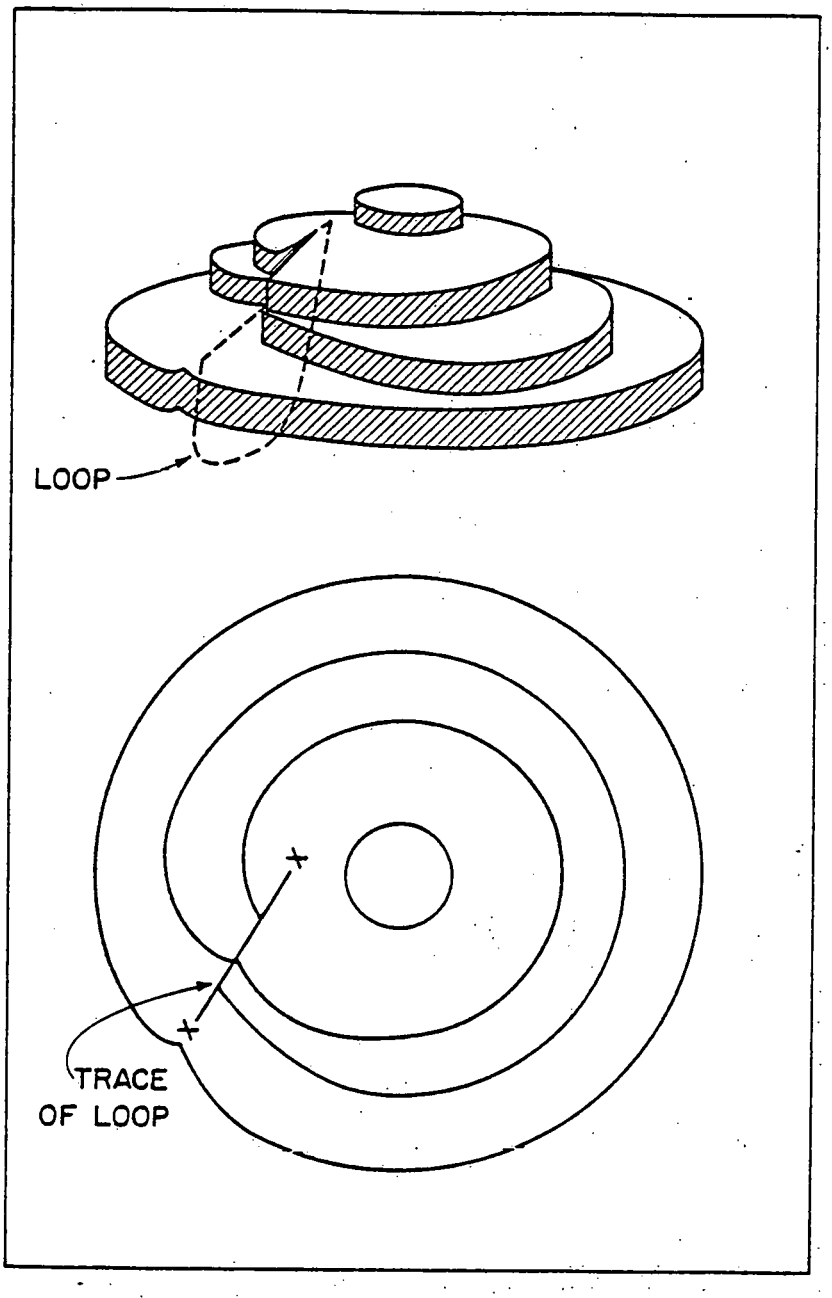

Fig. 34: A three-dimensional isometric drawing illustrating the effect of a dislocation loop emerging on a low index plane and the corresponding contrast expected in the FIM micrograph.

<110> type loops. Unannealed Neutron-irradiated Pt specimens exhibited both vacancy and interstitial type loops. In the case of gold which is an f.c.c. metal with almost the same atomic number as Pt, both types of loops are seen for light ion ($M_1 \leq 85$) irradiations. The fraction of interstitial loops decreased with increasing atomic number and was almost negligible for 20 keV Kr^+ irradiations. Though the fraction of interstitial loops may be, in all likelihood, very small for 20 keV Kr^+ irradiations of Pt it does not rule out the possibility of their occurence. The interstitial loop that we have detected could have been produced by the aggregation of SIA's at the surface, during the long-range migration. As mentioned earlier, the bulk of the SIA's are separated by comparatively large distances from the DZ by means of RCS's and as a consequence are more likely to reach the surface than recombine with the vacancies in a DZ.

It is very likely that the vacancy type loops are caused by the collapse of very dense DZ's. In the case of platinum or any other f.c.c. metals, Frank loops are formed by the collapse of vacancies onto the (111) plane. Perfect loops could be formed by the unfaulting of Frank loops through the reaction

$$\frac{a_0}{3}[111] + \frac{a_0}{6}[112] \rightarrow \frac{a_0}{2}[\bar{1}10] \qquad (3\text{-}20)$$

or directly (which would leave the loops on (111) planes) or by the collapse of vacancies onto {220} planes. The existence of a (110) vacancy platelet in Pt-4 at % alloy indicated that the second possibility is very likely. We have examined the width of the individual DZ's that have a high c_v. In DPKr2c, the width was a minimum along the [110] direction

and the projection of the positions onto the (001) plane showed that the bulk of the vacancies (78) lay on seven (110) planes. In DPKrlb, a total of 120 vacancies lay on eight [110] planes. The existence of these multi-layer plate-like structures indicated the possibility of a defect structure intermediate between that of a DZ and a loop. On the theoretical side Johnson[44] has predicted that a single layer vacancy-platelet on a {111} plane, in nickel, is stable to collapse into a perfect dislocation loop up to 180 vacancies. On the other hand, Savino and Perrin[43] have calculated by a computer simulation technique that a (111) planar vacancy aggregate, in copper of as few as six vacancies can readily collapse into a more stable configuration. A point which has to be kept in mind is that a collection of defects existing in a configuration of a much higher energy than a second configuration may not necessarily transform to the second configuration because of a kinetic barrier.

The formation of loops at low temperatures evidently requires the rearrangement of vacancies that have been created by the above-threshold recoils generated within the target by the incoming ion. The time scale involved in creating the DZ is 10^{-13} sec. After the creation of the DZ, the atoms within the vicinity of the DZ will have energies below the threshold, (in this case, 36 eV) but which can still be very large compared to the normal energy of the atom. This energy will be dissipated to the surrounding lattice. During this process, vacancies and SIA's in the vicinity of the DZ can apparently undergo a few jumps. The diffusion process can cause recombinations and clustering. The effect can be significant in DZ's having a high defect density. It has been customary to use θ_0, the effective maximum deposited energy per atom, which can be

estimated from analytical theories as a measure of the "thermal spike" effect. The quantity θ_0 describes an energy deposition average while the collapse process involves individual cascades and it is not immediately obvious how to relate the two. The results we have obtained for 20 keV Kr^+ on Pt indicates a whole range of cascade sizes and clustering of vacancies, a fact which is also confirmed by TRIM. The possibility exists that due to statistical fluctuations, the deposited energy density may be very high in some of the cascades that generated by ions of a particular mass and energy. The DZ's produced in such a cascade will also have a high vacancy concentration. In these high density DZ's, the vacancies can undergo further rearrangement to platelets or further collapse to loops. In the more diffuse cascades the energy is deposited over too large a volume to cause further rearrangements.

In one of the DZ's, DPKr2b, we noticed that in a region where there was a high density of vacancies, the field evaporation sequence indicated very severe distortions of the lattice and in some cases the arrangement of atoms on successive planes showed a spiral-like structure. This is illustrated in fig. 35. Frame A shows the (531) plane before irradiation. The atoms are arranged in regular rows and successive planes are concentric with each other. In a typical field evaporation sequence the outer atoms on the plane field evaporate first and the planes shrink in size, but always maintaining the concentric pattern. Frames 1 to 665 display the field evaporation sequence for the same plane in a region encompassing part of DPKr2b. Frame 167 to 254 illustrate the field evaporation for one plane that is complete in 297. Note the spiral-like appearance of the planes, instead of the concentric pattern in frame A. Because of this,

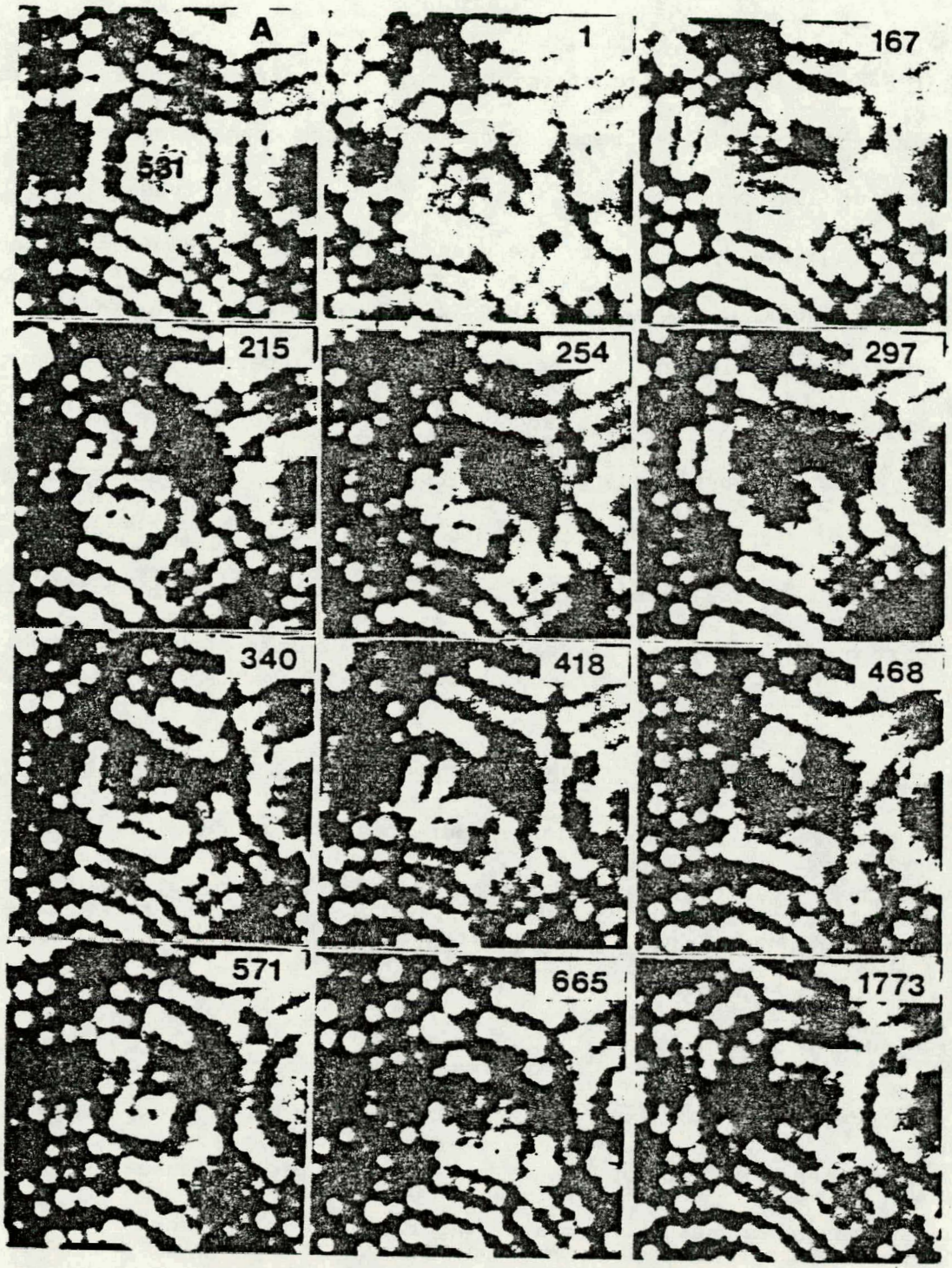

Fig. 35: A pulse field evaporation sequence illustrating a partially collapsed region in a dense DZ produced by a 20 keV Kr^+ ion in platinum.

it becomes difficult to associate atoms to a particular plane just by glancing at a single frame. For example, the atoms observed in the upper part in 297 do not belong to the plane which is observed to field evaporate in 340 and 418 but to the plane in the center in 468. In such cases, the necessity of fine field evaporation, whereby only a few atoms are removed per pulse and the recording of the pattern after each pulse becomes evident. In frame 1773 the vacancy concentration has become low enough that successive planes now appear concentric again. The sequence can be compared with fig. 16 which showed the vacancies in a diffuse DZ on successive (513) planes. The results indicated the possibility that in part of the DZ a partial collapse to a loop-like structure may have occurred.

III.3 20 keV Pt^+ irradiation

20 keV Pt^+ irradiation of pure platinum produced the same three morphological types of defects as 20 keV Kr^+. In all, we were able to detect four DZ's and one dislocation loop.

III.3.1 Depleted zones

Of the four DZ's we were able to obtain an approximate count of the vacancies in only two of the DZ's. Both had approximately 160 vacancies. We were unable to map the vacancies because in certain regions encompassing the DZ the field evaporation of the planes containing the vacancies became very irregular and it was difficult to keep track of the coordinates of the remaining atoms. In the other two DZ's, experimental difficulties prevented completion of the pulse-field evaporation before the entire DZ had been pulse-field evaporated. The pulse-field evaporation sequence of planes within the DZ as well as the bending of the atomic rows

adjoining the DZ appeared to indicate a strain field that could be ascribed to a partially collapsed DZ.

III.3.2 Dislocation loop

The field evaporation sequence for the loop is shown in fig. 36a. The loop appeared on the (513) plane and the contrast due to the loop is clear when comparing it with the contrast on the equivalent plane $(5\bar{1}3)$ also shown in the frame. The trace of the loop was deduced from the break in the rows of atoms in frame 28, and is illustrated by the broken line in fig. 36b. The trace was consistent with a habit plane of $(11\bar{1})$. This plane is tilted towards the LHS of the trace. Since the sense of the spiral is clockwise the planes on the LHS have been pushed down relative to those on the RHS of the trace. This implies that the loop is an intrinsic loop. The diameters of the loop are ω_1 = 20 Å and ω_2 = 3.5 Å.

III.4 Summary

1) The irradiation of platinum by 20 keV Kr^+ ions produces depleted zones, voids and dislocation loops.

2) The structure of the DZ's shows wide variations but the average properties are satisfactorily described by the current theories of ion-stopping. The damage profile obtained by adding the damage of the individual DZ's is very close to that calculated from these theories.

3) The average number of vacancies per DZ ($\langle\nu\rangle$) is approximately given by the modified Kinchin-Pease value. The fluctuations in ν are larger than that expected from linear cascade theory and is believed to be due to the occurence of non-linear cascades.

4) The dislocation loops have been analyzed as Frank loops. Both

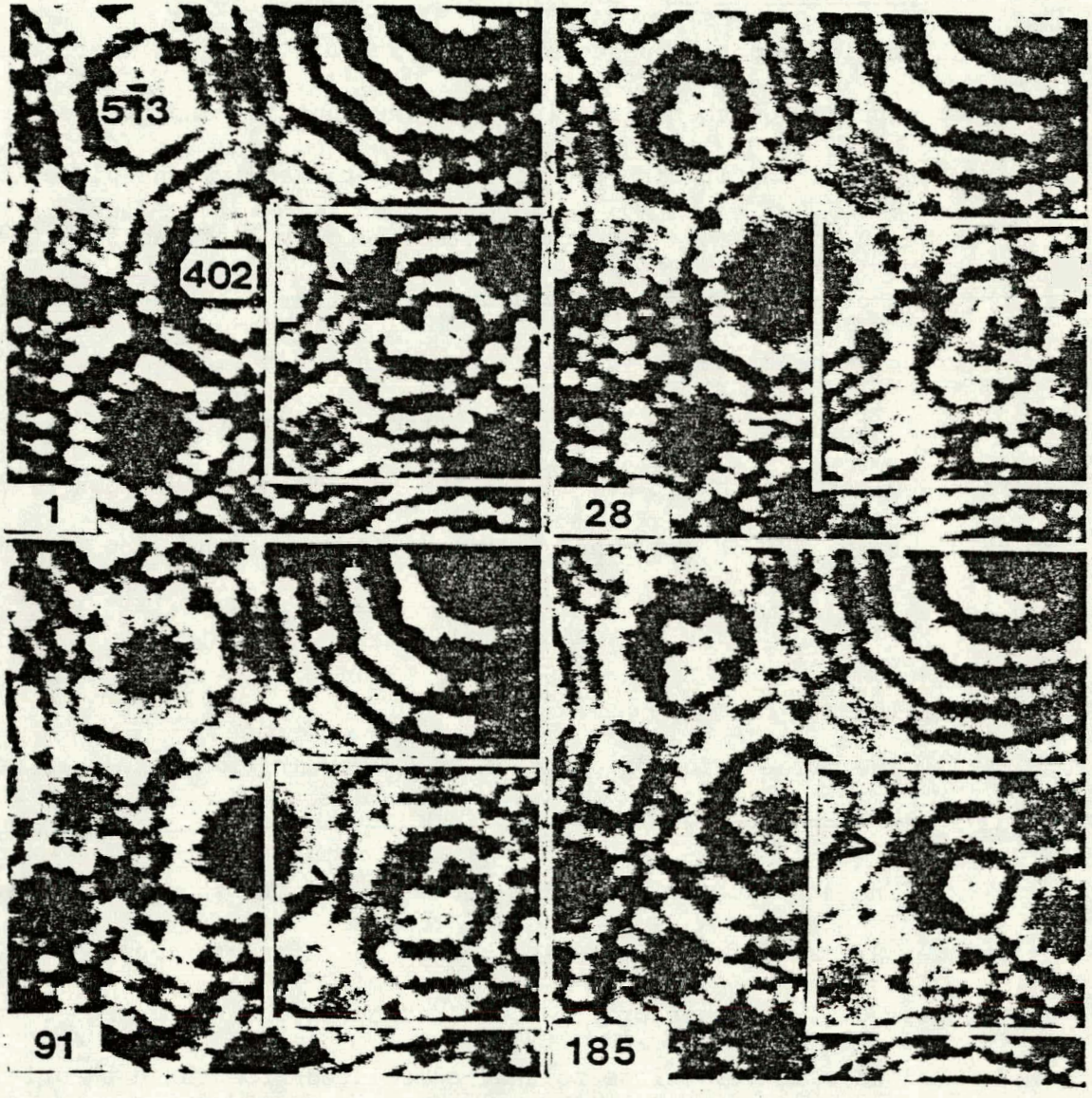

Fig. 36(a): A pulse field evaporation sequence showing the contrast from a dislocation loop emerging on the (513) plane of platinum.

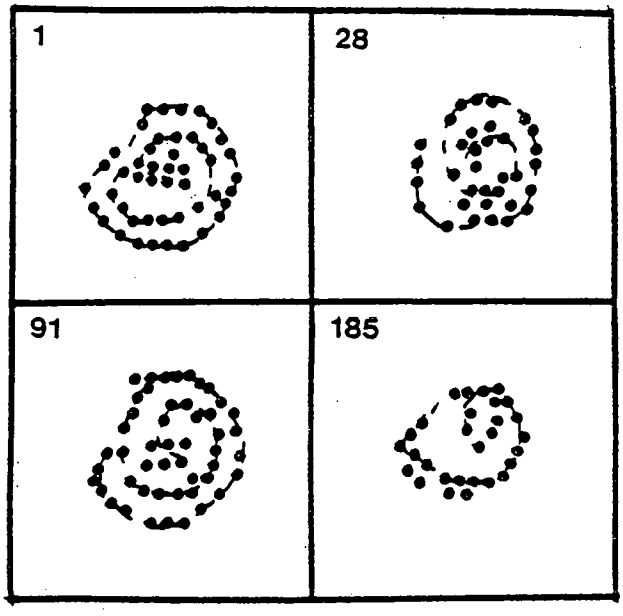

Fig. 36(b): A schematic diagram of atoms near the dislocation loop for the sequence shown in fig. 36(a).

interstitial and vacancy type loops were detected. Evidence was shown to indicate that the vacancy type loops were caused by the collapse of DZ's having a high vacancy concentration.

REFERENCES FOR CHAPTER III

1. M.J. Attardo and J.M. Galligan, Phys Rev Lett. 17, 191 (1966).

2. M.J. Attardo and J.M. Galligan, Phys Rev. 161, 551 (1967).

3. J. Inal and J.M. Galligan, Acta Met. 18, 557 (1970).

4. C.Y. Wei and D.N. Seidman, Phil Mag A. 37, 257 (1978).

5. C.Y. Wei, PhD Thesis, Cornell University (1978).

6. L.A. Beavan, R.M. Scanlan and D.N. Seidman, Acta Met. 19, 1339 (1971).

7. K.L. Wilson and D.N. Seidman in: Nuclear Energy, Proc 1973 Intern Conf on Defects and Defect Clusters in BCC Metals and their Alloys, Ed R.J. Arsenault (NBS, Gaithersburg, MD, 1973) Vol 18, p. 216.

8. W. Schilling, K. Sonnenburg, and H.J. Dibbert, Rad Effects. 16, 57 (1972).

9. J.F. Nicholas, An Atlas of Models of Crystals Surfaces (Gordon and Breach, New York 1965).

10. C.K. Johnson, Oak Ridge National Laboratory (USA) Report 3794 (1965) plus revisions (1970).

11. M. Dreschler and P. Wolf, Proc Intern Conf Electron Microscopy, 4th, Berlin, Spring Verlag (Berling), (1958).

12. K.B. Winterbon, P. Sigmund and J.B. Sanders, Kgl. Danske Videnskab. Selskab, Mat-fys. Medd. 37, No 14 (1970).

13. P. Sigmund, Rev Roum Phys 17. 823-870, 969-1000, 1079-1106 (1972).

14. P. Sigmund in Radiation Damage Processes in Materials edited by C.H.S. Dupuy (Noordhoff, Leyden, 1975), pp. 3-117.

15. J.R. Beeler, Jr, Phys Rev. 150, 470 (1966).

16. J.R. Beeler, Jr and M.F. Beeler, in Fundamental Aspects of Radiation Damage in Metals, edited by M.T. Robinson and F.W. Young Jr.

17. M.T. Robinson and I.M. Torrens, in Interatomic Potentials and Simulation of Lattice Defects, ed. P.C. Gehlen et al. (Plenum New York, 1972) p. 423.

18. M.T. Robinson and I.M. Torrens. Phys Rev. B. 9, 5008 (1974).

19. P. Sigmund, G.P. Scheidler and G. Roth, in Proc Int Conf Solid-State Physics Research with Accelerators, Brookhaven National Laboratory

Report No 50083 (1968), p. 374 (unpublished).

20. J. Biersack and L. Haggmark, unpublished report, to appear in J. Nucl Materials (1980).

21. G.H. Kinchin and R.S. Pease, Rep Prog Phys. 18. 1 (1955).

22. K.B. Winterbon, Ion Implantation Range and Energy Distributions (Plenum, New York, 1975).

23. P. Lucasson, in Fundamental Aspects of Radiation Damage in Metals, edited by M.T. Robinson and F.W. Young, Jr CCONF-751006-P1, U.S. Dept. of Commerce, Springfield, VA 1975), pp. 52-65.

24. J. Linhard and M. Scharff, Phys Rev. 124, 128 (1961).

25. G. Liebfried, Nukleonik. 1. 57 (1958).

26. C. Lehman, Nukleonik. 3, 1 (1961).

27. J. Linhard, M. Scharff and H.E. Schiott (Mat Fys Medd Dan Vid Selsk, 3, no 14 (Notes on Atomic Collisions II) (1963).

28. P.C. Banbury and I.N. Haddard, Phil. Mag. 14, 841 (1966).

29. C. Erginsoy, A. Englert and G. Vineyard, Phys Rev. 133, 595 (1964).

30. J.N. Lomer and M. Pepper, Phil Mag. 16, 1119 (1967).

31. P. Lucasson and A. Lucasson, Rad Effects. 39, 195 (1978).

32. P. Sigmund in Inelastic Ion-Surface Collisions, edited by N.H. Tolk, J.C. Tully, W. Heiland, and C.W. White. (Academic Press Inc, New York).

33. R.S. Averback, R. Benedek and K.L. Merkle, Phys Rev B. 18, 4156 (1978).

34. K.L. Merkle, R.S. Averback, in Fundamental Aspects of Radiation Damage in Metals, edited by M.T. Robinson and F.W. Young Jr (1975).

35. R.C. Fletcher and W.L. Brown, Phys Rev. 92, 585 (1953).

36. R. Benedek, M.O. Ruault, to be published.

37. P. Sigmund, Phys Rev. 184, 383 (1969).

38. P. Sigmund, Phys Rev. 187, 768 (1969).

39. J. Linhard, V. Nielsen, M. Scharff and P.V. Thomsen, Danske Videnskab Selskab. Mat-Fys. Medd. 33, 10 (1963).

40. J. Aidelberg, PhD Thesis, Cornell (1980).

41. M.I. Current, C.Y. Wei and D.N. Seidman, to be published.

42. C.Y. Wei, L.A. Beavan and D.N. Seidman, to be published in Phil Mag.

43. E.J. Savino and R.C. Perrin, J. Phys. F: Metal Phys. 4, 1889 (1974).

44. R.A. Johnson, Phil Mag. 16, 553 (1967).

IV. SELF-ION IRRADIATION OF TUNGSTEN

In this chapter we present the results of experiments on radiation damage produced in tungsten by tungsten ions whose energy ranged from 20 keV to 60 keV. These experiments are important for understanding the radiation damage created by fast neutrons, where the damage is caused by energetic recoil atoms of varying energy. The main aim of the work was to determine the change in morphology and point-defect structure of the radiation damage as the energy of the incoming ion was increased. The FIM is especially suited to this purpose as it is able to detect both uncollapsed clusters of vacancies and dislocation loops whereas the transmission electron microscope (TEM) technique is capable of seeing only dislocation loops and in some cases dense clusters and voids.

Wei[1] reported the results of 30 keV W^+ irradiations of W and analyzed four DZ's. Beavan *et al.*[2] mapped out two DZ's in detail for 20 keV W^+ incident ions. We have added some more data to the 20 keV W^+ irradiations as well as new information for 45 and 60 keV W^+ irradiations.

The experimental details were described in Chapt. II. The method of analysis was the same as the one described in Chapt. III for Pt and has been described in great detail for tungsten in ref 1. Hence we will present the results directly without further elaboration of how the various quantities were calculated.

IV.1 Depleted zones

IV.1.1 20 keV W^+ irradiations

We were able to map out two DZ's for 20 keV W^+ irradiations. The positions of the DZ's are shown in fig. 37. Together with the two DZ's

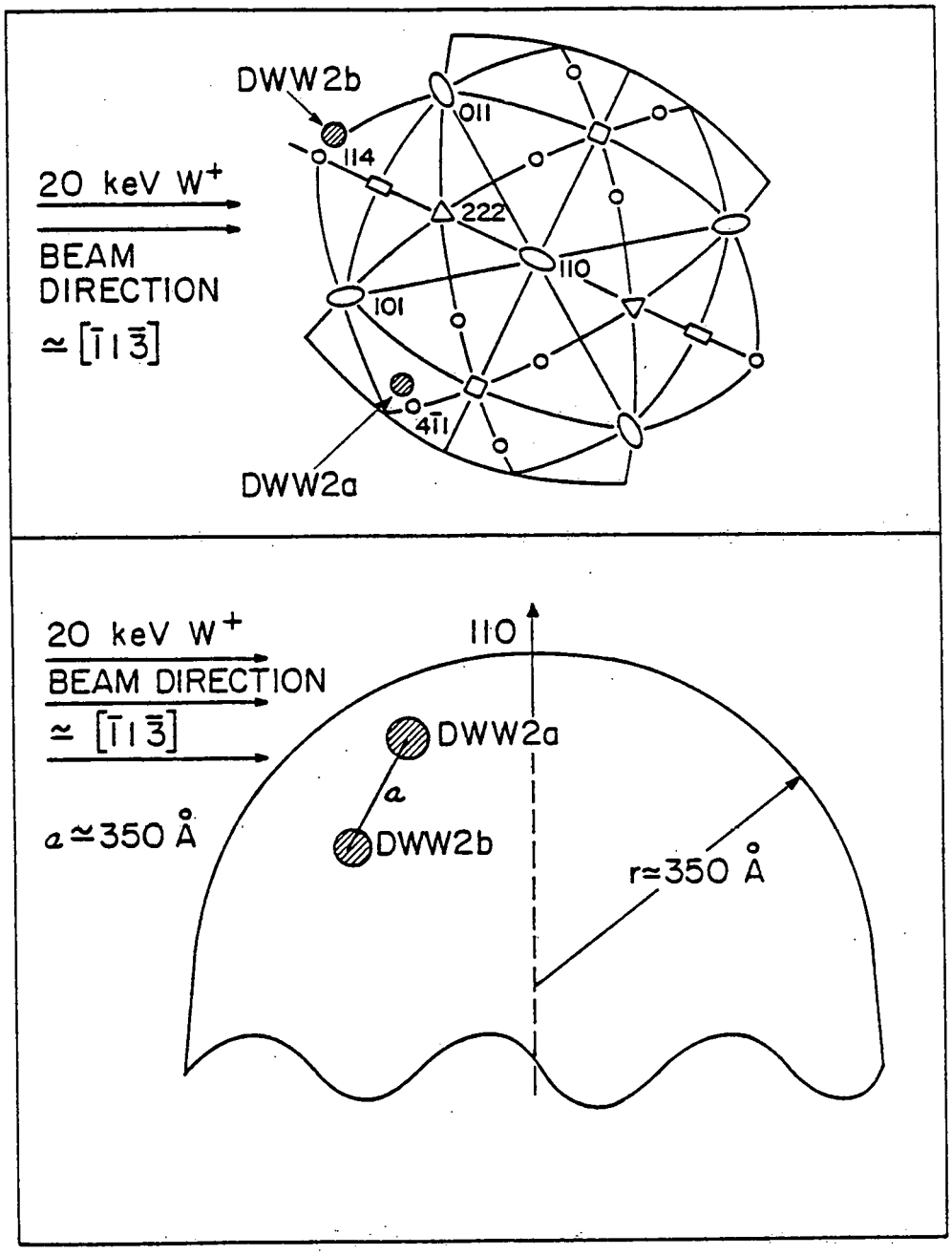

Fig. 37: (a) Partial 110 stereographic projection showing location of depleted zones DWW2a and DWW2b.
(b) A schematic cross-sectional view of the FIM tip specimen.

mapped out by Beavan et al.[2]; this gives a total of four DZ's mapped out for 20 keV self-ion irradiations of W. The number of vacancies (ν) and the vacancy concentrations c_v are given in table 4.1, and the range L, maximum and minimum dimensions and average dimensions are given in table 4.2.

The average number of vacancies expected for normal ion incidence, calculated from the TRIM program based on E_d of 43 eV is 146 ± 20. For ions incident at 60°, the average number of vacancies decreased to 121±29. Displacement cascades with as few as 30 vacancies were obtained in the computer simulation. The number of vacancies observed in the experimental DZ's were greater than expected but not significantly greater.

The range of the DZ's are within the limits expected from TRIM of 34.37 ± 13.43. From Winterbon's table,[5] however, we obtain L = 21 Å. The average size of the DZ's on the basis of TRIM is $\bar{\lambda}$ = 27 ± 8 Å. The average size of the experimental DZ's appeared to be much smaller than this, though they are within the 3σ limits.

The radial distribution functions N(i) and R(i)/Z(i) have been plotted in figs. 38 and 39. The plots for <N(i)> exhibit a sharp single peak which indicated a single large cluster of vacancies. In figs. 40 and 41 we show the OR TEP visualizations of the two DZ's, which indicate the compact nature of the two DZ's.

Analysis of the degree of clustering reveals that DWW2a has 30 monovacancies, three divacancies, three trivacancies and one each of 72 and 82 vacancies. DWW2b has 25 monovacancies, two divacancies, two quadravacancies, one cluster of 20 and one jumbo cluster of 133.

Comparison of the average R(i)/Z(i) for the three fully developed

TABLE 4.1

Number of vacancies and vacancy concentration in DZ's produced by 20 keV W^+ on W

DEPLETED ZONE (DZ)	NO. OF VACANCIES ν	VACANCY CONCENTRATION (c_v) at %
DWW2a	199	15.4
DWW2b	190	13.63
DZOa*	172	14.33
DZOb*	85	13.9

*From Beavan et al.[2]

TABLE 4.2

Range and dimensions of DZ's produced by 20 keV W^+ on W

DEPLETED ZONE (DZ)	RANGE L Å	DIAMETER λ_1 Å	DIAMETER λ_2 Å	MEAN DIAMETER $\langle\lambda\rangle$ Å	ELONGATION DIRECTION [hkl]
DWW2a	10 Å	21.4	15.3	17.11	[101]
DWW2b	30 Å	16.85	14.32	15.12	$[1\bar{1}0]$
DZOa*	40 Å	29.6	11	15.36	$[11\bar{1}]$

*From Beavan et al.[2]

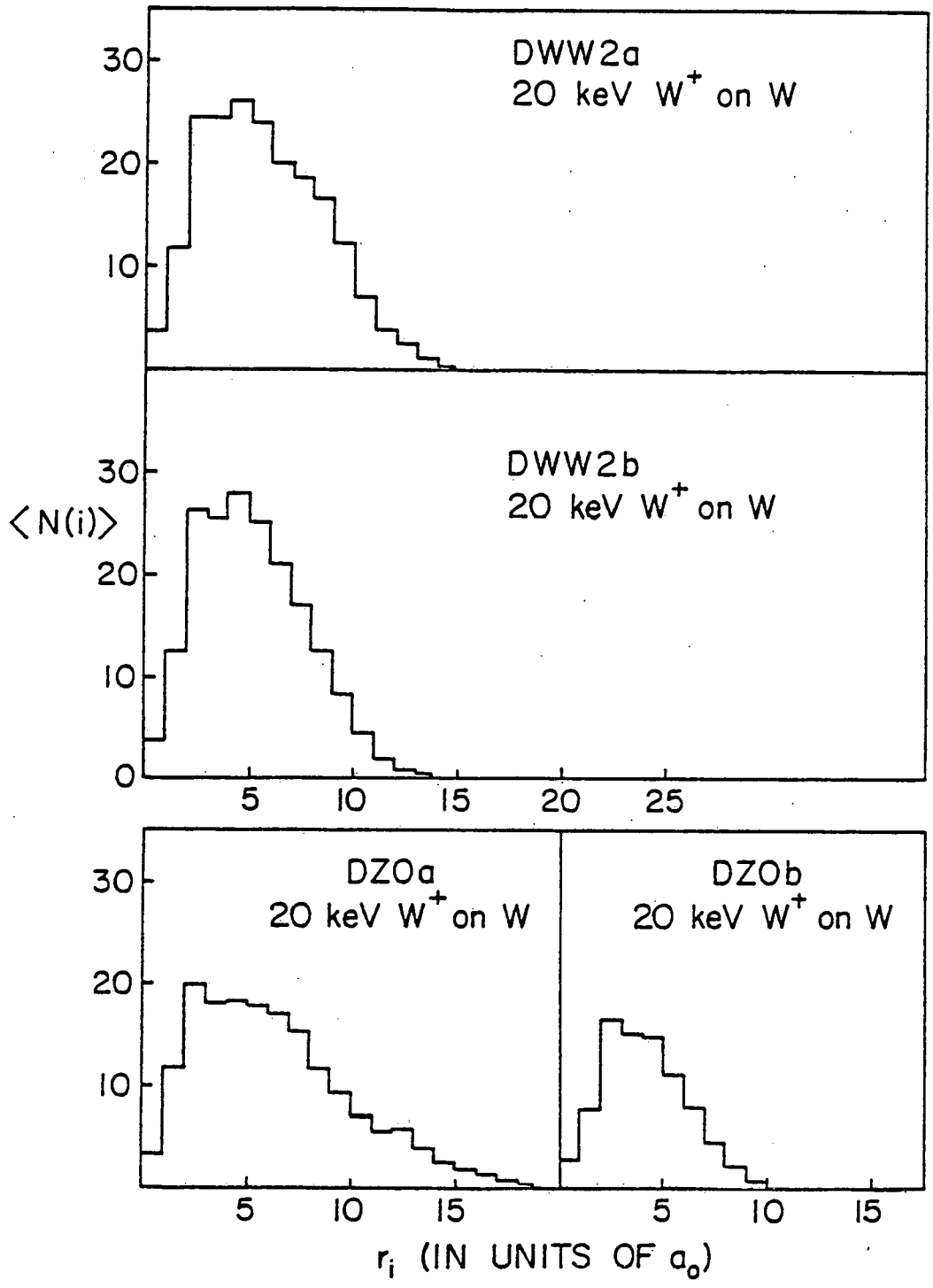

Fig. 38: The spectra of <N(i)>s for depleted zones produced by 20 keV W^+ irradiations of tungsten.

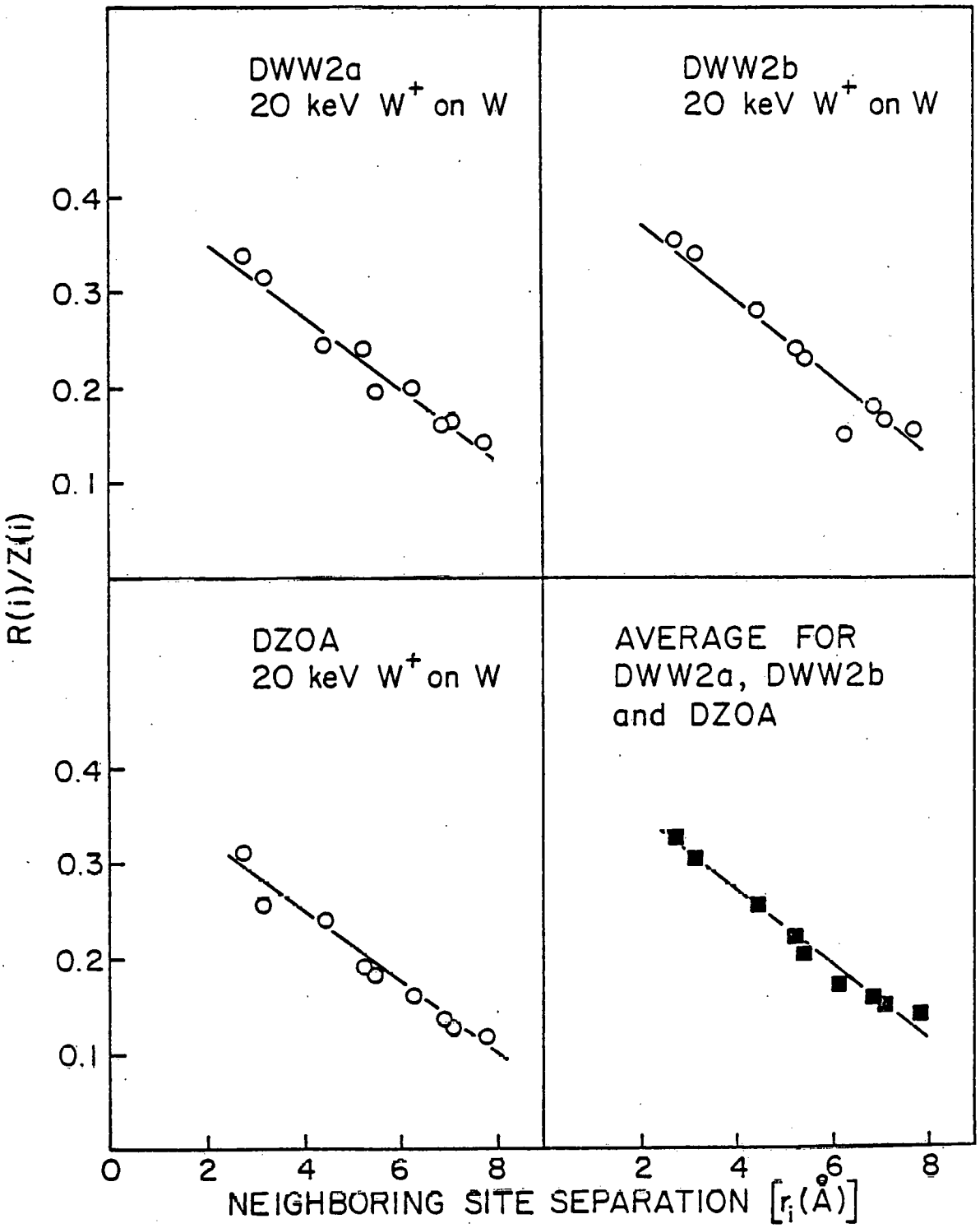

Fig. 39: The normalized radial distribution functions [R(i)/Z(i)] for DZs produced by 20 keV W^+ irradiations of tungsten.

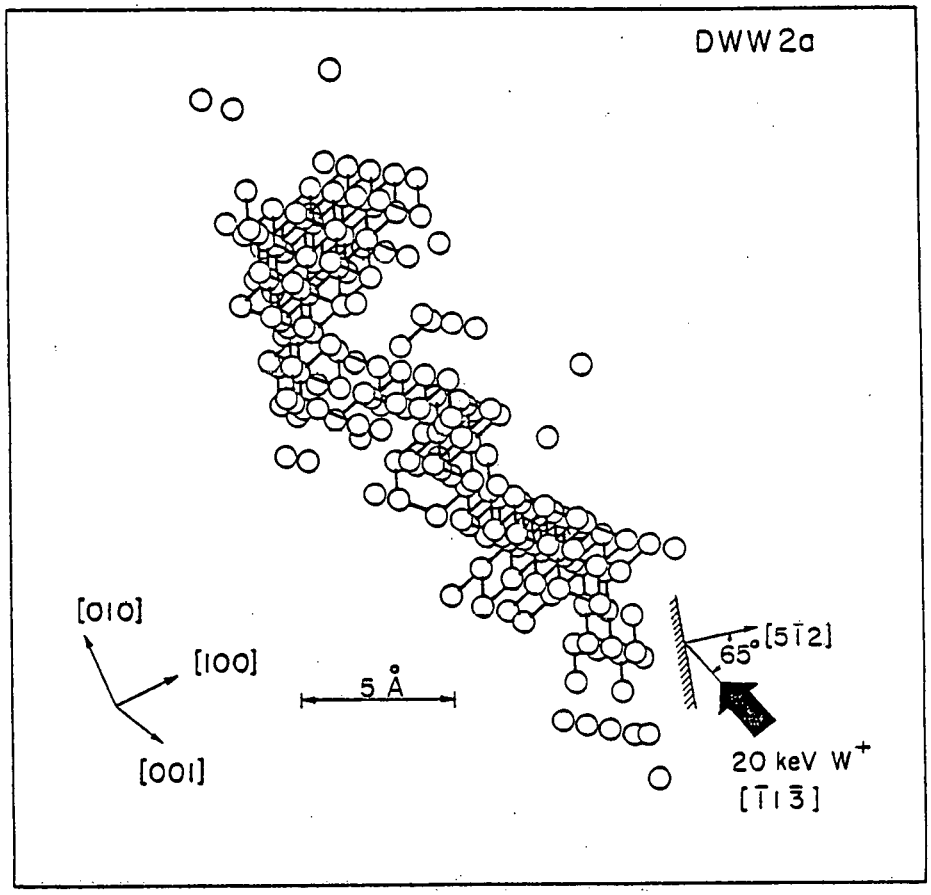

Fig. 40: An OR TEP drawing of depleted zone DWW2a.

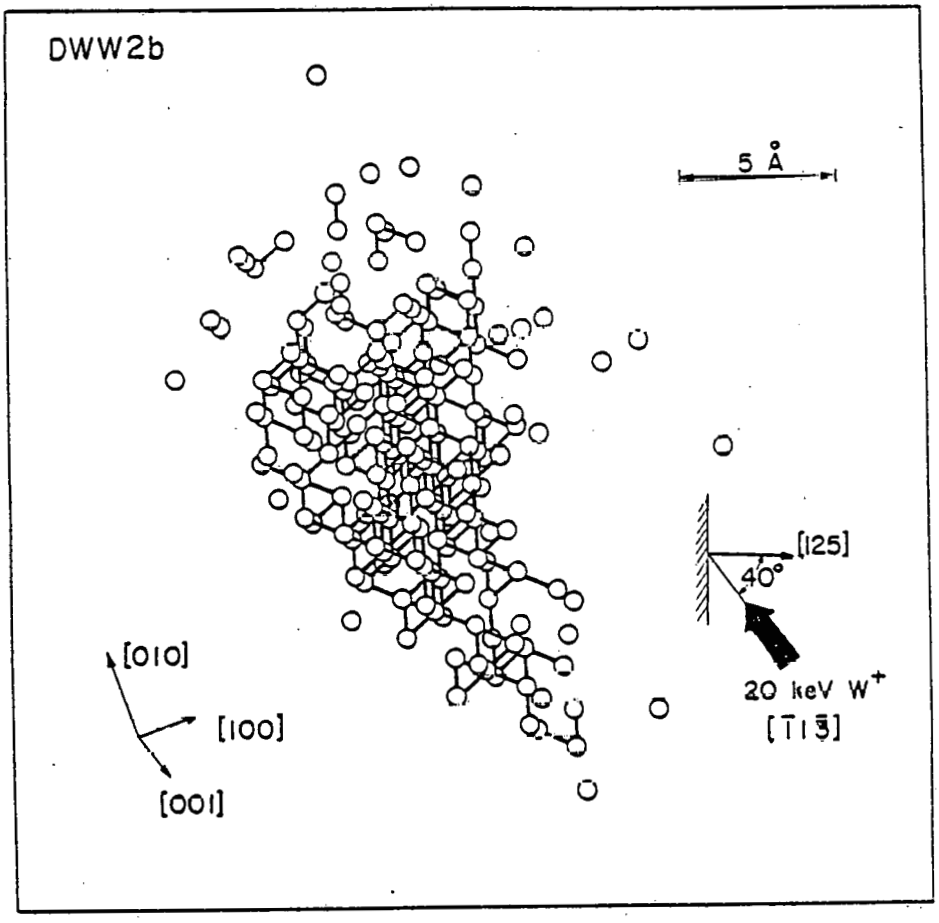

Fig. 41: An OR TEP drawing of depleted zone DWW2b.

20 keV W^+ DZ's with that for 30 keV W^+ DZ's showed them to be virtually identical. This confirmed the observation made in Ref. 3 that there was no pronounced dependence of R(i)/Z(i) on ion energy, only on the mass of the mass of the projectile ion.

IV.1.2 45 keV W^+ irradiations

Four specimens were irradiated but only in one of them did we obtain a DZ which could be mapped out in atomic detail. The position of the DZ in the specimen is shown in fig. 42.

The number of vacancies in this DZ was 298 which was close to the expected value of 329 ± 20. This DZ had an average vacancy concentration of 14.2%. Its L value was 213 Å, which is very much larger than the TRIM calculated range of 52 ± 20. The largest diameter (λ_1= 24.48 Å) was along [1$\bar{1}$0] and $\langle\lambda\rangle$ = 18.32 Å, which was smaller than $\langle\lambda\rangle_{TRIM}$ = 38 ± 11 Å, but still within the 3σ limits. The radial distribution functions are plotted in fig. 43. They indicated that most of the vacancies were in one single large cluster. This was confirmed by the analysis of the degree of clustering. There were 33 monovacancies, two divacancies, two trivacancies, one heptavacancy, one octavacancy, one cluster of 21 vacancies and one jumbo cluster of 215 vacancies. The ORTEP visualizations clearly showed the clustering of vacancies (fig. 44).

A second DZ was detected in another specimen but could not be mapped in atomic detail because portions of it lay on the outer rings of a low index plane. A rough estimate of the number of vacancies was ≈300, and the appearance of the DZ in successive frames of the micrographs indicated that the vacancies were practically in one big cluster. Near the center of the DZ the contrast was similar to that of a void. A rough estimate

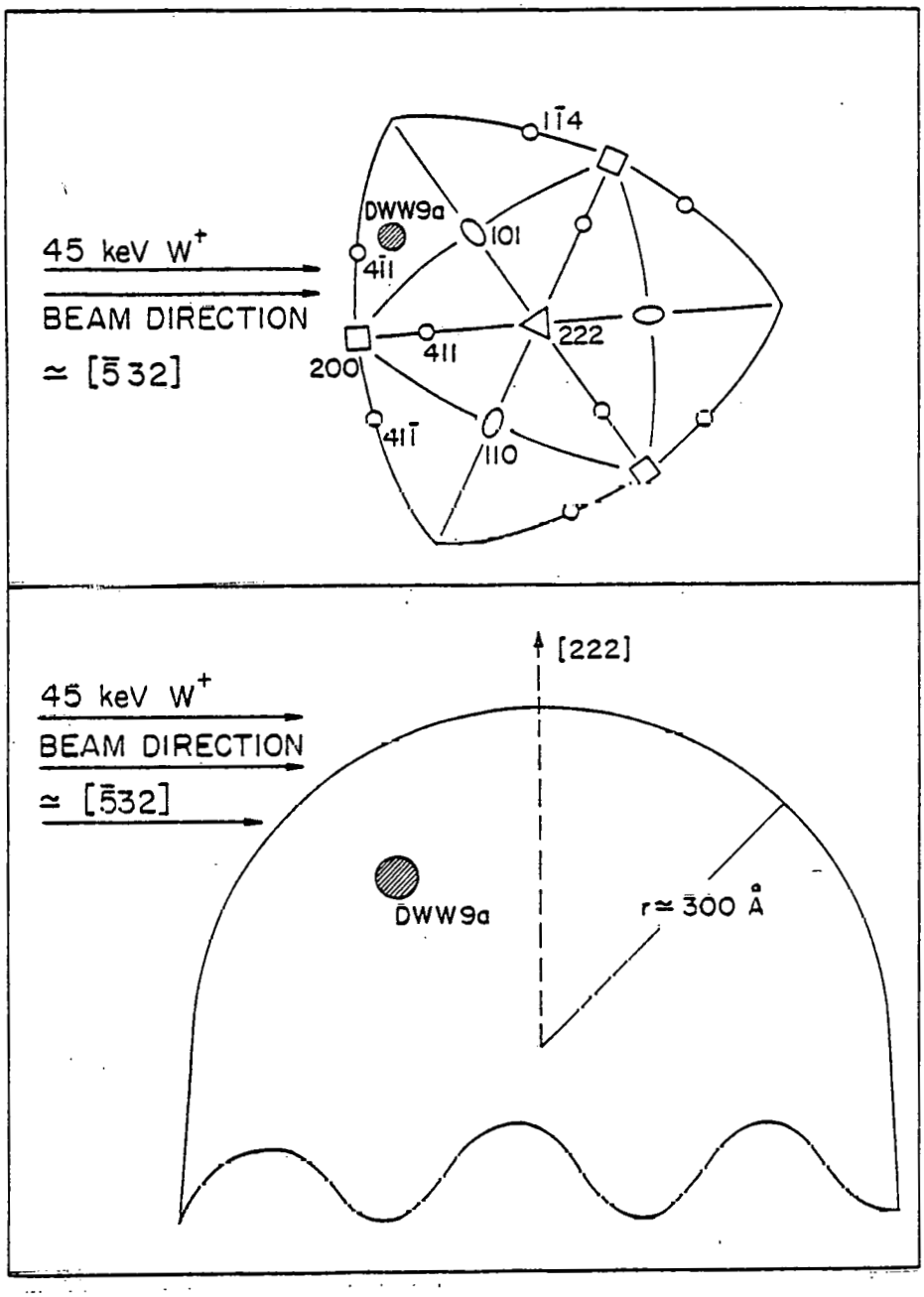

Fig. 42: (a) Partial 222 stereographic projection showing location of depleted zone DWW9a.
(b) A schematic cross-sectional view of the FIM tip specimen.

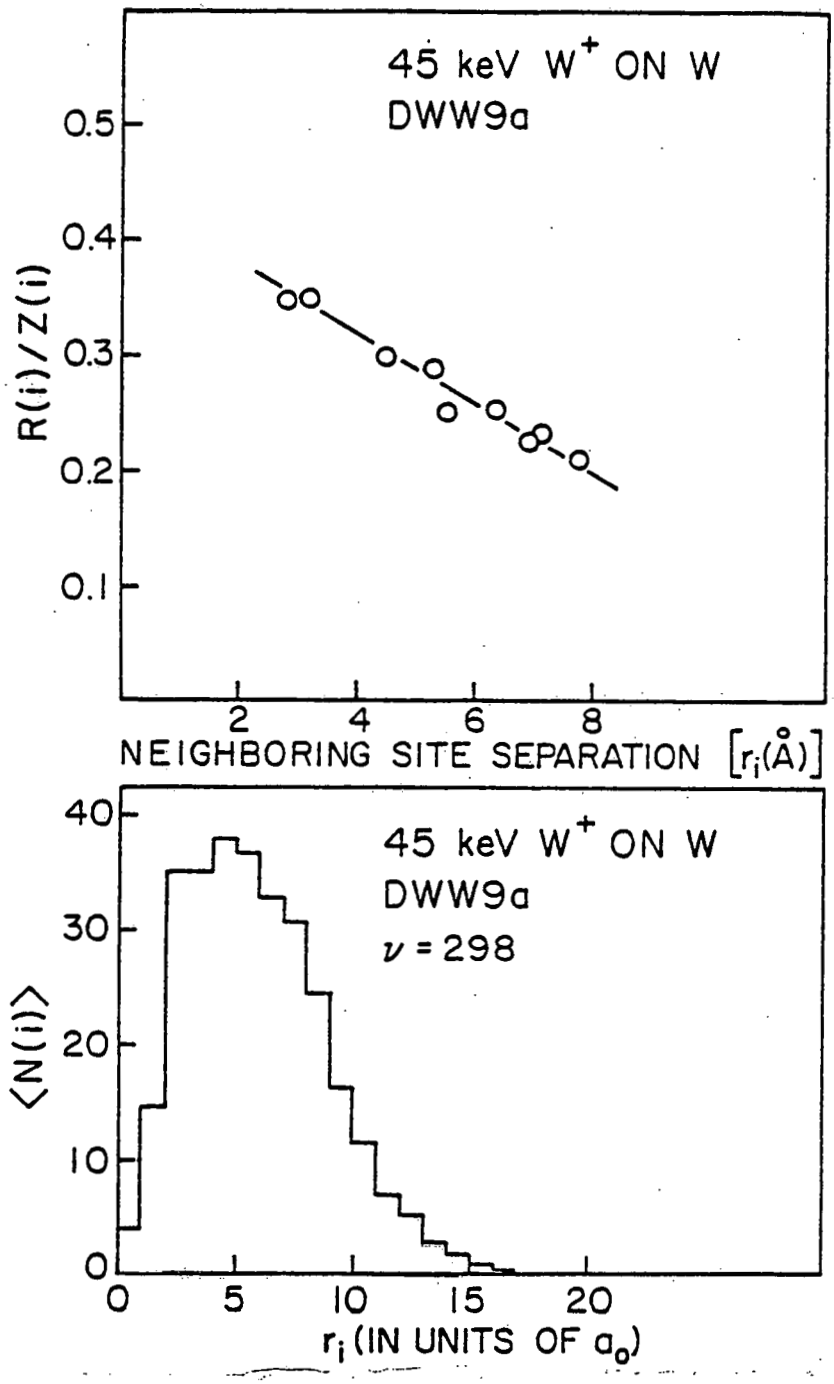

Fig. 43: (a) The normalized radial distribution function [R(i)/Z(i)] for depleted zone produced by 45 keV W^+ irradiation of tungsten.
(b) The spectra of <N(i)> for depleted zone produced by 45 keV W^+ irradiation of tungsten.

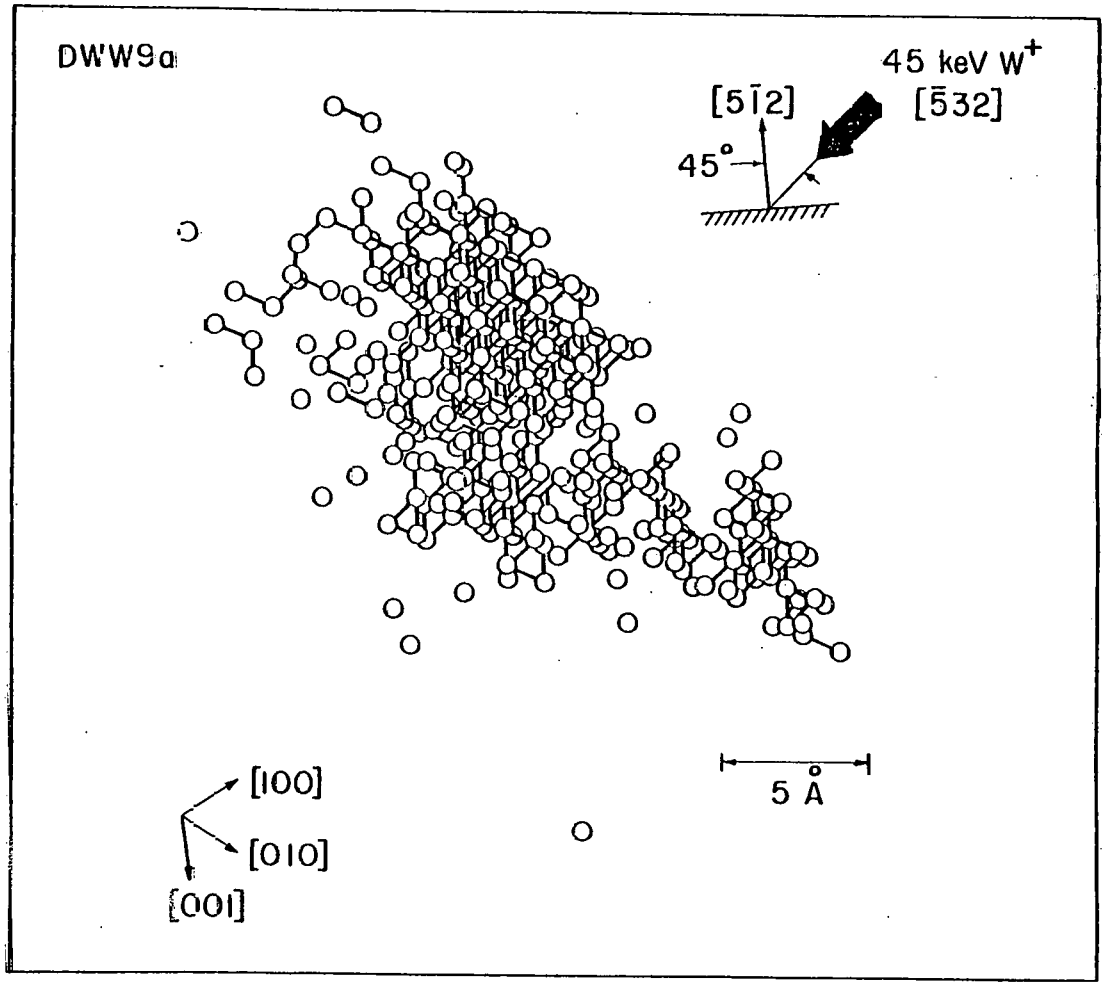

Fig. 44: An OR TEP drawing of depleted zone DWW9a.

of the size of the DZ was obtained by counting the number of planes over which the majority of vacancies extended--this procedure gave $\langle\lambda\rangle$ equal to 16 Å.

IV.1.3 60 keV W^+ irradiations

Out of three irradiated samples, only in one specimen were we able to find DZ's that could be completely analyzed. They were denoted as DWW7a and DWW7d. The DZ's were detected in a specimen with radius of ≈500 Å, which had a [111] fiber axis. Fig. 45a exhibits the 111 standard stereographic projections which show the top view of each specimen. The plane (or planes) in which a DZ was detected is indicated. Unanalyzed DZ's are also included. The cross-sectional side view of the specimen is shown in fig. 45. The separations between any two DZ's were indicated by the letters a,b,c, etc.

DWW7a was detected in the (534) plane. It contained 453 vacancies, which is close to the value of 410 ± 63 expected from the TRIM simulation. It was found ≈200 Å from the surface along the direction of the incident ion beam. This range is somewhat greater than the TRIM value of 76 ± 28.4 Å but not significantly different to ascribe it to channelling.

DWW7a was extremely dense and this was reflected in the very high c_v of 25%, which was comparable with the c_v of DZ's produced at much lower projectile energies. The compactness of the DZ was reflected in its dimensions. The diameter (λ_1) measured along the major axis was 17 Å and the diameter λ_2 measured along the minor axis was 13.32 Å. The major axis of the ellipsoid enclosing the DZ was along the [100] direction. The average diameter $\langle\lambda\rangle$ was equal to 14.44 Å. This value was very much smaller than the expected mean diameter of 52 ± 20 Å calculated from the

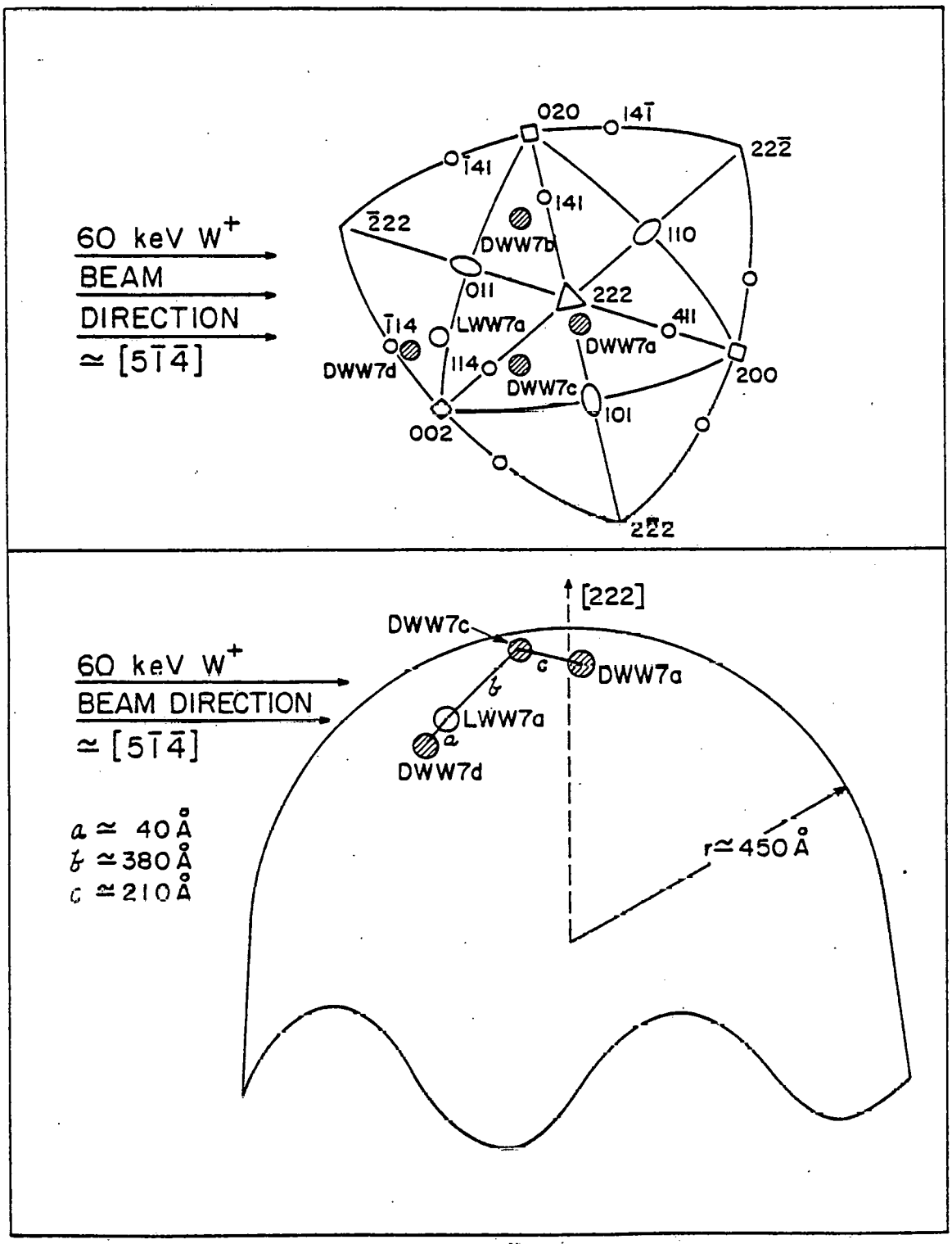

Fig. 45: (a) Partial 222 stereographic projection showing location of depleted zones produced by 60 keV W^+ irradiation of tungsten.
(b) A schematic cross-sectional view of the FIM tip specimen.

TRIM program.

R(i)/Z(i) and <N(i)> are plotted in fig. 46(a) and 47(a) and indicate a high degree of clustering. This was confirmed by the distribution of cluster sizes which were as follows: 37 monovacancies, one divacancy and one jumbo cluster of 414 vacancies. The ORTEP visualization of the DZ is shown in fig. 48.

DWW7d was found in the $(\bar{1}27)$ plane. It contained 200 vacancies. This value was small compared to the number detected in DWW7a and it was definitely outside the limits expected from fluctuations around the mean value. Moreover, it was well within the sample, at a distance L = 52 Å from the surface and it was unlikely that the small number was due to loss of energetic recoil atoms through the surface or backscattering of the incident ion. Close to the DZ, 70 Å, was another damaged region on the boundary between (013) and $(\bar{1}49)$. The contrast from this region indicated that it was a dislocation loop and when it crossed the $(\bar{1}49)$ plane, vacancies were seen on successive planes. It was very probable that DWW7d was a subcluster of a single DZ with the remainder of the vacancies collapsed into a dislocation loop. The formation of subclusters was expected at these energies on the basis of the kinematics of ion-ion collisions which predicted that the distance between energetic recoils along the path of the incident ion should increase with increasing projectile energy. Thus DWW7d is probably caused by an energetic recoil atom having an energy ≈20-25 keV based on the ν of DWW7d. An analysis of the various other quantities for this DZ and comparison with the 20 keV DZ's was useful in confirming this conclusion.

The value of c_v was 11.8%. This was about the same c_v as for 20 keV

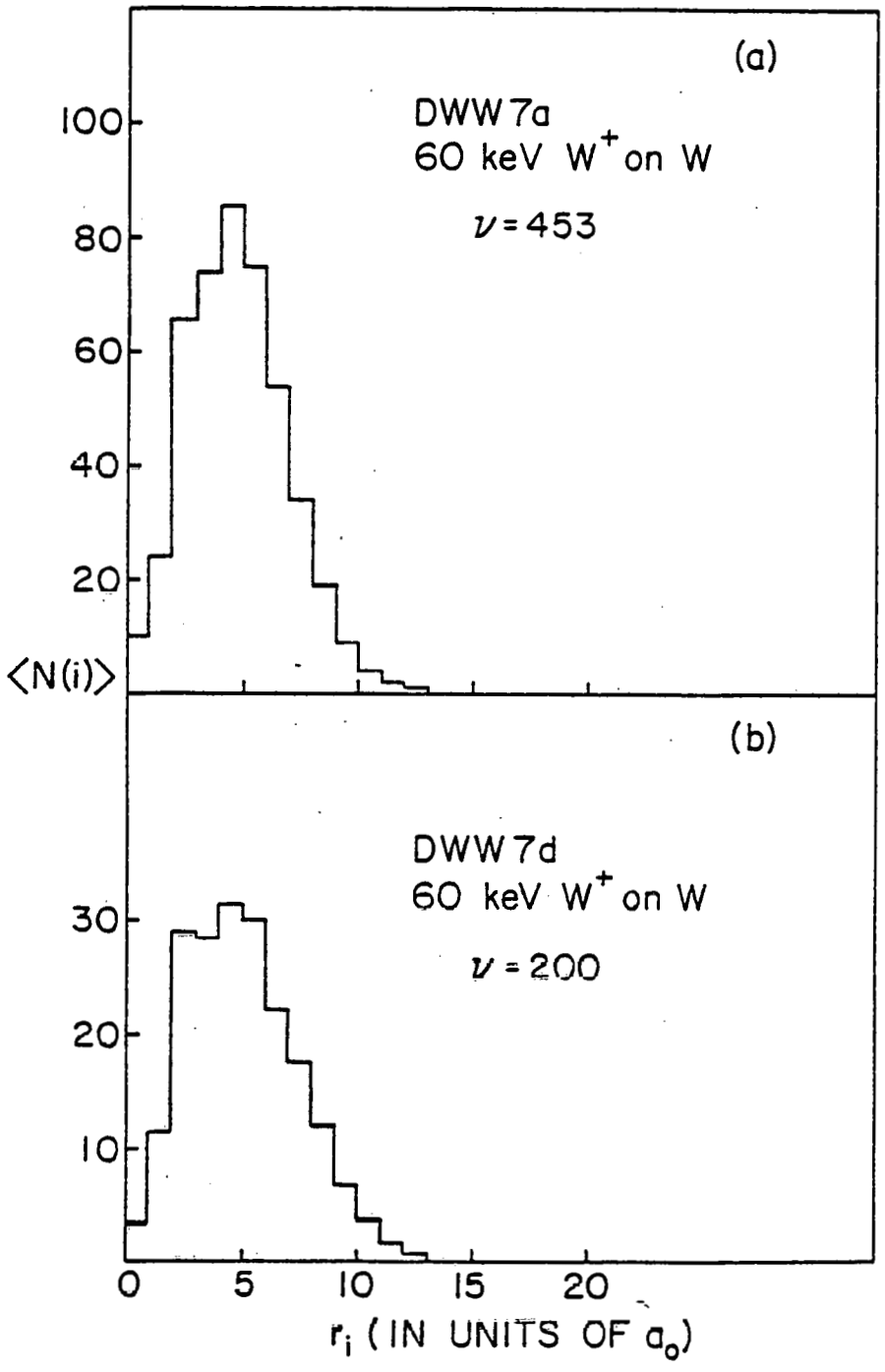

Fig. 46: The spectra of <N(i)>s for depleted zones produced by 60 keV W^+ irradiations of tungsten.

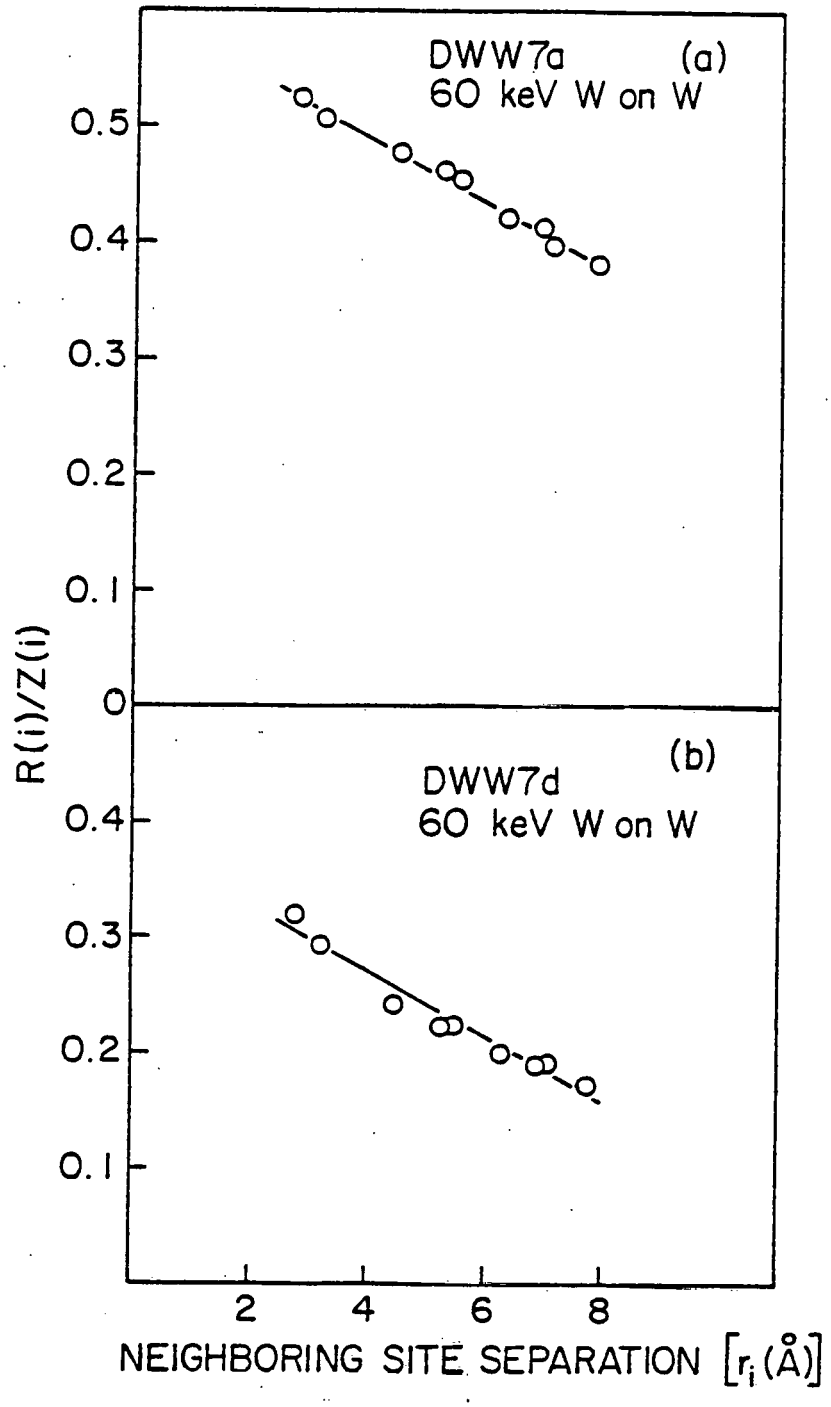

Fig. 47: The normalized radial distribution functions [R(i)/Z(i)] for DZs produced by 60 keV W^+ irradiations of tungsten.

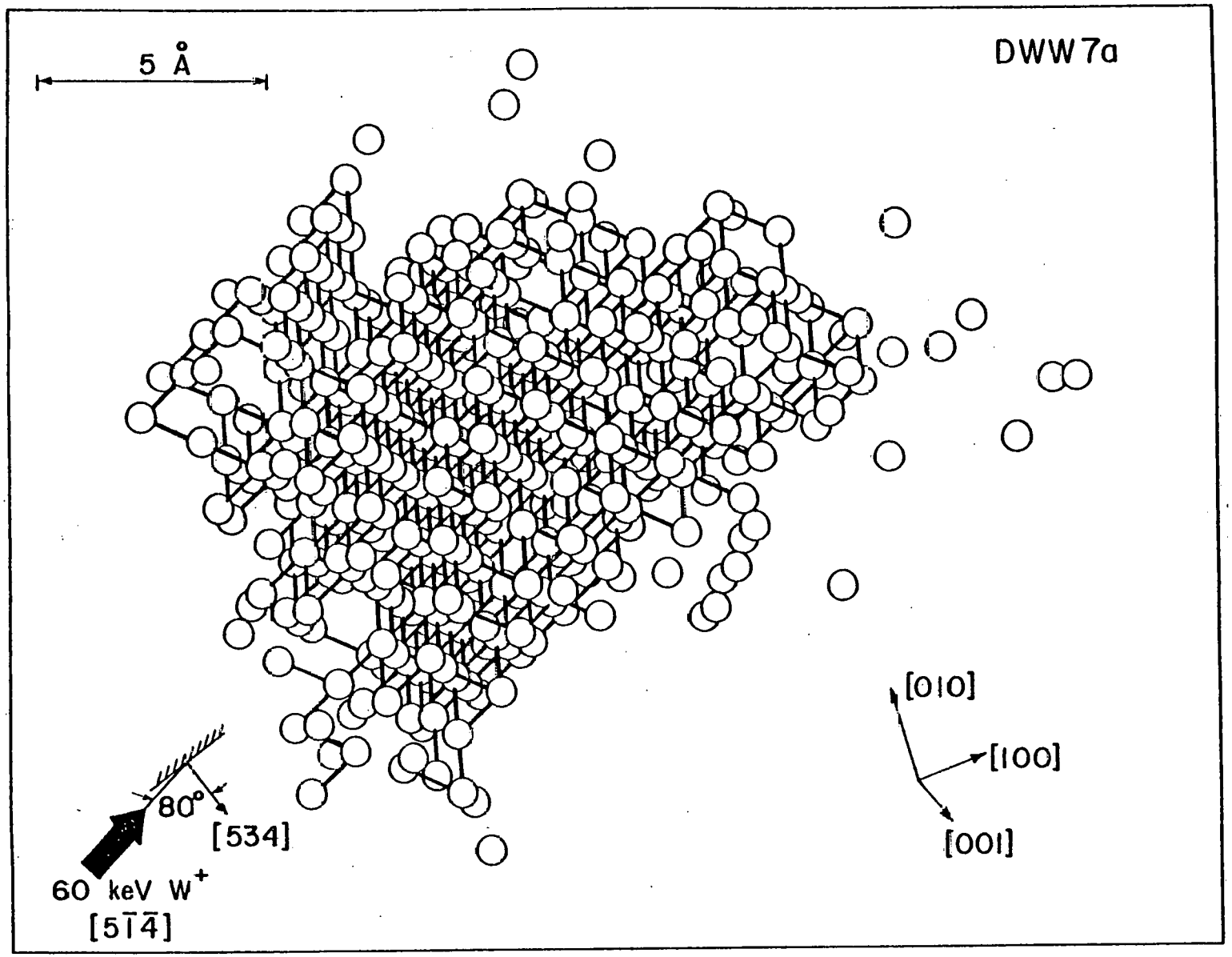

Fig. 48: An OR TEP drawing of depleted zone DWW7a.

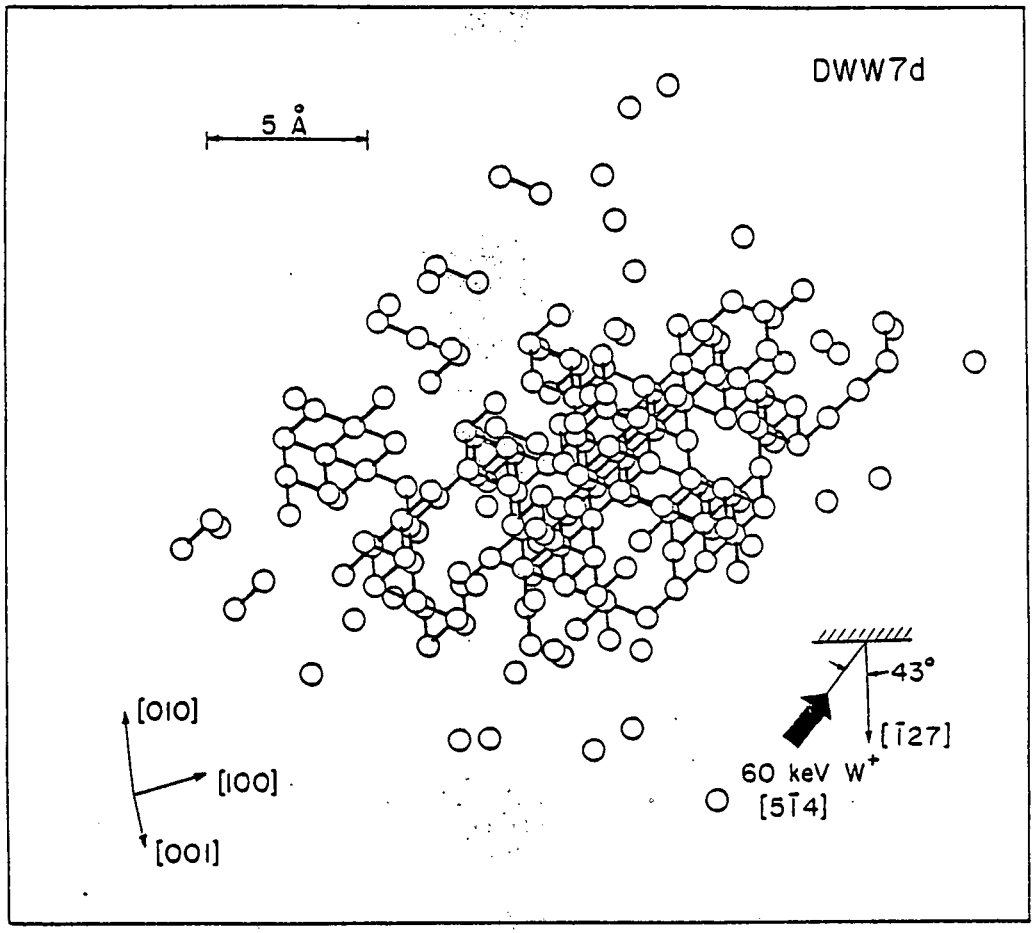

Fig. 49: An OR TEP drawing of DWW7d.

irradiations. The diameter λ_1 measured along the major axis was 17.61 Å and the diameter λ_2 measured along the minor axis was 14 Å. The major axis was along [1$\bar{1}$1] direction. The value of $<\lambda>$ was 15.09 Å, which is similar to the 20 keV DZ's.

The radial distribution functions are plotted in fig. 46b and 47b and they indicated a single cluster of vacancies. This was confirmed by the distribution of cluster sizes. There were 28 monovacancies, six divacancies, three trivacancies, one pentavacancy and one jumbo cluster of 146 vacancies. Thus the DZ is identical with the 20 keV DZ's confirming the conclusion that it had been caused by a 20 keV recoil W atom produced by the 60 keV incident ion.

IV.1.4 Discussion

IV.1.4a Number of vacancies

In fig. 50 we plot the number of vacancies per DZ as a function of the initial energy of the incident W^+ ion. We have included the data from [1] and [2]. For the 60 keV irradiations we have estimated the number of vacancies in DWW7d as 350, by adding the number of vacancies in the dislocation loop close to the DZ, which we estimated to be ≈150. (This may be a lower estimate.) Shown on the graph are $<\lambda>_{TRIM}$ for a single E_d value of 43 eV. These values are close to ν_{R-T}. Also shown are ν_{K-P} and ν_L. There is enough data at the lower energies to show that the experimental value of ν is well estimated by ν_{R-T}, whereas the values expected from Lucasson's model are too low. The ν at 45 keV and 60 keV confirm this trend.

As in the case of Pt, the scatter in ν_{exp} was far greater than that

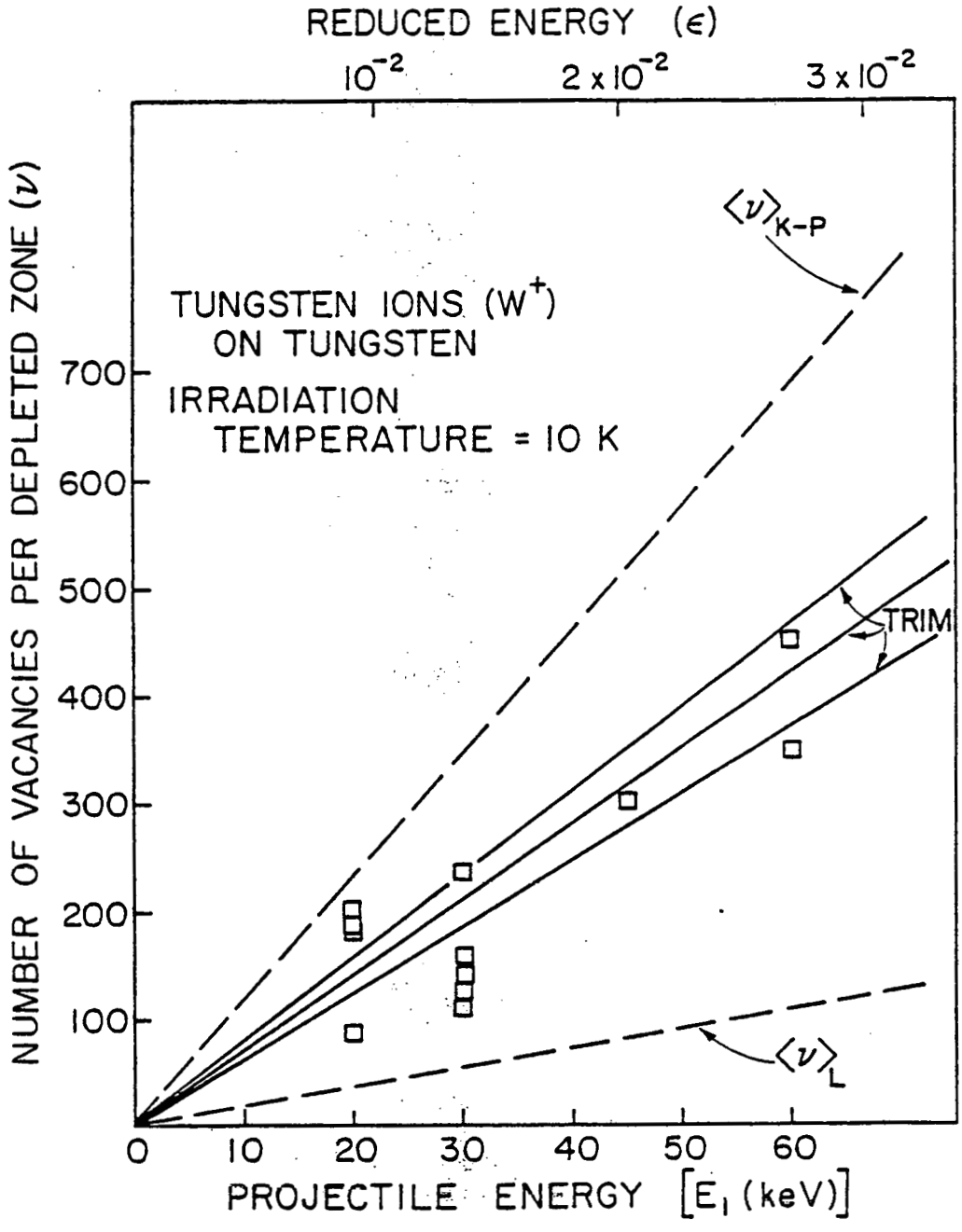

Fig. 50: Variation of ν with energy E_1 of a W^+ projectile incident on tungsten.

expected from theory for a single E_d value. This implies, as pointed out in Chap. III, the possibility of various other physical phenomena that have not been incorporated into the simple model of radiation damage, such as: (a) subthreshold displacements; and (b) the breakdown of the simple binary-collision approximation in dense displacement cascades.

The FIM results for W stand in contrast to the ν_{exp} determined in various other metals by resistivity measurements[4] as well as those determined by TEM.[8] When experimental and theoretical damage rates are compared it is useful to introduce an efficiency factor ξ that gives the ratio of the experimental to theoretical number of defects:

$$\nu_e = \xi \nu_{R-T} \qquad (4\text{-}1)$$

Our FIM results as we-l as previous FIM data indicated that $\xi = 1$, with ν_{R-T} calculated using the minimum value of E_d (E_d^{min}). In the case of tungsten, this is 43 eV.[6] The resistivity experiments give $\xi \approx 0.4$ for self-ion irradiations of the fcc metals Cu, Ag, Au[4] with ν_{R-T} calculated with an average threshold energy, E_d^{avg}, that is, 1.4 E_d^{min} for fcc and 2.2 E_d^{min} for bcc metals. These factors come from Lucasson's model. Thus, the resistivity measurements give a damage rate that is $\leq 1/3$ that of the FIM measurements. As mentioned in Chapt. III, we believe that this discrepancy is due to the assumptions underlying the calculation of absolute damage rates from measured resistivity changes.

The issue of close-pair recombination of SIA's with vacancies has been raised to account for the lower damage rates obtained by resistivity measurements. However, in our experiments carried out at temperatures below that at which SIA's migrate, only a small fraction of the expected

SIA's were detected in the immediate vicinity of the DZ. Experiments by Wei[7] indicated that the SIA's were separated from the DZ's by means of Replacement Collision Sequences (RCS's). The average distance was calculated to be 160 ± 120 Å. Thus, the issue of recombination of SIA's and vacancies does not appear to arise at all.

The value of ν_e has been obtained from TEM observations of defect clusters, employing the geometry and size of the observed black spots. Unfortunately, the geometry and size of very small black-spot defect clusters are not well-defined. The measured diameters is dependent to some extent on imaging conditions. In Au, Ag and Mo,[9-12] cascade efficiencies of the order of 0.5 or more were observed, though--once again--these efficiencies were calculated on the basis of the average threshold energy. A possible explanation for these low efficiencies is that the clusters observed by the TEM technique may not include all the vacancies that have been produced in the displacement cascade. A large number of vacancies may be present as smaller clusters or single vacancies and would not be visible in the TEM. Even for a single incident ion energy, there can be a large variation in the spatial distribution of vacancies from one displacement cascade to the next. Consequently, the fraction of the total number of vacancies in a displacement cascade that collapse to an observable cluster will also vary from cascade to cascade. Therefore, not only will the average ν_{TEM} be less than ν_{R-T} but the observed variation of ν will also be much broader than the actual variation. The distribution of ν has been measured for 250 keV Ag^+ self-ion displacement cascades at 523K.[13] Some of the cascades were seen to contain as many or more vacancies than expected from the modified K-P theory. Incidentally,

while the defect structure of elevated temperature irradiations have a more regular appearance compared with room-temperature irradiations, it was found that the yield and efficiencies stay rather constant up to the point where the cascade clusters begin to dissolve by thermal evaporation of vacancies. The activation energy for this process is the self-diffusion value. Thus, the distribution of ν measured at 523K can be considered to be representative of the distribution that would be observed in the TEM at lower temperatures also. At the same time this fact shows that the mechanism for separating vacancies and SIA's also works very effectively at temperatures where both SIA's and vacancies were highly mobile.

IV.1.4b Size and structure

In fig. 51, we have plotted the quantity $\langle\lambda\rangle$ of the DZ's as a function of E_1 and ε. For the case of 45 keV W^+ ions one of the values has been estimated and not determined rigorously, as was mentioned before. In the case of 60 keV W^+ ions, the dimensions of one of the DZ's was determined on the basis that it contains two subclusters having approximately equal number of vacancies, separated by a distance of 70 Å. Shown on the graph are $\langle\lambda\rangle$'s expected from TRIM and those expected from analytical models. In the case of the analytical models, we have shown the dimensions:

$$\langle D\rangle = 2[(\langle\Delta x\rangle_D)^{1/2}\ \langle y^2\rangle_D]^{1/3} \qquad (4\text{-}2)$$

expected for the cumulative damage distribution as well as the contracted dimensions:

$$\langle D_\delta\rangle = 2\delta^{1/2}[(\langle\Delta x\rangle_D)^{1/2}\ \langle y^2\rangle_D]^{1/3} \qquad (4\text{-}3)$$

where δ is a contraction factor that should take into account the decrease in width from going from the cumulative diameter to individual diameter.

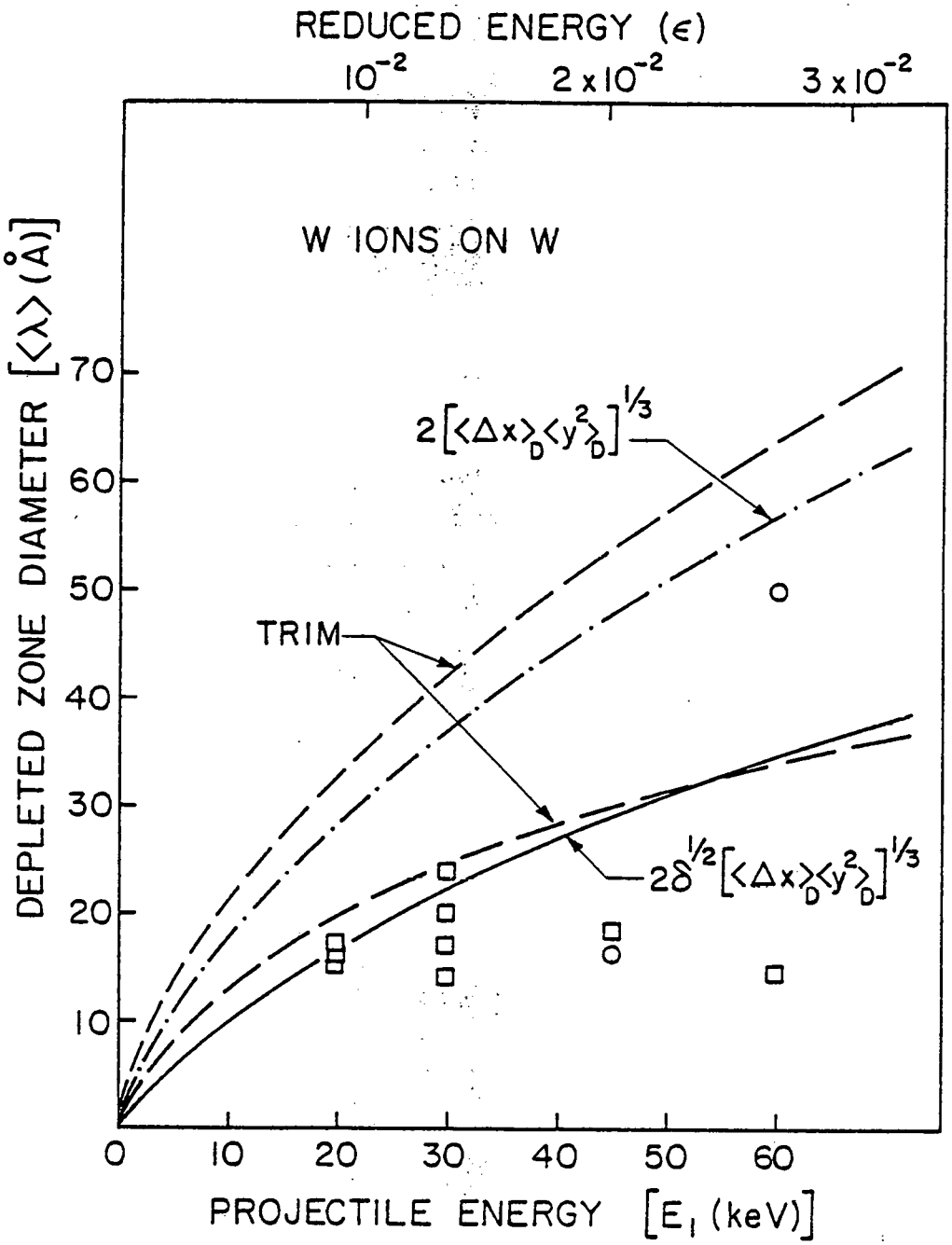

Fig. 51: Variation of the average dimensions of the depleted zones, produced by W^+ ions in tungsten, with energy E_1 of projectile ions.

The value of $\langle y^2 \rangle_D$ and $\langle \Delta x \rangle_D$ were obtained from Winterbon's tables while δ was obtained from [14] and is 0.6 for our case. The three curves shown for TRIM indicate the mean diameter and one standard deviation on either side of this diameter. The large variations in $\langle \lambda \rangle_{TRIM}$ is due to the irregular shape of the DZ's and the fact that the directions in which the dimensions were measured, namely x and y, were fixed whereas the DZ itself can have almost random orientation.

Both TRIM and analytical models predicted that the average dimensions should increase with increasing projectile energy E_1. In the range of ε that we covered, collision theory indicate that the radius of the DZ shall be proportional to $E_1^{2/3}$.[15]

The FIM data do not appear to be well-described by either the TRIM or analytical models, at the higher energies. In fact, $\langle \lambda \rangle$ appears to be almost constant after 30 keV. The large $\langle \lambda \rangle$ obtained in the case of one of the 60 keV DZ's was due to the break-up into two separate subcascades, each of which has relatively small dimensions. A sudden decrease in the dimensions of the DZ with energy was also noted for Kr^+ irradiations of W.[3] The dimensions of the DZ increased with energy until ≈60 keV but at 70 keV the DZ was extremely compact.

TEM data exists on the size of defect clusters produced by irradiation. However, the TEM measurements on pure metals suffers from the disadvantage that the TEM can detect only those clusters that exhibit strain field contrast. It is extremely likely that only part of the DZ may collapse and hence that the observed cluster will appear to be smaller than the actual DZ. The questions of collapse, the appearance of defect clusters in TEM, and their correlation with the actual distribution of

clusters were discussed in more detail in the section on dislocation loops.

Cluster size distributions have been studied in Au and Cu by Merkle,[16,9] Thomas et al.,[17] Pronko and Merkle,[18] Haussermann,[11] and Wilson.[19] In Au an increase in the mean cluster size with mean cascade energy was observed. In self-ion irradiations of Au, the cluster size increased rapidly up to ≈50 keV. Above 50 keV, only a slight increase in mean cluster size with energy occurred. This was due to the splitting into subcascades which proceeds rather linearly with damage energy. Therefore, the size of the individual subcascade stayed almost constant with increasing cascade energy.

In copper self-ion bombardment[19] found no significant change in the size distribution when going from 30 to 90 keV, which is in agreement with other observations. For Au^+ ion bombardment of Cu, an increase in cluster size was found in the region up to 70 keV.[11]

The uncertainty in the sizes of the DZ's involved in the TEM imaging of irradiated pure metals can be overcome by the use of ordered alloys as targets. Disordered regions are produced inside the cascade volume, because of the displacement of atoms from their normal lattice sites. Jenkins et al.[20,21] have recently observed the regions of disorder associated with the displacement cascades in Cu_3Au; in addition, they observed the cascades by the standard strain field image contrast effects. They used superlattice reflections to image local regions of disorder associated with DZ's. The size of these regions directly relates to the size of the regions within a cascade that contains a significant change in the long-range order parameter. The diameters of the cascades produced by Cu^+ ions with energies ranging from 5 keV to 200 keV, were measured and compared

with the transverse dimensions $2(\langle y^2 \rangle)^{1/2}$ calculated from the analytical models. The observed sizes agreed well with theory for low energies ($\leq$40 keV) but at higher energies they were much lower. The value of $\langle \lambda \rangle$ showed indications of levelling off at higher energies. The behavior qualitatively resembled what we have observed for W. Detailed comparison of the work on Cu_3Au and our results is complicated by the following reasons: (a) the mass of the target and of the projectile are different and as a consequence the deposited energy curves are different for the two cases; and (b) in the case of Cu_3Au, the dimensions of the volume over which disorder extends is measured, while in our case, these are measured over the volume containing vacancies. The two volumes will be different if the energy necessary to cause replacements (disorder) is very different from that necessary to cause displacements (vacancies). Moreover, it is unlikely that the disordered volume will change, due to residual movement of the lattice atoms after the cascade has been produced, unlike the case of vacancies, where rearrangement may occur, after they have been created, due to this residual motion. We expect that the volume containing the vacancies be contained within the volume encompassing the disorder.

The spatial extent of the cumulative damage profile will be determined in the main by the collisions of the projectile with the target atoms in the process of slowing down. The lattice is not very highly disturbed during this time period and the assumptions of linear cascade theory are valid. In the case of heavy ions incident on heavy targets, where the collision energy is deposited in a very small volume, the subsequent development of the collision cascade will lead to a large number of atoms being set into motion in a small volume. The transport of energy will no

longer be given by the linear cascade theory and as a result the spatial extent of the cascade can no longer be predicted by these theories. Moreover, in such high energy-density cascades, the DZ that is created during the collision cascade, the DZ that is created during the collision cascade may collapse to a smaller volume subsequently. This implies that while the dimensions of the cumulative damage profile may be satisfactorily predicted by linear-cascade theories, it is not possible to infer the width of individual DZ's by a simple contraction factor. Thus, the width of the cumulative profile may increase as $E^{2/3}$ but this would not be the case for the DZ's. This aspect will obviously have consequences for the vacancy concentrations in the DZ's that is discussed in the following section.

The structure of cascades has been investigated by several authors. The splitting of cascades into subcascades has been extensively studied in Au, by Merkle[18] and Thomas et al.[17] Subcascade formation is an universal feature of energetic cascades and comes from the fact that nuclear collision cross-sections increase with a decrease in energy. The densest cascades are therefore always produced at low energy. Secondary recoils of keV energies usually produce damage regions that strongly overlap and therefore do not give rise to individual subcascades. But as the cascade energy increases, the mean free path between energetic collisions also increases. This eventually leads to well separated DZ's. Since subcascade formation is a consequence of ion-ion collision process, the results on subcascade formation in self-ion irradiated Au can be compared directly with that of self-ion irradiation in W, as the atomic members and masses are very similar. Distinctly separated regions of the displacements have been found in binary collision cascade calculations.[22]

The separation into subcascades is aided by the process of channeling. Beeler[23] defines quasi-channeling as channeling over distances <1000 Å. In such an event, the PKA or an energetic secondary atoms is scattered into a chanel and travels a small distance in the channel. Upon dechanneling, a subcascade is formed. Attempts to correlate the spatial positions of subclusters to crystallographic channeling trajectories were made in ion-irradiated Au,[17] but have not been conclusive to date.

Thomas et al.[17] give 15 keV as the threshold for subcascade formation in self-ion irradiated Au when irradiating along [001]. In contrast to this, the self-ion irradiations of Au in a random direction, carried out by Merkle,[24] showed that a finite probability for observation of at least two clusters exists above 30 keV and a probability of 0.5 for more than one cluster is observed at ≈100 keV.

We have not observed any subclusters at either 20, 30 or 45 keV. One instance of subcluster formation was obtained in the case of 60 keV W^+ irradiations. These observations were consistent with the probabilities listed by Merkle for Au, given the number of observations made in the FIM for each of these energies.

The distance between the subclusters in the 60 keV cascade was 70 Å. Two views of the net DZ are shown in figs. 48 and 49. We concluded that one of the clusters was due to a self-ion (either an energetic recoil or the deflected primary ion) having an energy ≲40 keV. The average range of a 40 keV self-ion in W incident in a random direction is 55 Å, and that of a 20 keV ion 30 Å, so that if the two clusters originated in a collision that gave rise to two recoil atoms of 40 and 20 keV respectively then from simple kinematics the average distance should be ≈60 Å. This was close

to the observed separation of 70 Å.

Thomas et al.[17] studied the subclusters formed by 120 keV self-ion irradiation of Au. In the two subcluster cascades, the subclusters were approximately of equal size and were caused by ions having an energy ≈46 keV. The average distance between the subclusters was 128 Å which was significantly greater than the expected random collision range of 46 keV gold ions in amorphous gold. This was taken as evidence of quasi-channeling, even though the directions of the lines joining the two clusters did not show preference for lying in any particular crystallographic plane and in particular in the (111) planes, which would be the most effective planes for planar channelling. In the case of the subcluster observed in the FIM the line joining the two clusters made an angle of ≈30° to the [010] direction. For our one example the concept of quasi-channeling is not required.

The formation of subcascades has been observed in W, using the FIM, for lighter incident ions, and it has been shown that these can be explained on the basis of the kinematics of ion-ion collisions.

IV.1.4c Vacancy concentration

The estimated vacancy concentration (c_v^*) for the different energies was calculated from the expression:

$$c_v^* = \frac{(0.30)\ \nu_{R-T}\ \Omega_0}{(4\pi/3)(D_\delta/2)^3} \qquad (4\text{-}4)$$

where Ω_0 is the atomic volume for tungsten and the other quantities have been defined in the preceding sections. In table 4.3, a comparison is made between the average vacancy concentration in a DZ, ($\langle c_v \rangle$) and c_v^*, for different energies of W^+. The actual c_v's for the different DZ's are

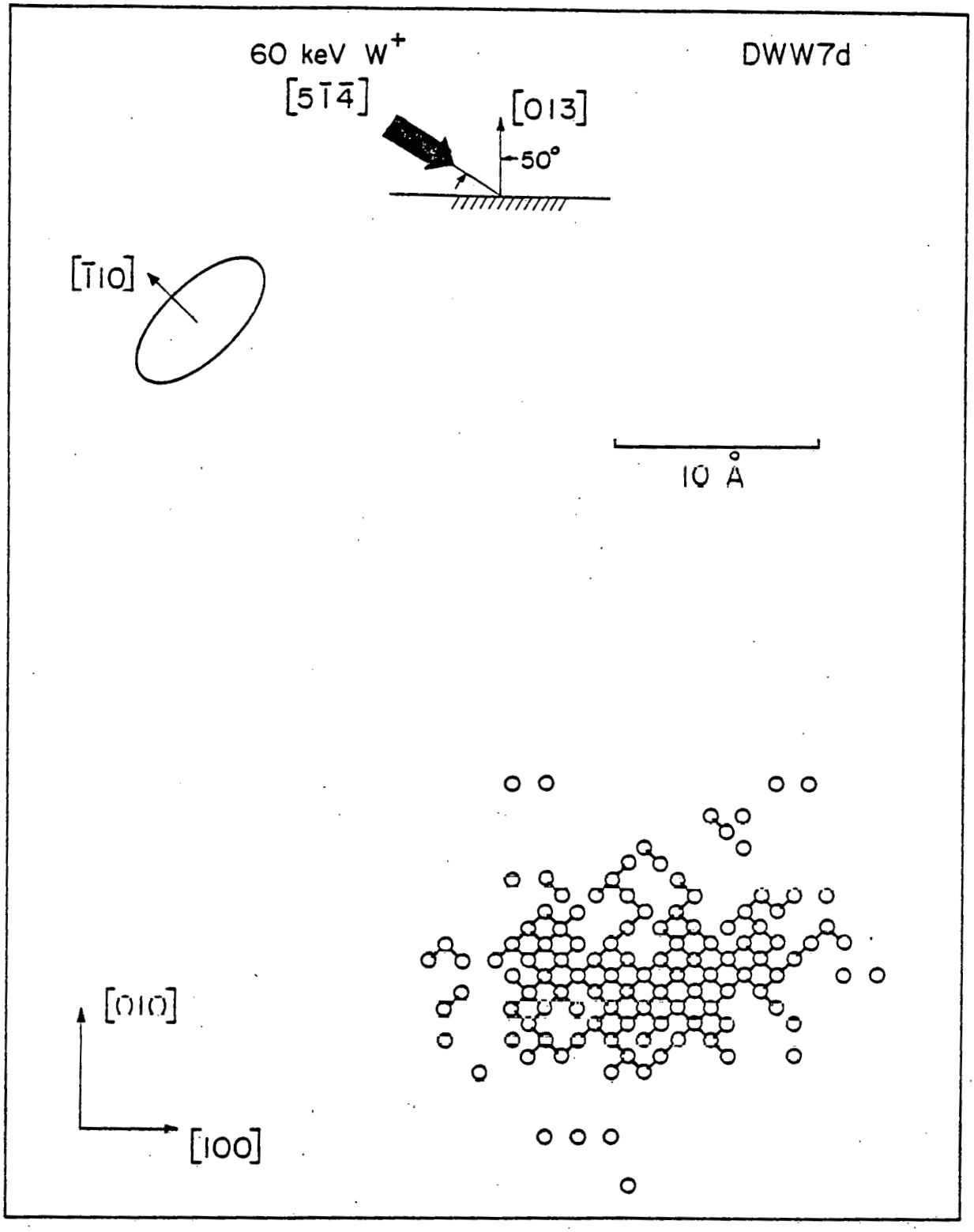

Fig. 52: First view of DWW7d showing the position of vacancy cluster and dislocation loop.

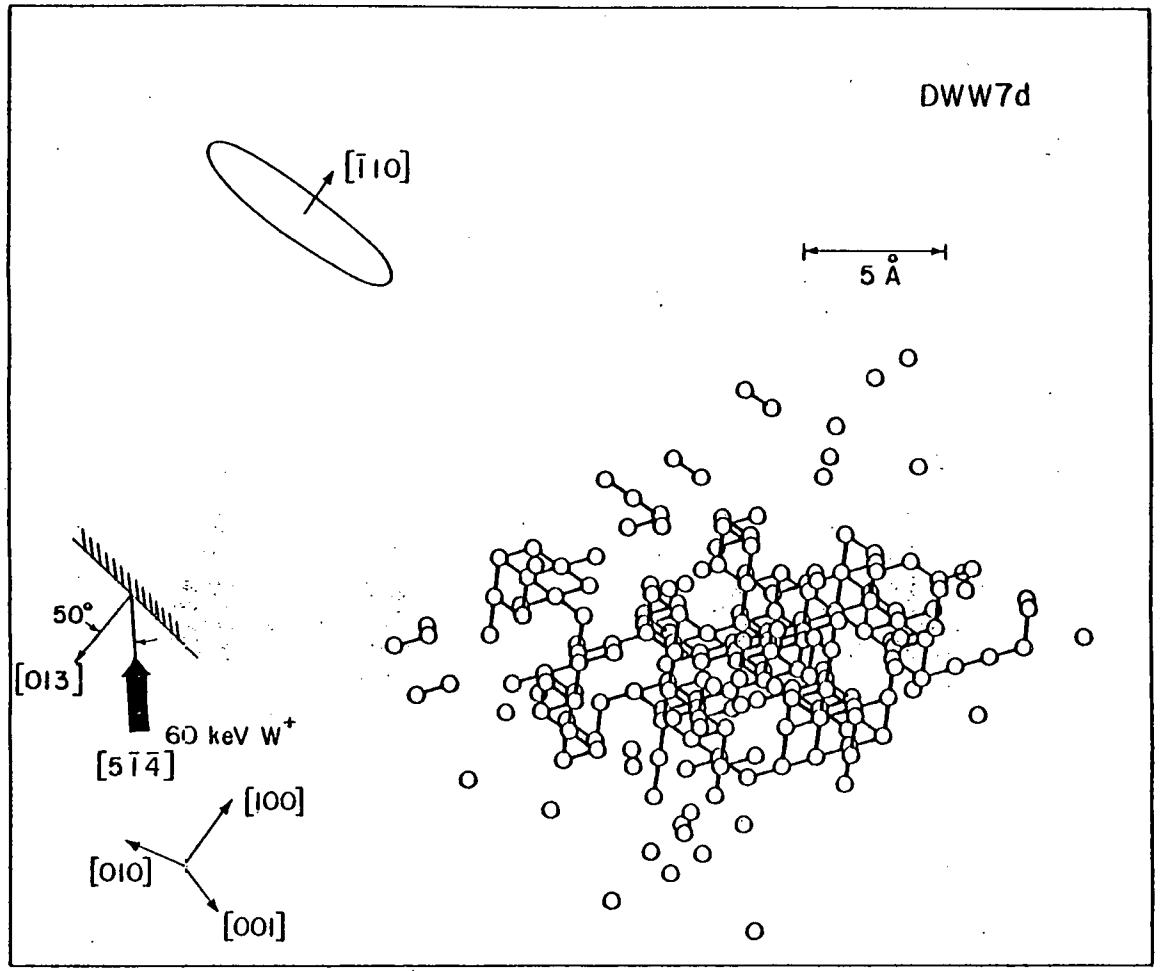

Fig. 53: Second view of DWW7d showing the position of vacancy cluster and dislocation loop.

TABLE 4.3

Experimental and estimated vacancy concentrations of DZ's produced by W^+ ions on tungsten

Energy of W^+ ion in keV (E)	Estimated vacancy concentration in at % (c_v^*)	Experimental vacancy concentration in at % (c_v)
20	32.4	14.3
30	22	20.2
45	14.2	14.2
60	9.46	17

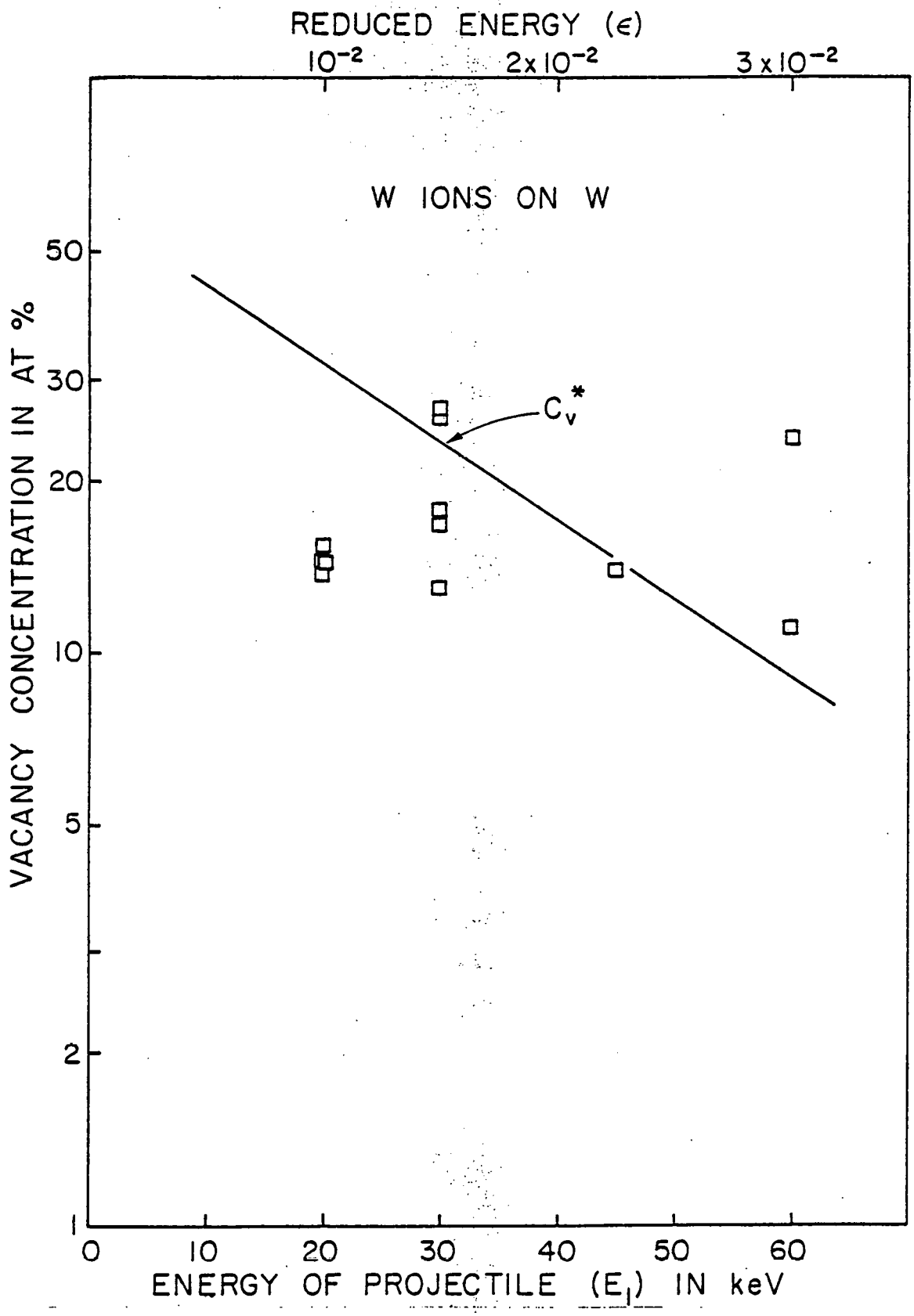

Fig. 54: Variation of vacancy concentration, c_v, with energy E_1 of W^+ projectile ions incident on tungsten.

shown in fig. 54, with a curve showing the variation of c_v^* with E_1. It is clear that c_v^* decreases as E^{-1}, while the $\langle c_v \rangle$ remain almost constant with energy. The E^{-1} dependence of c_v^* follows from linear cascade theory which predicts that D (and hence D_δ) should increase as $E^{2/3}$, whereas ν should increase as E. It is highly unlikely that for the case of W^+ on tungsten, the results of linear cascade theory will hold and hence the deviation of $\langle c_v \rangle$ from the expected behavior is not surprising.

IV.1.4d Clustering

In table 4.4, we have summarized the data on clustering of vacancies into nearest neighbor clusters of size n, for the DZ's produced by W^+ of different energy. The quantity $f = \frac{nN_n}{\nu}$ is the fraction of vacancies in clusters of size n, where N_n is the number of such clusters. The table reveals that the degree of clustering appears to be unchanged with energy. The majority of the vacancies are either in the form of monovacancies or in clusters containing more than five vacancies. Approximately 80-85% of the vacancies are in clusters of five or greater and 10% are in the form of monovacancies.

IV.2 Dislocation loops

As the energy of the irradiating particle increased the number of defects showing a loop-type contrast increased. No dislocation loops were seen in 20 keV irradiations; a single dislocation loop was reported for 30 keV irradiations. We observed two dislocation loops in the 45 keV irradiated samples and four loops in the 60 keV irradiated samples. Dislocation loops were first reported in ion-irradiated tungsten by Buswell[25] using the TEM technique in conjunction with FIM but a systematic study of the habit planes and Burgers vector ($\vec{b}$) was carried out by Hausser-

TABLE 4.4

Fraction of vacancies in first-nearest neighbor clusters of size n for W^+ ions on tungsten

$f = \frac{nN_n}{\nu}$ \ n	1	2	3	4	5
20 keV	0.12	.023	.019	.019	0.81
30 keV	0.12	.02	.00	.01	0.85
45 keV	0.11	.014	.02	.013	0.84
60 keV	0.10	.02	.014	.00	0.85

mann[26-28] and Jaeger *et al.*[29] for tungsten irradiated with 60 keV Au^+ ions. They found that the majority (≈99%) of the loops were perfect loops with $\vec{b} = \frac{a}{2}\langle 111\rangle$ which lay on {110} planes. In a few cases pure edge loops of the type $\vec{b} = \frac{a}{2}\langle 110\rangle$ and $\hat{n} = \frac{1}{2}\langle 110\rangle$ where $\hat{n}$ is the unit normal to the plane, were found.

Haussermann[28] and Jaeger[29] interpreted their results as follows:

(i) Dislocation loops of vacancy type are nucleated in the core of the DZ as pure edge loops on {110} planes with $\vec{b}_e = \frac{1}{2}\langle 110\rangle$;

(ii) If a loop reaches, during its growth, a critical radius ρ_c, estimated to be in the range $9\ \text{Å} \leq \rho_c < 20\ \text{Å}$ the stacking fault in area of the loop is eliminated by a shear over the area of the loop. The shear is described by a shear Burgers vector $\vec{b}_s = \pm\frac{1}{2}\langle 001\rangle$. This $\vec{b}_e$ is converted back into a perfect Burgers vector $\vec{b}_p$. Assuming, as a particular case $\hat{n} = \frac{1}{2}[110]$, $\vec{b}_e = \frac{1}{2}[110]$, and $\vec{b}_s = \frac{1}{2}[11\bar{1}]$ respectively we have:

$$\vec{b}_e + \vec{b}_s = \vec{b}_p = \tfrac{1}{2}[111] \text{ or } \tfrac{1}{2}[11\bar{1}] \text{ respectively.}$$

Thus, for a particular (110) plane there can exist two possible Burgers vectors corresponding to the two shear directions. If the vacancies can nucleate on the six possible (110) planes with equal probability there are altogether 12 different possible perfect loop types;

(iii) Not all the 12 types appeared with equal probability in the TEM study and this was explained by the fact that the two shear directions may lead to different total energies of the resultant sheared loops because of differences in the interaction energies with the surfaces. The critical loop size at which shear takes place, was assumed to be first reached for that shear direction which resulted after the shear--in the lower total energy. After the shear, the Burgers vector of the loop is perfect.

Then the loop may slip out of the foil if the image force by which the loop is attracted to the surface exceeds a critical value.

We have attempted to analyze the dislocation loops in a low index pole should convert the concentric rings into a spiral. The possible Burgers vector (or vectors) of the dislocation can be determined from the multiplicity p of the spiral defined by $p = \vec{b}.\vec{g}_{hkl}$ where $\vec{g}_{hkl}$ is the reciprocal lattice vector to the plane (hkl) on which the dislocation loop appears. The ends of a loop at the surface can be determined from the points at which the spiral starts and finishes and the habit plane from the trace on the FIM.

Because of the multiple combinations of possible $\vec{b}$ and $\hat{n}$ possible, in many cases the observed contrast pattern seen in the FIM may be satisfied by a number of combinations. We will therefore restrict ourselves to the possibilities determined from the TEM data and use a combination of arguments to determine the exact plane and Burgers vector.

IV.2.1 45 keV irradiations

The first dislocation loop was detected on the (101) plane. The pulse field-evaporation sequence is shown in fig. 55. The region of interest has been boxed in the figure and the frame numbers are shown in the upper right hand corners. In frame 1554 there is nor more any indication of the loop and comparison of this frame with the preceding ones clearly shows the spiral nature of the ring pattern. The ends of the spiral have been marked by vees.

We had for this case p = 1. The possible Burgers vectors which can give this are $\vec{b} = \frac{a}{2}[111]$ and $\frac{a}{2}[11\bar{1}]$. The possible habit planes for a $\vec{b} = \frac{a}{2}[111]$ are (110), (101), (011) and for $\vec{b} = \frac{a}{2}[11\bar{1}]$ they are (101), $(1\bar{1}0)$,

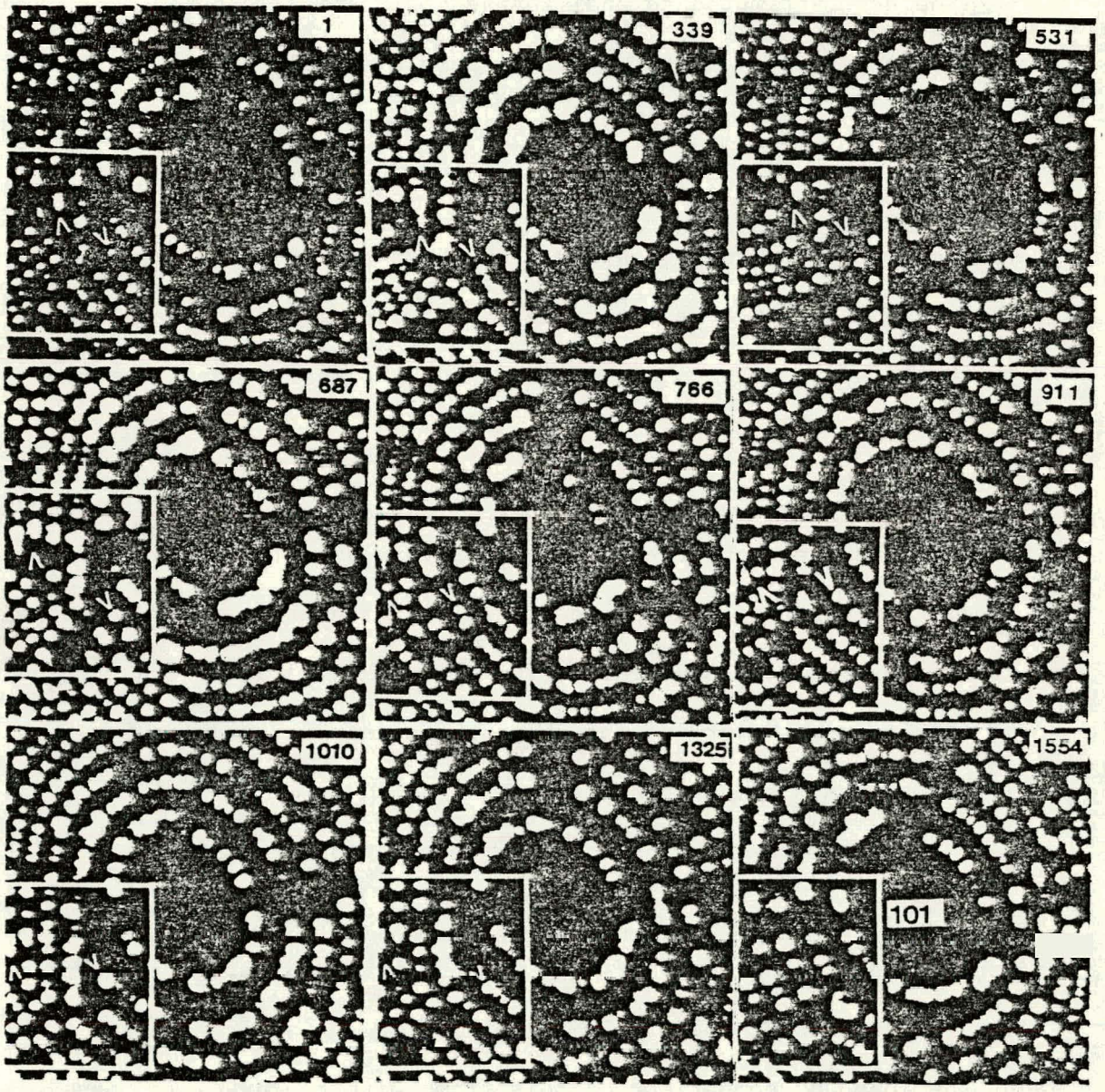

Fig. 55(a): Pulse-field evaporation sequence showing the contrast due to a dislocation loop emerging on a (101) plane.

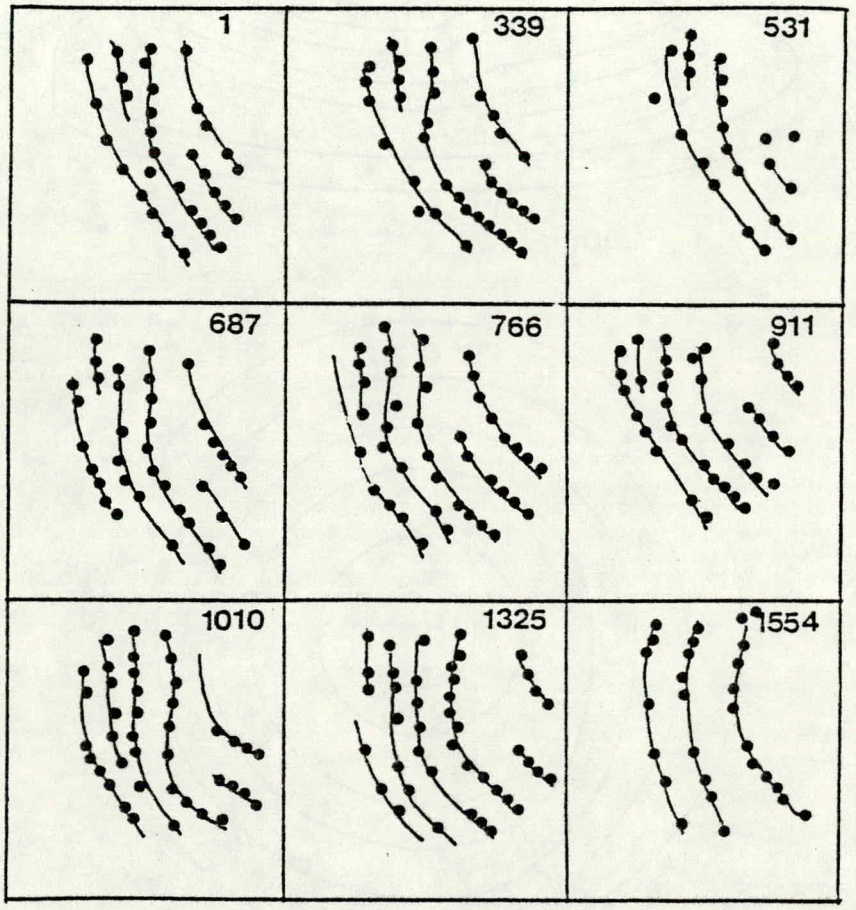

Fig. 55(b): A schematic diagram of atoms near the dislocation loop for the sequence shown in fig. 55(a).

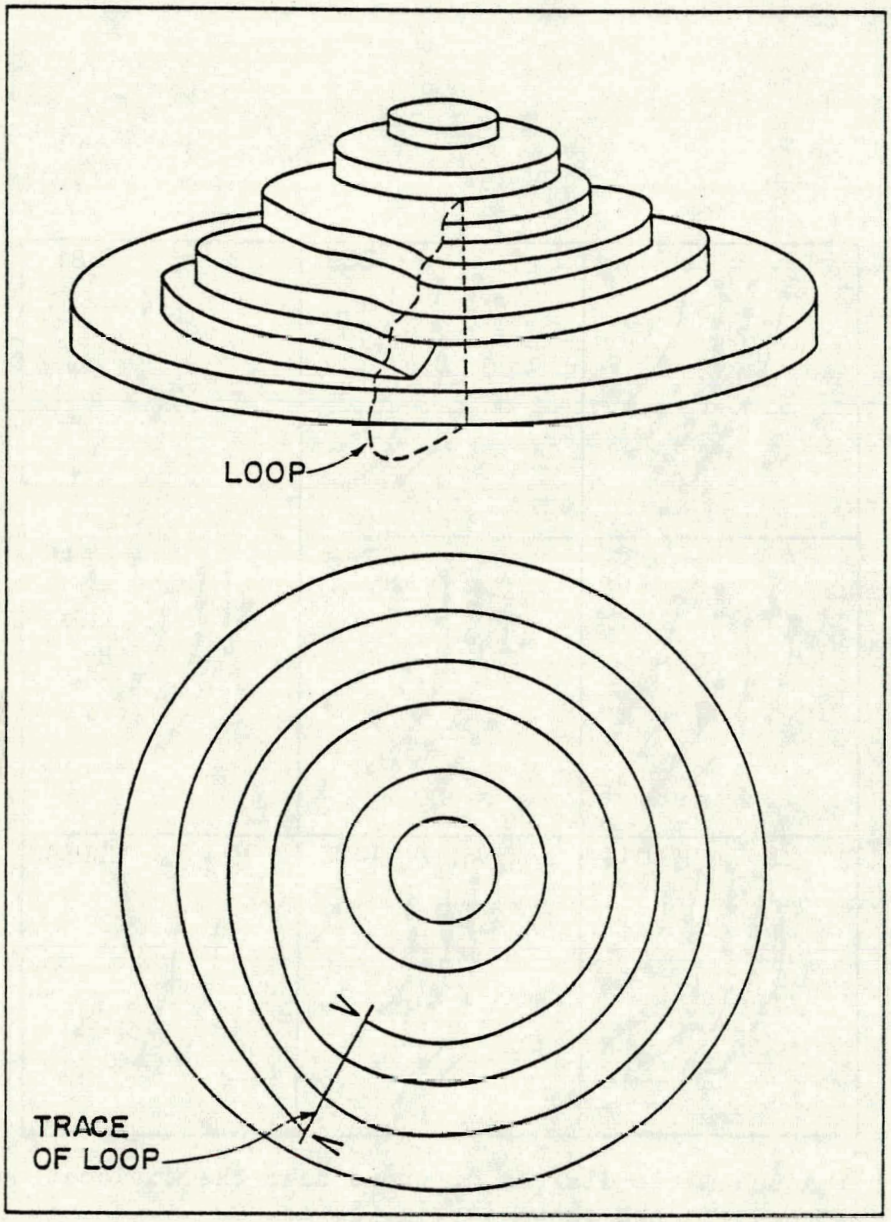

Fig. 56: A three-dimensional isometric drawing showing the effect of a dislocation loop emerging on a low index plane and the corresponding contrast expected in the FIM micrograph.

$(0\bar{1}1)$. The trace of the loop indicated that the plane was either (011) or $(1\bar{1}0)$. It is difficult to distinguish between these two possibilities. Measurement of the diameter of the loop gives $\omega_1 = 30$ Å; $\omega_2 = 40$ Å. It is clear that the diameter of the loop increases as the pulse field evaporation continues. In frame 1 it extends over only two (101) ledge widths; in frame 1010 it extends over three. Eventually it decreases (though not shown in the evaporation sequence).

A second small dislocation loop was detected on the outer rings of a (211) plane. The field evaporation sequence is shown in fig. 57(a). The region of the rings in which the contrast effect appears is boxed and in frame 1 is pointed out with vees. The contrast due to the loop no longer exists in frame 2149 and the rings in the region are unbroken or distorted. The arrangements of the atoms in the boxes are shown in fig. 57(b), and the dotted lines have been drawn to help to see the contrast. An isometric drawing of the pole, with the displacements produced by the loop would be very similar to fig. 56.

We had for this case p = 1. The possible Burgers vectors which can give this value are $\vec{b} = \frac{a}{2}[11\bar{1}]$ and $\frac{a}{2}[1\bar{1}1]$. The possible planes for $\frac{a}{2}[11\bar{1}]$ are (110), $(10\bar{1})$, $(0\bar{1}1)$ and for $\frac{a}{2}[1\bar{1}1]$ they are (101), $(1\bar{1}0)$ $(0\bar{1}1)$. The trace of the loop is difficult to determine because it extended over only a small distance; approximately three to four rings of the (211) plane; for some frames (1-860) the trace extends over the (723) plane, that adjoins (211), and the atomic resolution on this plane is sufficient to indicate the trace as a row of vacancies that was approximately in the $[\bar{1}21]$ direction. This was consistent with a habit plane of (101). After the habit plane was determined it was clear that the only possible Burgers

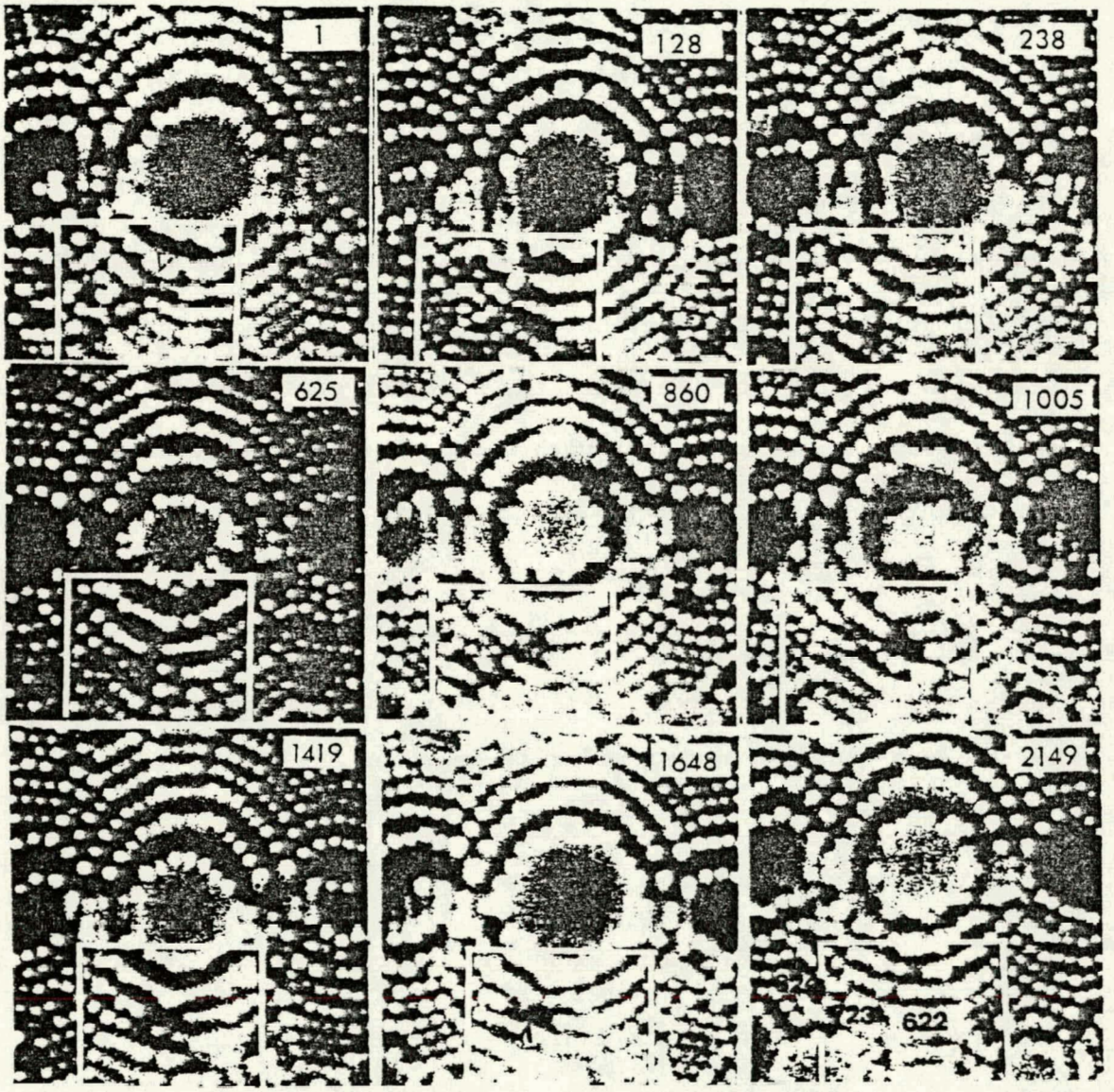

Fig. 57(a): Pulse-field evaporation sequence showing contrast due to a dislocation loop emerging on (211) plane.

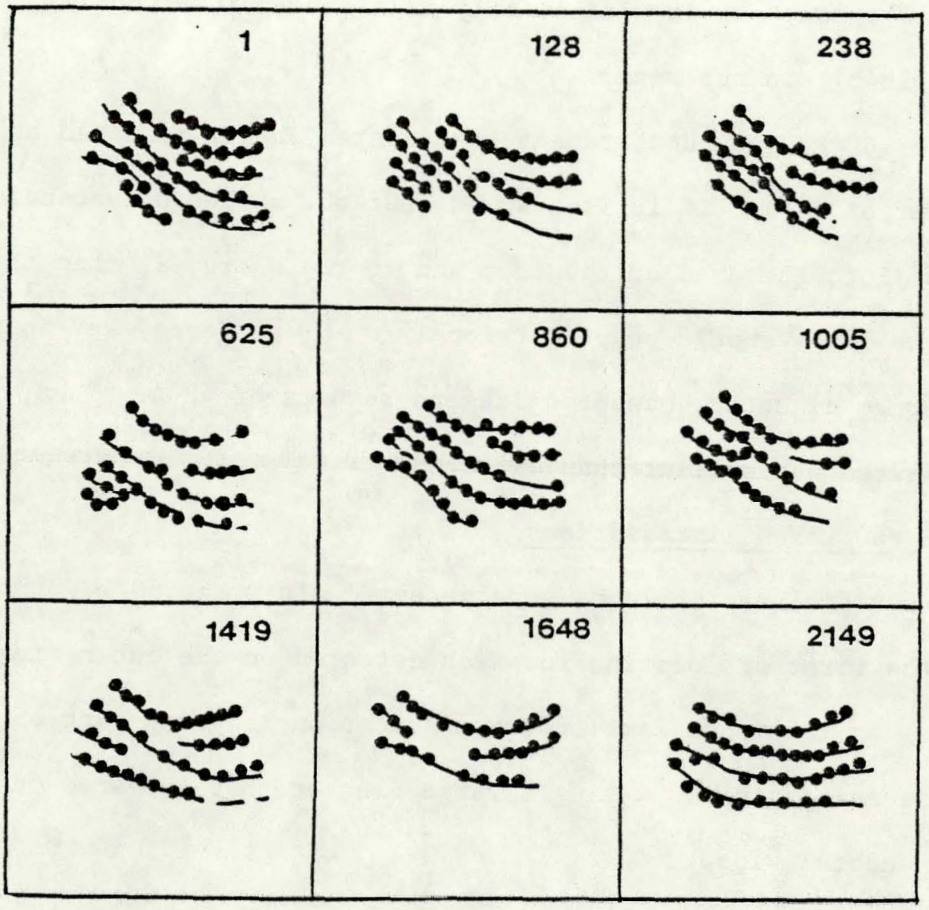

Fig. 57(b): A schematic diagram of atoms near the dislocation loop for the sequence shown in fig. 57(a).

vector was $\frac{a}{2}[11\bar{1}]$. Thus for this loop $\vec{b} = \frac{a}{2}[11\bar{1}]$ and $\hat{n} = \frac{1}{2}[101]$.

The diameters measured for this loop are ω_1 = 20 Å; ω_2 = 35 Å. It is possible to see the diameter of the trace increase and then decrease as the pulse field evaporation continues. In fact near the end of the loop (frame 1648) the trace does not extend beyond a single ledge width of the (211) plane and is visible only as a gap (pointed out with a vee in frame (1648)) in one ring.

For 60 keV Au^+ bombardment of tungsten Jaeger measured an average diameter of 55 Å. If it is assumed that the number of vacancies is proportional to the area of the loop and to the energy E_1 then the diameter d of the loops should be proportional to $\sqrt{E_1}$. For 45 keV ions we expect an average diameter, based on Jaegers results of 48 Å. Thus, the diameters we measured was smaller than expected.

IV.2.2 60 keV W^+ irradiations

Four dislocation loops were detected after the 60 keV irradiations.

The first dislocation loop was detected on the outer rings of the 013 plane. As mentioned earlier the dislocation loop was part of a single cascade consisting of a single large cluster that appeared on the $(\bar{1}27)$ plane and this loop.

The field evaporation sequence is shown in fig. 58a. The region around the (013) plane where the loop contrast appears is put in a box and the atom positions in this box are shown in fig. 53(a). Frame 1 shows the appearance of the plane before the loop contrast appears. In frame 104, the first contrast effects appear and the region is indicated with a vee. In later frames the contrast is very evident. An isometric drawing would be very similar to fig. 56.

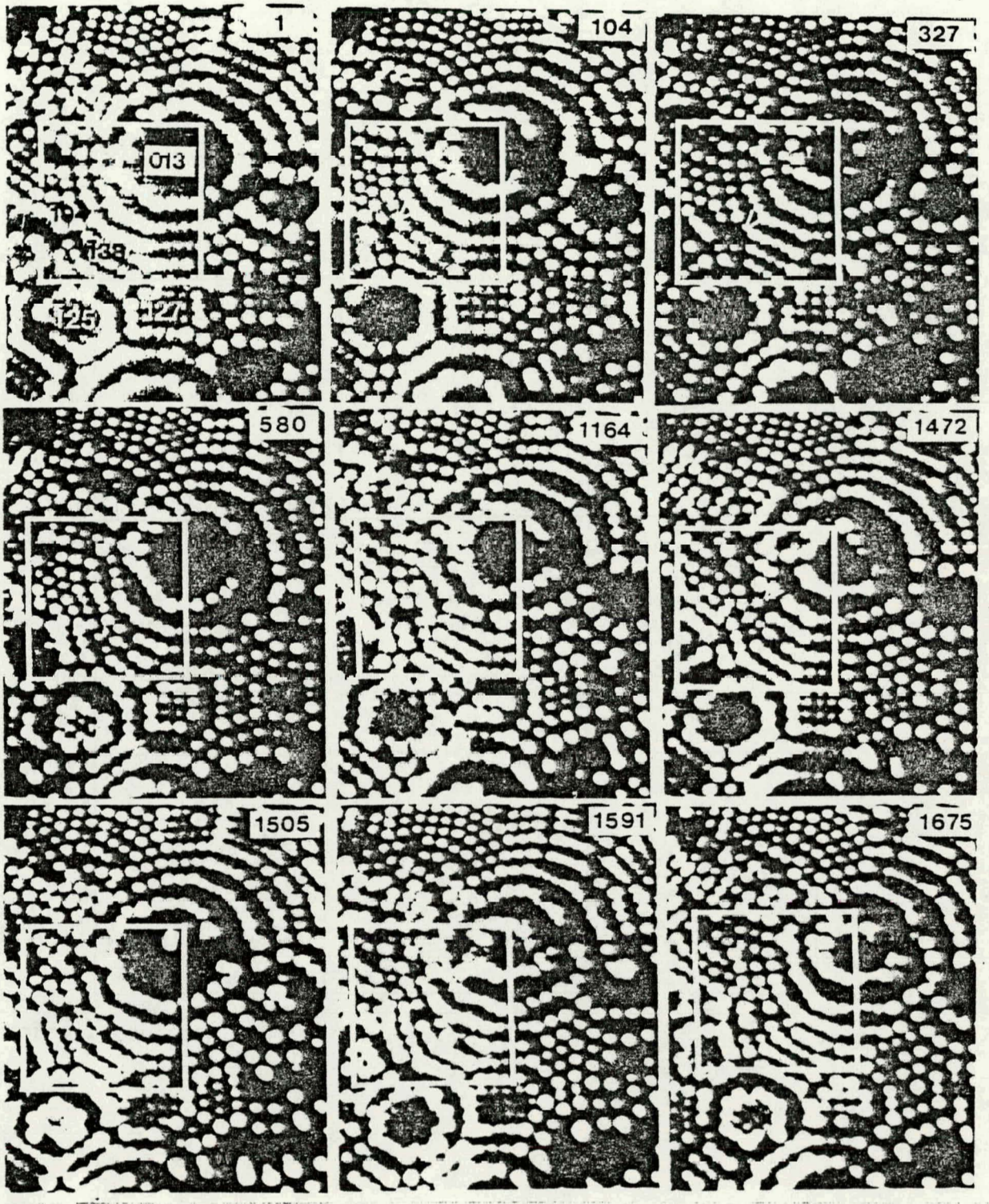

Fig. 58(a): Pulse-field evaporation sequence showing contrast due to a dislocation loop emerging on a (013) plane.

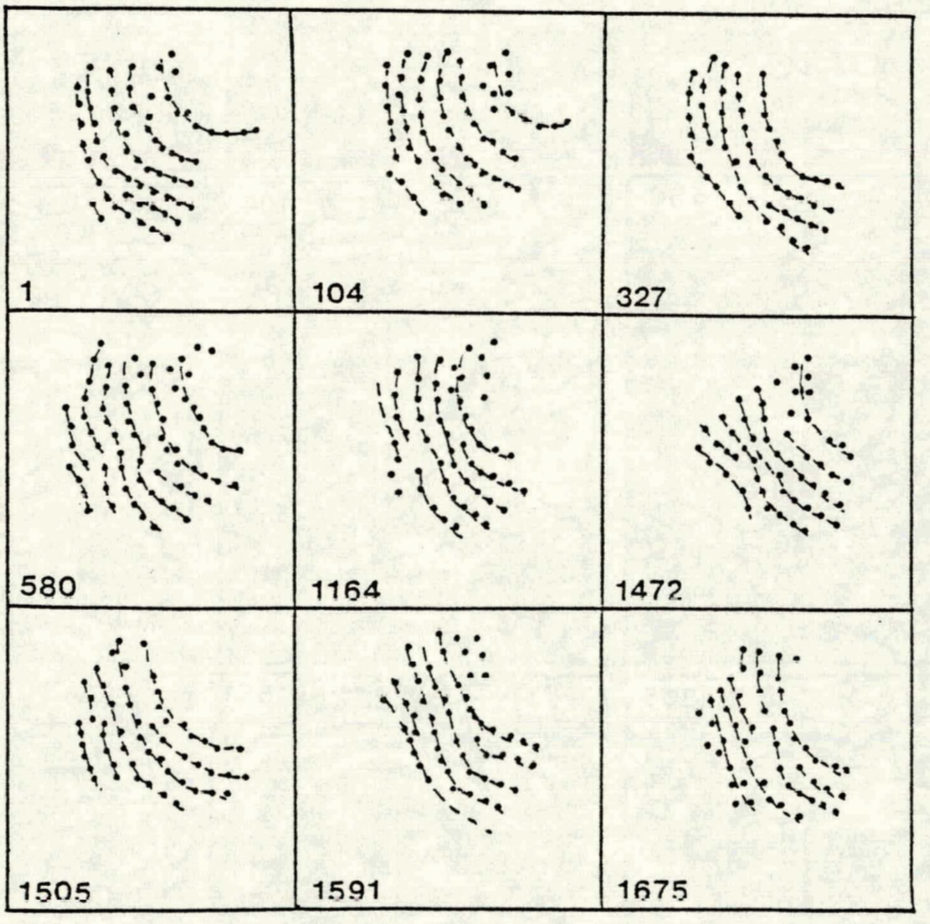

Fig. 58(b): A schematic diagram of atoms near the dislocation loop for the sequence shown in fig. 58(a).

We had for this loop p = 1. The possible Burgers vectors are $\vec{b} = \frac{a}{2}[1\bar{1}1]$ and $\frac{a}{2}[\bar{1}\bar{1}1]$. For $\vec{b} = \frac{a}{2}[1\bar{1}1]$ the possible habit planes are (101), $(1\bar{1}0)$, $(0\bar{1}1)$, and for $\vec{b} = \frac{a}{2}[\bar{1}\bar{1}1]$ they are $(10\bar{1})$, (110), $(01\bar{1})$. For part of the pulse field evaporation sequence the trace of the loop is visible on the $(\bar{1}49)$ plane which is adjacent to the (013) plane (e.g., frames 1164 and 1505) and vacancies were visible on the plane confirming the loop is of vacancy type. The trace of the dislocation loop is along the direction $[33\bar{1}]$ which makes the habit plane $(1\bar{1}0)$. Thus the only possible Burgers vector consistent with this was $\vec{b} = \frac{a}{2}[1\bar{1}1]$. The diameters of the loop are $\omega_1 \simeq 30$ Å and $\omega_2 \simeq 31$ Å.

The second loop was detected on the $(2\bar{1}1)$ plane. The contrast was a double spiral as seen in the field evaporation sequence in fig. 59(a). Thus we had p = 2. The only possible Burgers vector is $\vec{b} = \frac{a}{2}[11\bar{1}]$. The possible habit planes are (101), $(1\bar{1}0)$ and $(01\bar{1})$. The trace was difficult to determine because the loop appears to stay within the $2\bar{1}1$ pole so that only one end of the spiral can be determined with precision. However, the direction of movement of the point at which the double spiral began, indicated the trace to be that of a $(01\bar{1})$ plane. Hence the loop has a Burgers vector $\frac{a}{2}[1\bar{1}1]$ and it lay on the $(01\bar{1})$ plane. The diameter $\omega \simeq 45$ Å. ω_2 could not be determined as the field evaporation process was stopped and the specimen irradiated again before the contrast effects had disappeared fully. Approximately 11 $(2\bar{1}1)$ planes were evaporated for the period when contrast effects appeared; this gave a diameter of 17 Å until the point at which pulse field evaporation was ceased. After the irradiation the double spiral contrast effect no longer existed, indicating that the disturbance created by an incident ion close to the dislocation caused

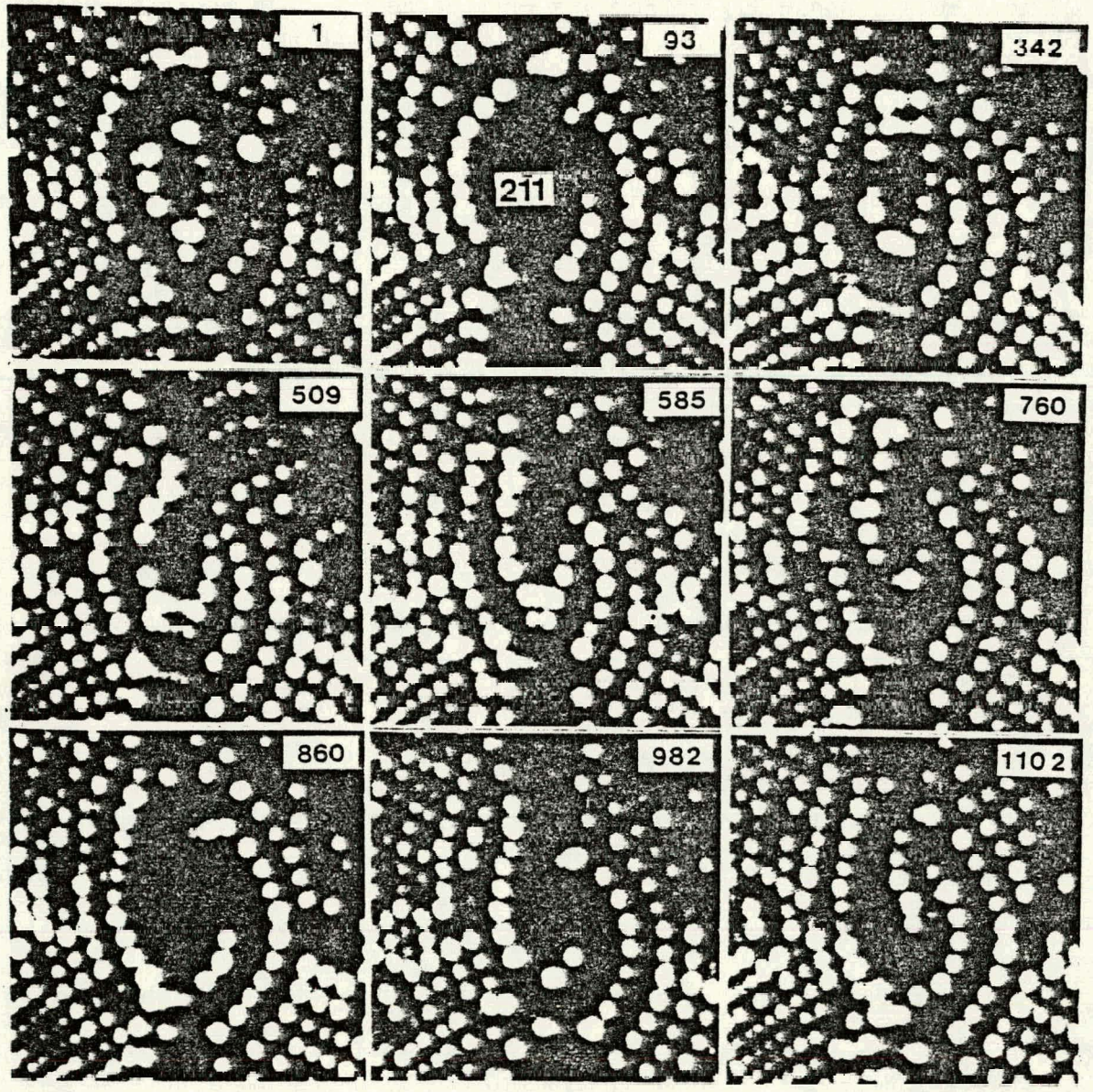

Fig. 59(a): Pulse-field evaporation sequence showing contrast due to a dislocation loop emerging on (2$\bar{1}$1) plane.

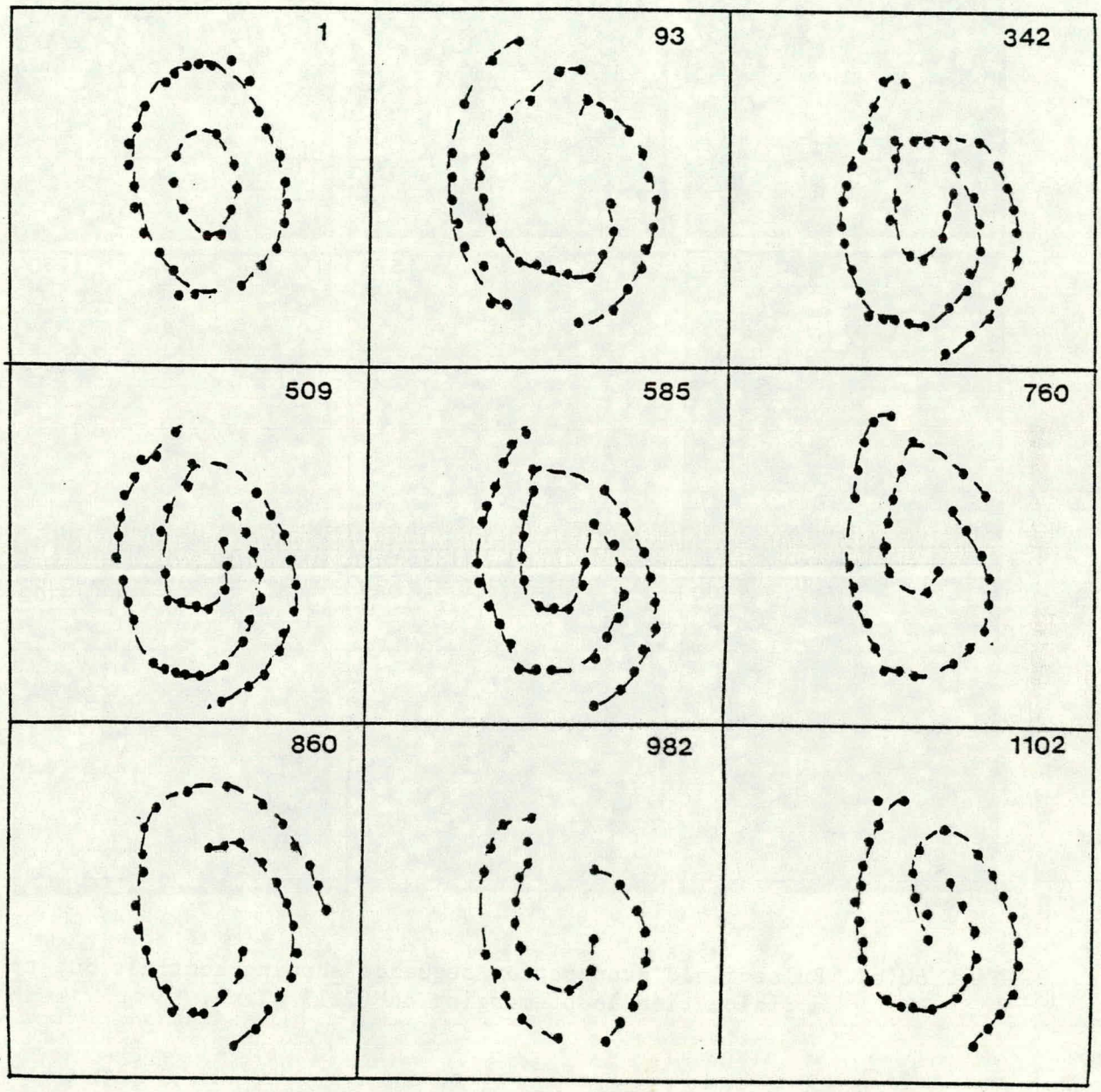

Fig. 59(b): A schematic diagram of atoms near the dislocation loop for the sequence shown in fig. 59(a).

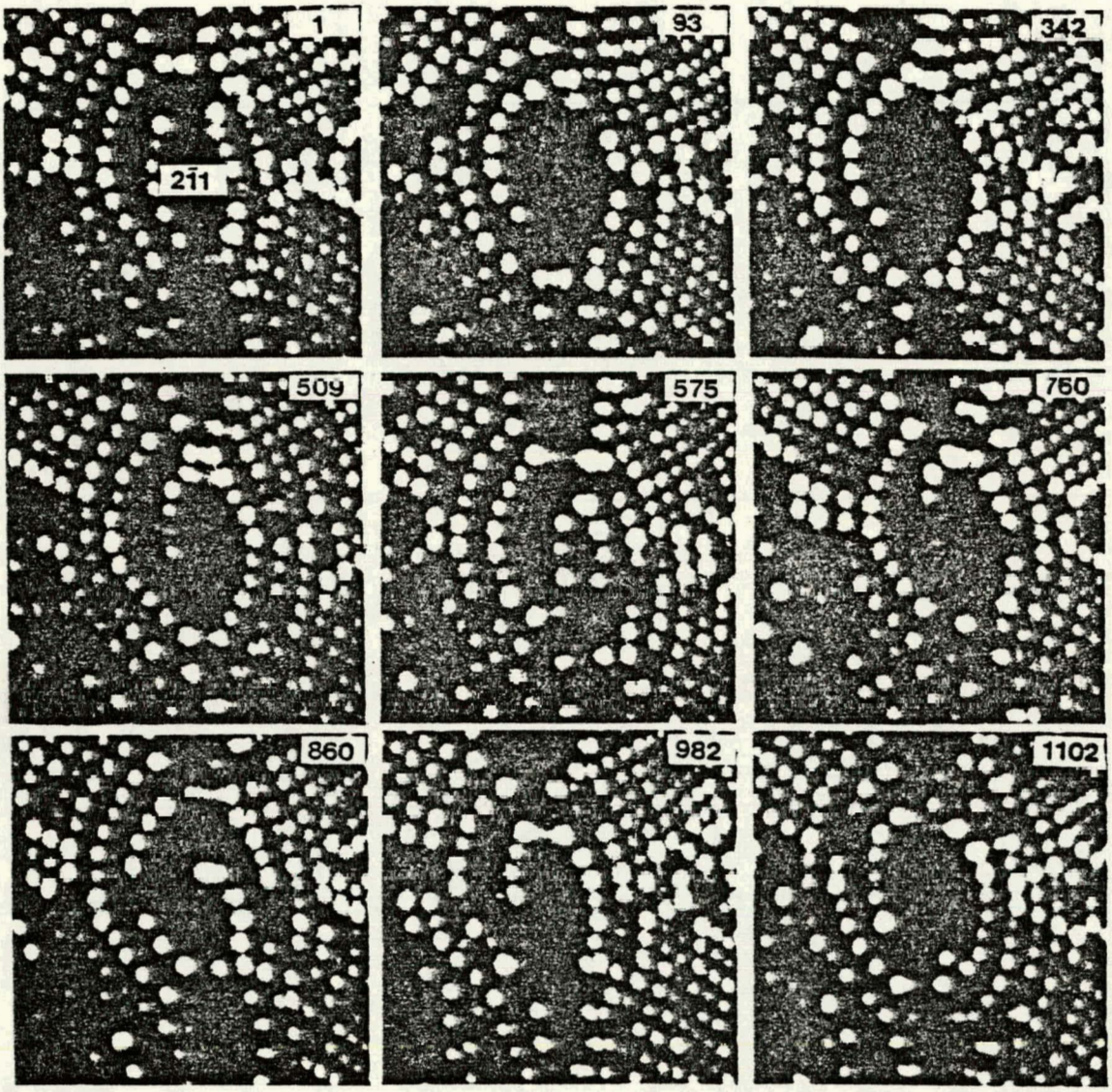

Fig. 60(a): Pulse-field evaporation sequence showing contrast due to a dislocation loop emerging on (2$\bar{1}$1) plane.

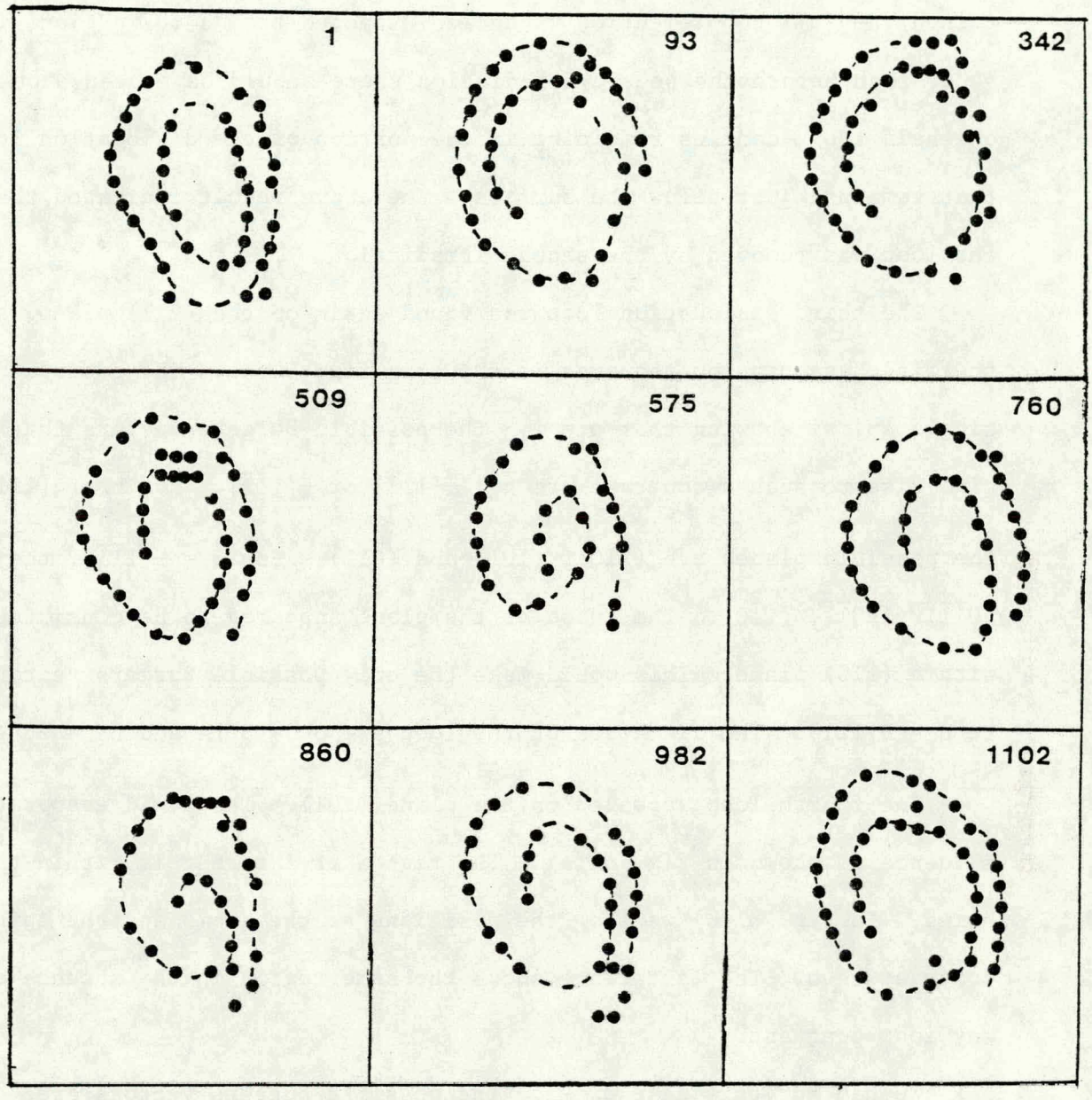

Fig. 60(b): A schematic diagram of atoms near the dislocation loop for the sequence shown in fig. 60(a).

a rearrangement of the atoms. If we assume that the dislocation loop contained the full complement of vacancies expected from a 60 keV ion, i.e., ≃400, then before the second irradiation there should have been about one-half the vacancies remaining in the portion of the dislocation loop that remained just below the surface. The above result indicated that the loop was removed by the second irradiation.

The third dislocation loop was found again on the $(2\bar{1}1)$ plane, and the field evaporation sequence is shown in fig. 60(a). The contrast is a single spiral showing that p = 1. The possible Burgers vectors that can give rise to such a contrast are $\vec{b} = \frac{a}{2}[111]$ or $\frac{a}{2}[1\bar{1}\bar{1}]$. For $\vec{b} = \frac{a}{2}[111]$ the possible planes are (110), (101) and (011). For $\vec{b} = \frac{a}{2}[1\bar{1}\bar{1}]$, they are $(0\bar{1}\bar{1})$, $(10\bar{1})$, $(1\bar{1}0)$. The trace of the plane appeared to be consistent with a (110) plane. This would make the only possible Burgers vector to be $\vec{b} = \frac{a}{2}[111]$. The diameters of the loop are ω_1 = 30 Å and ω_2 = 26 Å.

The fourth loop appeared on the plane (101). The field evaporation sequence is shown in fig. 61(a). The region of interest is within the boxes. In fig. 61(b) we show the positions of the atoms and the spiral contrast seen. The last frame shows the same region in the absence of any loop contrast.

We had for this case p = 1. The possible Burgers vectors are $\vec{b} = \frac{a}{2}[11\bar{1}]$ and $\frac{a}{2}[111]$. The possible planes for $\vec{b} = \frac{a}{2}[1\bar{1}1]$ are (101), $(0\bar{1}1)$, $(1\bar{1}0)$ and for $\vec{b} = \frac{a}{2}[111]$ are (101), (110) and (011). The trace of the loop would be consistent with the plane $(10\bar{1})$ which would make $\vec{b} = \frac{a}{2}[1\bar{1}1]$ as the only possible Burgers vector. The diameters for the loop were $\omega_1 \simeq 31$ Å and $\omega_2 \simeq 28$ Å. The diameter of the loop can be seen to decrease with the

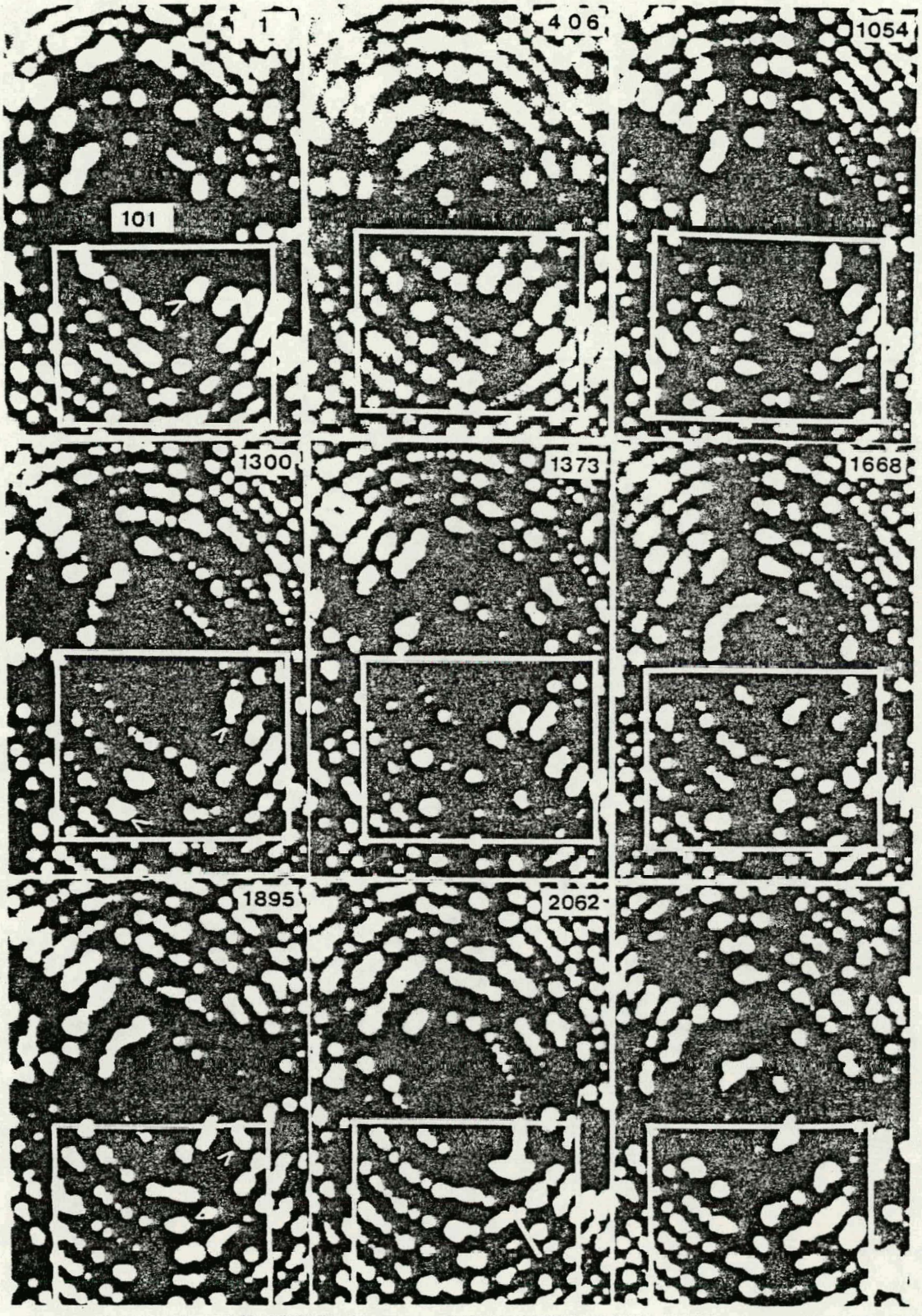

Fig. 61(a): Pulse-field evaporation sequence showing contrast due to a dislocation loop emerging on the (101) plane.

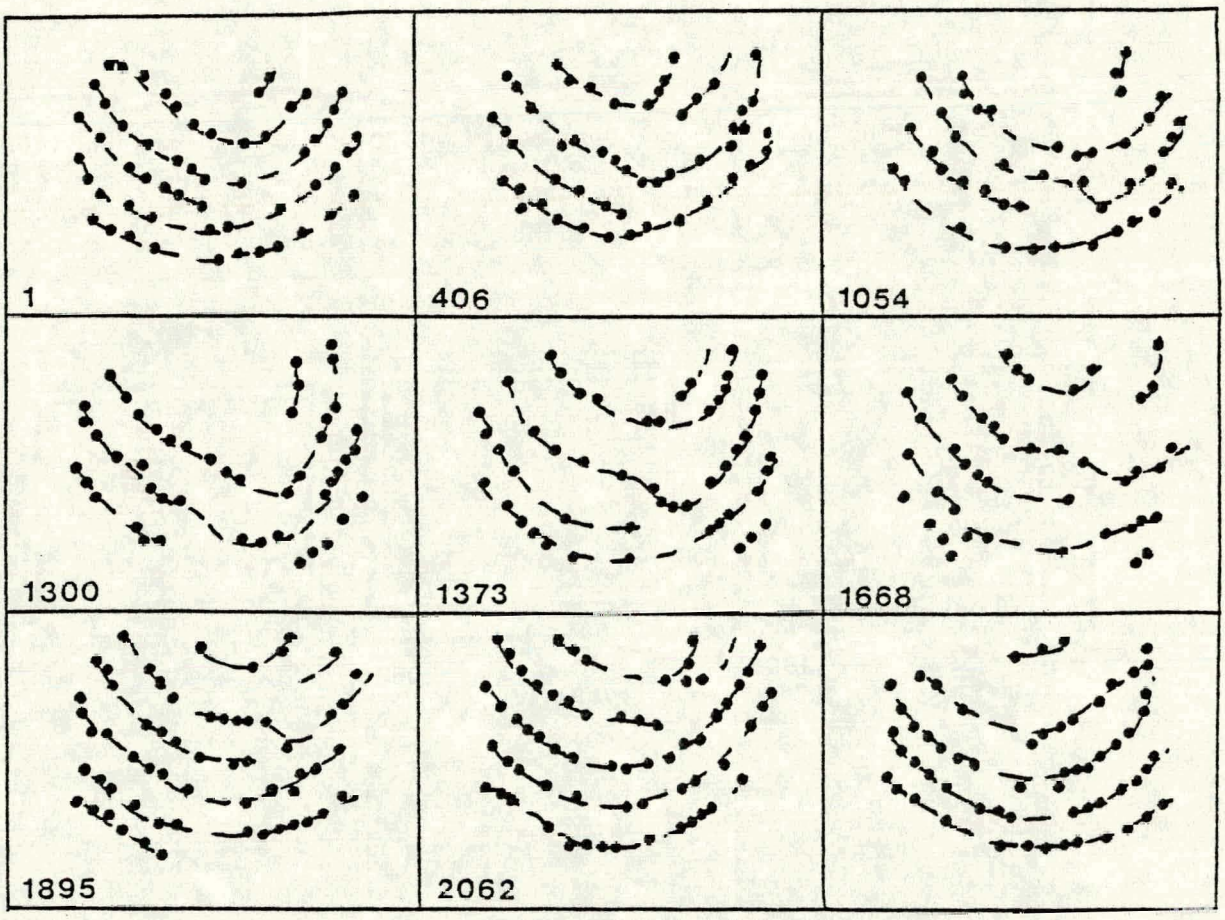

Fig. 61(b): A schematic diagram of atoms near the dislocation loop for the sequence shown in fig. 61(a).

field evaporation. In frame 2062 it appears only as a break in one ring. (Indicated with an arrow.)

IV.3 Discussion on dislocation loops

The FIM results show that the fraction of defects, caused by a single ion, that are dislocation loops, increased with increasing ion energy. This agreed with TEM observations on self-ion irradiated gold, silver and copper, where the yield increased with increasing energy of the self ions.[30] In table 4.4, we show the fraction of observed defects in the FIM specimen that were dislocation loops, for each of the different energies. It is not possible to relate this fraction directly to the TEM yield, though it is expected that there should be some proportionality between the two.

It is generally assumed that the dislocation loops are formed by the collapse of vacancy-rich center of a DZ. The fact that in our FIM specimens both dislocation loops and DZ's were observed certainly indicates that this is the mostly likely the case but the exact mechanism of collapse and the factors responsible for it have not been investigated.

TEM studies of metals irradiated with ions of the same energy but different mass, showed that the yield increased with increasing projectile mass.[31,32] The main difference between the cascades produced by ions of different mass is the average size of the cascade and hence c_v. Heavier ions produce on the average, DZ's with higher $\langle c_v \rangle$ than lighter ions. If c_v is the crucial factor then the above mentioned results can be explained. It has been suggested that the quantity θ_0, the average energy deposited per unit volume at the center of the cascade is a useful parameter for determining whether collapse will occur or not. The quantity θ_0 was calculated from analytical theories based on linear cascade theory.[34] However,

TABLE 4.5

FIM loop fraction and observed TEM yield for various energies

Energy in keV and species of projectile	No. of loops	Total no. of defects	FIM loop fraction (f)	Observed TEM yield
20(Ag + W)	0	8	0	*
30(W + Mo)	1	10	0.1	*
45(W)	2	6	0.3	*
60(W)	4	9	0.44	0.2[†]

*No data.

[†]Ref. 26.

if θ_0 was the governing parameter, then the yield should drop off with increasing E_1, as θ_0 decreases as E_1^{-1}, which is contrary to experimental observations. The difficulty in using θ_0 is due to the reasons stated before, namely that linear cascade theory cannot predict the size of the DZ's for the case when non-linear effects are predominant.

The FIM results on DZ's in W indicate that c_v, alone cannot be the parameter determining collapse, since at low energies ($\lesssim$30 keV) DZ's with high c_v are produced, and yet a negligible number of dislocation loops are observed. The number of vacancies in the DZ, ν is also crucial. From a knowledge of the self-energy of dislocation loops and voids it can be concluded that for a sufficiently large ν, the dislocation loop should be the lowest-energy configuration for the set of ν vacancies. Hence, it is expected the larger the ν, the greater will be the probability of collapse of a DZ into a loop. The critical number of vacancies, ν_m for which the dislocation loop will be the lowest energy configuration is obviously very much dependent on the self-energy of a loop and a void. The self-energies are not at all known precisely--calculations by different authors give values that differ by orders of magnitude.

The collapse process is generally called "athermal" because dislocation loops are detected even at very low temperatures of irradiations, where vacancies are not mobile. The term "athermal" is in our opinion a misnomer as it implies that there exists no energy barrier for the collapse process, which is not the case. In order for a DZ to change its configuration, there has to be movement of the vacancies. Any movement of vacancies occurs after the DZ has been produced, during the short time that it takes for the energy residing in the collision cascade (that encompasses the DZ) to be dissipated to the surrounding lattice. The

number of jumps (n) that atoms can make during this time can be calculated following the procedure first outlined by Seitz and Koehler[35] to explain the physical processes in an "energy spike," a microscopic region with a high energy density, such as that produced in a cascade generated in heavy ion irradiations of heavy targets. Subsequent papers[36,37] have added various modifications to the basic steps of Seitz's method. First, a temperature T is assigned to a region on the basis of the mean energy per atom. Next, the dissipation of energy is calculated from the bulk heat conduction equations. An analytical expression for the temperature at a particular point $\vec{r}$ at a time t, $T(\vec{r},t)$ is obtained. Finally, n is calculated from the expression:

$$n = \int_0^\infty\int\omega e^{-A/T(r,t)} d^3r dt \qquad (4-5)$$

where the integration is carried out over the entire volume and time; ω is the attempt frequency which is approximately the Debye frequency and of the order of 10^{13} sec^{-1} and A is the activation energy for migration. For incident energies in the range of 10 keV and for A = 1.5 eV the number of jumps turns out to be of the order of unity, indicating a small likelihood of rearrangement. However, there are several difficulties in these arguments. The most obvious one is the assumption that the dissipation of energy can be described by the heat conduction equations using the bulk thermal conductivity. The small volume of the cascade encompasses so few atoms that the use of bulk properties become meaningless. Also, the calculated temperature gradients are so enormous that linear response theory (inherent in the assumption of thermal conductivity) would break down. Secondly, the assumption of the bulk activation energy A would not be valid in a region containing a high c_v. In all likelihood, A would

be depressed to very low values and this would drastically change n since A appears in the exponential in eqn. (4-5).

The assumption of a kinetic process in the collapse of DZ's would explain why DZ's, voids and loops are observed simultaneously. Owing to statistical fluctuations, some cascades will have a higher energy density and hence higher vacancy concentration than others. In the denser cascades, the vacancies will be closer together, and the net kinetic energy will also be concentrated in a smaller volume. The DZ's arising from these cascades would have a high probability of collapsing in the time that it takes for the energy to be dissipated to the lattice. It is also likely that in this time scale, only partial collapse may occur or vacancies aggregate into voids. In more diffuse cascades, the rearrangement of vacancies would be very small, and the DZ's would remain diffuse.

The movement of vacancies within the DZ volume would be governed by an activation energy that would be dependent on the material. Hence, the degree of collapse of DZ's will be determined by the target material. An illustration of this point is provided by comparing the radiation damage in tungsten, gold and platinum which have atomic numbers close to each other. The cascades produced inside these materials by ions of the same M_1, E_1 should be similar. The morphology of damage is however quite different. Gold has the highest yield, platinum the next and tungsten has the lowest yield. This indicates clearly that the collapse is kinetically limited. Gold had the lowest bulk vacancy migration energy and tungsten the highest and the case of collapse is probably linked with this. The lower bulk vacancy migration energy, the more likely is a DZ to collapse in the material.

IV.5 Summary

1. The number of vacancies per DZ (ν) increases linearly with energy of the incident projectile (E_1) and can be predicted by the modified Kinchin-Pease formula.

2. The size of the DZ's did not increase with E_1, as expected from linear cascade theory. This was attributed to the production of nonlinear cascades in tungsten by the tungsten ions.

3. The vacancy concentration in the DZ's remained almost constant with increasing E_1, instead of decreasing as E_1^{-1} as predicted by linear cascade theory.

4. The fraction of defects that were dislocation loops, increased with increasing E_1. The contrast from these loops was consistent with a Burger's vector of $\frac{a}{3}$ <111> and a habit plane {110}. The dislocation loops in tungsten were produced by the collapse of dense DZ's, as in other materials. The ease of collapse is dependent on the nature of the material of the target and may be linked with the bulk vacancy migration energy.

REFERENCES FOR CHAPTER IV

1. C.Y. Wei, PhD Thesis, Cornell University (1978).

2. L.A. Beavan, R.M. Scanlan, and D.N. Seidman, Acta Met 19 (1971) 1339.

3. M. Current, C.Y. Wei, D.N. Seidman, to be published.

4. R.S. Averback, R. Benedek and K.L. Merkle, Phys Rev B, 18, 4156 (1978).

5. K.B. Winterbon, Ion implantation, Range and Energy Distributions (Plenum, New York, 1975).

6. F. Maury, M. Biget, P. Vajda, A. Lucasson and P. Lucasson, Radiat Eff. 38, 53 (1978).

7. C.Y. Wei and D.N. Seidman, to be published.

8. K.L. Merkle in "Radiation damage in metals" Eds N.L. Peterson and S.D. Harkness (American Society for Metals, Metals Park, OH 1976) p. 58.

9. K.L. Merkle, Radiation Damage in Reactor Materials, Vol. 1, IAEA, Vienna, 1969, p. 159.

10. K.L. Merkle and R. Lyles, to be published.

11. F. Haussermann, Phil Mag. Vol. 25, 1972, p. 537.

12. C.A. English, B.L. Eyre, H. Wadley, and A.Y. Statopoulous, Proceedings of the International Conference on Fundamental Aspects of Radiation Damage in Metals, Gatlinburg, 1975.

13. K.L. Merkle and R.S. Averback, Proceedings of the International Conference on Fundamental Aspects of Radiation Damage in Metals, Gatlinburg, 1975.

14. P. Sigmund, G.P. Scheidler and G. Roth, in Proc Int Conf Solid-State Physics Research with Accelerators, Brookhaven National Laboratory Report No. 50083 (1968), p. 374 (unpublished).

15. K.B. Winterbon, P. Sigmund, and J.B. Sanders, Mat Fys Medd, Dan Vid Selsk, 37, 1970, p. 14.

16. K.L. Merkle, Phys Stat Sol. 18, 1966, p. 173.

17. L.E. Thomas, T. Schober, and R.W. Baluffi, Rad Effects, 1, 257, 269, 279 (1969).

18. P.P. Pronko and K.L. Merkle, Applications of Ion Beams to Metals, ed by S.T. Picraux, E.P. EerNisse, and F.L. Vook. (Plenum Press) ('74) p. 481.

19. M.M. Wilson, Phil. Mag., 24, 1023, 1973.

20. M.L. Jenkins and M. Wilkens, Phil. Mag. 34, 1155 (1976).

21. M.L. Jenkins, N.G. Norton, C.A. English, Phil. Mag., 40, 131 (1979).

22. J.R. Beeler, J. Nucl Mat, 53, 207 (1974).

23. J.R. Beeler, Phys Rev, 150, 470 (1966).

24. K.L. Merkle, L.R. Singer and R.K. Hart, J. Appl. Phys., 34, 2800 (1963).

25. J.T. Buswell, Phil Mag, 22 (1970) 787.

26. F. Haussermann, Phil Mag. 25, 561 (1972).

27. F. Haussermann, Phil Mag. 25, 583 (1972).

28. F. Haussermann, M. Rühle and M. Wilkens, phys. Stat Sol (b), 50, 445 (1972).

29. W. Jaeger, M. Wilkens. phys Stat Sol (a). 32, 89 (1975).

30. B.L. Eyre, J Phys F, 3, 422 (1973).

31. M.L. Jenkins, C.A. English and B.L. Eyre, Phil Mag A. 38, 97 (1978).

32. M. Wilkens, Proceedings of the International Conference on Fundamental Aspects of Radiation Damage in Metals, 1975.

33. M.O. Ruault, H. Bernas, J. Chaumont. Phil Mag A. 39 757 (1979).

34. P. Sigmund, Appl Phys lett. 25, 169 (1974).

35. F. Seitz and J.S. Koehler, Solid State Phys. 2, 307 (1956).

36. G.H. Vineyard, Rad Eff. 29, 245 (1976).

37. G. Carter, D.C. Armour, S.E. Donnelly, R. Webb, Rad Eff. 36, 1 (1978).

V. NONLINEAR EFFECTS IN IRRADIATED TUNGSTEN

In this chapter we consider effects of bombardment on tungsten by energetic dimers which consisted of two heavy atoms, with a total energy of E_1. On impact with the target's surface the dimer breaks up into two single projectile atoms of equal energy $E_1/2$, which then proceed to make independent collisions with the target atoms. For a large fraction of their total path the projectile atoms will be very close to each other so that the collision cascades generated by them will to some extent overlap during the time period of formation of the cascades. The significance of heavy ion dimer irradiations become clear when we look at the way in which the energy may be dissipated by an energetic particle in a solid via elastic collisions. Figure 62 shows two different views, based on Sigmund's model.[1] Figure 62(a) shows a collision cascade and fig. 62(b) a spike.* In both cases energy is ultimately shared by a great number of atoms. The difference between the two situations lies in the fact that while only a small fraction of all atoms within a certain cascade volume are in motion in fig. 62(a), essentially all the atoms within a spike volume move in fig. 62(b). The picture of a cascade applies when there is a long mean free path between significant collision events--as in the case of light ion-bombardment--such that the energy is spread out over a large volume. Conversely, in a spike, energy is dissipated at a high rate, within a small volume. The difference between the two situations is characterized most illustratively when two cascades (or spikes) are generated at the same time on top of each other, as in the case of bombardment with a dimer. When two genuine cascades are superimposed, the statistical nature of the

*The term "spike" has a long history, and it has been involved in many different concepts over the years. In this chapter, the term will be used only to characterize the situation sketched in fig. 62(b).

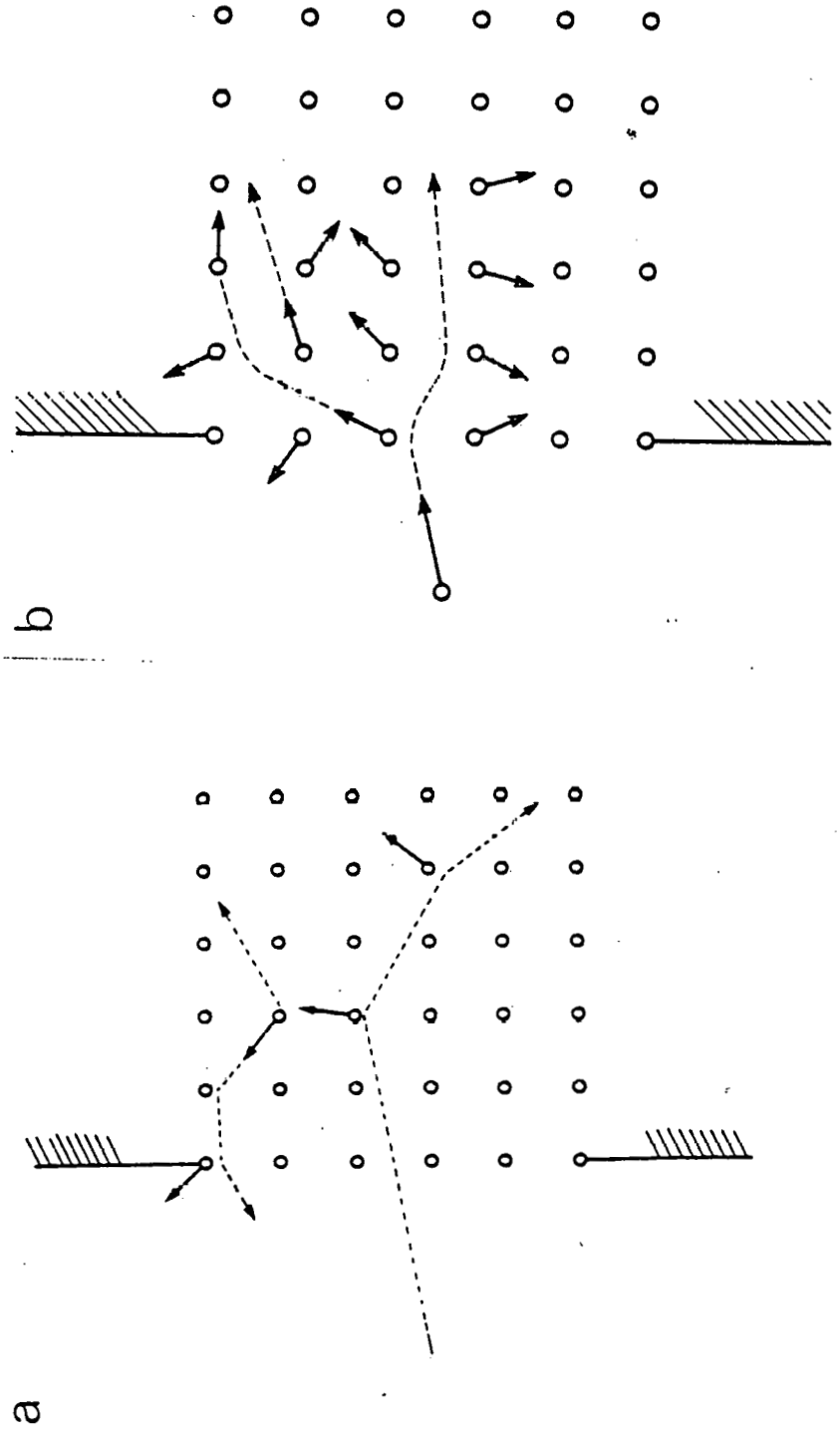

Fig. 62: (a) A linear cascade.
(b) A non-linear cascade.

collision events will prevent a strict overlap in the two cascades. Because of the small fraction of atoms moving in either case, the two cascades superimpose so that the total number of moving atoms is twice as large as in either cascade and the energy distribution is essentially unchanged. This is to say that in each energy interval there will be twice as many atoms as there was in the case of monomer irradiation. The system is linear. When two spikes are superimposed on the other hand energy will be dissipated essentially within a single spike volume, that is the total number of atoms in motion will increase only insignificantly compared to the case of monomer irradiation. Consequently, the available energy per atom must approximately double. The energy distribution will be different from that for monomer irradiation. The system is nonlinear. Since the number of vacancies produced $\langle \nu \rangle$ depends significantly on the energy distribution of the atoms, the non-linearity should reflect itself in $\langle \nu \rangle$, that is, the $\langle \nu \rangle$ for a heavy ion dimer is expected to differ from the sum of the $\langle \nu \rangle$'s of the constituents of the dimers. Moreover, as we have pointed out in previous chapters, the collapse of DZ's to loops is dependent on the deposited energy density and hence the yield may be significantly enhanced. The sputtering yield, also is very closely tied to the energy distribution of atoms and the difference between linear and nonlinear systems should reflect itself in the sputtering yields. In a linear system, one expects the sputtering yield to be proportional to the number of impinging particles regardless of their correlation in space and time. In a nonlinear system such a simple relationship is not expected. The sputtering yield of a dimer is expected to differ from the sum of the sputtering yields of the constituents of the dimer. An illustration of

these features was observed by Anderson and Bay[2]; they compared the sputtering yields due to molecular ion bombardment with those for atomic ions at the same velocity. Approximate linearity was observed for light-ion bombardment while a drastic enhancement was observed for heavy-ion bombardment.

We have attempted to detect the effects of nonlinearity on the nature of the damage produced in tungsten by comparing the damage produced by heavy-ion dimers with that produced by atomic ions having the same velocity. FIM specimens were bombarded with 40 keV Ag_2^+ and W_2^+ dimers and the results compared with those from the bombardment with 20 keV Ag^+ and W^+ ions. The nature of the DZ's produced by 20 keV Ag^+,W^+ ions were not very different and we therefore consider the results for Ag and W together.

V.1 Depleted zones

V.1.1 20 keV ion irradiations

The details of the 20 keV W^+ ion irradiations have been given in Chap. IV. Three tungsten specimens were irradiated with 20 keV Ag^+ ions and three DZ's were analyzed in detail. A vacancy count was done for another DZ which was not completely analyzed. Figure 58 exhibits the standard stereographic projections that show the top view of each specimen. The plane (or planes) in which a DZ was detected is indicated. The cross-sectional side views of the specimens are also shown. The vacancy count and vacancy concentrations for the DZ's are given in Table 5.1 and the range, maximum and minimum dimensions and average dimensions in Table 5.2.

We obtained $\langle \nu \rangle_{TRIM} = 143 \pm 12$. The number of vacancies observed in the experimental DZ's was much greater than this and in the case of DWA5a it was significantly larger. The discrepancy is commented on later in the

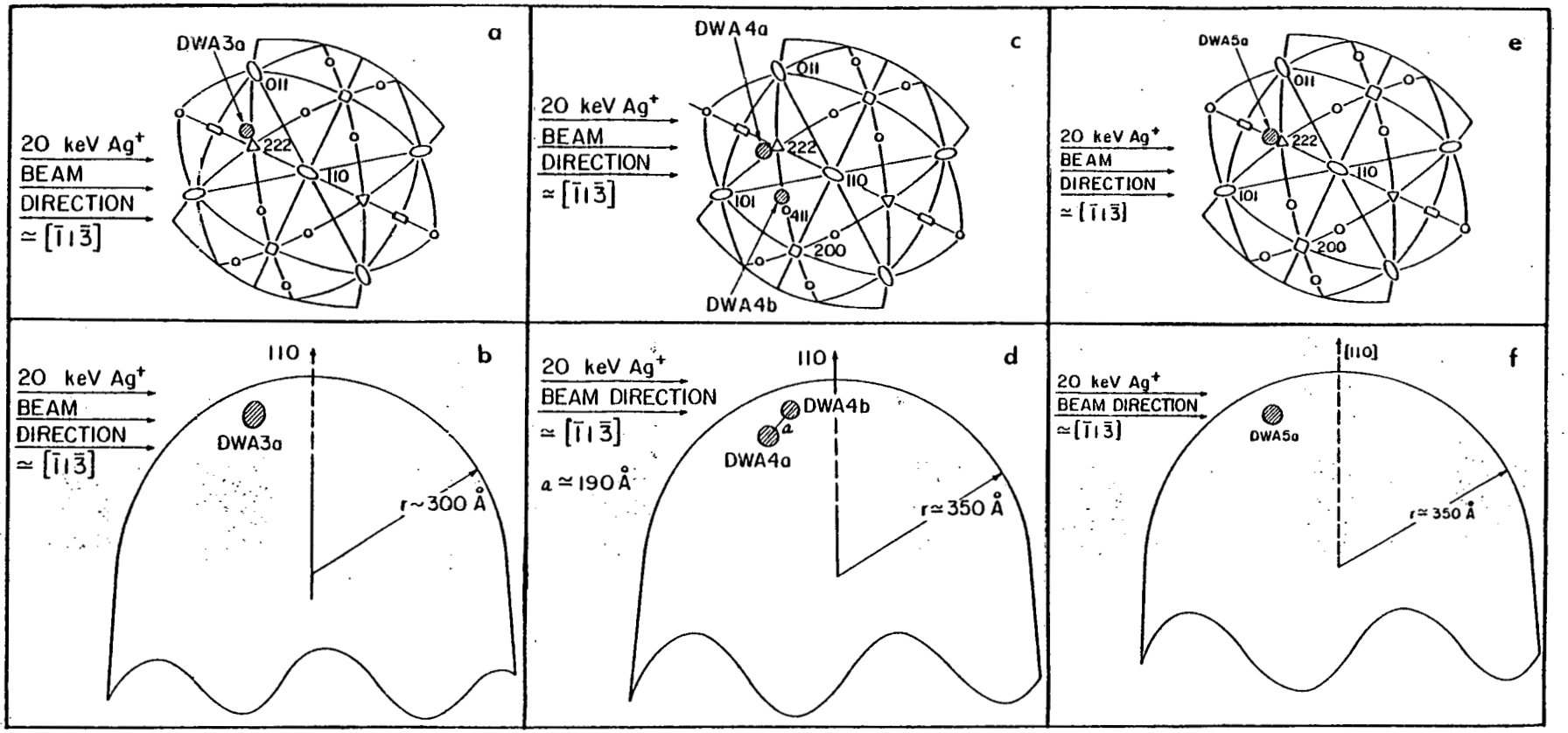

Fig. 63: (a), (c) and (e) are partial 110 stereographic projections showing location of depleted zones produced by 20 keV Ag^+ irradiation of tungsten.
(b), (d) and (f) show schematic cross-sectional views of the FIM tip specimens.

TABLE 5.1

Number of vacancies and vacancy concentration of DZ's produced by 20 keV Ag^+ on W

DEPLETED ZONE	NO. OF VACANCIES ν	VACANCY CONCENTRATION (c_v) at %
DWA3a	269	10.8
DWA4a	155	4.9
DWA4b*	≈150	---
DWA5a	201	12.1

*only vacancy count available.

TABLE 5.2

Range and dimensions of DZ's produced by 20 keV Ag^+ on W

DEPLETED ZONE (DZ)	RANGE (L) Å	ELONGATION DIRECTION [hkl]	DIAMETER λ_1† (Å)	DIAMETER λ_2† (Å)	MEAN DIAMETER $\langle\lambda\rangle$ (Å)
DWA3a	50	$[10\bar{1}]$	26.38	16.03	18.9
DWA4a	60	$[11\bar{1}]$	32.45	21.8	24.9
DWA5a	47	$[\bar{1}11]$	16.54	13.02	14.1

†λ_1, λ_2 are defined in the text.

chapter.

The range of the cascades were within the limits expected from the TRIM program L = (35.3 ± 14.84 Å). From Winterbon's tables L = 43 Å. The average size of the vacancy clusters on the basis of the TRIM program was $\langle\lambda\rangle$ = 31 Å. The average size of the DZ's was smaller than this value.

The radial distribution functions are plotted in fig. 64 and 65. They show a sharp single peak indicating a single cluster. Though the R(i)/Z(i) for the individual cascades fluctuated, the curve representing the average of the three cases is almost identical to the average for 30 keV Mo^+ on W. The atoms Ag and Mo have almost the same atomic number and the similarity is therefore not surprising. As mentioned before, and in [3], the average R(i)/Z(i) curves depend on M_1 but do not appear to be particularly sensitive to E_1. In fig. 66-68, we show the ORTEP visualizations of the 3 DZ's which indicate the compact nature of the DZ's.

An analysis of the degree of clustering revealed that DWA3a contained 48 monovacancies, 11 divacancies, four trivacancies, one pentavacancy, one hexavacancy, and one jumbo cluster of 176 vacancies. DWA4a had 56 monovacancies, 13 divacancies, two trivacancies, one quadravacancy, one pentavacancy, one heptavacancy, one octavacancy, one cluster of 19 and one of 24 vacancies. DWA5a has 34 monovacancies, 5 divacancies, two trivacancies, one quadravacancy, one hexavacancy and one jumbo cluster of 141 vacancies.

V.1.2 Results for 40 keV dimers

Four sets of irradiations with dimers were carried out, two each for Ag_2^+ and W_2^+. In all four DZ's were analyzed, two for Ag_2^+ and two for W_2^+. One of the DZ's for W_2^+ was a surface cascade and contained only a small number of vacancies relative to the other three. Figures 69 and 70

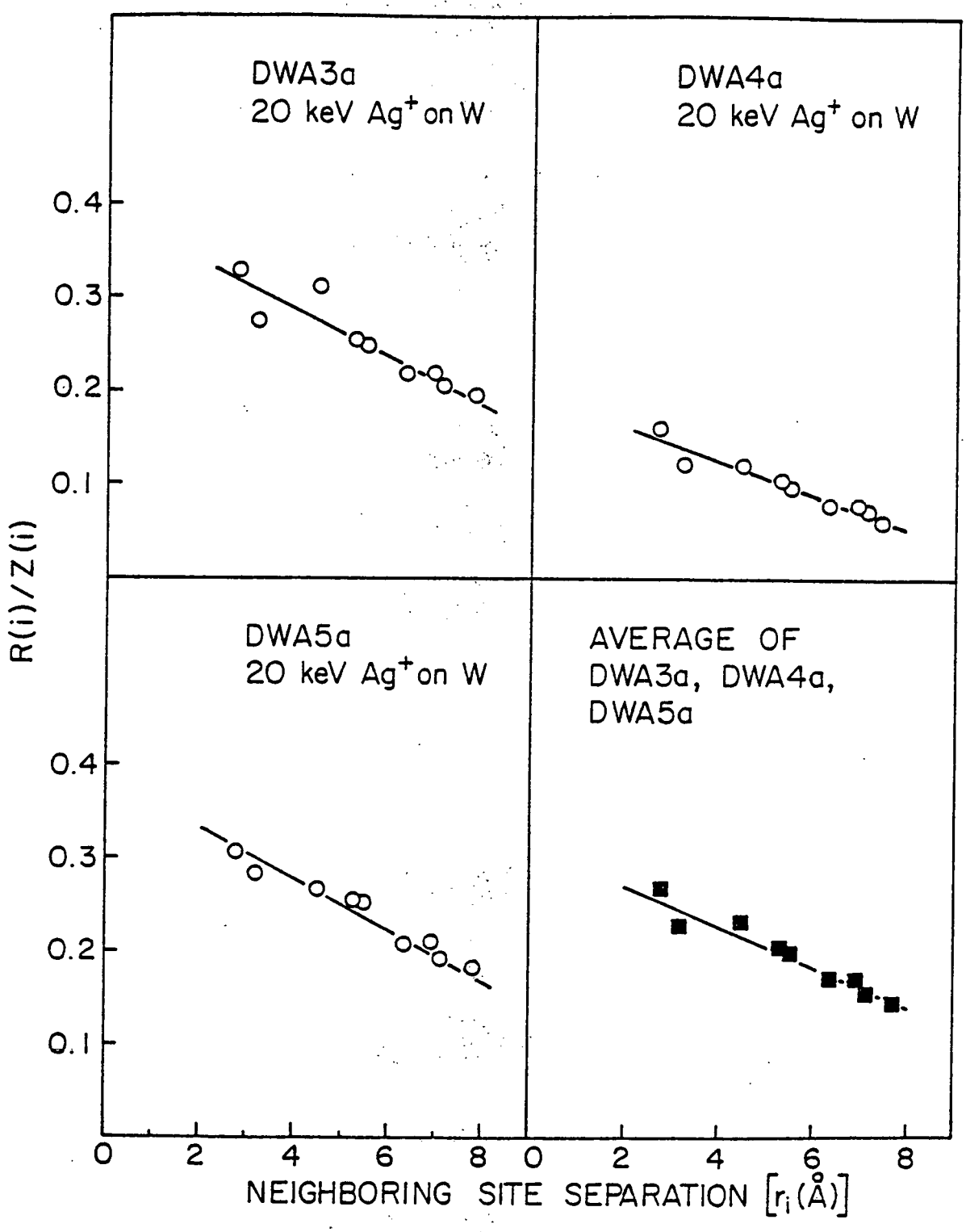

Fig. 64: The normalized radial distribution functions [R(i)/Z(i)] for depleted zones produced by 20 keV Ag^+ irradiation of tungsten.

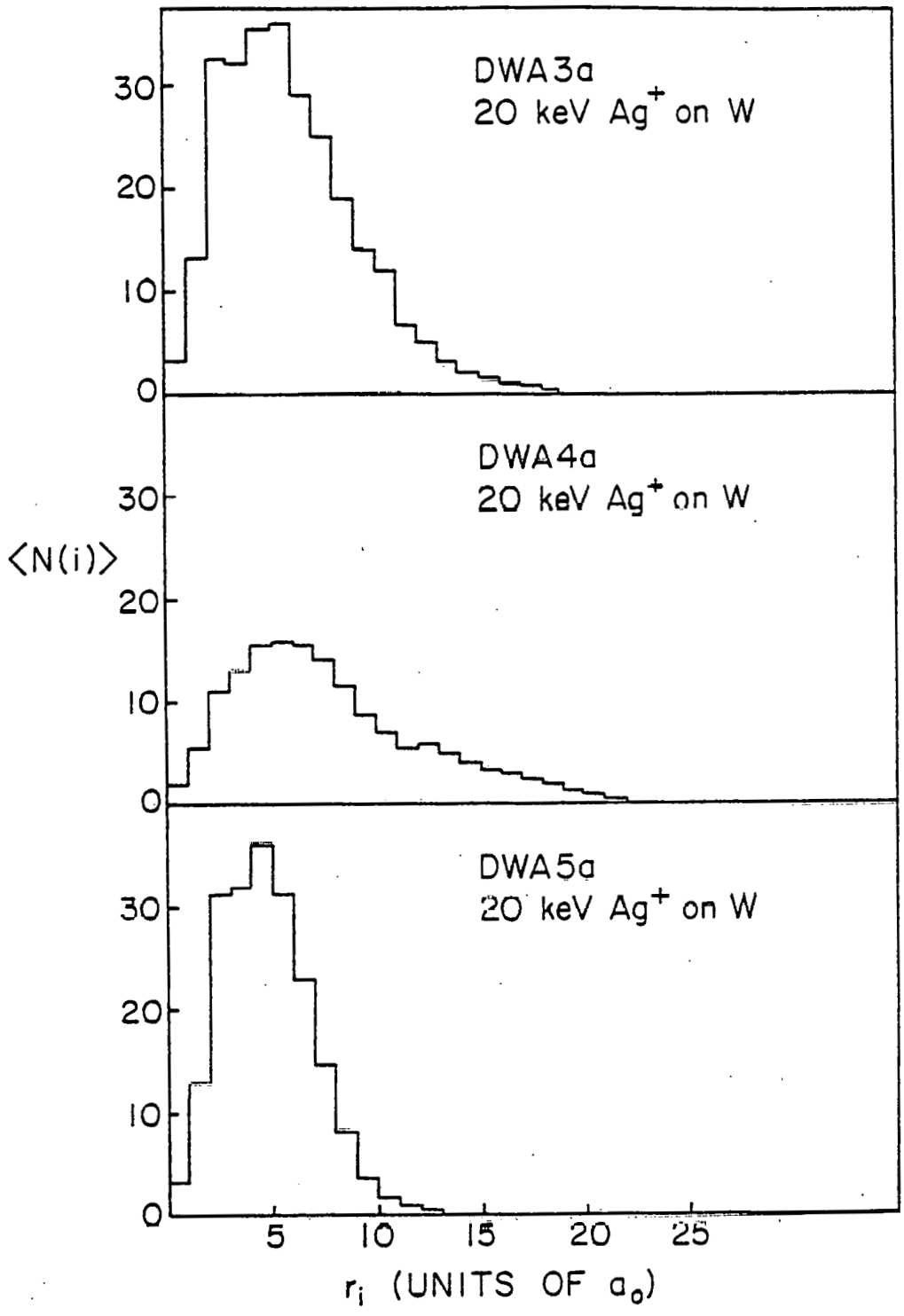

Fig. 65: The spectra of <N(i)>s for depleted zones produced by 20 keV Ag^+ irradiations of tungsten.

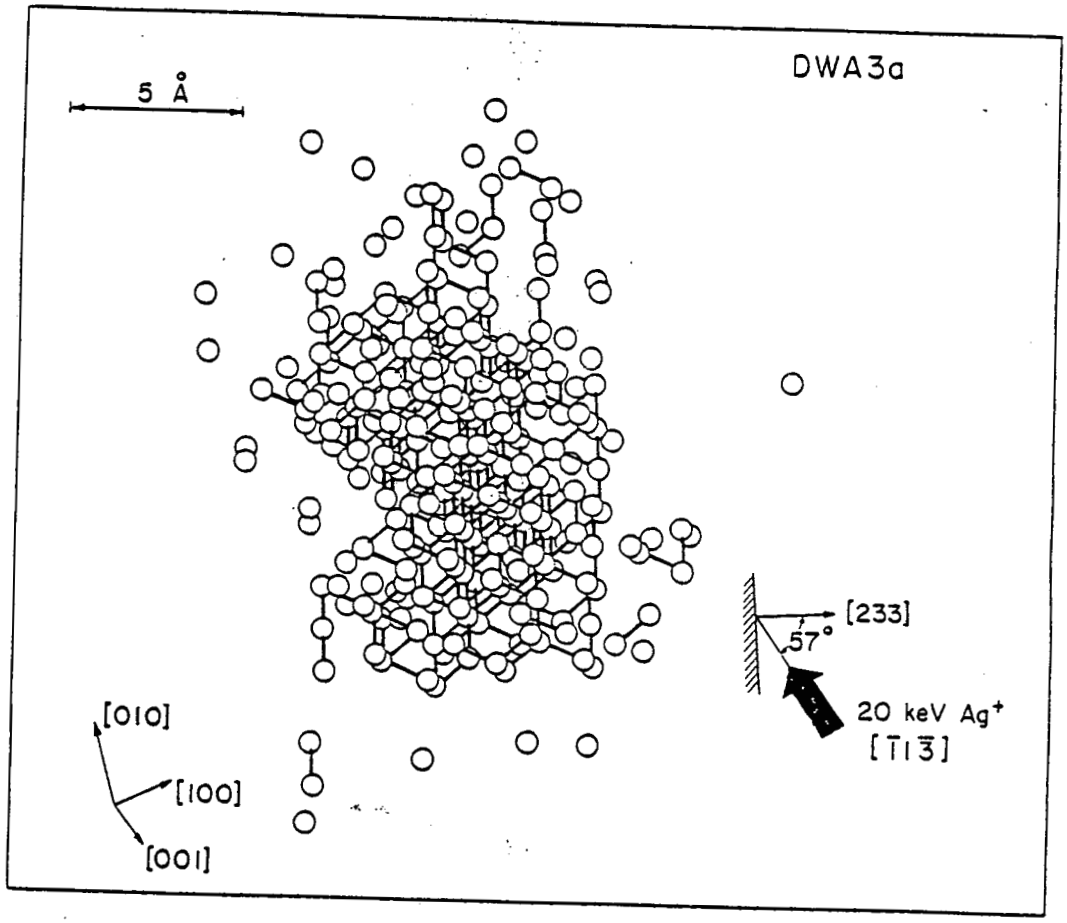

Fig. 66: An OR TEP drawing of DWA3a.

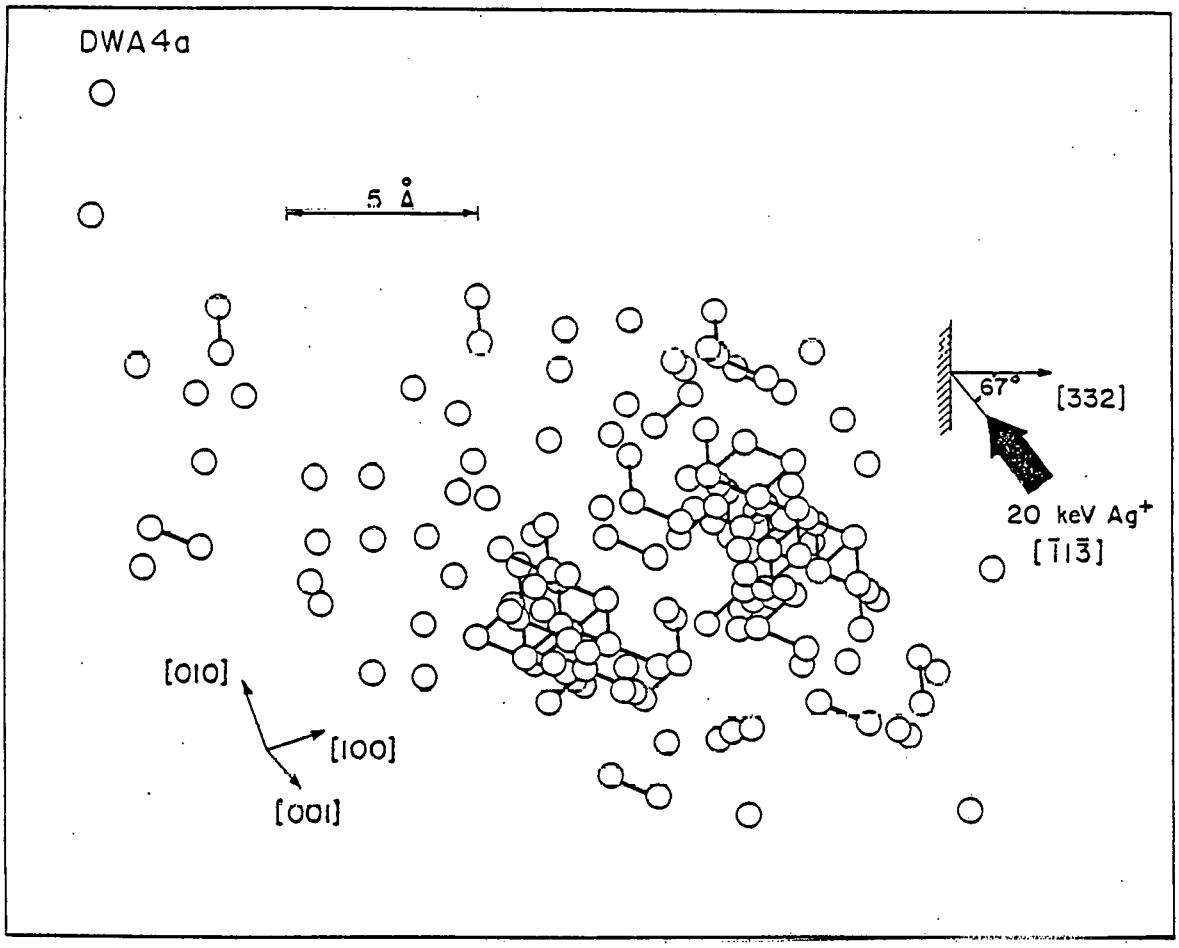

Fig. 67: An OR TEP drawing of DWA4a.

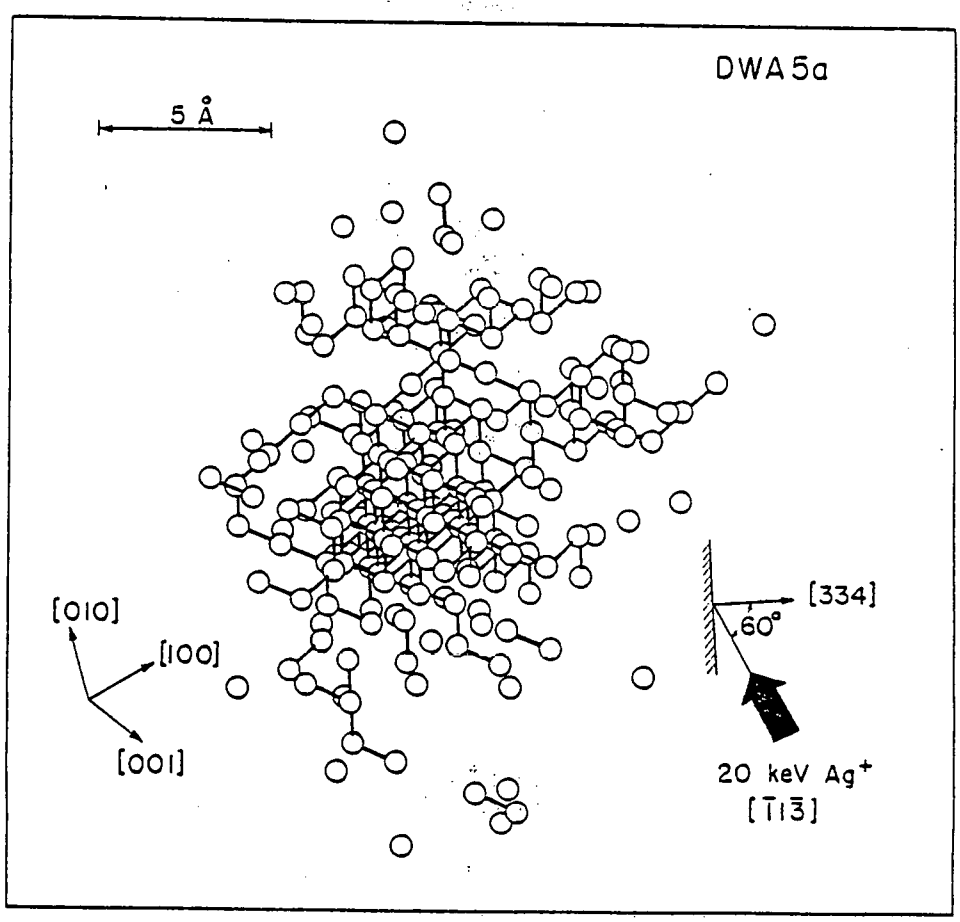

FIG. 68: An OR TEP drawing of DWA5a.

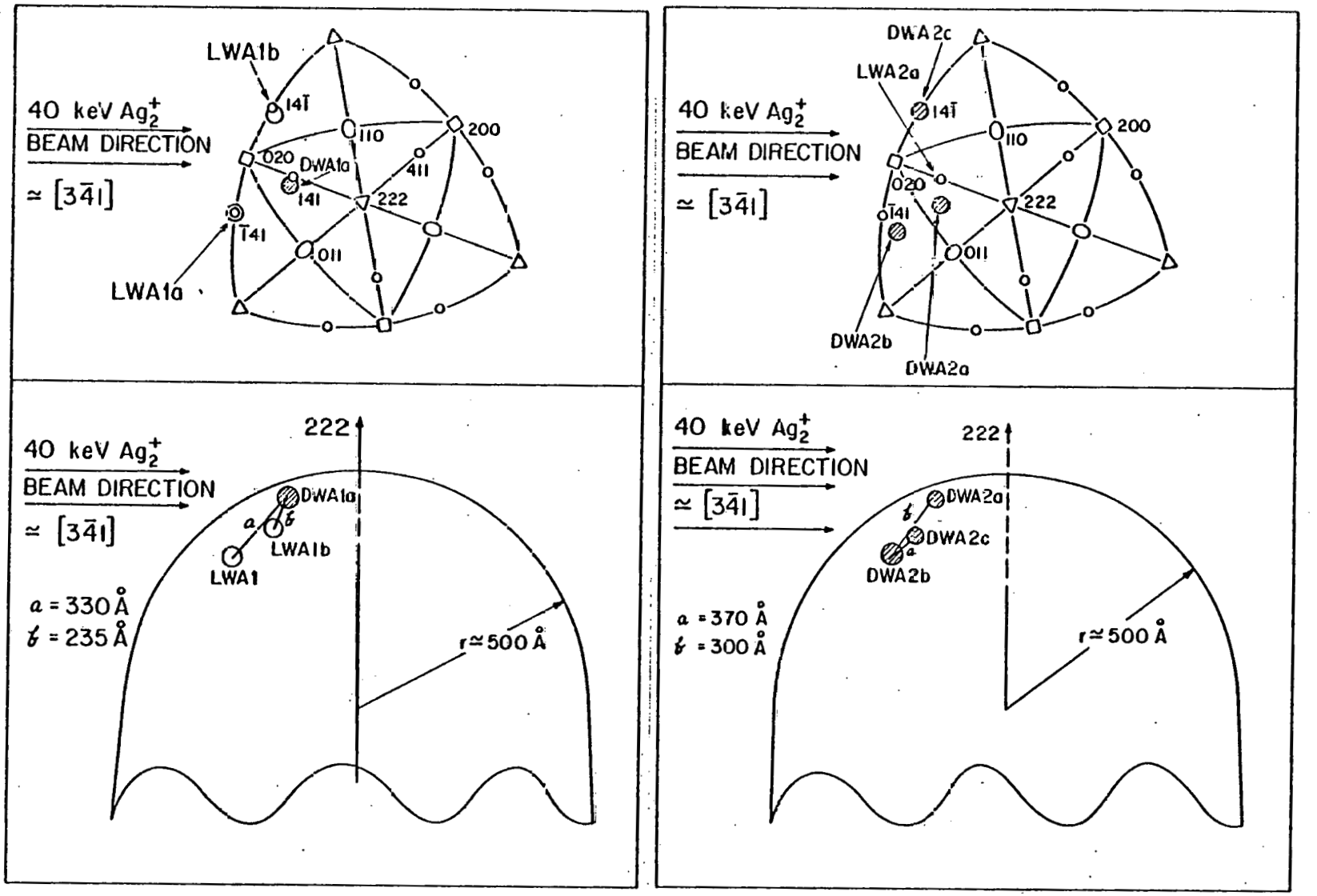

Fig. 69: (a), (b) Partial 222 stereographic projections showing location of depleted zones produced by 40 keV Ag_2^+ irradiation of tungsten.
(c), (d) Schematic cross-sectional views of the FIM tip specimen.

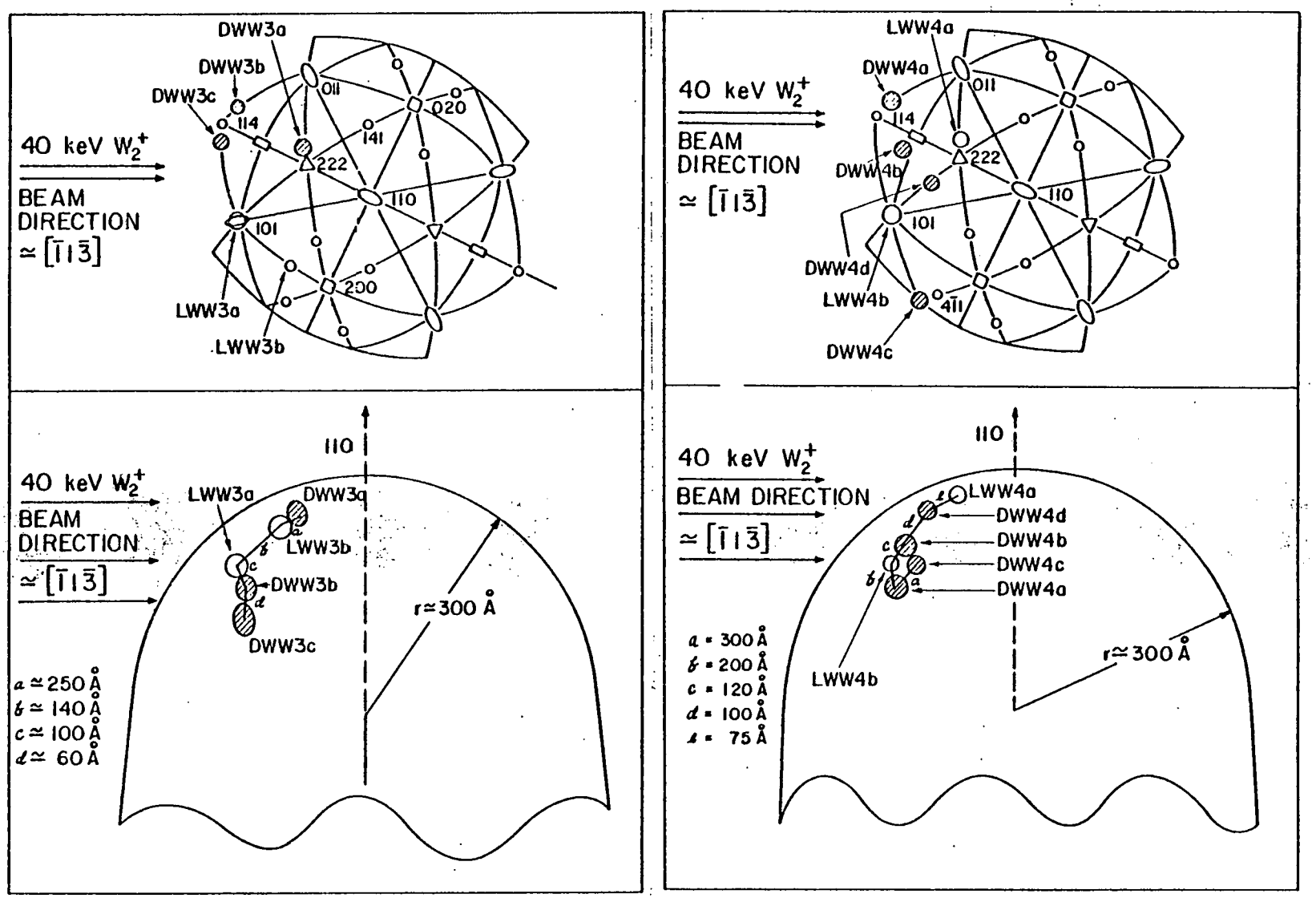

Fig. 70: (a), (b) Partial 110 stereographic projections showing location of depleted zones produced by 40 keV W_2^+ irradiations of tungsten.
(c), (d) Schematic cross-sectional views of the FIM tip specimens.

show the standard stereographic projections that show the top view of each specimen. The plane (or planes) in which a DZ was detected is indicated. We have also shown in the fig. 69 and 70 the positions of DZ's that were detected but not analyzed. The cross-sectional side views of the specimens are also shown.

The vacancy count and vacancy concentration for the DZ's are given in Table 5.3 and the range, maximum and minimum dimensions and average dimensions are given in Table 5.4.

The radial distribution functions <N(i)> and R(i)/Z(i) are plotted in figs. 71 and 72. The <N(i)> for DWW3a and DWW4a indicate a single cluster for these DZ's while that for DWA1a indicates the presence of two clusters, and that for DWA2a indicates that the DZ is somewhat diffuse. These features are also reflected in the R(i)/Z(i) graphs. The W_2^+ DZ's formed far tighter clusters than the Ag_2^+ DZ's. The ORTEP visualization of the DZ's shown in figs. 73 to 76 confirm the above conclusions.

An analysis of the degree of clustering revealed the following:

DWA1a has 155 monovacancies, 12 divacancies, four trivacancies, three quadravacancies, three pentavacancies, two clusters of 9, one cluster of 110 and one cluster of 329. DWA2a has 111 monovacancies, 23 divacancies, four trivacancies, four quadravacancies, one pentavacancy, two hexavacancy, two heptavacancies, one octavacancy, one cluster of 15, one cluster of 19, one cluster of 43, one cluster of 64, one cluster of 80.

DWA4a has 54 monovacancies, 17 divacancies, one trivacancy, two quadravacancies, three pentavacancies, one hexavacancy, one cluster of nine, one cluster of 36 and one jumbo cluster of 428.

DWA3a has 19 monovacancies, one trivacancy, one pentavacancy, and one

TABLE 5.3

Number of vacancies and vacancy concentration in DZ's produced in dimer irradiations of W

DEPLETED ZONES (DZ)	NUMBER OF VACANCIES ν	VACANCY CONCENTRATION (c_v) at %
DWA1a	675	9
DWA2a	446	7.3
DWA2b*	≈650	---
DWW3a†	190	12.2
DWW4a	593	8.13

* Vacancy count only available.

† Surface cascade.

TABLE 5.4

Range and dimensions of DZ's produced by dimer irradiations of W

DEPLETED ZONES (DZ)	RANGE (L) Å	ELONGATION DIRECTION [hkl]	DIAMETER λ_1 (Å)	DIAMETER λ_2 (Å)	MEAN DIAMETER $\langle\lambda\rangle$ (Å)
DWA1a	30	$[1\bar{1}1]$	44.52	27.7	32.4
DWA2a	36	[100]	31.3	24.28	26.4
DWW3a	5	$[10\bar{1}]$	25.3	15.8	18.48
DWW4a	25	$[1\bar{1}0]$	33.08	24.06	26.76

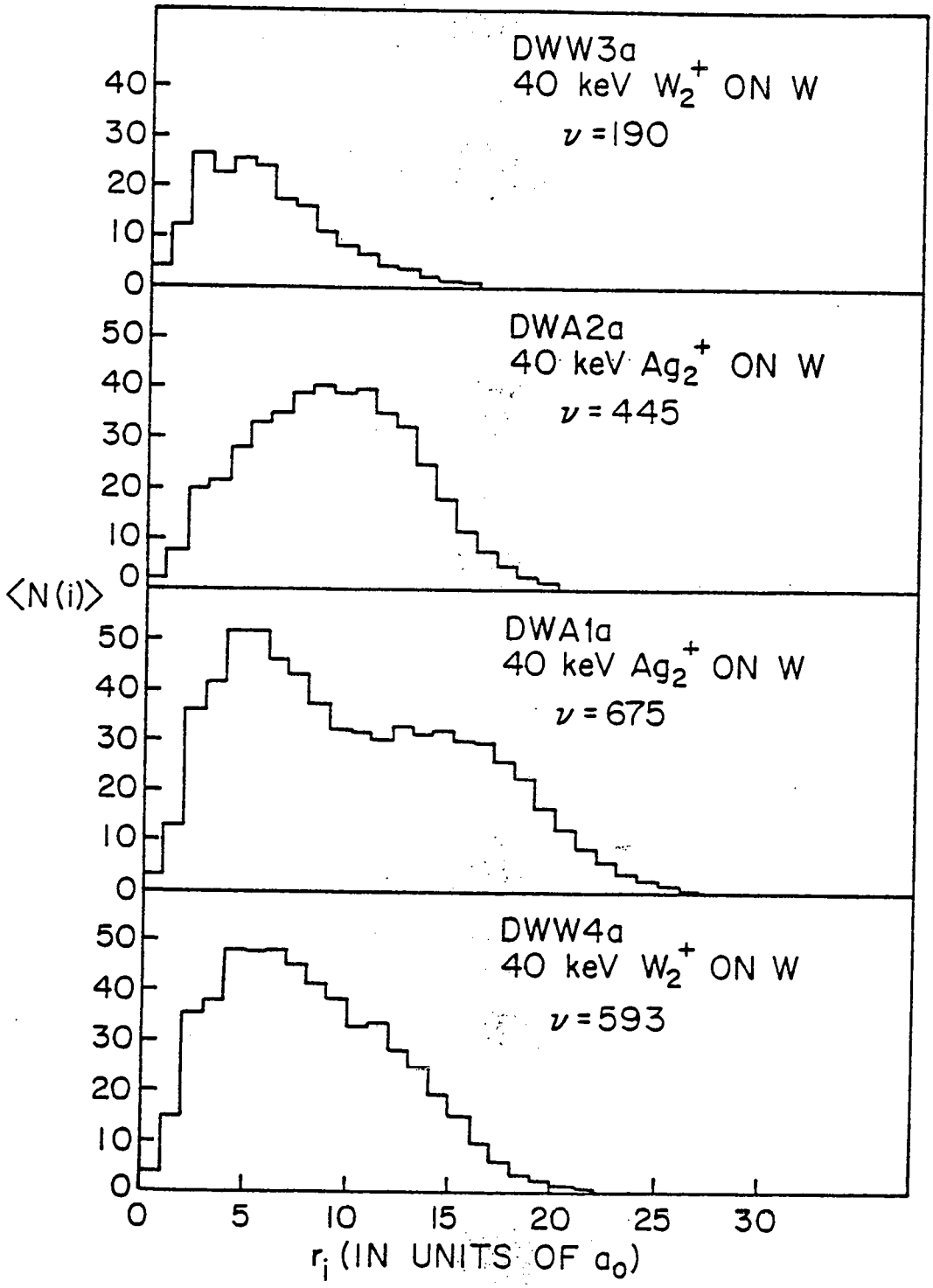

Fig. 71: The spectra of <N(i)>s for depleted zones produced by 40 keV Ag_2^+ and W_2^+ irradiations of tungsten.

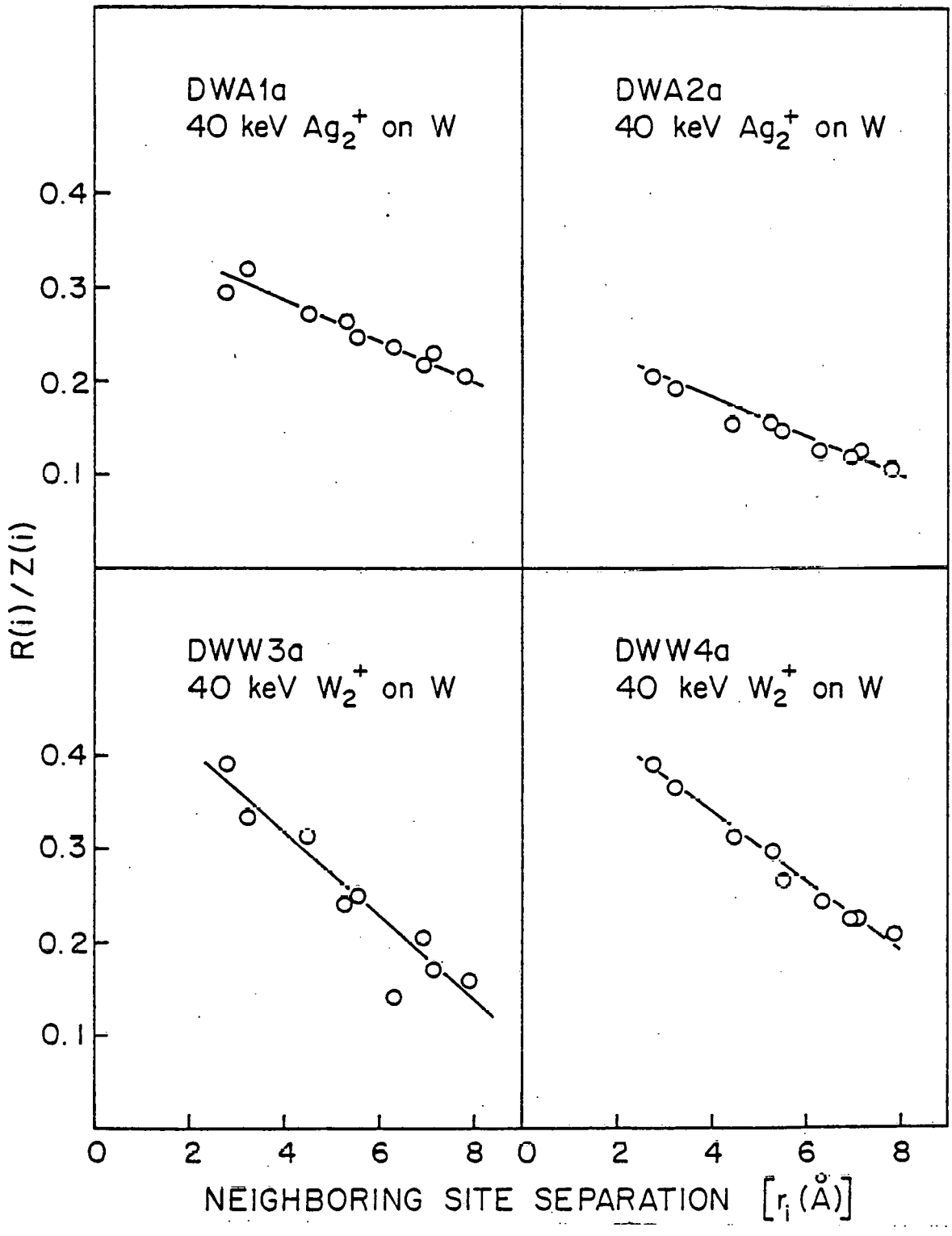

Fig. 72: The normalized radial distribution functions R(i)/Z(i) for depleted zones produced by 40 keV Ag_2^+ and W_2^+ irradiations of tungsten.

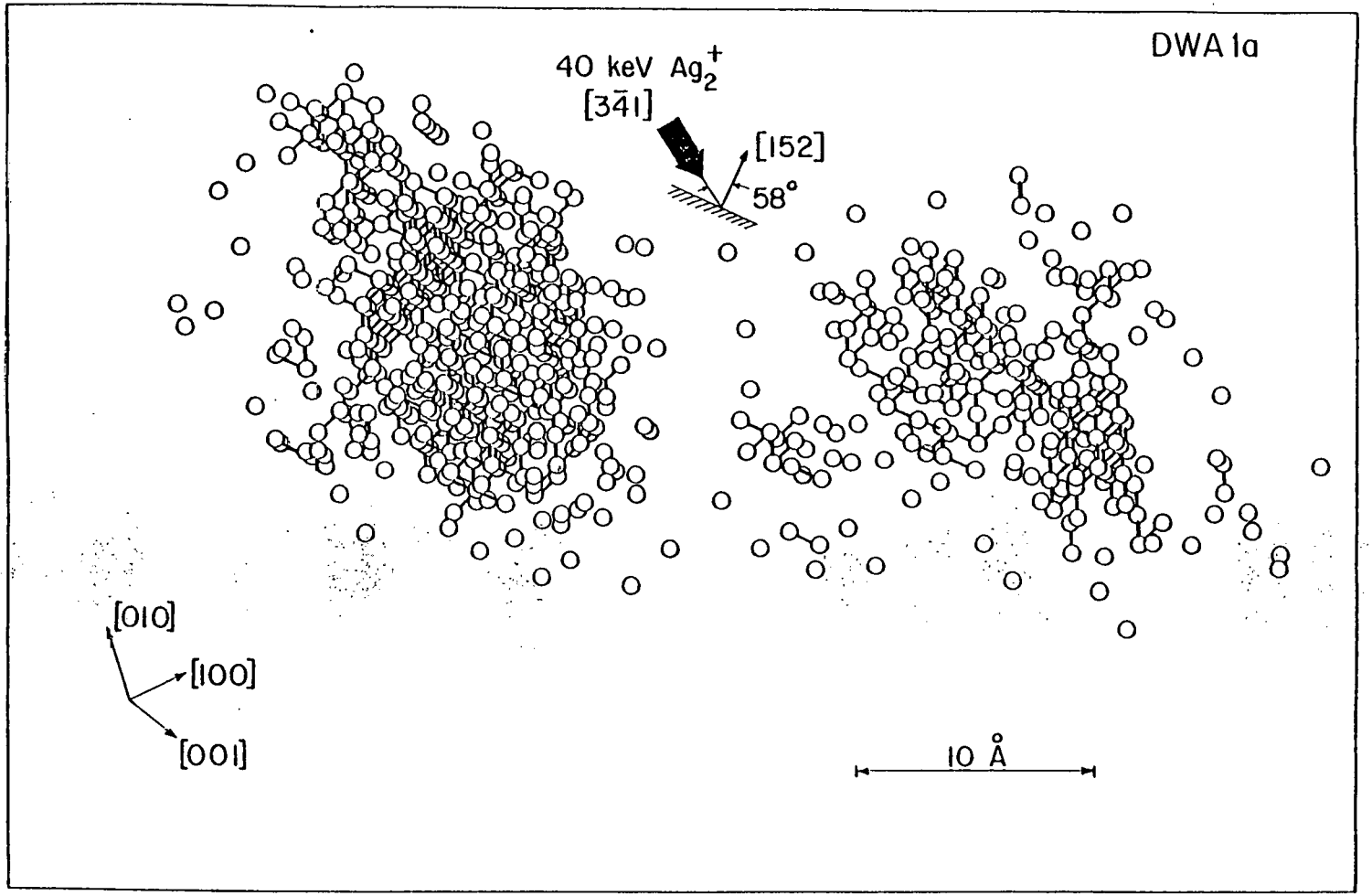

Fig. 73: An OR TEP drawing of depleted zone DWA1a.

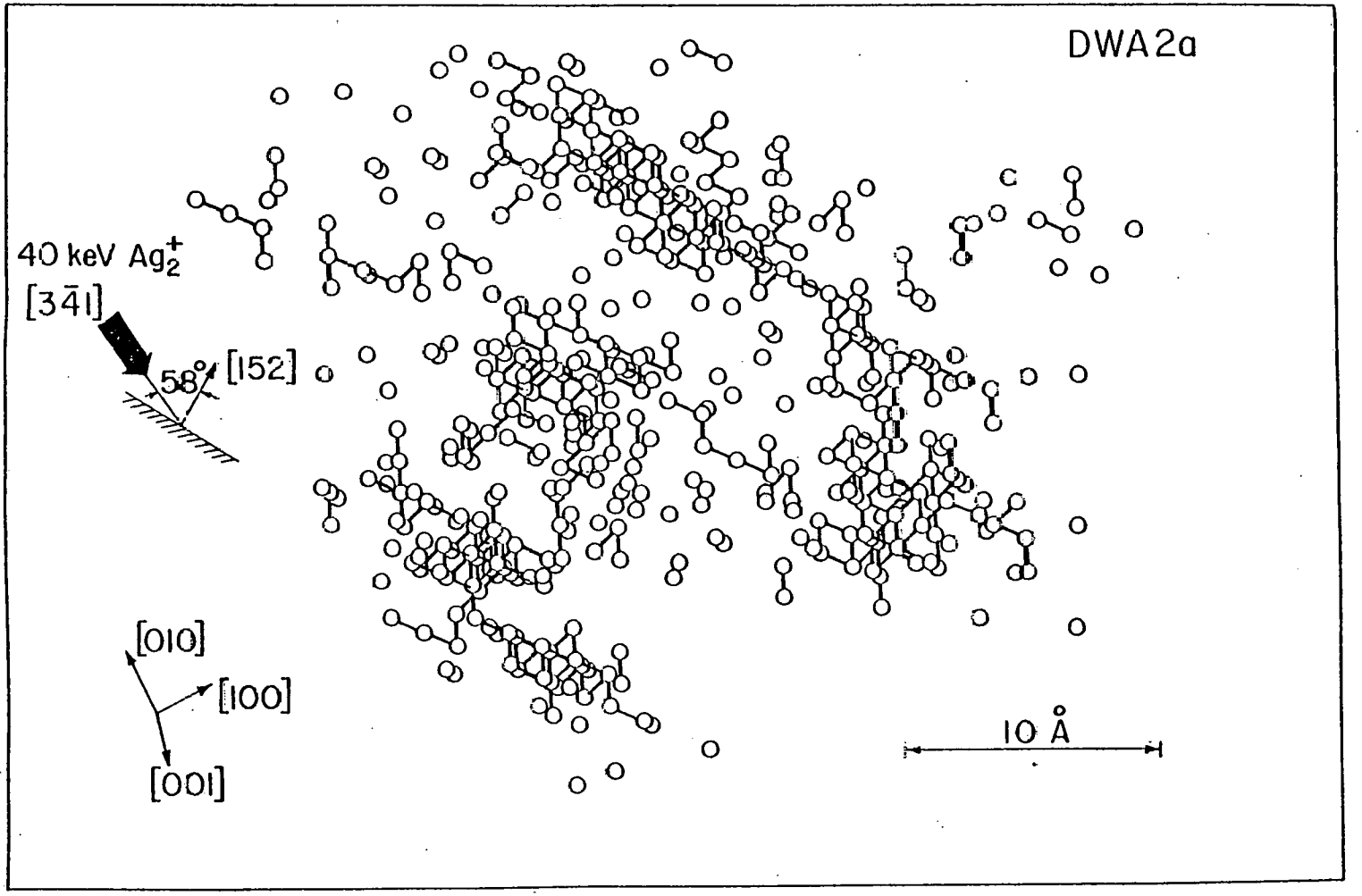

Fig. 74: An OR TEP drawing of depleted zone DWA2a.

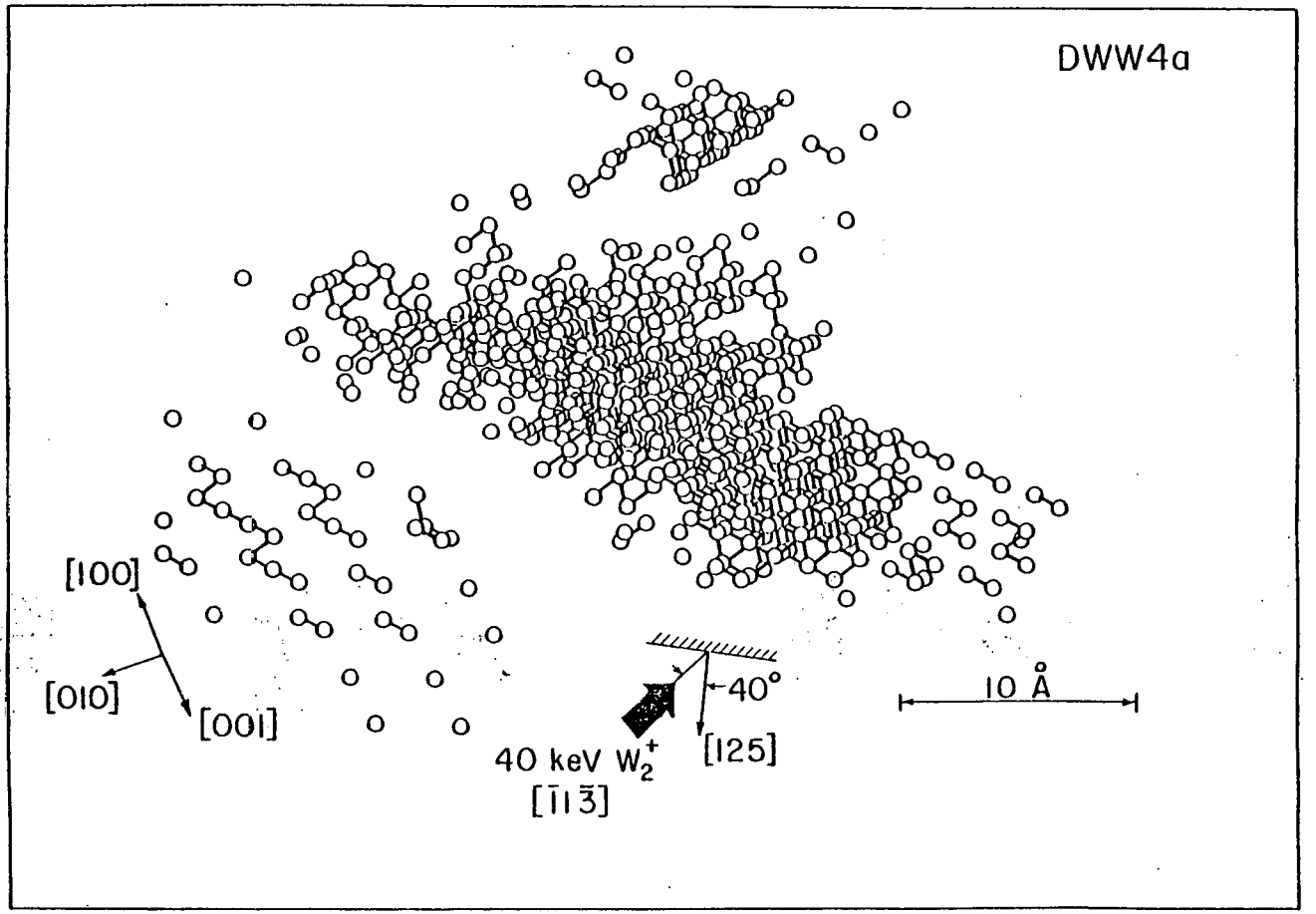

Fig. 75: An OR TEP drawing of depleted zone DWA4a.

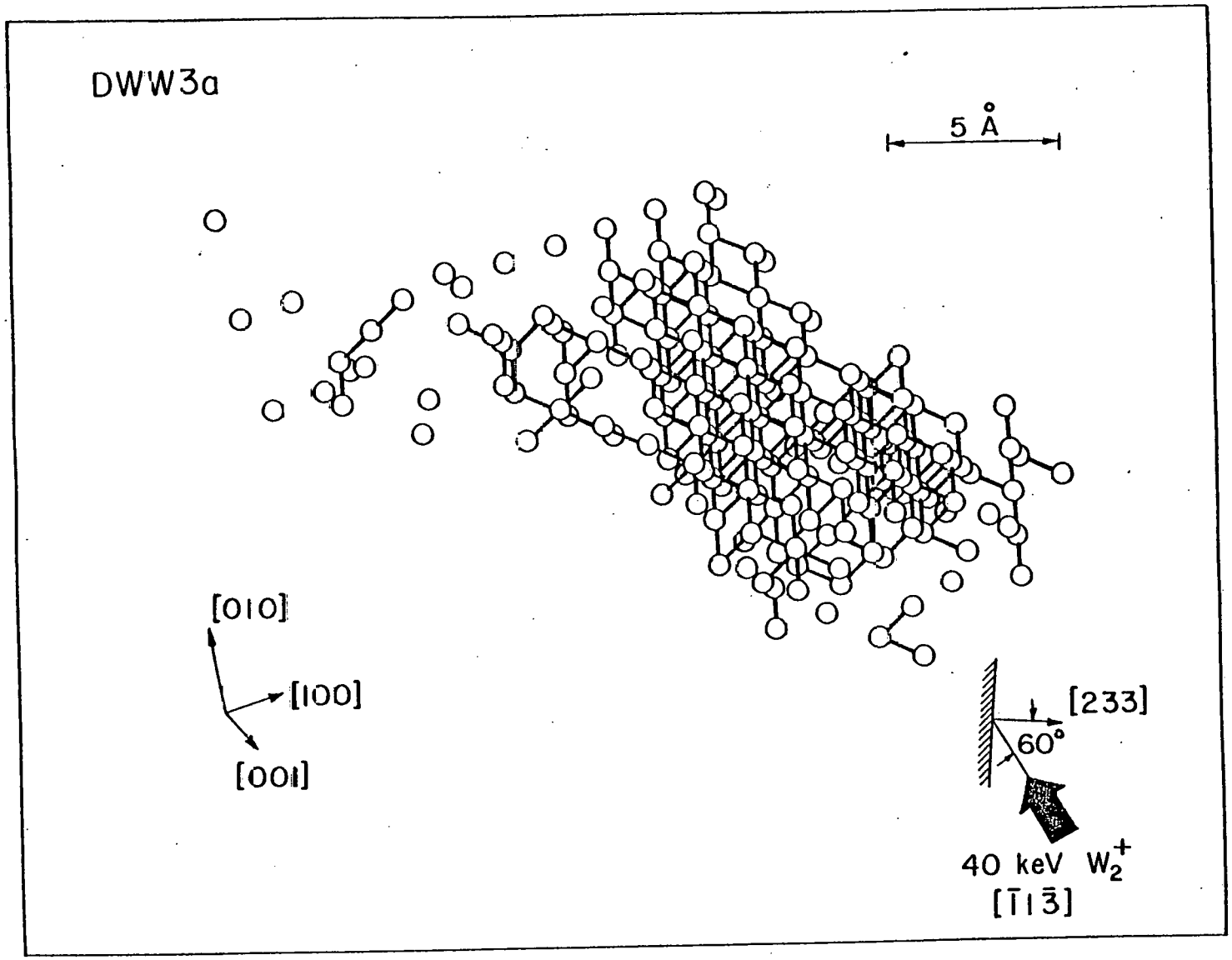

Fig. 76: An OR TEP drawing of depleted zone DWW3a.

jumbo cluster of 163. It is clear that in the W_2 irradiations the majority of the vacancies were formed in a single big cluster.

V.1.3 Comparison of monomer and dimer irradiations

Spike effects should be pronounced for heavy ions on heavy targets at not too high ion energies. One criterion of whether an ion will produce a spike or not is given by the quantity θ_0, the effective maximum energy density.[4] For 20 keV Ag^+ on W, $\theta_0 \simeq 7.5$ eV/atom and for 20 keV W^+, $\theta_0 \simeq 15$ eV/atom. The sublimation energy of W is 8.7 eV so that we can expect the spike effect from Ag^+ and W^+ to be quite pronounced.

In the case of 20 keV heavy ions (Ag^+ and W^+) irradiation of W, $\langle\nu\rangle = 190$ for seven DZ's (four Ag^+ and three W^+). This is somewhat greater than the expected value of $\langle\nu\rangle = 145$ obtained from TRIM program or from the modified Kinchin-Pease theory using a single threshold value of 43 eV. The fluctuations were also very large with a count of 269 vacancies being made for one of the DZ's--this value is even greater than the unmodified Kinchin-Pease estimate. If this DZ is left out then $\langle\nu\rangle$ falls to 177 for the six remaining DZ's.

The possibility of very large number of vacancies is due to the spike-like nature of the cascade. As a consequence of this, statistical fluctuations may lead to much higher energy densities in some individual cascades than in others. The high energy density would lead to an energy distribution that is different from that calculated assuming simple binary collisions, or to various physical processes, such as the lowering of the threshold energies within the volume of the cascade. Both of these would lead to an enhancement of point defect production. A point to note is that the spike-like nature may appear only in very few individual cascades

and an average over a large number of cascades may not necessarily exhibit this behavior.

Excluding DWW3a, which was a surface cascade--and therefore not fully developed--the average number of vacancies for the DZ's detected in the dimer irradiations were $\langle\nu\rangle = 590$. This is far greater than twice the $\langle\nu\rangle$ for the monomers and clearly indicates nonlinearities in the defect production rate. If $\langle\nu\rangle_{dimer}$ is the number of defects produced per incoming ion for the dimer then

$$\frac{(\langle\nu\rangle)_{dimer}}{(\langle\nu\rangle)_{monomer}} = \frac{295}{190}$$

$$= 1.55$$

It is instructive to compare these results with the ratio of sputtering yields of monomers to dimers. The sputtering yield δ and the damage level $\langle\nu\rangle$ are connected to the same physical process, namely the dissipation of energy of an incident projectile ion in a cascade. The sputtered atoms come from cascades close to the surface. As the properties of the cascades are independent of the depth at which they are produced, various properties of the sputtered atoms should reflect what is occurring inside the cascade. Since only those atoms that possess energy greater than the sublimation energy V (within a distance $\delta \sim$ <5 Å - from the surface) are finally sputtered, it is clear that the energy distribution inside the cascade will critically affect the sputtering yield. The same is true for the damage level according to the simple threshold model, where all the atoms having energy greater than the threshold energy E_d are displaced. Thus spike effects that are observable as nonlinearities in S should also be observable as nonlinearities in the damage level.

Andersen and Bay[2] measured the dimer to monomer yield ratios for Se and Te irradiations, where the atomic and molecular ions had the same velocity for each species. The collision cascades produced by Te on Au should be very similar to that of Ag on W. Andersen and Bay measured a dimer to monomer yield ratio of ≈2.2, showing very strong nonlinearity. Our damage levels for Ag and W monomer and dimer irradiations also show strong non-linearities.

The extent to which the cascades caused by the individual atoms of the dimer superimpose should be given by a comparison of the average dimensions of the 20 keV monomers and that of the dimers. The value of $\langle\lambda\rangle$ for the six fully developed cascades due to 20 keV monomers (Ag and W) is 17.5 Å. That for three fully developed cascades due to the 40 keV dimers is 28.5 Å. The cascades due to the dimers are much larger than that due to the single atoms, but not twice as large, indicating that the cascades overlap to some extent. However, the degree of overlap is most likely to be a very strongly fluctuating quantity.

The average concentration of vacancies c_v is much less for the dimer DZ's than it is for the monomer DZ's. However, the c_v's that are calculated are not representative of the local concentrations in different regions of the cascades, which can fluctuate considerably. This is clear from an examination of the ORTEP visualizations. The formation of large clusters in DWA1a and DWW4a indicates very high vacancy concentrations in certain regions of the DZ's and these may be the regions in which the cascades due to the individual atoms of the dimers overlapped.

In fig. 77, we have plotted $\langle R(i)/Z(i)\rangle$ for the dimers and monomers, separately for the case of Ag and W. The curve for 20 keV Ag^+ on W. Now

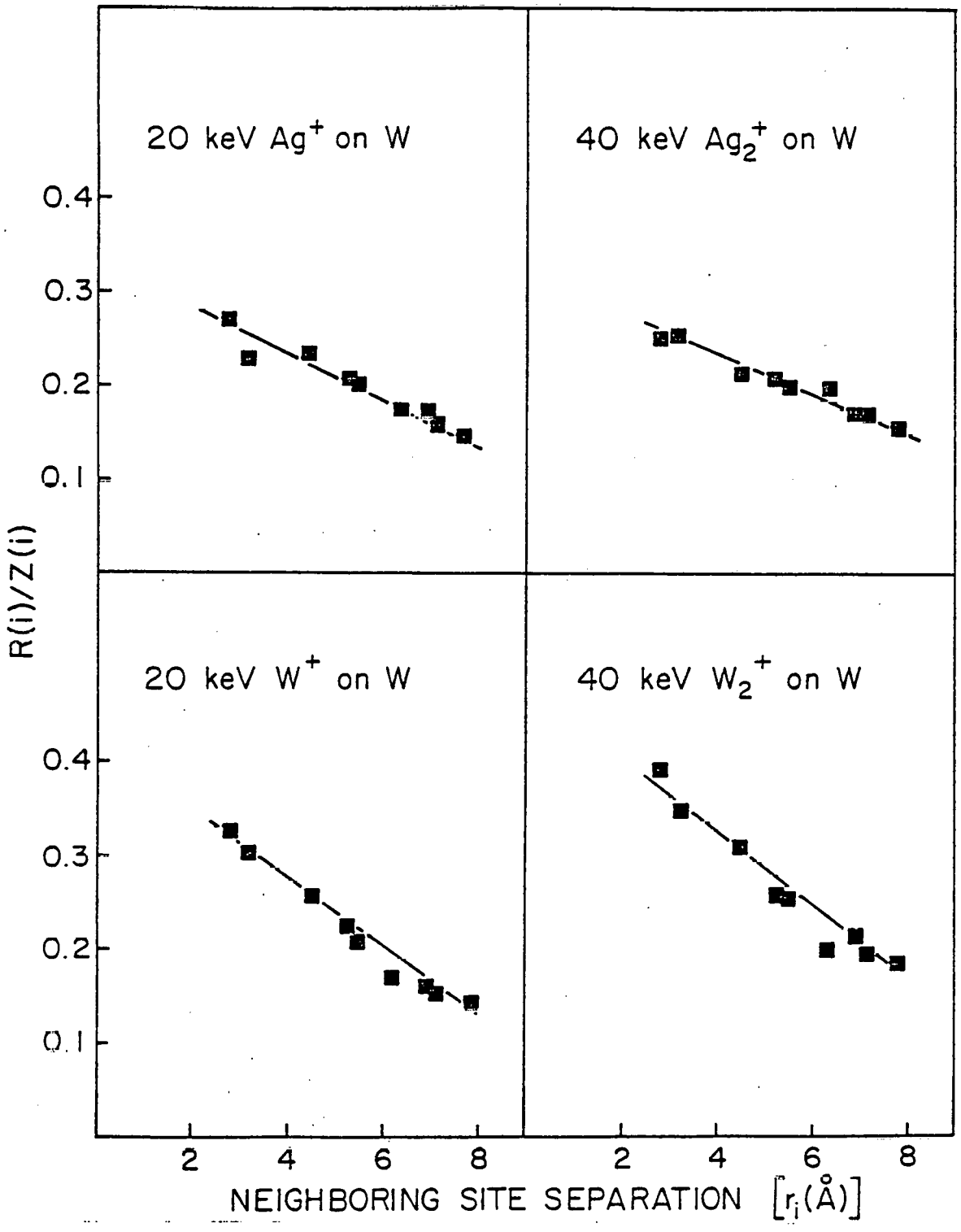

Fig. 77: A comparison of the normalized radial distribution functions [R(i)/Z(i)] for depleted zones produced by dimer and monomer irradiations of tungsten.

$\langle R(i)/Z(i) \rangle$ measures the average local environment around the vacancies in a DZ. When an average is taken over several DZ's, the averages should represent the local environment around vacancies for the cumulative damage distribution, that is, it should give an idea of the nature of the vacancy distribution when a beam of ions is impinging on the target. It was pointed out earlier that, although the deposited energy should be the same for dimers and two monomers the damage level should be higher in the first case due to nonlinear effects. As a consequence, we would expect that R(i)/Z(i) should be higher in the case of dimers. The fact that this was not the case for our Ag^+ results appeared to be the result of the small number of DZ's examined which may not have been enough to predict the general trend. The degree to which the cascades due to the atoms of the dimers may overlap is also subject to statistical fluctuations and this would affect the degree of non-linearity. For example, in the two experimental Ag_2^+ DZ's the difference in ν is very large. It was clear that in one of the DZ's with the large ν there were very large clusters indicating a high degree of overlap while in the other for which ν was not so large, the DZ was diffuse indicating possibly that there was little overlap of the individual cascades.

In the case of the W_2^+ irradiations the average R(i)/Z(i) was much greater than the W^+ irradiations but in light of the above comments no definite conclusions could be reached.

In table 5.5, we have summarized the data on clustering of vacancies into nearest neighbor clusters of size n, for the DZ's that are produced by both Ag and W monomers, and by Ag and W dimers. The fraction of vacancies in the form of monovacancies, for the case of Ag is 0.22 and the

TABLE 5.5

Fraction of vacancies in first-nearest neighbor clusters of size n for monomer and dimer irradiations of tungsten

$f = \frac{nN_n}{\nu}$ \ n	1	2	3	4	≥5
Ag	0.22	0.09	0.04	0.001	0.63
Ag_2	0.237	0.06	0.02	0.025	0.65
W	0.12	0.023	0.019	0.019	0.81
W_2	0.09	0.04	0.00	0.00	0.84
Mo	0.2	0.07	0.035	0.00	0.68

fraction in the form of clusters having five or greater number of vacancies is 0.63. The corresponding fractions for Ag_2 are 0.24 and 0.65, which is virtually identical to that for Ag. Comparison of the data for W and W_2 in table 5.5 reveals that the degree of clustering was again identical, for W and W_2. The results indicated that the degree of clustering of the vacancies was unchanged by irradiating with dimers instead of monomers, though it was sensitive to the M_2. The fraction of vacancies in the form of large clusters (≥ 5) increased with M_2, while the fraction of monovacancies correspondingly decreased. The dependence of the degree of clustering on M_2 was further emphasized on comparison of data for Ag and Mo irradiations of tungsten. The degree of clustering was almost identical, which was to be expected since M is almost equal for the two elements.

V.2 Dislocation loops

No dislocation loops were detected in the case of 20 keV Ag or W irradiation of tungsten. Several examples of dislocation loop contrast were obtained in the case of dimer irradiations. The analysis of a few of them is given below.

V.2.1 Results

The 3 examples given below are from 40 keV Ag_2 irradiation of tungsten.

The first example is of a dislocation loop appearing on a (141) plane. The pulse-field evaporation sequence is shown in fig. 78a. Frame 1 shows the contrast when the effect of the loop is not yet very evident. The break in the second ring indicated with a vee indicates that the loop is about to appear. The subsequent frames clearly show a single spiral. The

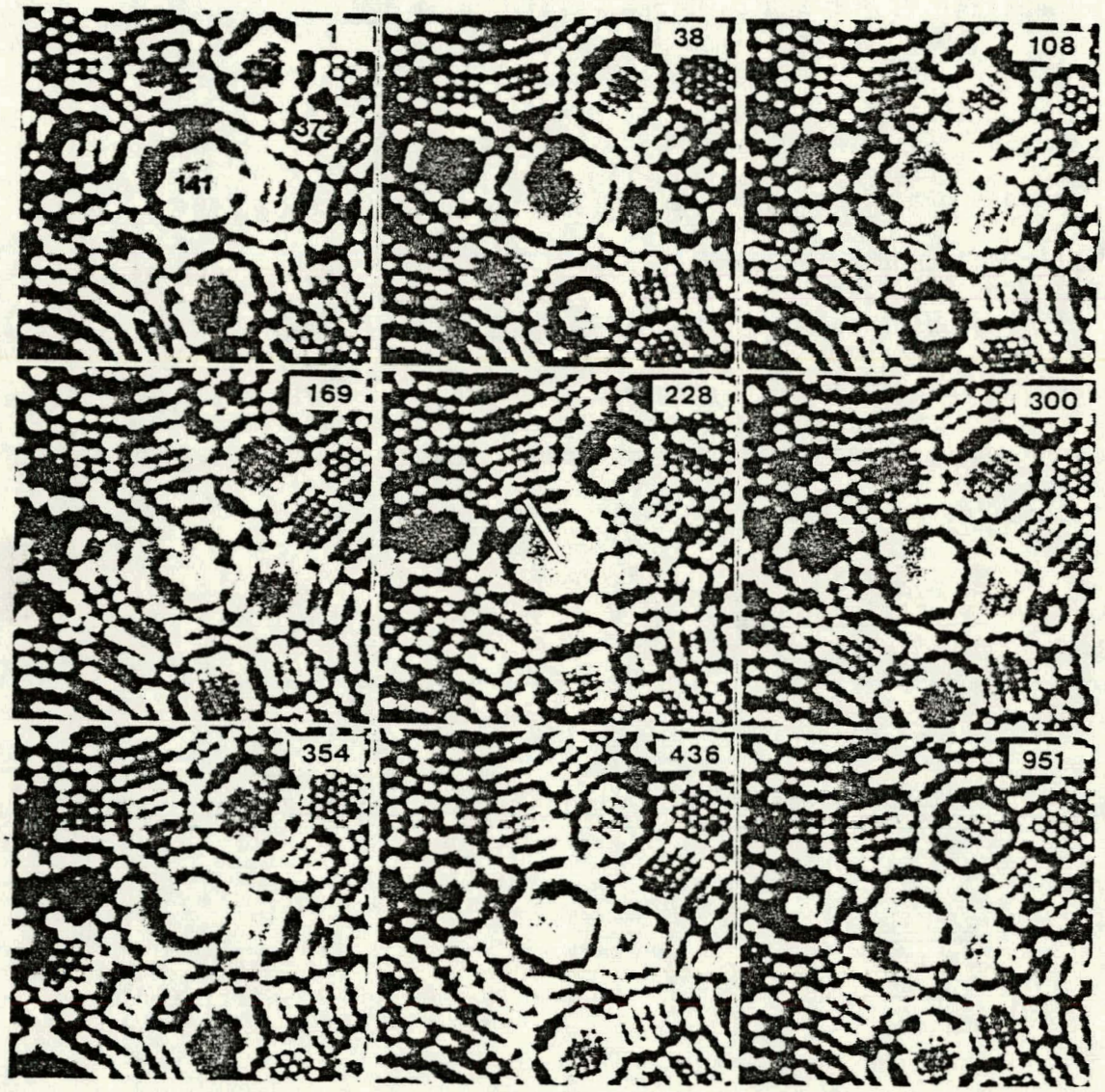

Fig. 78(a): Pulse-field evaporation sequence showing contrast due to dislocation loop emerging on the (141) plane.

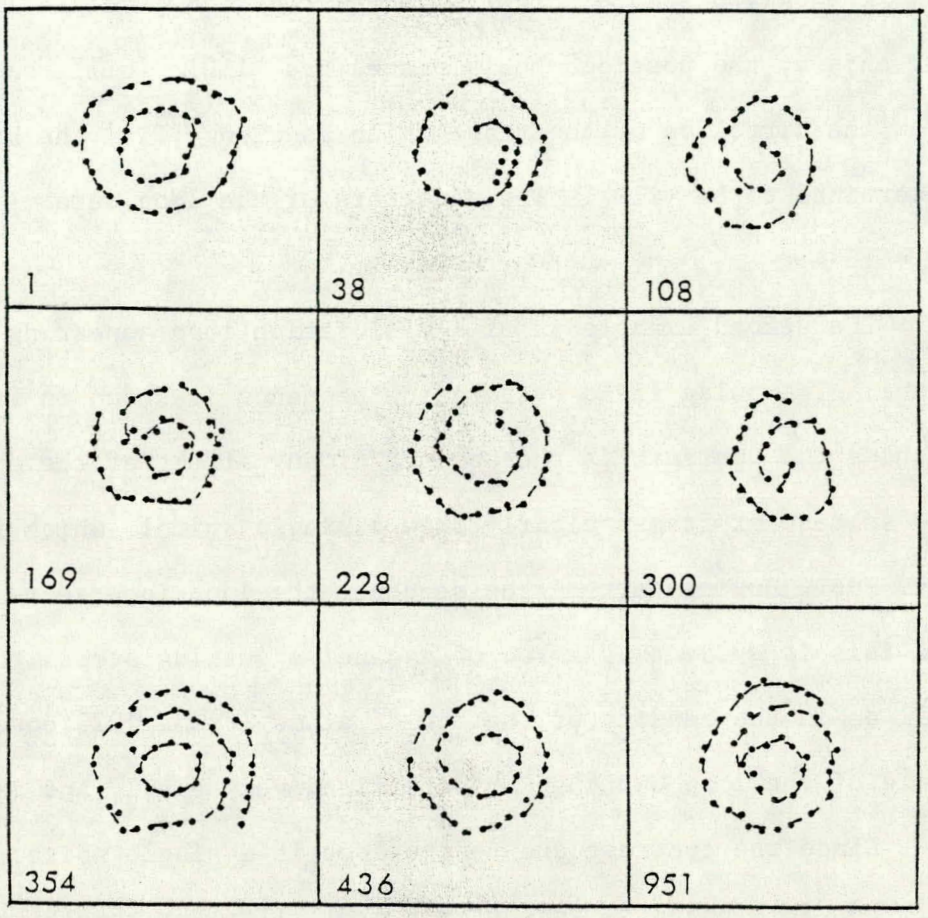

Fig. 78(b): A schematic diagram of atoms near the dislocation loop for the sequence shown in fig. 78(a).

spiral has been outlined in fig. 78b. The trace of the loop is indicated in 228 and was taken to extend from where the spiral begins and where it ends.

The only possible Burger's vector that can give p = 1 is $\vec{b} = \frac{a}{2}[\bar{1}1\bar{1}]$. For this $\vec{b}$, the possible habit planes are $(1\bar{1}0)$, $(0\bar{1}1)$, and (101). From the direction of the trace which is along $[11\bar{5}]$ the habit plane was determined to be $(1\bar{1}0)$. The diameters of the loop were ω_1 = 20 Å and ω_2 = 15 Å.

The second example is of a dislocation loop appearing on a $(\bar{1}41)$ plane. The pulse field evaporation sequence is shown in fig. 79a. Frame 1 shows the contrast is the absence of any effect of the dislocation loop. The subsequent frames clearly show a single spiral, which is outlined in fig. 79b. During part of the sequence the loop intersects the $(\bar{1}72)$ plane and this is evident as a row of vacancies cutting across the plane as well as in the bending of the row of atoms (Frame 1023 onwards). The trace of the loop can then be determined very easily and is drawn in 1203.

Since the contrast due to the loop is a single spira, p = 1. The only possible Burger's vector is $\vec{b} = \frac{a}{2}[111]$. For this $\vec{b}$, the possible habit planes are (101), (110), (011). The trace lies in the direction $[51\bar{1}]$ on the $(\bar{1}72)$ plane which required that the habit plane be (011). The diameter ω_1 = 50 Å; the value of ω_2 could not be determined as the field evaporation was stopped before the contrast due to the loop disappeared.

The third example is of a dislocation loop on $(14\bar{1})$ plane. The pulse field evaporation sequence is shown in fig. 80(a). Frame 1327 shows the contrast when the loop has been evaporated through and the effect of the loop no longer exists. The loop initially intersects the $(14\bar{1})$

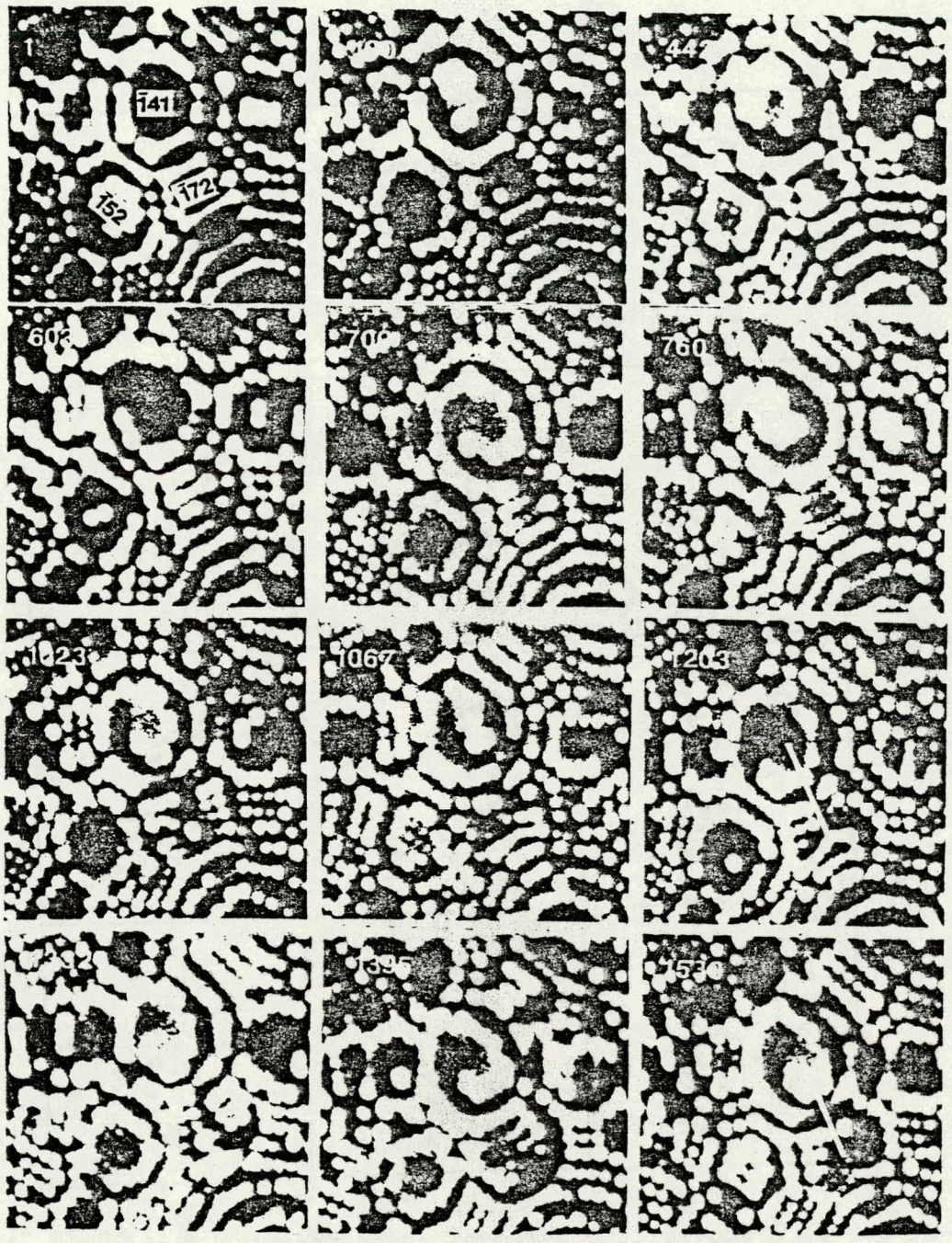

Fig. 79(a): Pulse-field evaporation sequence showing contrast due to dislocation loop emerging on the $(\bar{1}41)$ plane.

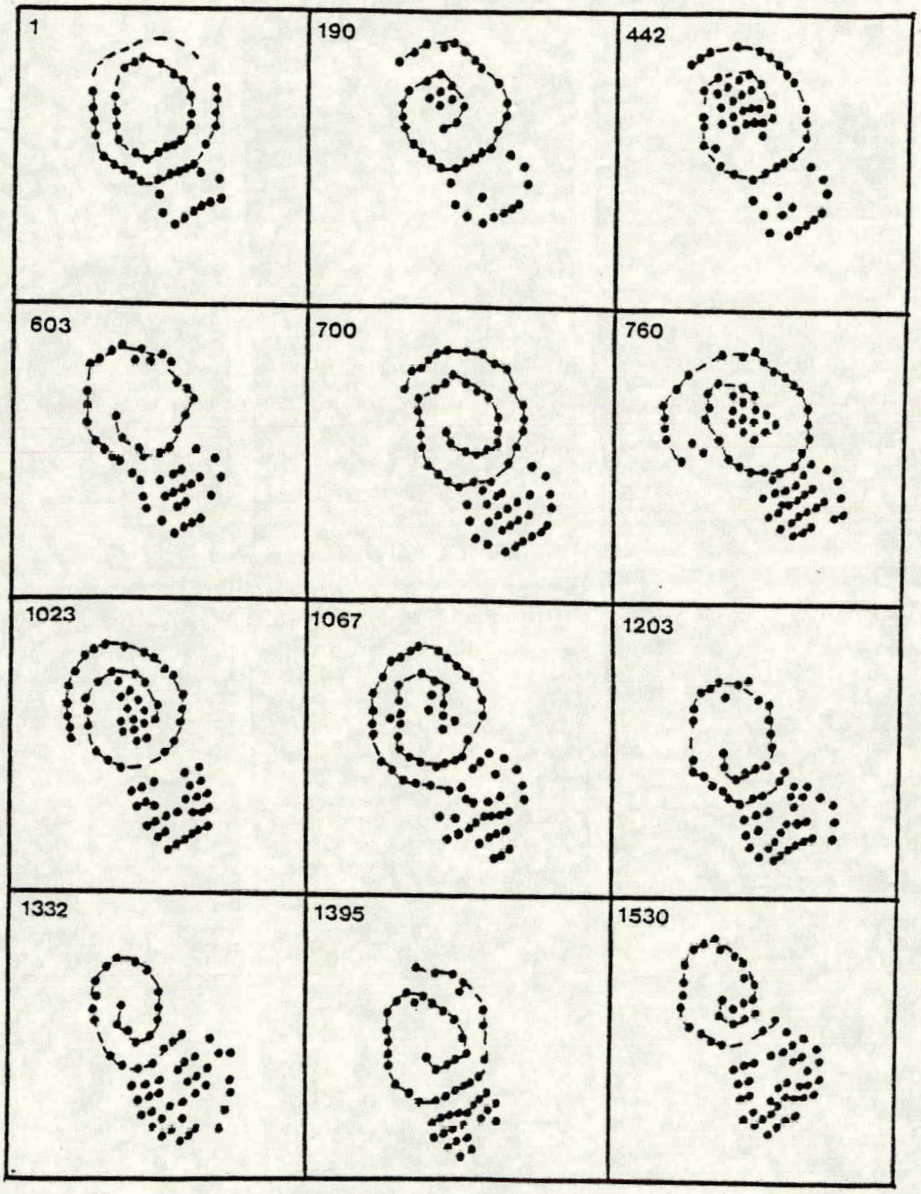

Fig. 79(b): A schematic diagram of atoms near the dislocation loop for the sequence shown in fig. 79(a).

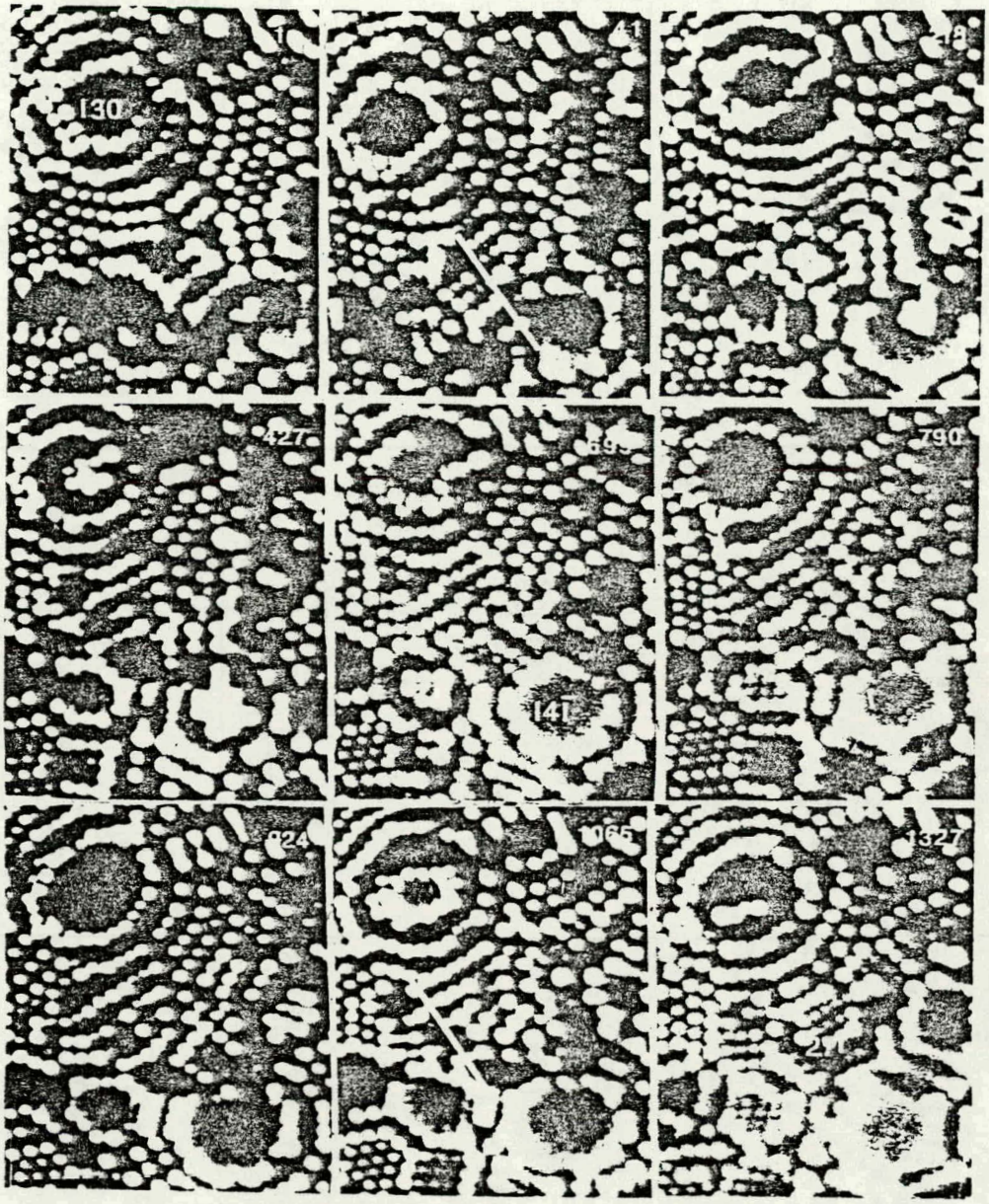

Fig. 80(a): Pulse-field evaporation sequence showing contrast due to dislocation loop emerging on the (14$\bar{1}$) plane.

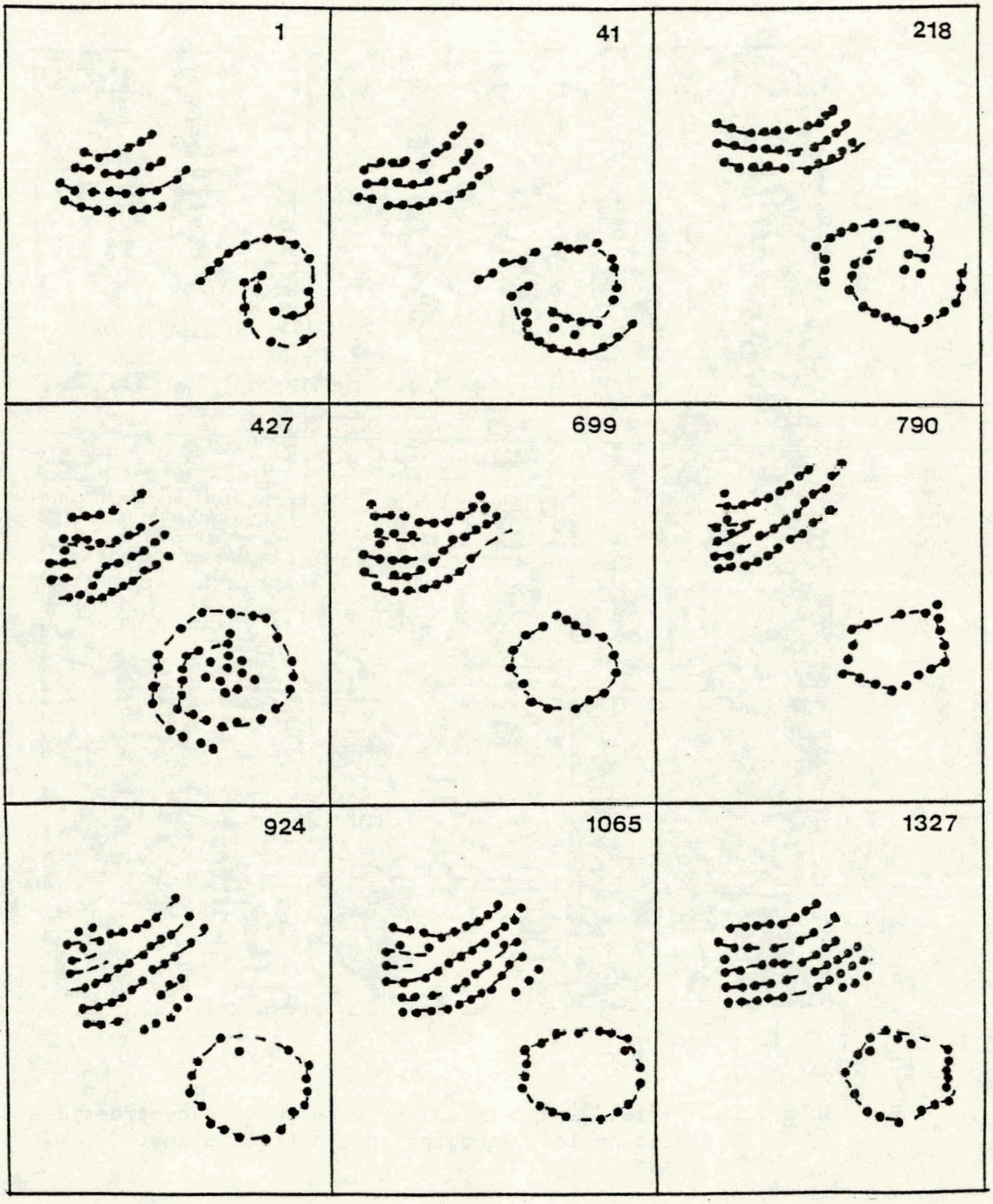

Fig. 80(b): A schematic diagram of atoms near the dislocation loop for the sequence shown in fig. 80(a).

plane as shown in frames 1 to 427 giving rise to a double spiral, which is shown more clearly in fig. 80(b). As the field-evaporation continues the loop moves towards the (130) plane causing a distortion of the rings as is evident in frames 427 to 1066. The loop cuts across the (271) plane as a result of the atoms on the plane do not appear in regular rows as long as the effect of the loop persists. This is clear in frames 1 to 1065. In 1327, the plane appears very regular again. The position of the trace is shown in frames 41 and 1065.

Since the contrast due to the loop is a double spiral p = 2. The possible Burger's vectors are $\vec{b} = \frac{a}{2}[111]$ and $\vec{b} = \frac{a}{2}[\bar{1}1\bar{1}]$. The effect of the loop on the rings of (130) is also to create a double spiral. Only one end of the spiral can be seen, where one end of the loop intersects the (130) plane. The other end of the spiral is not visible as it lies on a different plane. Thus we have p = 2 for the effect of the loop on the (130) plane which means that only $\vec{b} = \frac{a}{2}[111]$ can be the Burger's vector. The possible habit planes corresponding to this Burger's vector are (110), (101), (011). The trace of the loop on the $(14\bar{1})$ plane lies along the $(5\bar{1}1)$ direction which restricts the habit plane to (011). The diameters of the loop were ω_1 = 53 Å and ω_2 = 22 Å.

V.2.2 Discussion

The difference in morphology of the damage between the monomer and dimer irradiations is quite striking. While no dislocation loops were detected in the case of 20 keV Ag and W irridations, almost half the defects in the case of 40 keV Ag_2 and W_2 irradiations were dislocation loops. The close spatial and temporal correlations between the cascades generated by the components of the dimer was believed to be responsible

for the greater degree of collapse. As pointed out earlier, the average recoil energy of an atom in the collision cascade generated by a heavy dimer will be almost twice that of an atom in the cascade generated by a monomer. As a consequence we would expect that the time taken for the energy of the cascade to be dissipated to the surrounding lattice to be larger for the case of dimers than for monomers. Assuming that the collapse of the DZ to a loop involves the motion of vacancies, this greater time will increase the likelihood of collapse.

The nonlinear effects in the DZ's and the collapse of DZ's to loops for dimer irradiations clearly points out the importance of considering the development of the cascade produced by the individual projectiles. Note that the shape of the damage profile is expected to be the same for a beam of 20 keV Ag ions and a beam of 40 keV Ag_2 ions, since the latter breaks up into a beam of 20 keV ions inside the target. But the level of damage and the morphology of damage will be different in the two cases.

V.3 Summary

1. The number of vacancies produced per component ion of a heavy dimer projectile is 1.55 times that produced by a projectile having the same energy and momentum as each of the component ions, indicating the nonlinear effect in cascades having a high energy density.

2. The fraction of defects that are dislocation loops increase dramatically on bombarding with dimers instead of monomers.

REFERENCES FOR CHAPTER V

1. P. Sigmund in Inelastic Ion-Surface Collisions, ed. by N.H. Tolk, J.C. Tully, W. Heiland and C.W. White, (Academic Press, Inc, New York).

2. H.H. Andersen and Bay, H. J Appl Phys. 45, 953 (1974); ibid. 46, 2416 (1975).

3. M. Current, C.Y. Wei and D.N. Seidman, to be published.

4. P. Sigmund, Appl Phys Lett, 25 (1974).

APPENDIX A: FIM CONTRAST DUE TO DISLOCATION LOOPS

A.1 Perfect loops

The dislocation loops were identified by the contrast pattern observed in the FIM micrographs. The contrast expected from a dislocation loop can be understood on simple geometric grounds using the fact that the FIM image can be simulated with remarkable success on purely geometric grounds. This was first demonstrated by Moore[1] in a computer simulation of images of a perfect crystal based on two simple ideas. The first one is that the surface of a field-ion microscope specimen can be atomically smooth and approximately spherical, and the second one following an observation by Müller,[2] that the imaged atoms are those that protrude most from the surface. The image of the region surrounding a pole of a field-ion specimen can be understood if the region is thought to conform to a smoothly curved surface as illustrated in Fig. A-1(a). The diameter of the consecutive crystal planes building up this region is limited by the surface. If only the atoms at the plane edges are considered to protrude enough to image, the projected image of this region is clearly a series of concentric rings, as shown in Fig. A-1(b). Images of faulted crystals are analyzed by first considering the possible surface displacements caused by the fault and thereafter imposing a smooth envelope on the faulted surface as above. Dislocation contrast is derived from the fact, first pointed out by Cottrell,[3] that a perfect dislocation line intersecting a stack of lattice planes will convert this stack into a helical ramp. This is true both for screw dislocations and for any dislocation as long as the Burgers vector ($\vec{b}$) of the dislocation has a component along the normal to the planes. The pitch of the helical ramp is, by the definition of a perfect

dislocation, an integral number of spacings. If this integer is greater than one, the stack of planes is actually converted into several interleaved ramps, each of the same pitch. The effect of a dislocation line emerging from a plane of a FIM specimen is illustrated in figs. A-1(c), (d), and (e). In figs. A-1(c), a dislocation line has converted the stack of planes into a helical ramp and in fig. A-1(d), the effect of field evaporation is indicated. The latter is realized by imposing a smooth surface upon the ramp. The projected image of this configuration is a continuous spiral is shown in fig. A-1(e).

The pitch of the helical ramp can be determined analytically as follows; the pitch is the magnitude of the projection of location onto the plane normal. If the unit normal of the plane is $\vec{n}$, the pitch (p) is given by:

$$p = \vec{b} \cdot \vec{n} \qquad \text{(A-1)}$$

The reciprocal lattice vector $\vec{g}_{hkl}$ of a plane (hkl) is in the direction of the normal to the plane so,

$$\vec{n} = \vec{g}_{hkl} d_{hkl} \qquad \text{(A-2)}$$

and therefore

$$p = (\vec{g}_{hkl} \cdot \vec{b}) d_{hkl} \qquad \text{(A-3)}$$

For a perfect dislocation $\vec{b}$ must be a lattice vector and hence,

$$\vec{g}_{hkl} \cdot \vec{b} = \text{integer} \qquad \text{(A-4)}$$

It is convenient to omit d_{hkl} and to write

$$p = \vec{g}_{hkl} \cdot \vec{b} \qquad \text{(A-5)}$$

The value of p, i.e., an integral number, indicates the multiplicity of the image spiral caused by the dislocation. A case where p = 2 is

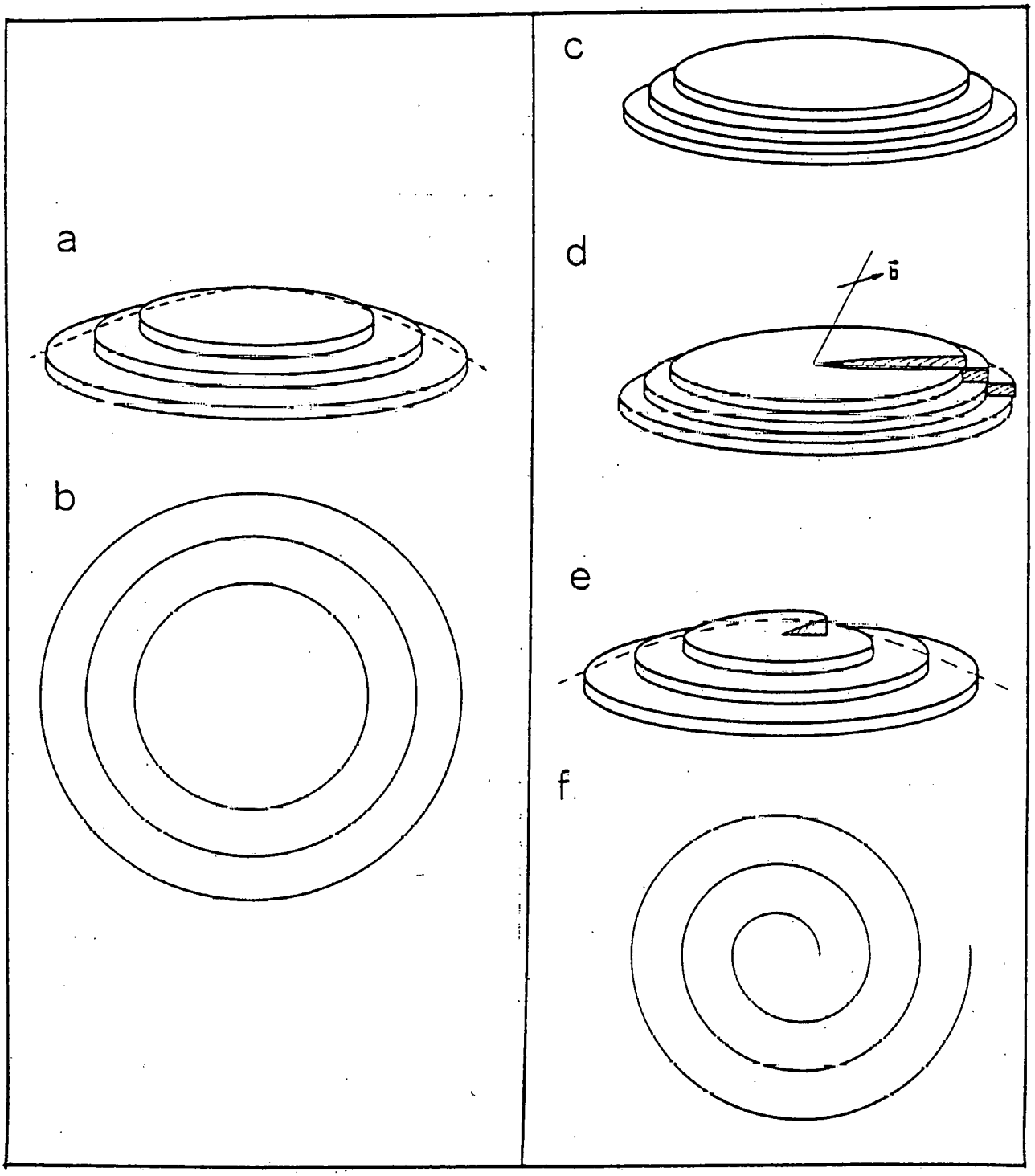

Fig. A-1: Geometrical Image formation of -
(a) - (b) perfect tip
(c) - (f) tip containing the dislocation

schematically illustrated in fig. A-2. It would correspond to, e.g.,

$$\vec{g} = \frac{1}{a}[113] \quad \text{and} \quad \vec{b} = \frac{a}{2}[\bar{1}01]$$

Perfect dislocation loops and dipole pairs are treated simply by combining the effects of single dislocations. The two dislocations in a dipole pair have equal but opposite Burgers vectors. Hence they will cause spirals of opposite sense when emerging in the same pole, and the spiral started at one will end at the other. Plane rings enclosing both dislocations will be unbroken since the net $\vec{b}$ is zero. Figure A-3 illustrates two cases with $|p| = 1$. In fig. A-3(a), the two dislocations emerge on the same plane and in fig. A-3(b) on different plane ledges. Dislocation loops obviously behave to first order, in the same manner. If $p > 1$, a similar system of multiple spirals is expected.

A.2 Faulted loops

A planar fault in a crystal is characterized by a displacement vector $\vec{R}$, which is defined as the displacement of one side of the crystal relative to the other. Where the fault plane cuts the surface of the crystal a step will result. The height of the step normal to the surface plane, is the projection of $\vec{R}$ on the plane normal. A parameter q analogous to p of (A-1) can be defined for the fault.

$$q = \vec{g}_{hkl} \cdot \vec{R}, \qquad \text{(A-6)}$$

where the unit of q is again the lattice spacing d_{hkl}. Since $\vec{R}$ describes a fault it must not be a lattice vector of the primitive lattice

and q may not necessarily be an integer, though it can also be. For stacking faults on {111} in fcc crystals the value of q is always of the form n/3, where n is an integer (including zero).

The image contrast expected when a stacking fault intersects a pole in a field-ion tip is a series of broken plane rings as illustrated in figs. (A-4). Figure A-4(a) and (b) illustrates the pattern obtained for the case of an intrinsic and extrinsic stacking fault, respectively. An intrinsic stacking fault in fcc corresponds to the removal of one (111) plane, the extrinsic to the insertion of one extra (111) plane. This will introduce one fault in the regular stacking sequence (ABCA), in the intrinsic case, and two consecutive faults in the extrinsic case. The broken ring contrast results because the surface of the sheared stack of planes must conform to an approximately hemispherical shape. The case illustrated in fig. A-4 corresponds to the case for which $|q| = 4/3$. The shaded region represents the portion of the plane that is removed by field evaporation in order to obtain a hemispherical surface. Thereafter as the field evaporation continues, the smallest ring will alternately appear on either side of the fault.

Partial dislocations bound stacking faults. The Burgers circuit used to define the Burgers vector of a partial dislocation must start and end on the associated stacking fault. Hence, the Burgers vector of a partial dislocation will be the same as the displacement vector of the stacking fault, or differ from it by a lattice vector. Equation (A-6) is valid for partial dislocations with $\vec{R}$ replaced by $\vec{b}_p$.

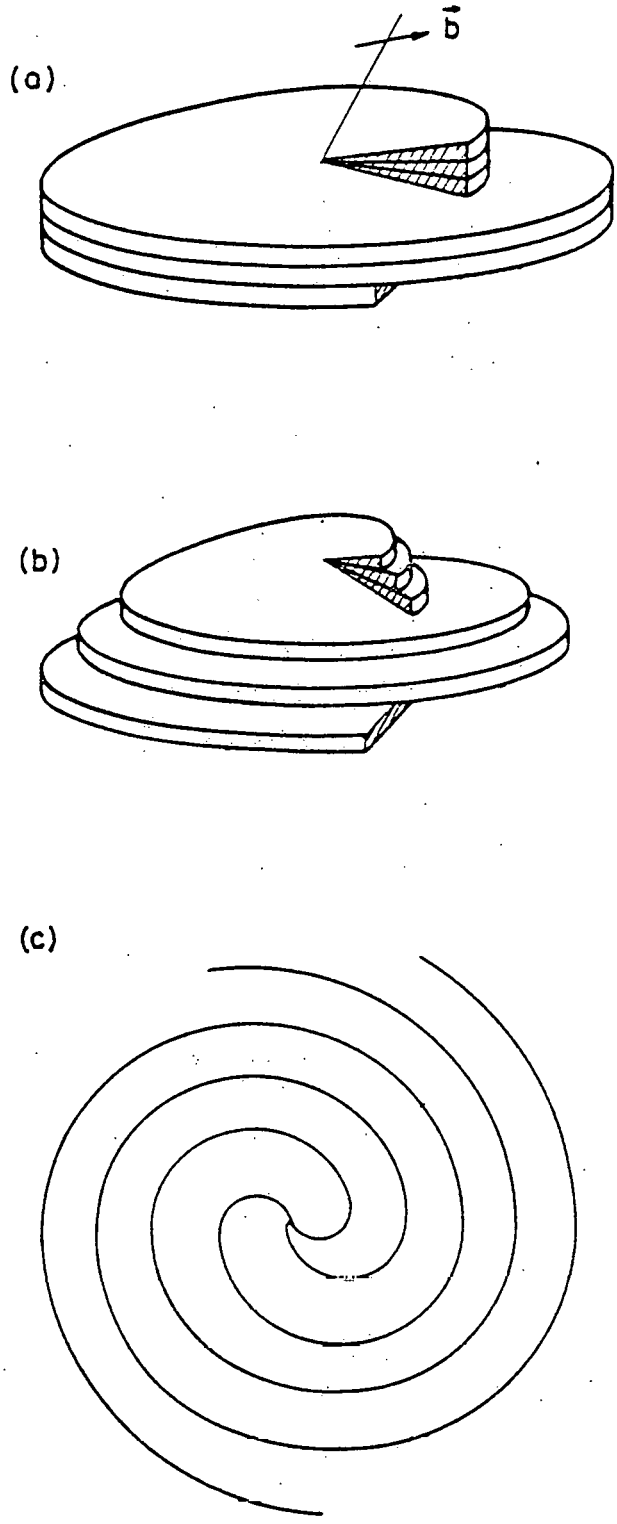

Fig. A-2: FIM image for a dislocation loop for which p = 3.

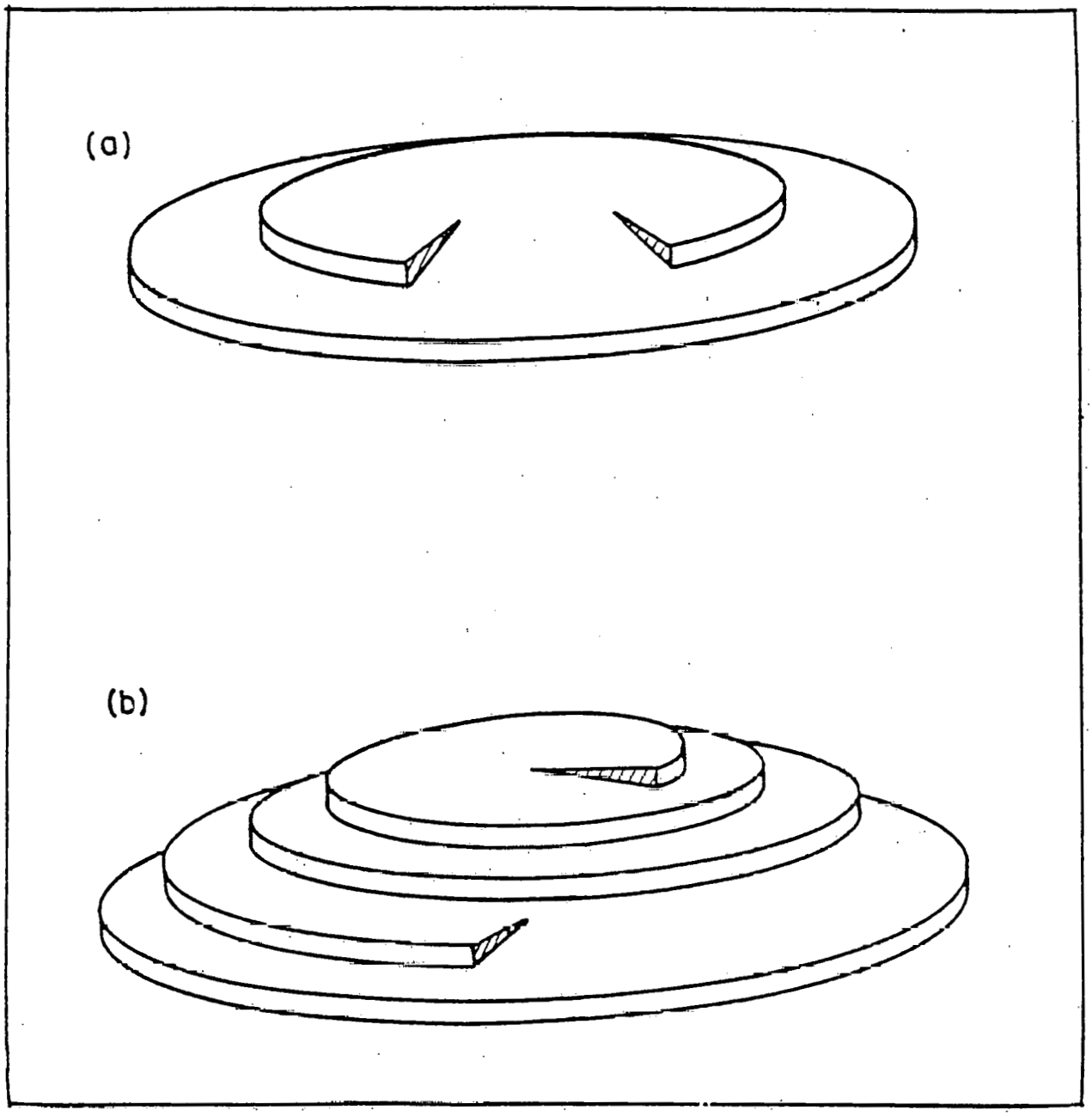

Fig. A-3: Effect of perfect dislocation loop on stack of planes (after Ref. 6).
(a) both dislocations emerging on same ledge
(b) dislocations emerging on different ledges.

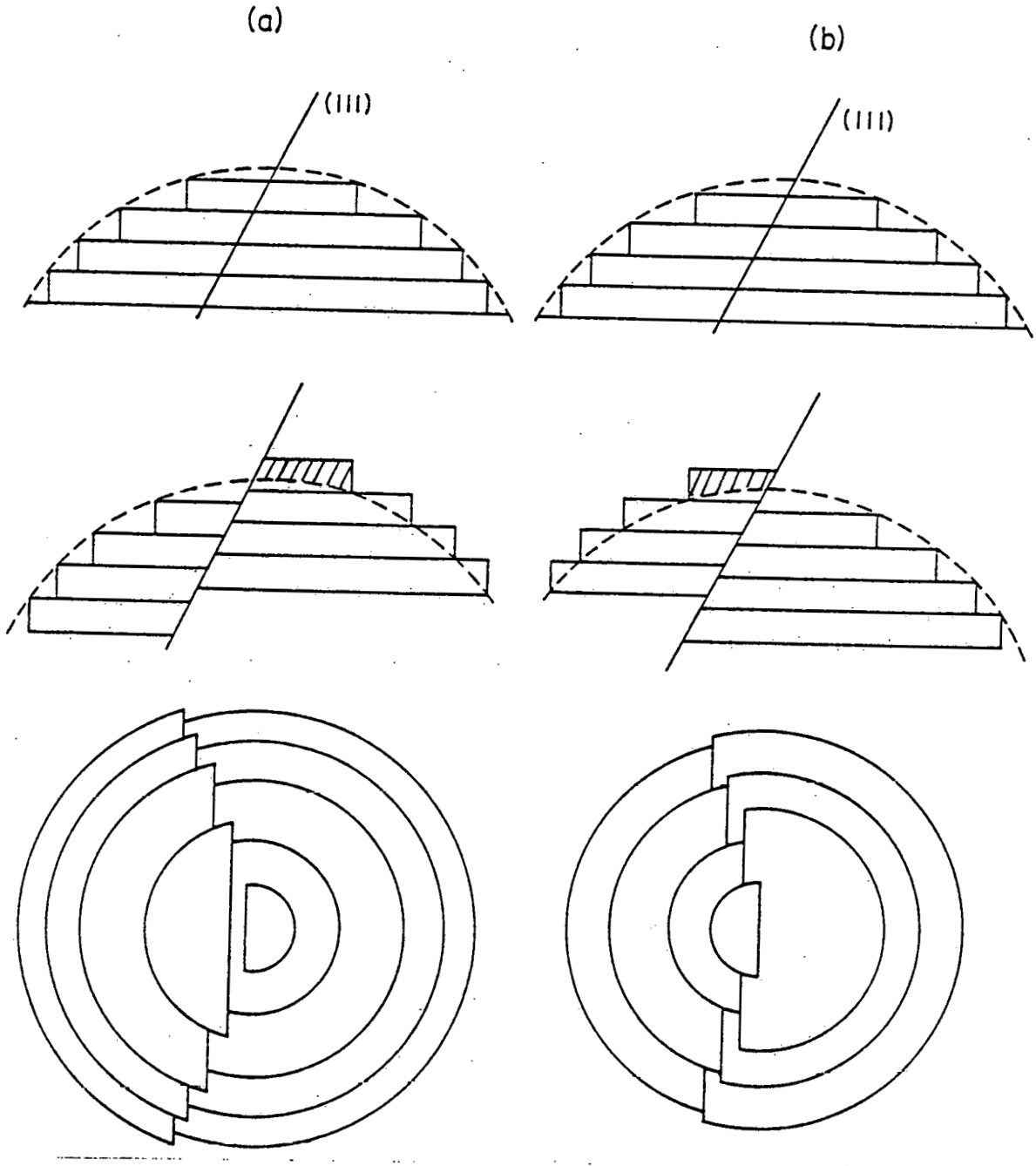

Fig. A-4: Image formation of pole cut by stacking fault. (after Ref. 7)
(a) intrinsic fault
(b) extrinsic fault.

We will be interested primarily in Frank particles which occur only in loops since these are the partials expected from ion irradiations of Pt. The loops are formed by the collection of point defects into disks on the {111} planes. A disc of vacancies, and the collapse of planes above and below the plane of the disc creates an intrinsic loop. A disk of interstitials between two {111} planes constitutes an extrinsic loop. The dislocation bounding the Frank loop is of pure edge character, and its Burgers vector is of the form a/3 <111>.

The image contrast from partial dislocations is a combination of dislocations and stacking fault contrast. The spiral contrast of a dislocation will be stepped if q is non-integral. If q is integral a kink will develop at the fault, because the row of atoms on the plane will be displaced by the projection of $\vec{R}$ onto the plane and will not be continuous across the fault.

When both partials of a dislocation loop emerge in the same pole, rings enclosing none or both of the partials will be unbroken. Rings enclosing one partial will be stepped. This case is illustrated in fig. A-5.

It is possible to distinguish between intrinsic and extrinsic faults in certain cases, provided that the habit plane of the loop is known. The clearest case is of a Frank loop with partials emerging on the same pole. The image in this case consists of two sets of half-rings divided by a fault. A ring enclosing the loop will be unbroken, and it is possible using the plane corresponding to the ring to determine which side of the tip relative to the fault has been pushed up. The side with the smaller rings will be the side that has been pushed up. For example, in Fig. A-6

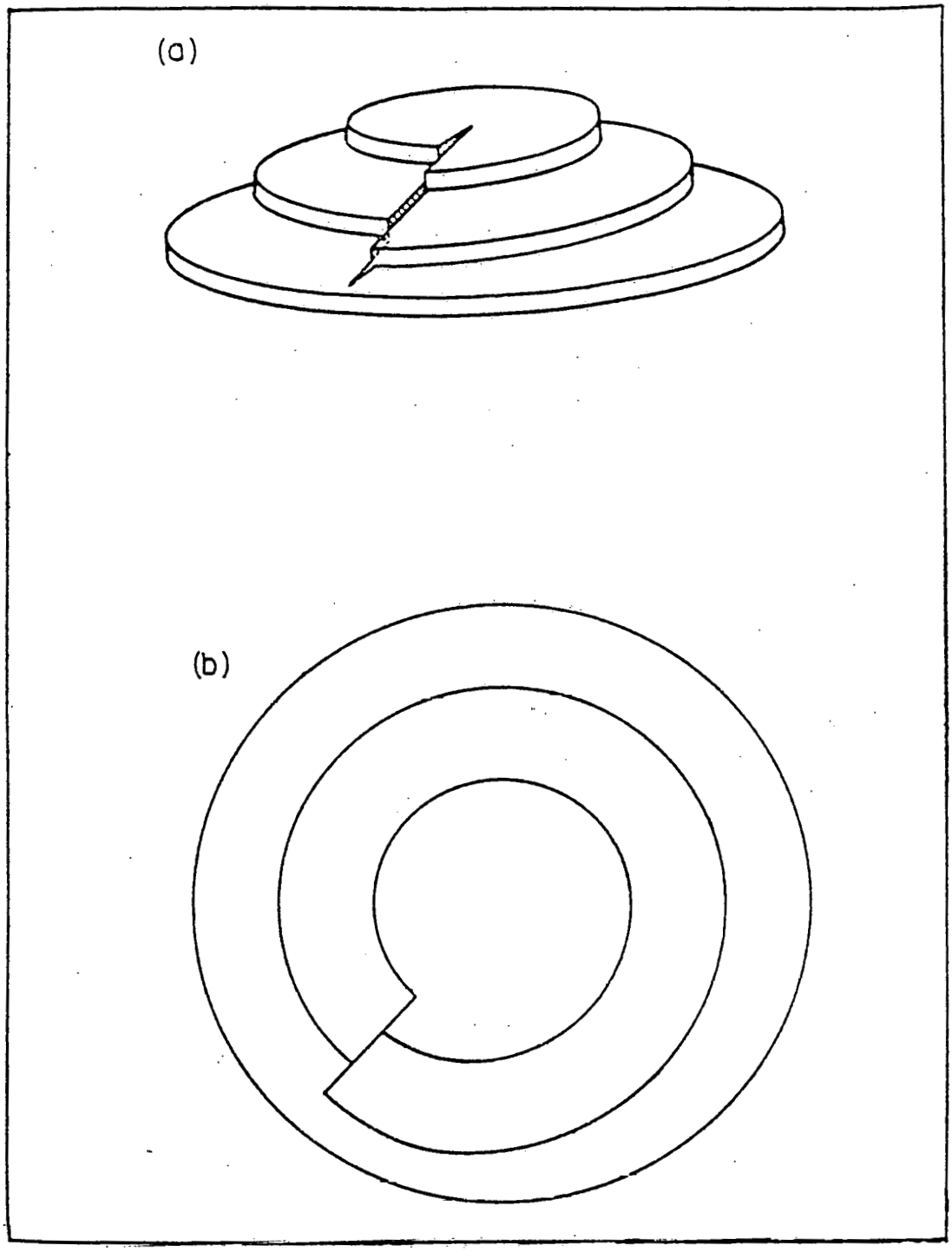

Fig. A-5: Geometrical Image formation of faulted dislocation loop emerging in one pole
(a) stack of planes intersected by one loop
(b) resulting image.

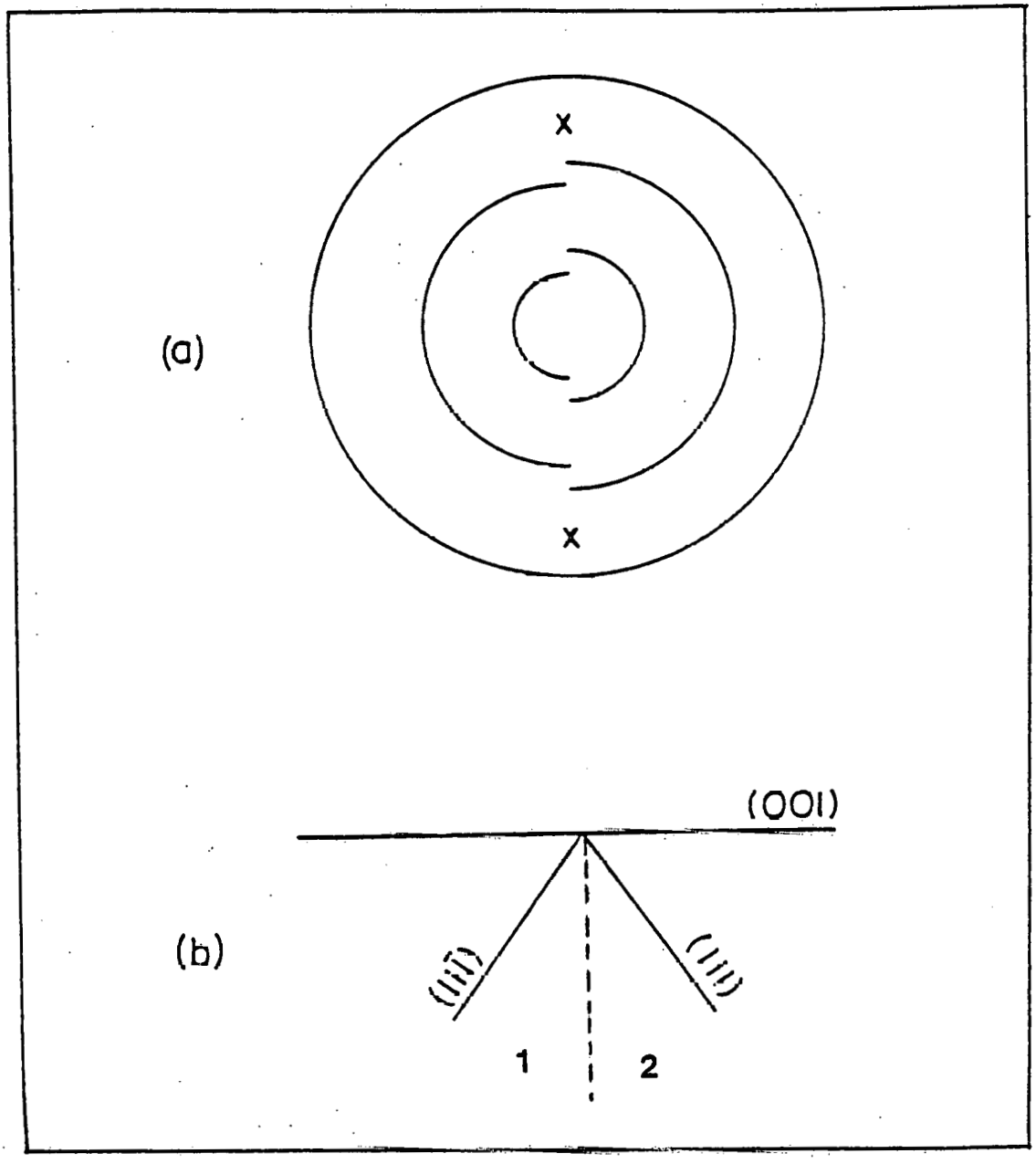

Fig. A-6: (a) Image of a pole intersected by a Frank dislocation loop.
(b) Geometry of the situation in (a).

side 1 of the tip has been pushed up. If the loop is on the $(11\bar{1})$ plane it must be an interstitial loop because the strain field due to the extra disc of atoms will push side 1 up. If the loop is on (111) it is a vacancy loop as this will cause side 2 to move downwards compared to side 1. A similar sort of argument can be used to determine the nature of a loop showing a spiral contrast--from the sense in which the spiral unwinds--if the habit plane is known.

So far we have considered the case of dislocations emerging on low index planes. In higher index planes the same type of spiral structures are expected but the spiral will stand out less prominently because of the small number of rings encompassing the plane. However, the strain field of the dislocation loop will cause the atoms to be displaced from their normal lattice positions. As all the atoms are visible in high index planes, a fact that was utilized to map out the vacancies the displacement of the atoms will reflect itself in a field evaporation sequence that will be different from that observed from a perfect crystal. Figure A-7 shows a section of the crystal containing a vacancy loop. The loop lies in the (111) plane. We shall consider the evaporation sequence of successive (110) planes. Though (110) is a low index plane, the arguments presented subsequently are equally valid for a high index plane, and we have chosen this plane merely for convenience. Since a high index plane normally covers only a small portion of the specimen's surface, we can approximate the spherical envelope by a plane surface in the immediate vicinity of the plane. Successive positions of the tip surface are indicated by dotted lines and as the field-evaporation proceed, the surface moves from right to left. In position 1, the atoms on the plane are

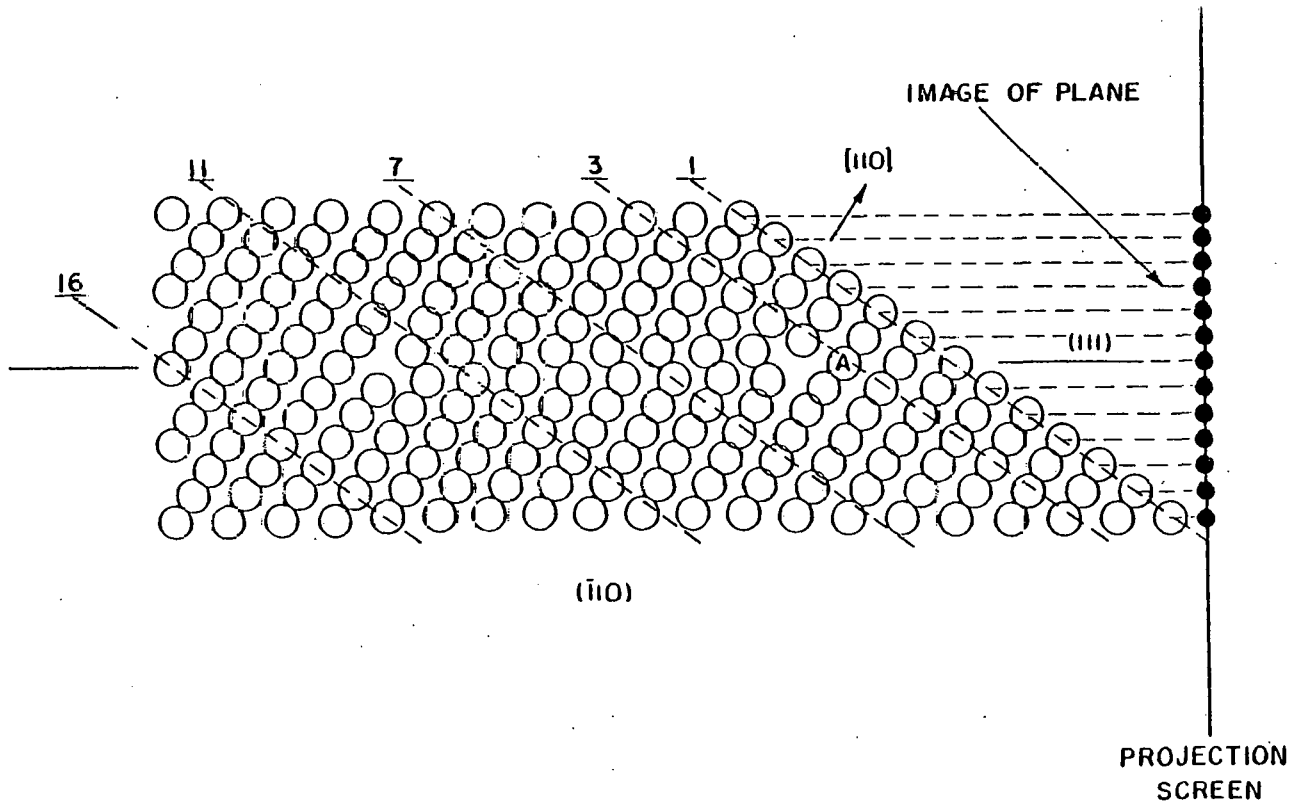

Fig. A-7: View of a plane cutting through a vacancy loop on (111).

hardly affected by the strain field of the loop, and all the atoms on the plane will be imaged. In position 3, the atoms close to the loop are already being sufficiently displaced and the atoms in the middle may not be imaged simultaneously as those at the outer edges. In position 7, the plane intersects the loop. The lower part of the plane will be imaged first and then the upper half. It is clear that at this stage the field evaporation sequence will show an unwinding spiral rather than a series of parallel planes. If track is kept of the atoms in a plane it is possible to detect the vacancies that constitute the loop. As the surface approaches the plane, the positions of the atoms will in all likelihood be changed from their original position, i.e. when the loop was inside the crystal. As the field evaporation proceeds through to 11, the FIM micrograph should stay very much the same. Once the surface has passed through the loop, the field evaporation sequence should once more indicate a series of parallel planes. Thus, a change in the field evaporation sequence of high index planes caused by the strain field of loops, can be used to detect the presence of loops. Uncollapsed clusters of vacancies do not have a long-range strain field, and hence do not greatly affect the field evaporation sequence, a face that allows the mapping of vacancies in the DZ's by the method outlined previously.

The simple geometric model is useful in explaining the contrast expected from dislocations but restricts the configuration to simple types and the positions of the loops to low index poles. It gives the gross features of the contrast and allows in many cases the determination of some of the parameters of the loop but it is not capable of dealing with the finer features of the contrast. Computer simulation should be

more useful. In this method a three-dimensional point-lattice is defined with respect to some coordinate system. This lattice is interested by two concentric hemispherical surfaces so that a thin hemispherical shell is enclosed. The computer is instructed to find those lattice points which lie within the shell, and to plot their coordinates in orthographic projection. The resulting patterns bear a striking resemblance to FIM images. Defects such as dislocations can be incorporated into the lattice; the displacements of lattice atoms caused by them can be computed and the shell model applied to the strained crystal. Several results of computer simulations of dislocations in FIM tips have been reported, which confirm the simple geometric picture outlined before. A more thorough investigation of the contrast expected from small dislocations in f.c.c. metals--such as we would expect to observe in ion irradiated platinum--has been reported by Stolt and Washburn. In principle it should be possible to obtain more information on the nature of the loops observed in FIM by comparing the experimental field evaporation sequence with computer simulations for different configurations fo the dislocation loop.

REFERENCES FOR APPENDIX A

1. A.J.W. Moore, J. Phys. Chem. Solids 23, 907 (1962).

2. E.W. Müller, Z. Physik 156, 399 (1959).

3. A.H. Cottrell, Theory of Crystal Dislocations (Blackie, London, 1964).

4. K. Stolt, PhD thesis, Berkeley and references therein.

5. K. Stolt and J. Washburn, Phil Mag. 34, 1169 (1976).

6. D.A. Smith, M.A. Fortes, A. Kelly and B. Ralph, Phil Mag. 17, 1065 (1968).

7. V.T. Son and J.J. Hren, Phil Mag. 22, 675 (1970).

APPENDIX B: DERIVATION OF RANGE OF ION IN FIM SPECIMEN

Assume that the tip is represented by a hemisphere of radius R. The x,y,z axes are chosen as shown. The equation of the hemisphere is:

$$x^2 + y^2 + z^2 = R^2 \qquad \text{(B-1)}$$

We choose the polar angles θ and Φ as shown. Then:

$$\begin{aligned} x &= R \sin\Phi \sin\theta \\ y &= R \sin\Phi \cos\theta \qquad \text{(B-2)} \\ z &= R \cos\Phi \end{aligned}$$

If the DZ's due to the incoming beam are created at a distance L, along the beam direction, measured from the surface, then the ions will be on the surface of a hemisphere given by:

$$(y + L)^2 + x^2 + z^2 = R^2 \qquad \text{(B-3)}$$

We shall assume that the process of field evaporation causes the hemispherical surface of the tip to move down a distance Δ, without a change in the radius R. We are interested in the distance Δ at which the specimen surface will intersect the center of the DZ.

We will have for the new surface:

$$(z - \Delta)^2 + y^2 + x^2 = R^2 \qquad \text{(B-4)}$$

and then from (B-3) and (B-4):

$$\begin{aligned} \Delta &= [(R^2 - (x^2 + y^2)]^{1/2} - [(R^2 - x^2) - (y + L)^2] \\ &= R\cos\Phi - [R^2\cos^2\Phi - 2yL - L^2]^{1/2} \qquad \text{(B-5)} \\ &= R\cos\Phi\left[1 - \left(\frac{L(2y + L)}{R^2\cos^2\Phi}\right)^{1/2}\right] \end{aligned}$$

expanding

$$\left(1 - \frac{L(2y + L)}{R^2\cos^2\Phi}\right)^{1/2}$$

we get:

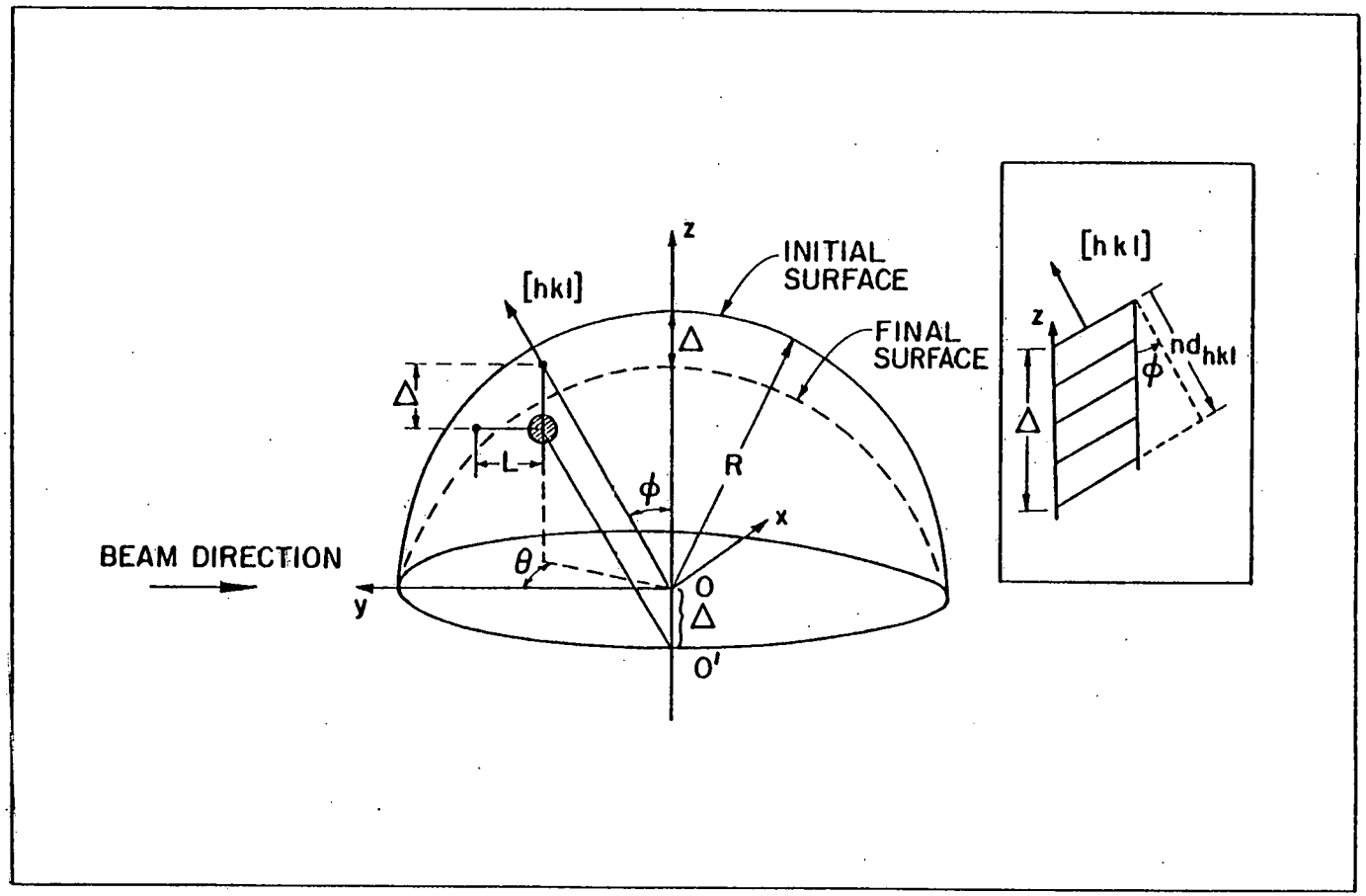

Fig. B-1: Schematic diagram showing quantities used to calculate range of ion in FIM specimen.

$$\Delta = R\cos\Phi\left[\frac{L\tan\Phi\cos\theta}{R\cos\Phi} + \frac{1}{2}\frac{L^2}{R^2\cos^2\Phi} - \frac{d^2\,4y^2}{8R^4\cos^4\Phi}\right]$$

$$= R\cos\Phi\left[\frac{L\tan\Phi\cos\theta}{R\cos\Phi} + \frac{L^2}{2R^2\cos^2\Phi} - \frac{L^2\sin^2\Phi\cos^2\theta}{2R^2\cos^4\Phi}\right] + \ldots$$

$$= L\tan\Phi\cos\theta + \frac{L^2}{2R\cos\Phi}(1 - \tan^2\Phi\cos^2\theta) + \ldots \qquad \text{(B-6)}$$

The second term can be neglected compared to the first if,

$$L\tan\Phi\cos\theta >> \frac{L^2}{2R\cos\Phi}$$

or,

$$\sin\Phi\cos\theta >> \frac{d}{2R}$$

$$d << 2R\sin\Phi\cos\theta \qquad \text{(B-7)}$$

Usually in the FIM, the micrograph only covers

$$\Phi \lesssim 45°$$

$$\sin\Phi = \frac{1}{2}$$

$$d << 2R\cos\theta \qquad \text{(B-8)}$$

If (B-8) is satisfied then,

$$\Delta \simeq L\tan\Phi\cos\theta \qquad \text{(B-9)}$$

If n, [hkl] planes have been evaporated then from the diagram in the inset we have

$$\Delta = n\,d_{hkl}/\cos\Phi \qquad \text{(B-10)}$$

and substituting in (B-9), we get

$$n\,d_{hkl} \simeq L\sin\Phi\cos\theta$$

$$L \simeq \frac{n\,d_{hkl}}{\sin\Phi\cos\theta} \qquad \text{(B-10)}$$

If condition (B-8) is not satisfied, the exact expression derived from (B-3) and (B-4) by eliminating z is:

$$L = R[1 - (\sin^2\Phi \sin^2\theta + (\cos\Phi + \Delta/R)^2)]^{1/2}$$

$$- R \sin\Phi \cos\theta$$

$$= R[\sin^2\Phi \cos^2\theta + 2 \cos\Phi\frac{\Delta}{R} + (\frac{\Delta}{R})^2]^{1/2} - R \sin\Phi \cos\theta \qquad \text{(B-11)}$$